December 2022

Strain Development and Partitioning Across a Transpressional Shear Zone Along a Quartzite- Metagabbro Contact in the Black Hills Uplift, South Dakota

Eric L. Schuemann
University of Wisconsin-Milwaukee

STRAIN DEVELOPMENT AND PARTITIONING ACROSS A TRANSPRESSIONAL SHEAR ZONE ALONG A QUARTZITE- METAGABBRO CONTACT IN THE BLACK HILLS UPLIFT, SOUTH DAKOTA

by

Eric L. Schuemann

A Thesis Submitted in

Partial Fulfillment of the

Requirements for the Degree of

Master of Science

in Geosciences

at

University of Wisconsin – Milwaukee

December 2022

ABSTRACT

STRAIN DEVELOPMENT AND PARTITIONING ACROSS A TRANSPRESSIONAL SHEAR ZONE ALONG A QUARTZITE- METAGABBRO CONTACT IN THE BLACK HILLS UPLIFT, SOUTH DAKOTA

by

Eric L. Schuemann

The University of Wisconsin-Milwaukee, 2022
Under the Supervision of Professor Dyanna Czeck, PhD

The Nemo region of South Dakota's Black Hills offers an ideal location to study transpressional shear zones because it hosts an exposed Archean lithological boundary between two contrasting rheological units, the Boxelder Creek Quartzite (BCQ), a rift-depositional quartzite, and the Blue Draw Metagabbro (BDM), a metagabbro sill, deformed within a ductile shear zone that represents the beginning of main-phase formation of the North American continent as we know it today. The tectonic setting of the Black Hills is at the eastern edge of the Archean Wyoming province, located near the Trans-Hudson Orogeny suture zone that formed between the Wyoming and Superior Provinces.

The methods used in this study to achieve an updated analysis of the Nemo Group Shear Zone (NGSZ) are: (a) measure deformation fabrics (foliation and lineation) of discrete shear zones at the meter to kilometer scale to determine local and regional differences in strain and vorticity; (b) measure the aspect ratios and acute angles of "diamond-shaped" lozenges formed by shear bands observed in the NGSZ metagabbros and quartzites to quantify strain gradients across the NGSZ; (c) compare field data to kinematic models; and (d) supplement mesoscale analysis with microstructural analysis to identify shear sense indicators and record general mineralogical orientations within the Blue Draw Metagabbro and the Boxelder Creek Quartzite.

In order to analyze the Nemo Group Shear Zone (NGSZ) kinematic models with varying inputs for shear obliquity (ϕ), extrusion obliquity (v), and kinematic vorticity (Wk), and shear zone boundary strike and dip were compared to field measurement of lineation and foliation orientations and used to constrain transpression models. Modeling results suggest that the NGSZ zone strikes ~340 with steeply inclined boundaries. It accommodated both left-lateral simple shear and shortening accommodated by pure shear with steep to subvertical extrusion. Modeling results determined the fabrics most closely matched simple shear dominated models with high kinematic vorticity numbers (0.8-0.9). Lineation orientations vary significantly throughout the NGSZ, which is likely due to variations in strain magnitude and small changes in the pure shear related extrusion direction. Modeling results determined that extrusion likely deviated up to 20° from vertical in either NW or SE directions.

Field measurements indicate strain partitioning within the high-strain, heterogeneous metagabbro is dominated by bands of strong foliation that encircle meter to kilometer scale blocks with less deformation. Deformation character ranges from mylonitic to ultra-mylonitic within zones of high strain, and little to no deformation moving to the east and west into zones of lower strain, away from central shear zone. Strain is more homogenous in the BCQ unit, with closely spaced foliations throughout.

The bulk structural data indicates consistency with a transpression model, but the deformation was manifested differently in each lithology. Within the quartzite, the strain was more homogeneous indicated by consistent tightly spaced foliations. Strain geometries indicate plane strain to moderate flattening. Indications of previous deformation fabrics and folds were not generally observed. Within the metagabbro, strain was extremely heterogeneous on the meter scale, and the deformation was at least partially controlled by the influence of prior folds. Fold

hinges nucleated blocks of low strain while high strain zones wrapped around these blocks. Strain shapes ranged from mild constriction to plane strain to flattening to extreme flattening, with most locations having either plane strain or flattening. The kinematic models and strain recorded by the lozenges, primarily suggests simultaneous left-lateral shearing and shortening at the NGSZ. This heterogeneity of deformation may be related to the influence of D_1, D_2, and D_3 fabrics that predated or formed syn-deformational in the NGSZ or may be due to heterogeneity in kinematics or degree of strain within the NGSZ.

TABLE OF CONTENTS

LIST OF FIGURES

LIST OF TABLES

Appendix Tables

ACKNOWLEDGEMENTS

Most importantly, thank you to my beautiful and hilarious field assistant, and future wife, Leah Claire. You have sacrificed so much for me, and you are an expert at taking strike and dip measurements *while* faking rocks are even cool. Thank you also to all my family and friends (D-Bird, Moco, Ryan, Perkins, and fortunately, so many more) who have supported me in life and throughout this enterprise. Who'd a thunk? Geology? Really?

Thank you to Dr. Dyanna Czeck for guidance, patience, and being an honest critic, and to my thesis committee, Dr. Barry Cameron & Dr. Lindsay McHenry. Also, a shout out to all of the UWM Geosciences faculty and fellow students who have been with me for this last leg of my journey. I love this school and I love Milwaukee, thanks in no small part to you.

Thank you to my mentors along the way, Tari Mattox (Physical Sciences Chair, Grand Rapids Community College) & Dr. Ginny Peterson (Grand Valley State University), who gave me the geology bug and have continually encouraged me to chase it.

Special thanks to Dr. Steve Allard, who has championed this area for decades, was the inspiration for this research, and tragically was not able to see the fruits of this project. Rest easy, friend. We sorely miss your brain, your enthusiasm, and your warm smile. And… it turns out you were likely on to something here! I hope that someone is inspired to follow in your footsteps and can use this research as a useful place to start.

Thank you for funding from UWM, the Tobacco Root Geological Society, and the Wisconsin Geological Society. Also, I'd like to thank the residents of Nemo, SD for being welcoming and a lot of fun.

And finally, I'd like to thank my brothers, Dustin and Wade, and my sister, Heather, who always made me feel like a cool older brother and have encouraging me to excel even when I wasn't always feeling so cool. I'm amazed and proud of you all! Thank you to my mother, Candace, for making me brash (in a good way) and encouraging me to not be afraid to go for it. You've never given up on me! And my father, Glenn. Thank you for building me up and teaching me hard work, humility, grace, and humor. I know you would be proud.

I have nothing but gratitude for all of you.

Chapter 1: Introduction

1.1. Purpose

The purpose of this research is to test whether the structures in the Nemo region in the Black Hills, SD are consistent with transpression, determine whether there are kinematic model variables that constrain transpression, and document how transpression is expressed across two rheologically distinct units. The Nemo Group Shear Zone (NGSZ) is located at a Paleoproterozoic boundary that deformed earlier Neoarchean sedimentary and igneous rocks. It has been studied by many previous researchers and many of the structures exhibited by the rocks in this area have been documented and explained within the context of a series of folding events (Runner, 1934; Bush, 1982; Sims & Peterman, 1986; Redden & DeWitt, 2008). However, an updated model proposed by Allard & Portis (2013) suggests that transpression likely occurred at the NGSZ. Allard & Portis (2013) point out that Paleoproterozoic rocks in the Black Hills of southwestern South Dakota record deformation associated with suturing of Precambrian terranes with penetrative fabrics related to shearing in a number of localities, including the NGSZ. Their research characterizes a ~4-km-wide, pervasive, thick-skinned shear zone, which deforms regional-scale folding events in the Black Hills portion of the Wyoming craton. The proposed addition of a transpressional shear zone to the tectonic history of the region is important because it provides evidence for the obliquity of collision not otherwise suggested by the earlier folding events.

The goal of the following research is to identify kinematic models that accommodate the strain fabrics observed in the NGSZ rocks across a contact between two distinct lithologies (a metagabbro and a quartzite) in the Black Hills NE region, which borders the western margin of the southern Trans-Hudson Orogen (sTHO). Kinematic modeling offers possible explanations for

two important questions about the Precambrian assembly of the North America continent. First, can transpression models presumed from the data offer a more accurate recounting of the tectonic history of suturing between the Wyoming and Superior provinces during the sTHO deformation? Second, what constraints can be placed on transpression models that contribute to the fabrics present in the NGSZ based on extrusion obliquity, kinematic vorticity, and the geometry of the shear zone boundary? Crucially, an additional variable of fluid interaction as an agent of contact metamorphism, either during shear deformation or post-deformation, must also be considered in addition to the structural fabrics that record regional metamorphism during transpression.

In the recent community document outlining "Grand Challenges" in tectonics (Huntington & Klepeis, 2018), understanding variations in rheology and fault zone/ ductile shear zone behavior throughout the lithosphere are considered critically unresolved problems. Developing a quantitative understanding of how the lithosphere deforms at all depths, on time scales ranging from microseconds to billions of years, is a key factor in understanding the evolution of planetary formation and processes. A key challenge in understanding these processes is the ability to quantify the mechanical properties of rocks in nature and to understand how rheology and the existence of prior fabrics control physical deformation processes. Rheology is complex and depends on intrinsic properties (rock type, mineralogy, grain size) and also external factors such as temperature, pressure, stress, and the influence of hydrothermal fluids. The rheology of different rock types in the mid-crust, given the same bulk stress conditions, influences how strain is distributed and/or localized with more competent rocks generally displaying heterogeneity and weaker rocks generally displaying more homogeneity (Fossen, 2016).

1.2. Contribution of the Black Hills

This work will contribute to the understanding of the tectonic evolution of the Black Hills, South Dakota. Various researchers have extensively studied the Precambrian and Phanerozoic deformation of the Black Hills region over the last century; however, a concise mapping of more localized fabrics and other observable structures has not been performed for at least ten years, and no detailed structural mapping within the last twenty years (Runner, 1934; Bush, 1982; Sims & Peterman, 1986; Redden & DeWitt, 2008). Since that time, advances in the analysis of transpressional shear zones has shed new light into the kinematics of transpressional deformation and the partitioning of strain that allows structural geologists to better interpret the resulting structures in the field (Tikoff and Fossen, 1993; Czeck and Hudleston, 2003; Díaz-Azpiroz et al., 2019). Transpression results from oblique collision and, in its most general form, contains components of horizontal simple shear parallel to the zone boundary and pure shear across the zone boundary that accommodates shortening (e.g. Tikoff and Fossen, 1993). More complex models of transpression allow for inclined boundaries (Fig. 1-1B), an oblique simple shear component (Fig. 1-1A, C), and/or an oblique extrusion direction that allows extension related to pure shear to be in a nonvertical orientation (the extrusion direction shown in Fig. 1-1C).

Recent research has documented structural features throughout the Black Hills region including S-C fabrics, lineations, and foliations that are consistent with transpression models (Allard & Portis, 2013; Greenberg & Allard, 2019), warranting an updated analysis of structural features which may allow for an updated transpressional model for the Black Hills. The hypothesis that this area did indeed undergo transpression and includes fabrics indicative of both pure and simple shear can be tested by comparing shear fabrics, the partitioning of strain within and across the lithological contact, and hopefully quantify the amount of shortening versus lateral

displacement. Through structural field mapping, the goal is to document the structures across the Nemo Shear Zone to determine how strain is accommodated in the two contrasting lithologies into discrete versus localized structures and whether the transpressional strain components (left-lateral strike-slip, thrust, flattening and/or constriction) vary spatially within and between lithologies. Some microstructural fabrics can also confine some of the conclusions derived from the field observations and modeling, finally providing a generalized update for the deformational tectonic history of the sTHO, and the Black Hills uplift in particular.

1.3. Contribution of the Nemo Group Shear Zone

The NGSZ offers an ideal location to study these challenges because it hosts a small (<4 km along strike) moderately-exposed lithological boundary between two contrasting rheological units, quartzite and metagabbro, contained within a much larger (100 km along strike) ductile shear zone. The Blue Draw Metagabbro (BDM; **Fig. 1-2**, denoted as Xbd on Redden & Dewitt, 2008 map) is a relatively rigid unit surrounded by the less competent Boxelder Creek Quartzite (BCQ; denoted as Xbc on Redden and Dewitt, 2008 map).

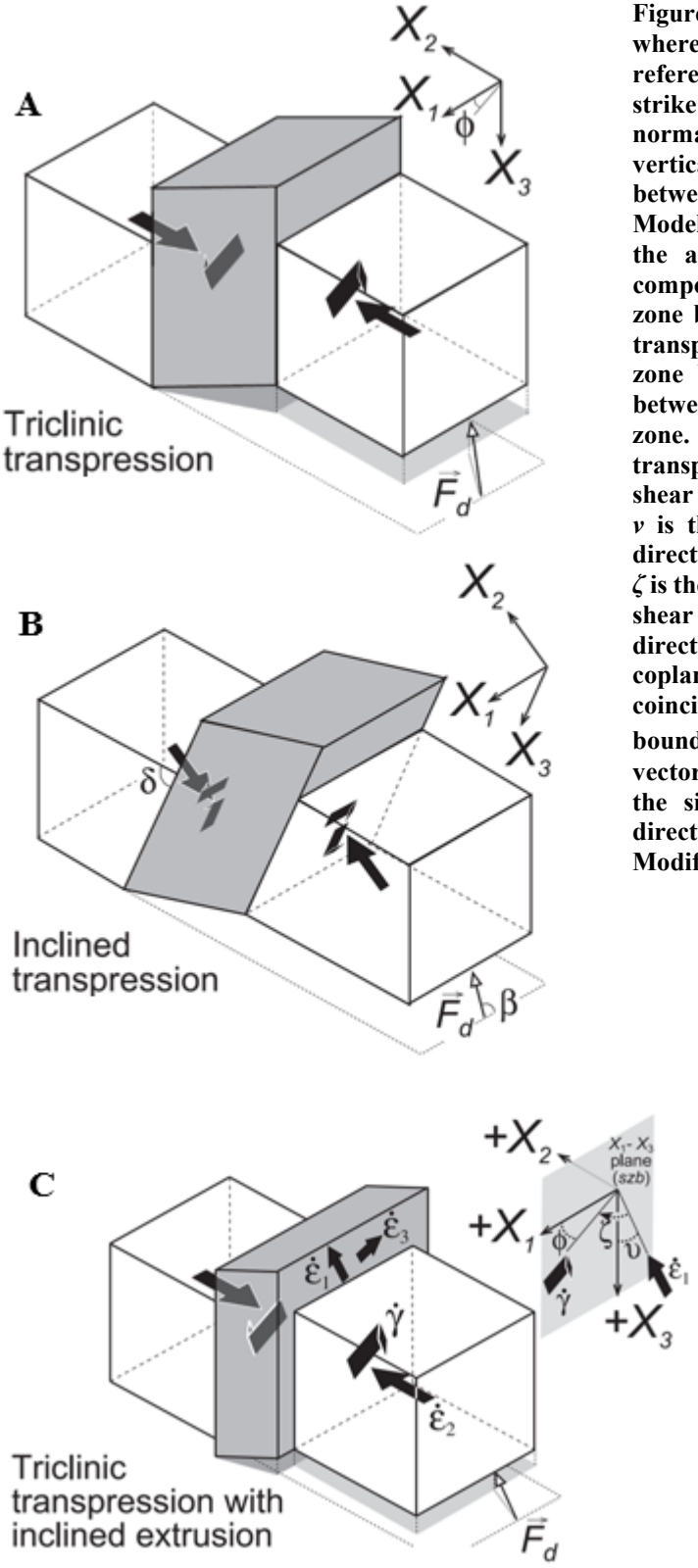

Figure 1-1: Transpression models where X_1, X_2, X_3 are coordinate axes of reference frame with X_1 parallel to the strike of the shear-zone boundary, X_2 normal to the boundary, and X_3 is vertical. F_d is the convergence vector between the zone-bounding blocks. (A) Model of triclinic transpression. ϕ is the angle between the simple-shear component and the strike of the shear-zone boundary. (B) Model of inclined transpression. δ is the dip of the shear-zone boundaries, and β is the angle between F_d and the strike of the shear zone. (C) Model of triclinic transpression with inclined simple shear and inclined extrusion direction. υ is the angle between the extrusion direction and the dip of the shear zone. ζ is the acute angle between the simple-shear direction and the extrusion direction. The three angles are coplanar and located in the surface coinciding with the shear-zone boundary (X_1-X_3 plane). $\dot{\varepsilon}_{1,2,3}$ are vectors of pure shear. Note that both the simple shear and the extrusion directions are parallel to plane X_1-X_3. Modified from Fernández et al., 2013.

44.2369° N,
103.4726° W

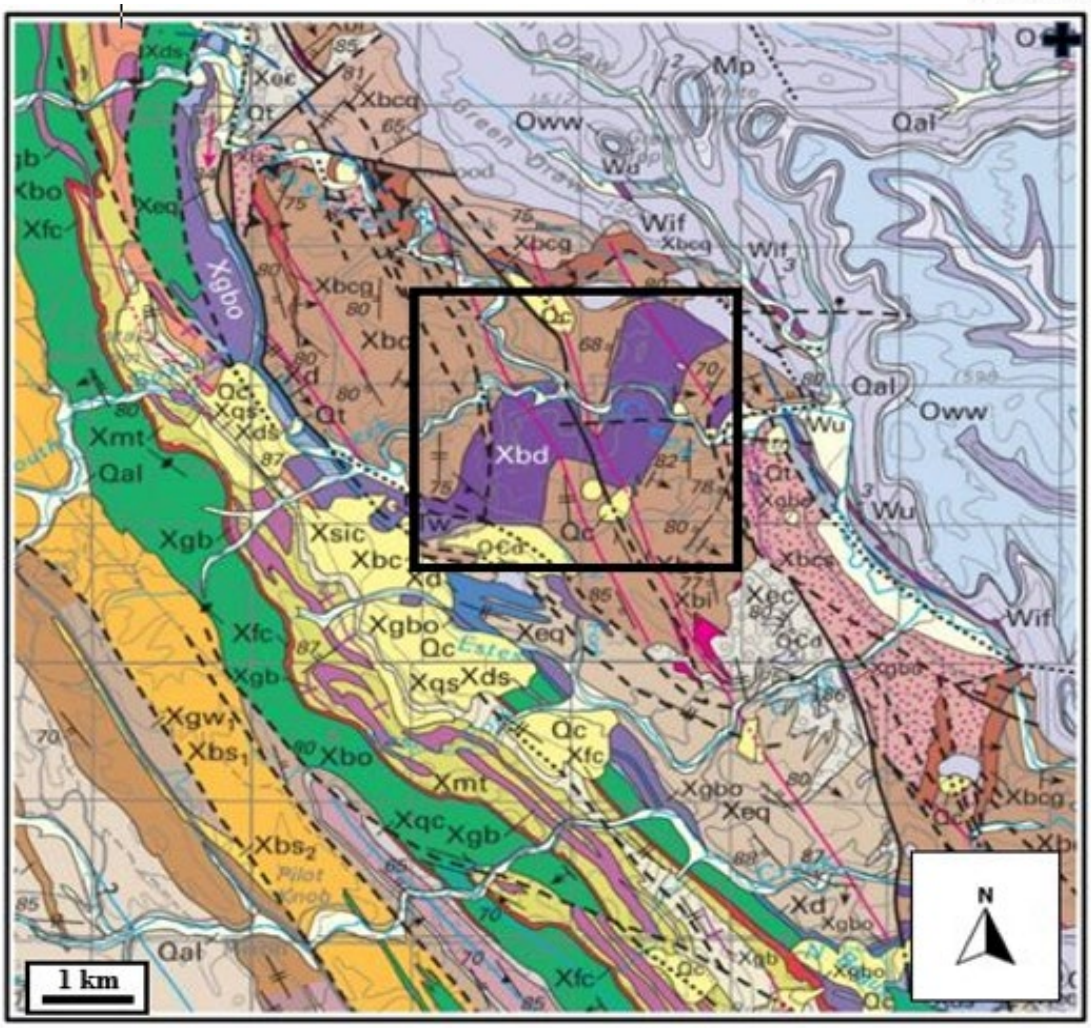

Figure 1-2: Geological map of Nemo Group rocks (black box). Xbd (purple): Blue Draw Metagabbro. Xbc (brown): Boxelder Creek Quartzite. Pink lines are faults that bound and are parallel to the hypothesized Nemo SZ. Modified from Redden and DeWitt, 2008.

Chapter 2: Geologic Background

2.1 Tectonic Setting

The Black Hills (**Fig. 2-1**) are located at the eastern edge of the Archean Wyoming province, located near the Paleoproterozoic Trans-Hudson Orogeny (THO) suture zone that joined the Wyoming and Superior Provinces (Gosselin et al., 1988). The oldest rocks exposed in the Black Hills are Neoarchean ~2.60 Ga granites and metasedimentary rocks, proposed to have formed along the margins of the Wyoming province during crustal accretion (Allard and Portis, 2013). The Archean rocks preserve an extensive geologic history of early subduction events followed by Paleoproterozoic rifting events (evidenced by deposition of sedimentary layers and mafic dikes) presumably related to the late Archean breakup of the Superior craton. A southerly (present-day direction) collision may have followed this rifting stage resulting in the Central Plains Orogeny (CPO) at ~1.63-1.80 Ga, as evidenced from magnetic and gravity anomalies in Nebraska, Kansas, and Missouri (Sims & Peterman, 1986). While this has been differentiated from the THO (Sims & Peterman, 1986), some rocks in the Black Hills share this relative age, unlike the THO to the north. Following the CPO collision, the Black Hills experienced a prolonged Paleoproterozoic collision, part of the THO, with multiple deformation phases locally identified (Allard & Portis, 2013).

2.2. Trans-Hudson Orogeny

The Canadian Shield is comprised of Archean island-arc accretions and represents the earliest stable mass of cratons and micro-cratons from which Laurentia, and later North America, would form (Hoffman, 1988). Within this system, the THO represents the largest and most

continuous preserved collisional belt formed in the Paleoproterozoic, during the interval 2.0 – 1.8 Ga (Corrigan et al., 2009). St. Onge et al. (2006) suggested that the THO is analogous in character, duration, scale and crustal structure to the present-day continent-continent collision in Himalaya-Karakoram-Tibetan Orogeny (**Fig. 2-2**). The THO extends N-NE from present-day South Dakota, in a region defined by Bedrosian and Finn (2021) as the southern Trans-Hudson Orogeny (sTHO), where it is presumed to be truncated to the south by the CPO (Sims & Peterman, 1986). It crosses approximately 3000 km of North America and Greenland into Scandinavia and was part of the supercontinent Nuna prior to the opening of the North Atlantic Ocean (Hoffman 1988; Corrigan et al., 2009; Bedrosian & Finn, 2021).

The sTHO formed during the closing of the Eastern Manikewan Ocean (**Fig. 2-3**), with subduction of the oceanic plate initiating at <1.86 Ga. The tectonic activity is dominated by convergence of the Hearne-Medicine Hat Block-Wyoming cratonic assemblage at the western margin and the Superior craton at the eastern margin, along with the incorporation of various micro-cratons, island arcs, and magmatic zones including the Sask micro-terrane and overlying Flin Flon arcs (Hoffman, 1988; Corrigan et al., 2009; Bedrosian & Finn, 2021). Conspicuously absent in this model is the influence of the subsequent CPO, which favors the view that the CPO and THO are not correlated, and that in fact the CPO (along with the Cheyenne belt and the Spirit Lake tectonic zone) may have formed due to convergence and subduction of the Yavapai province beneath the THO at ~1.78 – 1.71 Ga (Bedrosian & Finn, 2021). The THO contains intraoceanic rocks (shelf carbonates, quartz arenite, shales, greywacke turbidites, and fluvial arkose) flanked by ensialic belts (Hoffman, 1988). Extensive evidence for this nearly full Wilson-cycle sequence is found well-exposed throughout Manitoba, Saskatchewan, and northern Ontario as accretionary sedimentary packages, thin-skinned thrust belts complexes, arc assemblages, and subduction

driven magmatic suites, all of which formed or altered Archean basement lithologic margins (Hoffman, 1988; Bickford et al., 1990; Corrigan et al., 2009).

2.3. Models for Black Hills Formation

The north-south trending portion of the sTHO, which represents the east-west collision of the Archean Wyoming and Superior provinces (Gosselin et al., 1988; Hoffman, 1988; Chamberlain et al., 2002 & 2003; Bedrosian & Finn, 2021), contains the present-day Black Hills Uplift at its southern extent and is largely concealed by the Phanerozoic sediments of the northern Great Plains (Sims & Peterman, 1986; Redden et al., 1990; Sims et al., 1991). The problem outlined by Redden et al. (1990) when attempting to correlate the Black Hills Uplift to the THO is that the area lies 300 km from THO units in Wyoming and 1100 km from units in Saskatchewan. However, first-order gravimetric and aeromagnetic data, along with U-Th-Pb dating, allowed for subsurface modeling by Redden et al. (1990) and Dahl et al. (1999; 2006) to suggest that the Dakota Orogeny and the subsequent Black Hills Uplift formed syn-deformationally to the Canadian portion of the THO.

Redden et al. (1990) provided a tectonic interpretation of the events that formed the Black Hills, though subsequent research has provided alternative models (Sims et al., 1991; Dahl et al., 1999; Chamberlain et al., 2003; Dahl et al., 2006; Boening & Nabelek, 2008). The early model by Redden et al. (1990) and later models are largely similar in terms of deformational sequences in the Paleoproterozoic (<2.0 – 1.71 Ga). However, a key difference lies in the late Archean tectonic setting, notably the geochronology of basin formation and sediment infill which form the oldest units in the Black Hills. Redden et al. (1990) placed the initial deposition of eroded Archean and

Paleoproterozoic clastic sediment (correlated with passive margin deposition of the 2.3 – 2.0 Ga Snowy Pass Supergroup) into an extensional setting within the Wyoming craton, which contains western-sourced fluvial and marine deposits infilling an eastern basin. Following this long sequence, gabbro sills intruded at 2.17 Ga and were subsequently folded between 2.17 and 1.98 Ga due to plate margin contraction related to the THO. Deepening of the basin then occurred at ~1.96 Ga, as evidenced by deposition of black shales, turbidites, and tholeiitic basalt emplacement. Redden et al. (1990) posited that due to the composition of these marine sediments, the intracontinental basin model is favored over a back-arc setting.

The deposition of turbidites was then briefly interrupted by an "unknown" deformational event (as evidenced by extensional basaltic flows, with tuffs dated at 1.88 Ga) followed by the deposition of a thick and widespread shale unit (younger than 1.88 Ga but older than 1.71 Ga) in the central Black Hills. This was possibly coeval with the bulk of the 1.85 – 1.71 Ga folding events (Redden et al., 1990). Nappe-like folds (F_1) occurred in this interval with predominantly east-northeast fold axes with shallowly southeastern dipping axial planes. Rocks were subsequently subjected to F_2 folding with steep axial planes and north-northwest fold axes. The 1.71 Ga Harney Peak Granite then formed due to melting of Archean and Paleoproterozoic crust, possibly related to subduction of the CPO (Yavapai northern margin) to the south (Bedrosian & Finn, 2021). This intrusion is the primary temporal constraint of bulk deformation in the Black Hills as F_1 and F_2 structures are altered or deformed by this younger igneous activity (Redden et al., 1990; Sims et al., 1991).

More recent models diverge with respect to the intrusion dates of gabbroic sills, notably from which (for the purposes of this study) the BDM was later formed (Dahl et al., 2006) and therefore constrain the deposition of the BCQ to >2.48 Ga. These updated models propose from

$^{207}Pb/^{206}Pb$ upper- intercept ages that the gabbroic sills that later metamorphose to the BDM are from continental breakup and rifting between the eastern edge of the Wyoming craton and the southern edge of the Superior craton at 2.48 Ga ± 6 Ma. Dahl et al. (2006). These models also propose that layered mafic intrusions of similar ages and thickness occur as far east as Sudbury, ON, and that these intrusions spatially align with Kenorland supercontinent reconstructions of the positions of the Wyoming and Superior cratons. This hypothesis has since been supported by subsequent research (Ernst & Bleeker, 2008; Ernst et al., 2013; Ciborowski et al., 2015) that examines the mafic dike swarms associated with the Matachewan LIP in both the Superior and Wyoming provinces that possibly marks the initiation of the breakup of Kenorland and created the environment in which the THO sequence initiated with ~2.0 Ga convergence of the then migrated Wyoming province to the western margin of the Superior province (Corrigan et al., 2009).

2.4. Precambrian Geology of the Black Hills

A substantial portion of the overall geology of the Black Hills is defined by Precambrian activity (**Fig. 2-4**). The 2.60 – 2.50 Ga Neoarchean rocks (Bear Mountain metasedimentary rocks in the SW (poorly exposed) and Little Elk Granite (18 km NE of Nemo) were formed along the edge of the Wyoming craton during crustal accretion, with subduction related melting of crustal granodiorite and melting of the overlying sedimentary rocks during crustal thickening (Allard and Portis, 2013). While the overlying metasedimentary units (including the BCQ; ~2.49 Ga) may bridge the Archean and Paleoproterozoic, the crystalline rocks exposed in the Black Hills (including the BDM at 2.48 Ga, though not necessarily related to later < 2.48 – 1.71 Ga felsic and mafic intrusions) are Paleoproterozoic (Dahl et al., 2006; Allard and Portis, 2013). The central portion of the Black Hills contain most of the post 2.48 Ga igneous rocks, including gabbroic sills

(1.883 Ga ± 5 Ma), alkalic tuffs, welded debris flows, conglomerates, and quartzite (1.884 Ga ± 29 Ma). Following a long period of deformation (~1.88 – 1.715 Ga), the Harney Peak granite and associated pegmatites intrude in the central and south-central portions of the Black Hills (Redden & Dewitt, 2008).

2.5. Nemo Group Geology

The Nemo Group (NG) contains rocks that were deposited or intruded during the Neoarchean (≥2.48 Ga). The group contains metamorphosed clastic sedimentary rocks, fining up from metaconglomerates to quartzites and phyllite (Redden et al., 1990), that were deposited in a possible transgressive sequence in the post-breakup rift basin between Superior and Wyoming. This group contains the Wyoming craton-bearing remnants of the Matachewan LIP mafic sills, locally identified as the BDM, which intruded into the upper portion of the BCQ sediments at 2480 ± 6 Ma (Dahl et al., 2006). The NG was therefore deposited before the bulk of the Black Hills folding events (1.85 – 1.71 Ga) and exhibits correlated pre-D_1 deformational fabrics possibly associated with the Redden et al. (1990) "unknown" deformation event (**Fig. 2-5**; Dahl et al., 2006; Redden & Dewitt, 2008; Allard & Portis, 2013). Observed F_1 fold nappes, related to D_1, caused by north verging island-arc accretion at ~1780 Ma tilted and thickened the rock sequence without producing a local penetrative fabric. F_2 upright folds with east-west axial surfaces, recorded by axial planar cleavage, subsequently refolded F_1 and may record the suturing of the Wyoming and Superior blocks between ~1770 Ma to ~1747 Ma (Redden et al., 1990; Dahl et al., 1999 & 2006; Allard & Portis, 2013).

F_3 steep folds with NW-SE striking axial planes that fold F_2 features (1740-1715 Ma), once thought to be absent in the Nemo area (Redden, 2008) or minor localized features related to Harney

Peak intrusion (Redden and DeWitt, 2008), may be more prevalent in the Black Hills region than previously thought (**Fig. 2-6**; Allard & Portis, 2013). D_3 may have been a substantial thick-skinned event resulting in synchronous shearing and folding. D_3 is likely the result of a ductile transpressional shear zone that has left-lateral and east-side up components of oblique shear with steeply dipping, N-NW striking foliation (Allard & Portis, 2013). Recent geophysical research (Bedrosian & Finn, 2021) further supports this model of convergence of the Wyoming and Superior cratons and suggests that this convergence was oblique, with a change in σ orientations possibly related to a change in plate motion from lateral to orthogonal. As is the case with all of the Paleoproterozoic deformation events in the Black Hills, the timing of D_3 transpression can be constrained by the youngest Proterozoic unit in the Black Hills region, the Harney Peak Granite (ca. 1715 Ma). This may have intruded syn-deformational (Allard and Portis, 2013) or post-deformational (Lee, 1996; Van Boening & Nabelek, 2008; Ciborowski et al., 2013) as evidenced by extensive hydrothermal alteration in the Nemo Group rocks.

Finally, while folds near the Harney Peak Granite likely record localized D_4 deformation related to granite intrusion and dome formation, dated between 1.71 Ga ± 3 Ma and 1.69 Ga ± 2.9 Ma (Redden et al., 1990; Hark 2009; Hark et al., 2010; Allard & Portis, 2013), the NG rocks do not record these structures. It is likely however, that this bulk intrusion, along with other regional igneous activity, contributed to hydrothermal alteration in the Nemo area (Redden et al., 1990; Redden & Dewitt, 2008; Hark, 2009; Van Boening, 2007).

2.5.1 Blue Draw Metagabbro

The Blue Draw Metagabbro forms a 1,000-m-thick differential sill that intrudes the thick quartzite of the Boxelder Creek Formation (Redden & Dewitt, 2008; Ernst et al., 2013; Ciborowski et al., 2015). The intrusion is thought to be the product of at least two magma pulses which fractionated into a sequence of rocks which grade from peridotite at the base of the intrusion to gabbronorite at the upper margin (Ciborowski et al., 2013). Earlier work by Lee (1996) further discriminates portions of the sill through geochemical analysis. The sill contains a lower zone of serpentinite (10% of sill); a lower middle zone of amphibolite (14%); an upper middle zone of myrmekitic and granophyric amphibolite (70%); and an upper zone of myrmekitic and granophyric granodiorite (6%). Major element and trace element compositions indicate that the lower zone was an olivine-rich cumulate (Lee, 1996). Later work by Van Boening & Nabelek (2008) posits that the BDM is the largest single mafic body in the Black Hills, dated at ~2.48 Ga. Though conventionally thought to be a rift-related sequence (Redden et al., 1990; Dahl et al., 2006), geochemical results indicate that these rocks may derive from a continental arc setting related to a subduction zone, in agreement with earlier model proposed by Redden et al. (1990). Deformational and other metamorphic features observed in the BDM are foliations and lineations related to D_2 and D_3 (perhaps coincidental to shear fabric formation), hydrothermal alteration, and fluid mass transport (Allard & Portis, 2013).

2.5.2. Boxelder Creek Quartzite

The Boxelder Creek quartzite consists of a variety of clastic lithologies including chloritic quartzite and metamorphosed conglomerates and paraconglomerates, containing quartzite and banded iron-formation clasts with minor amounts of dolomite and veined quartz clasts (Redden & Dewitt, 2008). This unit grades laterally to the northeast into distal equivalents consisting of

siltstone, shale, and dolomite. Locally, abrupt terminations of thick conglomerate subunits indicate the likelihood of growth faults. The distribution and sediment types in the Boxelder Creek Formation indicate a rift environment (Redden et al., 1990; Dahl et al., 1999 & 2006; Redden & Dewitt, 2008). Subsequent folding and shearing (Allard & Portis, 2013) have produced structures within the quartzite ranging from blocky, undeformed metasedimentary rocks in zones of low or absent deformation, to highly sheared and foliated structures in high deformation zones (Redden & Dewitt, 2008

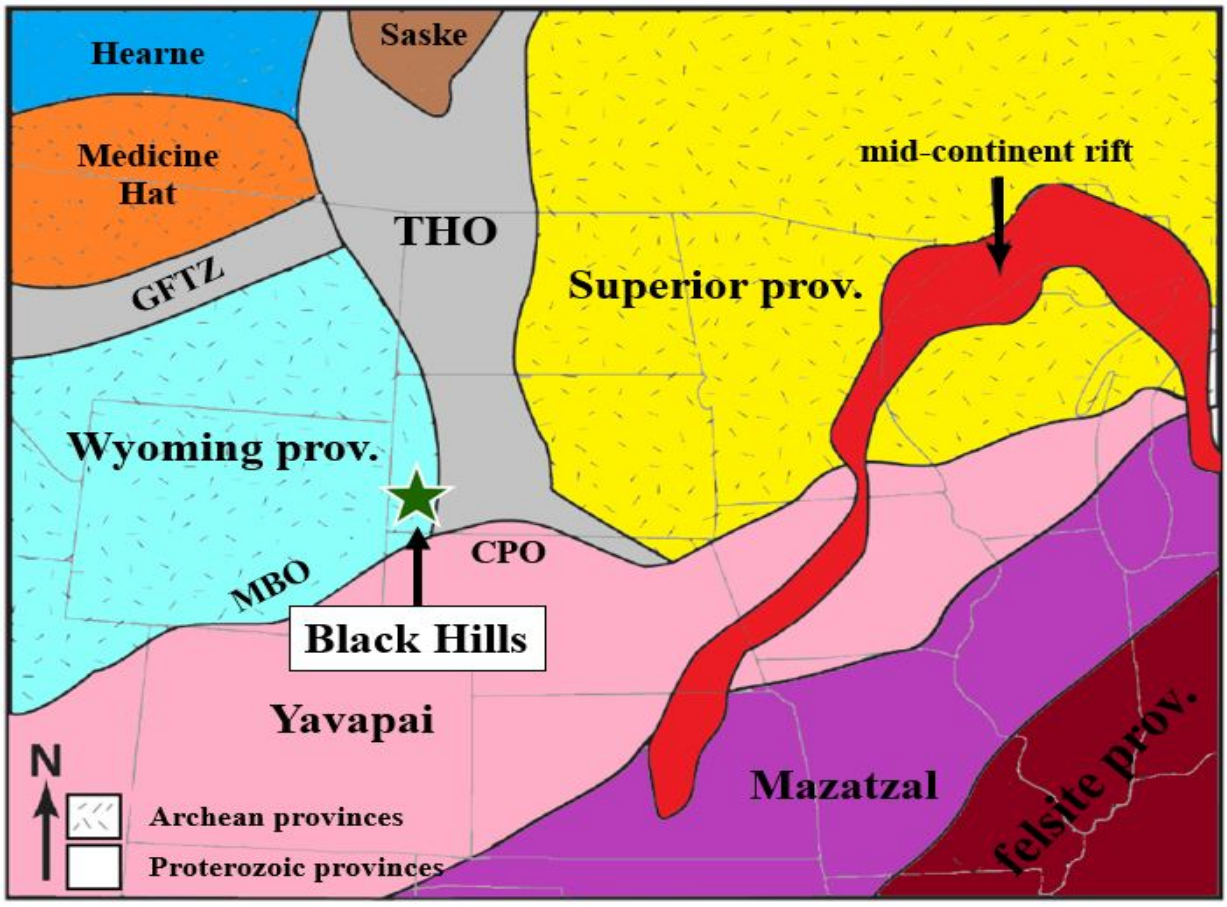

Figure 2-1: Tectonic province map of North American continent with locations of cratons, major orogens, and the Black Hills Uplift indicated by the green star. MBO = Medicine Bow Orogeny; CPO = Central Plains Orogeny; and GFTZ = Great Falls tectonic zone. Modified from Figure 1 inset map in Allard & Portis (2013).

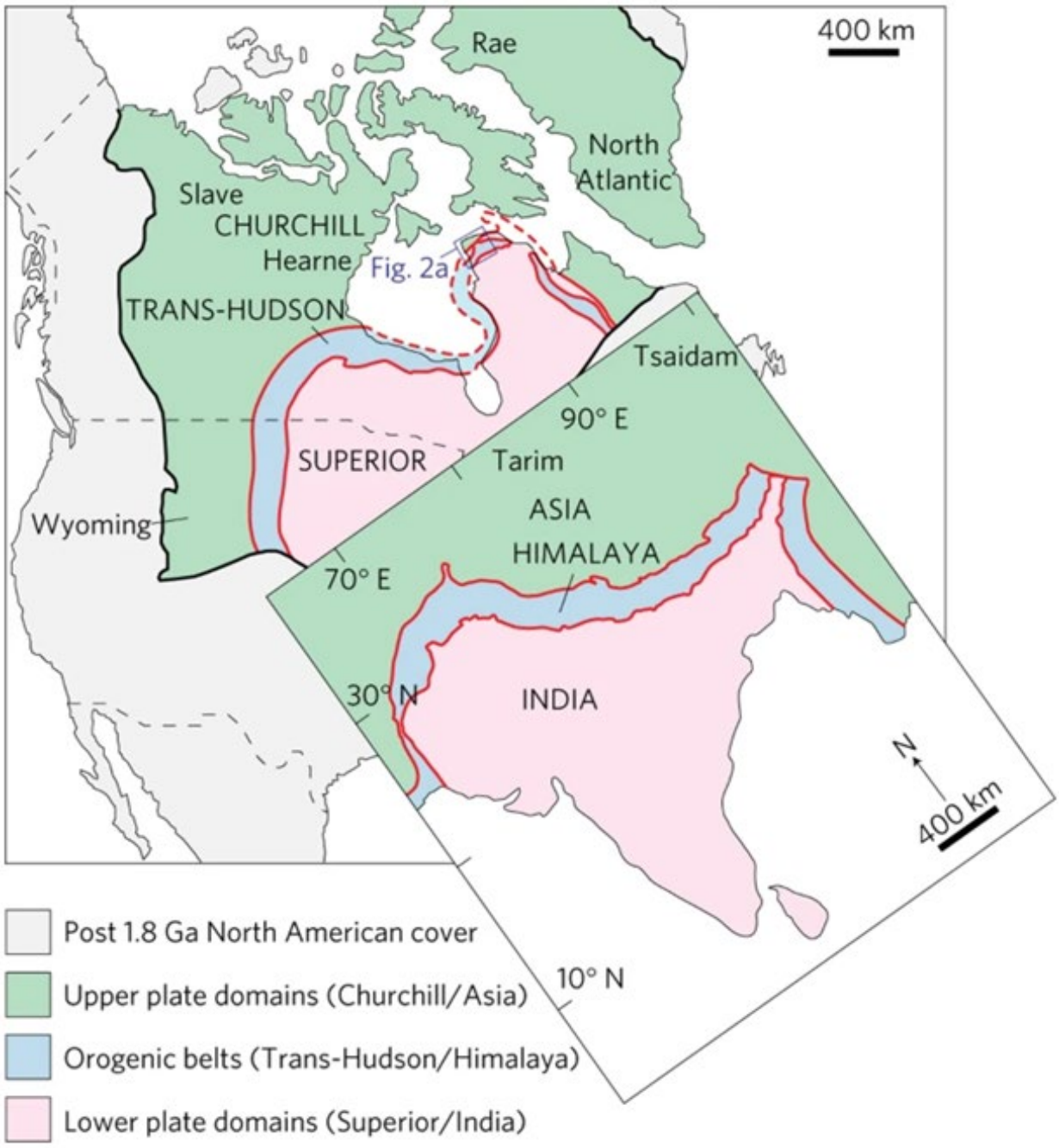

Figure 2-2: Geological map of North America, including Greenland, showing the extent of the Trans-Hudson Orogen and the location of bounding Archean crustal blocks and cratons, as compared to present-day convergence of the Asian and Indian Plates. The blue area outlined in red represents the THO and Himalayan Orogen. The pink shows the correlation between the Precambrian Superior Province and the modern-day Indian subcontinent, and the green compares the Asian continent to the Churchill craton, which includes the Wyoming Province. From Weller & St. Onge, 2017.

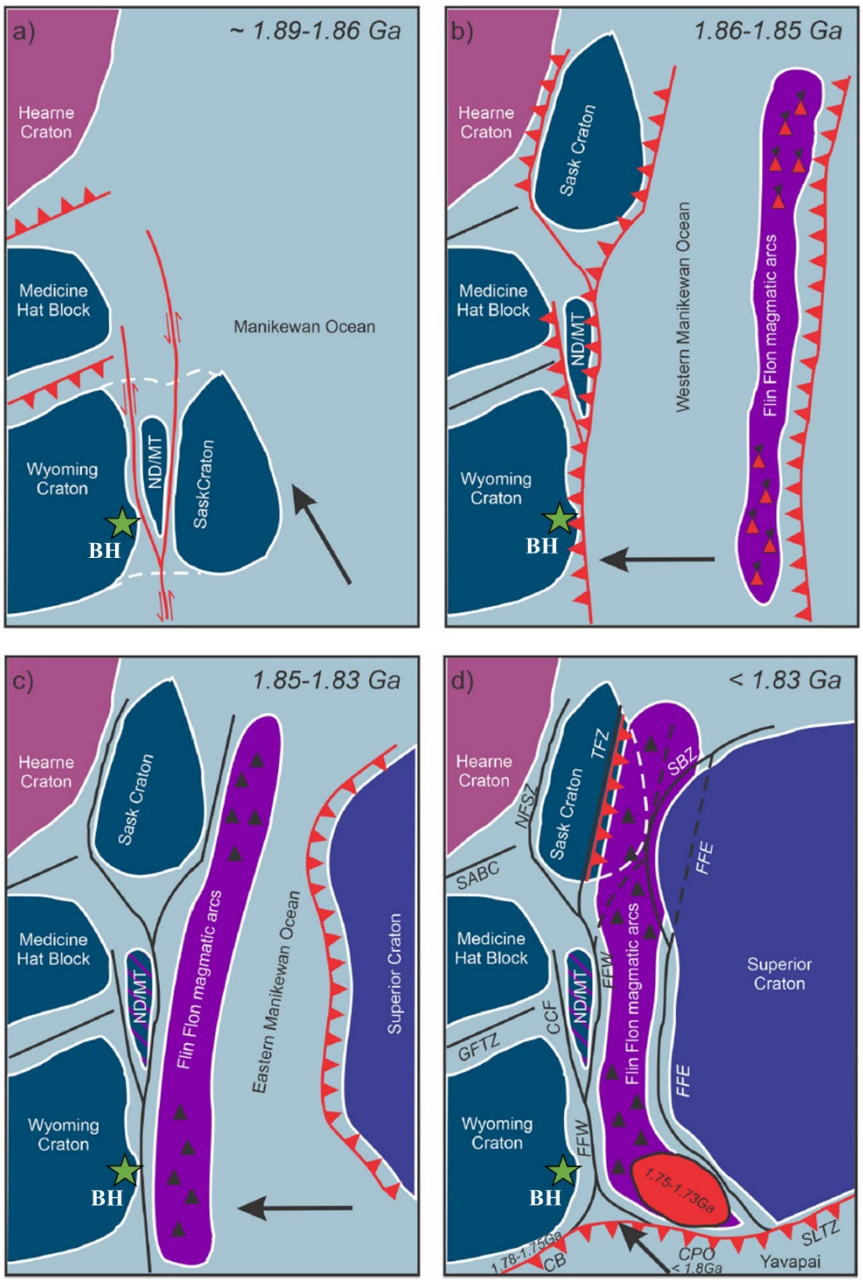

Figure 2-3: Modified from Bedrosian & Finn, 2021. Maps illustrating the general evolution of the sTHO, with the main tectonic elements shown as relating to Black Hills formation, denoted by green star, with the large black arrow indicating the dominant stress vector in each phase. (a) Oblique convergence at ~1.89 – 1.86, with northward translation of the ND/MT block and Sask craton (fragments of the Wyoming craton); (b) Subduction of the western Manikewan Ocean beneath the western cratonic assemblage (~1.86 – 1.85 Ga); (c) Closure of the eastern Manikewan Ocean (~1.85 – 1.83 Ga); (d) Convergent deformation between the Wyoming, Sask, and Superior cratons during terminal closure with subsequent accretion of the Yavapai province and post-orogenic igneous intrusions. (For a full THO tectonic sequence in North America, see Corrigan et al., 2009, Fig. 2).

44.4504° N,
103.1650° W

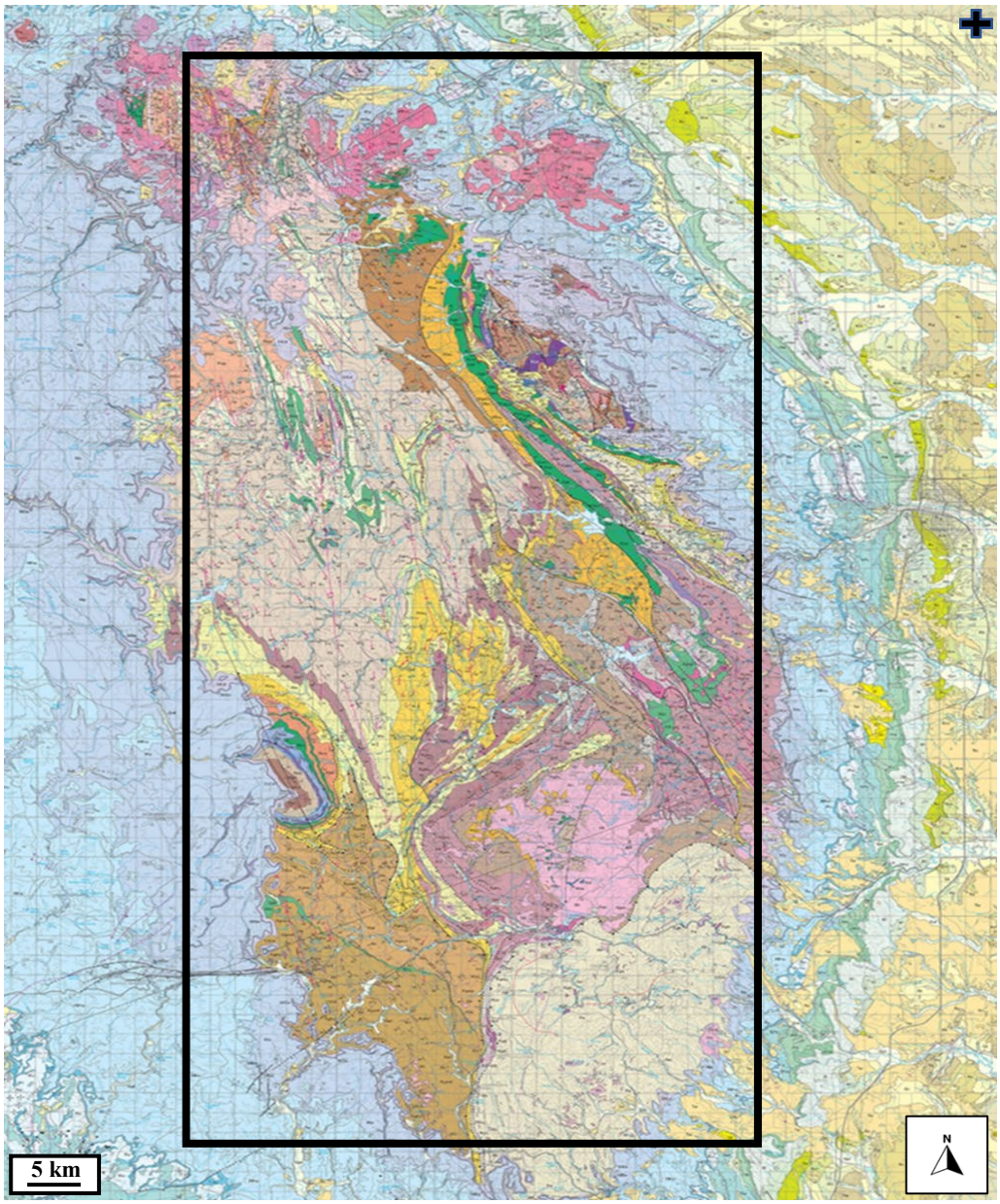

Figure 2-4: Geologic map of the Black Hills, SD. Precambrian rocks (igneous and metasedimentary; denoted in pink & lavender (granites and pegmatites related to 1.71 Ga Harney Peak intrusions); brown, yellow, and light pink (metasedimentary clastic rocks: course-grained sandstones, greywackes and shales); green (metamorphosed basalts); and dark purple (BDM) make up the bulk of uplifted units (highlighted within the black border). Phanerozoic units are denoted in light blue and tan. See original text for unit descriptions and abbreviations. Modified from Redden & Dewitt, 2008.

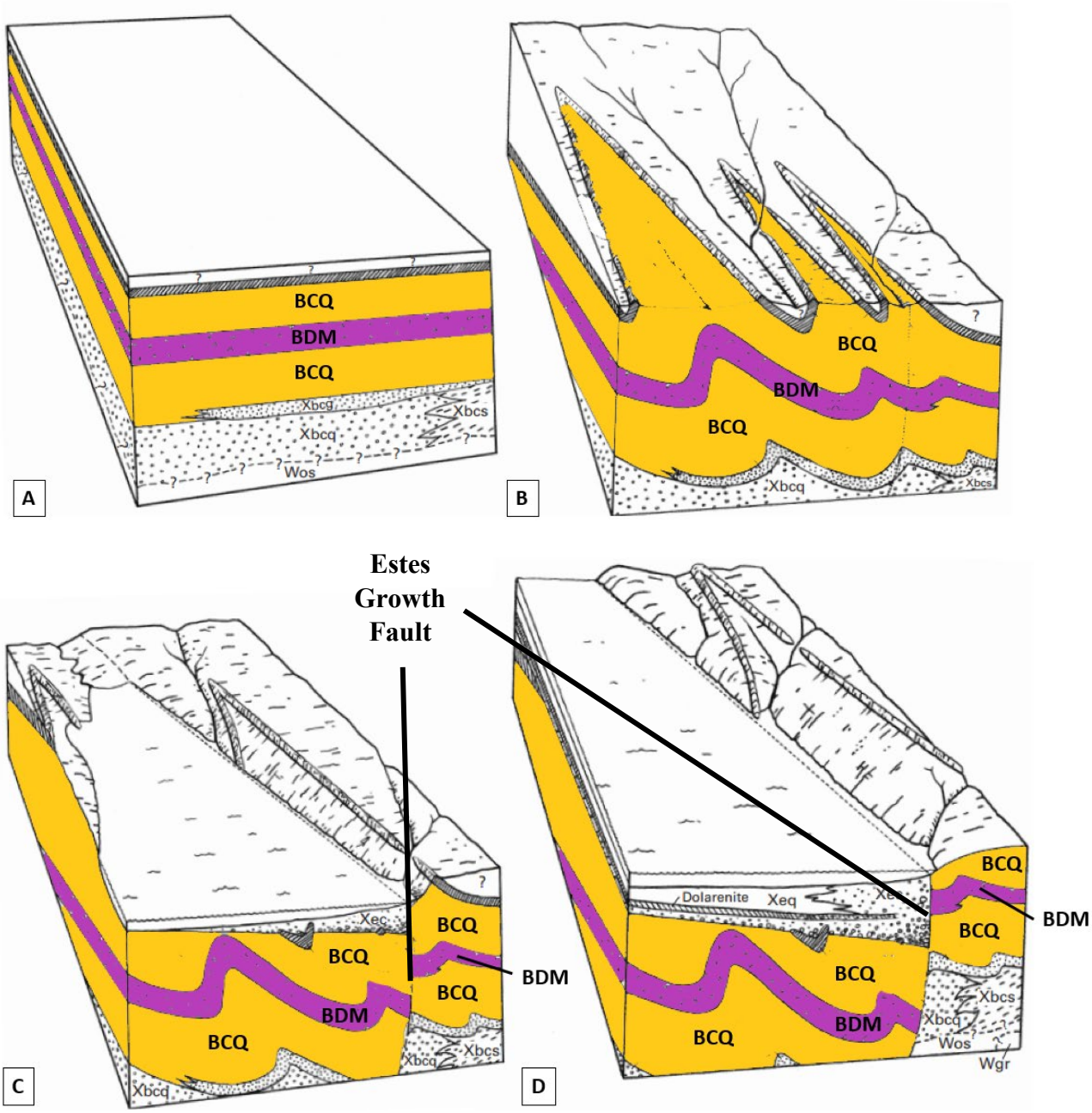

Figure 2-5: Generalized block diagrams showing stratigraphic and structural events in the Nemo area and development of Estes growth fault. Surface terrane is hypothetical, and view is to the north. Not to scale. A: Original stratigraphic sequence of Boxelder Creek Formation (units BCQ: orange). Gravity-differentiated, 2.48 Ga Blue Draw Metagabbro (unit BDM: purple) sill is also shown (prior to folding). B: Reconstruction of earliest (pre-D1) deformation and erosion preceding development of Estes fault. C: Early stages of development of the Estes fault. D: Continued development of Estes growth fault and associated conglomerate and quartzite. Modified from Redden & Dewitt, 2008.

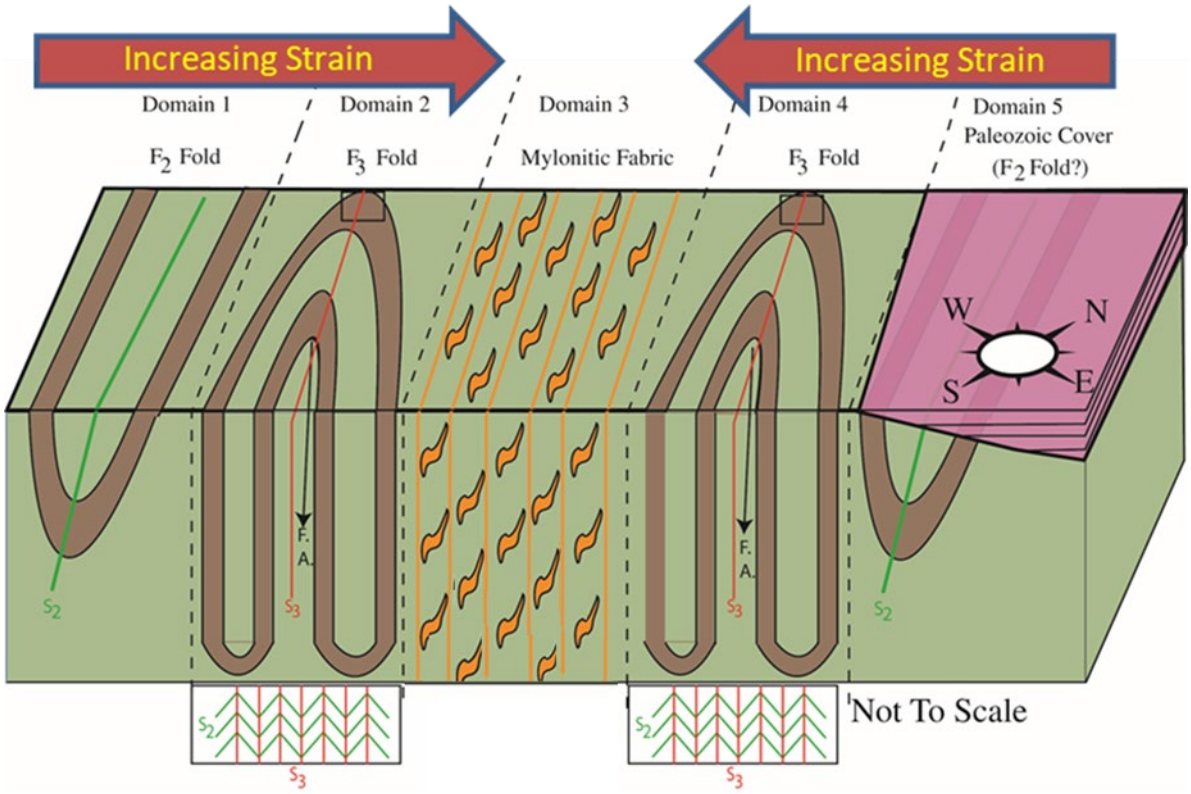

Figure 2-6: 3D block diagram depicting an interpretation for F_2 and F_3 deformation domains in the Black Hills. F_1 folds formed via north-verging shortening and were subsequently refolded by E-W folding (F_2) during suturing of the Wyoming and Superior provinces. Synchronous F_3 folds with steep NW/SE axial planes and localized shear zones, denoted by Domain 3, indicate continued shortening and left-lateral/east end up displacement. Modified from Allard & Portis, 2013.

Chapter 3: Methods

3.1. Overview

The methods used to analyze the Nemo Group Shear Zone (NGSZ) include structural fabric mapping and subsequent correlation of structural fabrics to kinematic models with varying inputs for shear obliquity (ϕ), extrusion obliquity (v), and kinematic vorticity (Wk) to constrain transpression models; measuring three-dimensional lozenge shapes as a proxy for strain; and supplemental petrographic analysis. The excellent geologic map by Redden and DeWitt (2008) provides accurate geologic contacts and locations of outcrops. New structural mapping is focused on detailed measurement of, a) deformation fabrics (foliation and lineation) and discrete shear zones at the meter to kilometer scale to determine local and regional differences in strain and kinematics, and (b) aspect ratios and acute angles of "diamond-shaped" lozenges (as a proxy for the strain ellipsoid), which are often bounded by shear bands, to quantify strain geometries (constriction, plane strain, and flattening strain). These mesoscale analyses are supplemented with microstructural analysis to identify shear sense indicators, record mineral fabric orientations, and record metamorphic alteration within the BDM and the BCQ across strain gradients.

3.2. Site selection

Sites for structural analysis were selected based on meso- and macro-scale deformation gradients identified in the field, and all mapping sites are located within a defined boundary of ~4 km^2 concentrated around the center of the apparent z-shape within the mapped BDM (**Fig. 3-1)**. In addition to field measurements of strain fabrics, samples were collected at a number of sites.

However, time constraints and equipment limitations allowed for only four thin-sections to be prepared. Therefore, samples for thin section preparation were chosen from an "unknown" phyllite layer within the BCQ that exemplified highly evolved shear banding (site NG2132; Fig 3-8), from BDM and BCQ samples collected at the only observed exposure of the contact between the two lithologies (sites NG2145A & NG2145B; Fig. 3-9), and outside of the highly strained zone at an undeformed but hydrothermally altered metagabbro (site NG2157; Fig 3-10).

3.3. Structural fabrics

Orientations of foliation and lineation fabrics can be used to determine orientations of finite strain, where foliation is perpendicular to the minimum finite strain direction and the lineation is parallel to the maximum finite strain direction (e.g. Robin & Cruden, 1994; Tikoff & Greene, 1997). Additionally, strength and spacing of these fabrics can serve as indicators of strain and can therefore be used as proxies for strain magnitude (e.g. Shea and Kronenberg, 1993; Bukovská et al., 2016). Structural fabrics may vary between the quartzite and metagabbro, which would allow for evaluation of how kinematics (orientations and relative amounts of shearing and flattening) and strain magnitude may have partitioned across this rheological boundary.

For the purposes of this study, foliation planes are considered to be any planar arrangement of minerals including the outer edges of a polygonal feature, for example a lozenge, or the tightly spaced foliations of a shear band. Measurements were concentrated primarily within the BDM and BCQ in the zone of high strain defined in **Figs. 3-1, 3-2, 3-3 and 3-4** (sites NG2101 - NG2117; NG2122 - NG2125; and NG2129 - NG2156) and supplemental measurements made outside of this zone (sites NG2116 - NG2119; NG2121; NG2126 - NG2128; and NG2157).

The plane of observation and orientation of kinematic indicators such as rotated porphyroclasts, S-C fabrics, and asymmetric folds can be used to find the orientation of the noncoaxial strain component to compare to existing shear zone models (for example, left lateral vs. thrust vs. oblique simple shear) (e.g., Díaz-Azpiroz et al., 2019).

3.4. Lozenge angles and aspect ratios

While the dominant fabrics in the study area are anastomosing foliations, another prominent feature that can be seen in both rock types are shear band bounded lozenge structures that have weathered in three-dimensional "diamond" patterns. In order to learn how the lozenges develop with increasing strain and interpret how they accommodate deformation across the Nemo Shear Zone, I analyzed outcrops that record strain gradients at the meter scale.

As outlined in Ponce et al. (2013), lozenges in heterogeneous rocks are generated by rheological contrasts, where the lozenge is formed by a relatively competent material surrounded by a more deformed incompetent material, with the more competent material adopting a lozenge shape after deformation. Lozenges predominantly develop during ductile deformation and form through shear zone interconnections. Mitra (1979), Gapais et al. (1997), Carreras (2001), and Carreras et al (2010) suggest that lozenges and other lens-shaped structures are often bounded, and are therefore defined by, networks of anastomosing shear bands. These bands generally consist of parallel to subparallel, closely spaced foliations and represent areas of high strain relative to the more competent bounded lozenges. As such, there is an inverse relationship (**Fig. 3-6**) between the changes in long axis angle acuity and the shape of the lozenges (Ponce et al., 2013). This is particularly true if there are components of both lateral shear and shortening (Carreras et al., 2010)

which cause the shear bands to rotate. Since lozenge shapes and orientations in progressive strain are dependent on kinematics (**Fig. 3-7**), their shape can serve as a proxy for the finite strain ellipsoid. However, two factors complicate using lozenges as strain indicators.

The first problem, as pointed out by Gapais et al. (1987), is that using the lozenge shape as an analogue for the 3D strain ellipsoid is only warranted in rocks where lozenges form without preexisting foliations. Secondly, without full 3D exposure, it is difficult to use them as proxies in kinematic analysis (Ponce et al., 2013). However, the geometries and changes in aspect ratio and long-axis acute terminal angle in two dimensions can give a sense of strain magnitude (Gapais et al., 1997; Ponce, 2010). For symmetric lozenges in zones of lower strain, the acute angle of the long axis in both the XZ-plane (perpendicular to foliation and viewed vertically) and the YZ-plane (perpendicular to foliation and observed in map view) will be greater than corresponding angles in zones of higher strain where this angle becomes more acute (Mitra, 1979; Ponce et al., 2013). In asymmetric lozenges, the angle between the long and short axis also decreases with continued strain. Similarly, the aspect ratios of the lozenges (L/W) increase as the acute angle decreases from low to high strain (**Fig. 3-7**). In rocks without a preexisting foliation, lozenge shapes can possibly be used to determine relative amounts of flattening vs. constriction and thus a comparison might be made to various transpression models (Gapais et al., 1997).

Based on previous studies and the prevalence of lozenge geometries in the NGSZ study area, we measured and documented any observable lozenge geometries and aspect ratios in two dimensions in the field. Where lozenges were not well-exposed, I reconstructed lozenge geometries by combining multiple foliation orientations measured at individual outcrops. Three-dimensional lozenge shapes were also estimated where observations could be made on multiple planes. I also calculated lozenge long-axis acute angles using Google Earth and the Allmendinger

stereonet program. Consequently, I was able to use these lozenge geometries as a proxy for strain and plotted them on Flinn plots to estimate relative flattening, plane-strain, and constricting deformation between the BDM and BCQ.

3.5. Sampling Locations and Thin Section Preparation

Zones of high strain and areas outside of the shear zone with little to no visible deformation were chosen for sampling and microanalysis. In order to analyze microstructures and mineralogical changes representative of local strain gradients within the study area, I selected three samples (metagabbro, quartzite, and one unknown containing visible metallic minerals) for thin section preparation and analysis based on similar foliation strike orientations (within 10° of 340° azimuth so as to analyze microstructures from comparable reference frames). In addition, one undeformed sample of metagabbro was selected as a structural and mineralogical control.

Analysis of the samples in thin section (described in Chapter 4) focused primarily on microstructures, evidence for fluid interaction, and the relationship between fluid and deformation (the presence of syndeformational quartz growth in strain shadows, for example). Samples were cut along the XZ-plane of finite strain (parallel to lineation and perpendicular to foliation), the traditional plane of observation in shear zones (see Fossen, 2006). The undeformed gabbro, which had no foliation or lineation, was marked and cut to correspond to the common foliation plane of the other three (strike ~340°). Once completed, I cut 24 mm x 24 mm x 45 mm billets. Two notches were cut on the ends of the billets to denote down-plunge lineation direction. Spectrum Petrographics, Inc. (Vancouver, WA) made the thin sections from these billets.

3.6 Petrographic analysis

I used a Leica DM4 P polarizing microscope in Dr. Czeck's lab in the Department of Geosciences at UW-Milwaukee to analyze thin sections made from the samples from section 3.3.1. In plane- & cross-polarized light, the thin sections were analyzed for mineralogy and microstructural fabrics, including strain shadows, grain bulging, recrystallization, undulose extinction and pressure seams.

3.7. SEM/EDS Analysis

Following the gathering of petrographic data, I applied a carbon-coating to the thin sections to reduce charging, using the Edwards vacuum coating unit, and analyzed using the Hitachi S-4800 FE-SEM, in Dr. Heather Owen's lab in the Department of Biological Sciences Electron Microscope Laboratory at UW-Milwaukee. Using the Hitachi SEM, I produced back-scatter electron images for areas of interest (the composition of opaques found in the NG2132 phyllite sample, for example) and using the characteristic X-rays from the Bruker Quantax EDS system I was able to produce dot-maps and elemental spectra to quantify bulk composition.

3.8. Comparisons to Kinematic Models

In order to constrain the kinematic nature of the shear zone, some key variables must be quantified to understand the transpression models that fit the field data. These variables include the obliquity of the simple shear component, the obliquity of the pure shear component, the strike and dip of the shear zone boundary, and the obliquity of the extrusion angle. I generated

models by varying the input values for kinematic vorticity, simple shear obliquity, and extrusion obliquity, with constant initial constraints on the hypothesized region-scale shear zone geometries. The models were produced using Excel macros constructed by Fernández & Azpiroz (2009).

Field data were used to constrain which kinematic models were more thoroughly evaluated in the Excel/macro software. The shear zone boundaries were initially set with strike and dip of 340° and 90° to match the average foliation orientation; after initial consideration of models, some variation in dips was considered. Left-lateral shear sense indicators, primarily S-C fabrics and deflections, indicated sub-horizontal shearing, so only shear obliquities (ϕ) of -20°, 0°, 20° were considered. No field data could be used to constrain extrusion obliquities (υ) or kinematic vorticity number (Wk), so all possible ranges were considered. Considered extrusion obliquities (υ) range from 0° - 180° in 10° increments (19 in total). Considered kinematic vorticity numbers (Wk) range from 0 – 0.999999 in increments of 0.1 (11 in total). These parameters resulted in 627 kinematic models to be evaluated and compared with foliation and lineation orientation. The model outputs the trend and plunge of the finite strain ellipsoid principal axes, X>Y>Z, where X is considered parallel to lineation and Z is perpendicular to foliation. Using measured orientations of lineations from the field, any models that output X axes with orientations of ~45° to subvertical plunging in both the N-NW and S-SE quadrants and poles to foliation between ~0° - 30° were considered possible fits.

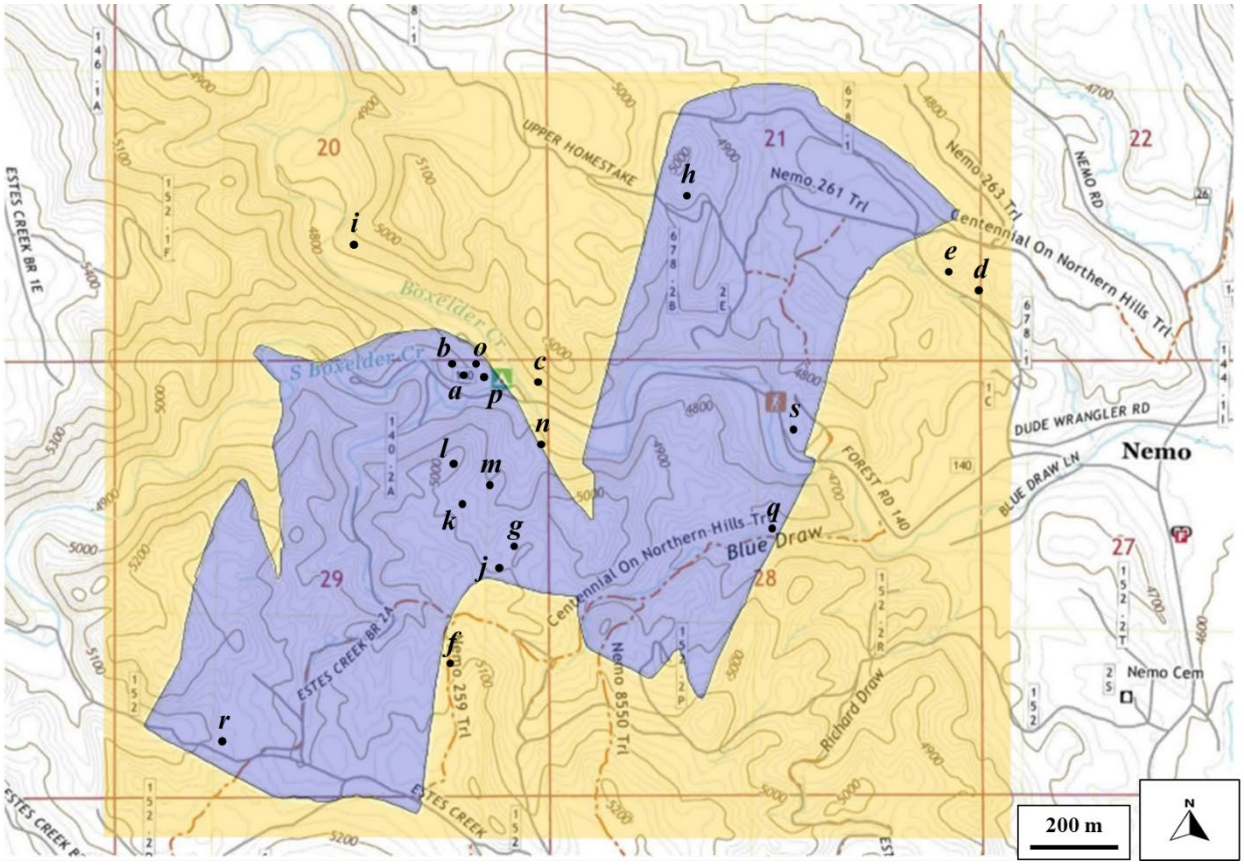

Fig. 3-1: BDM, sites NG2101- N2104, high shear zone crosscutting Knob Hill west of Boxelder Forks Campground; b: BDM, sites NG2105- NG2111, western face of Knob Hill and traversing along a NW trending ridge with steady elevation gain; c: BCQ, sites NG2115, outcrop bounded by up-ridge talus slope east of Boxelder Forks Campground; d: BCQ, sites NG2116 & NG2117, SW of junction between Upper Homestake and Centennial on Northern Hills Trl; e: BCQ, sites NG2118 & NG2119, SW of junction between Upper Homestake and Centennial on Northern Hills Trl; f: BCQ, sites NG2122 & NG2123, just west of Nemo 259 Trl, north of Estes Creek 152; g: BDM, sites NG2124 & NG21125, located in "Bear Scat Valley" (BSV), NW of the junction b/w Nemo 259 Trl & Estes Creek BR 2A; h: BDM, sites NG2126- NG2128, on Upper Homestake west of Nemo 261 Trl; i: BCQ and phyllite, sites NG2129- NG2132, NW from Boxelder Forks Campground along a foot path on the northern bank of Boxelder Creek, upslope before the first forge; j: BDM, sites NG2133 & NG2134, BSV; k: BDM, sites NG2135, NG2136, & NG2146, BSV; l: BDM, sites NG2137- NG2139, top of ridge approaching South Boxelder Creek on western side of BSV; m: BDM, sites NG2140- NG2143, E of BSV along a faded ATV trail; n: BDM/BCQ contact, sites NG2145a & NG2145b, upslope west of ATV trail at wooden gate near end of valley; o: BDM, sites NG2147- NG2150, northern face of Knob Hill; p: BDM, sites NG2152- NG2156; NE face of Knob Hill; q: BDM, site NG21R07, ridge north of the Centennial on Northern Hills Trl heading west from ATV parking on Forest Rd 140; r: BDM, site NG2121, west of the Estes Creek/Estes Creek BR 2A junction; s: BDM, site NG2157, east side of Forest Rd 140 just past the contact near the horse trail crossing.

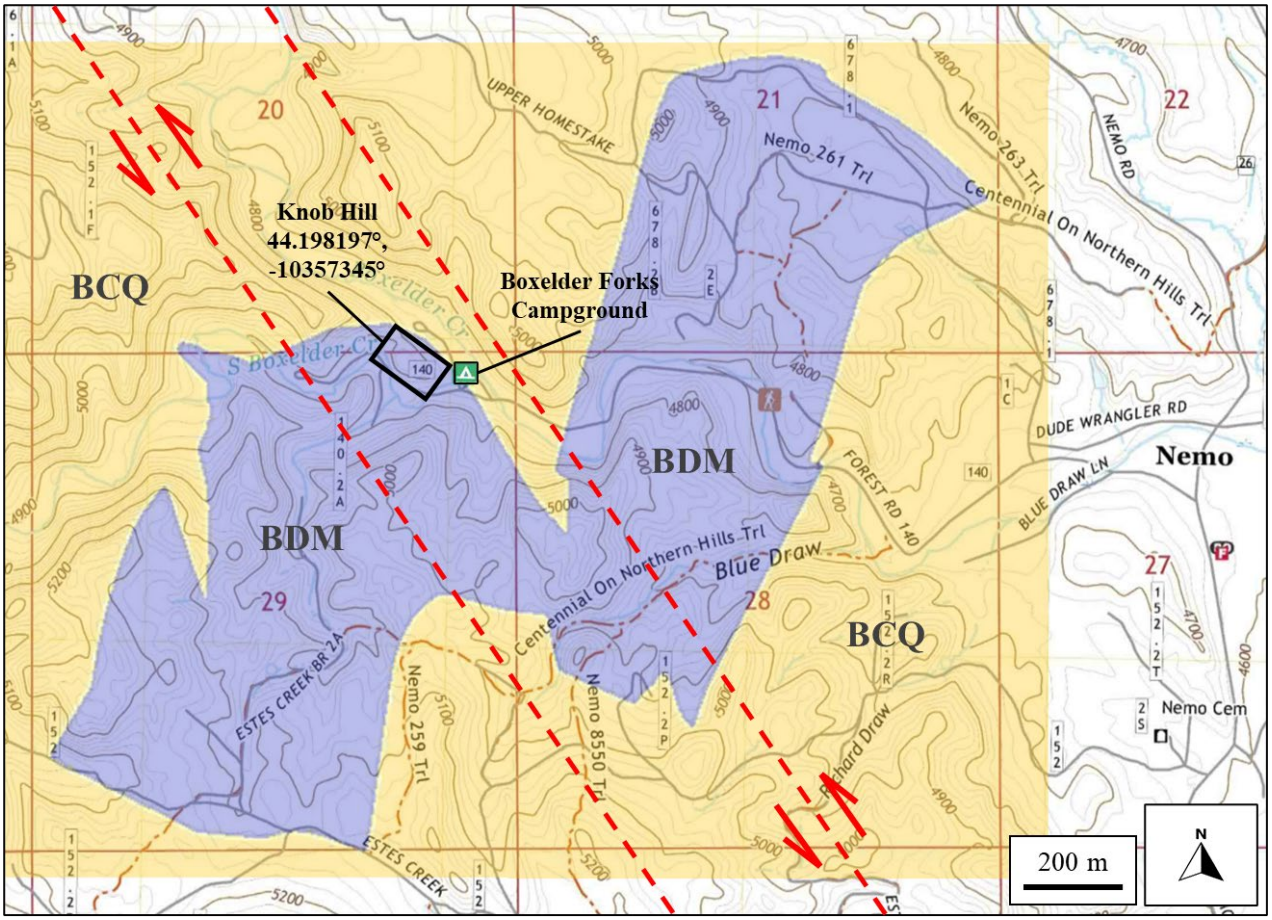

Figure 3-2: Knob Hill outcrop (indicated in box) west of Boxelder Forks campground was chosen for lozenge and shear band relationships based on heterogeneity observed in the field at the meter to decameter scale, primarily measuring fabrics traversing from west to east on the NE face of the outcrop. Red dashed lines indicate hypothesized zone of highest stain within the study area, based in part by field observations and Redden & Dewitt (2008) fault locations and orientations. Shear indicators based on Allard & Portis (2013) local and regional sinistral shear models.

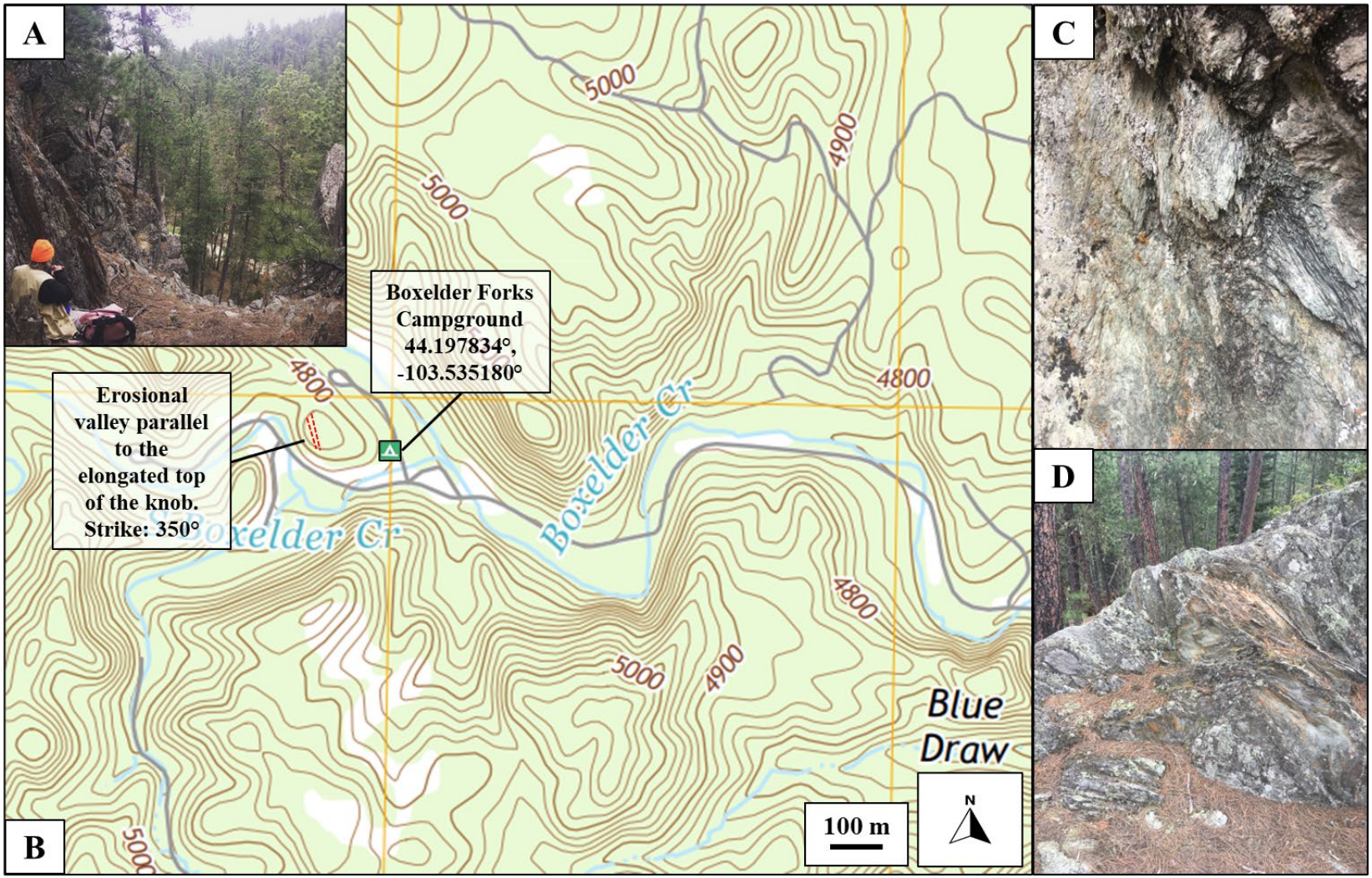

Figure 3-3: Erosional feature cutting through Knob Hill at ~345° - 350° trend (azimuth). Surface erosion is proposed to be constrained by amount of strain present in the rocks (higher strain = higher extent of erosion). B: Map view of erosional feature cutting Knob Hill (red dashed lines). C: High strain/shear bands in XY plane, bounding the west side of the erosional valley. D: High strain/shear bands in XY plane bounding the east wall of the erosional valley. Field sites for additional measurements were chosen based on the orientation of this feature both across Boxelder Creek to the SE and into the BCQ unit to the NW.

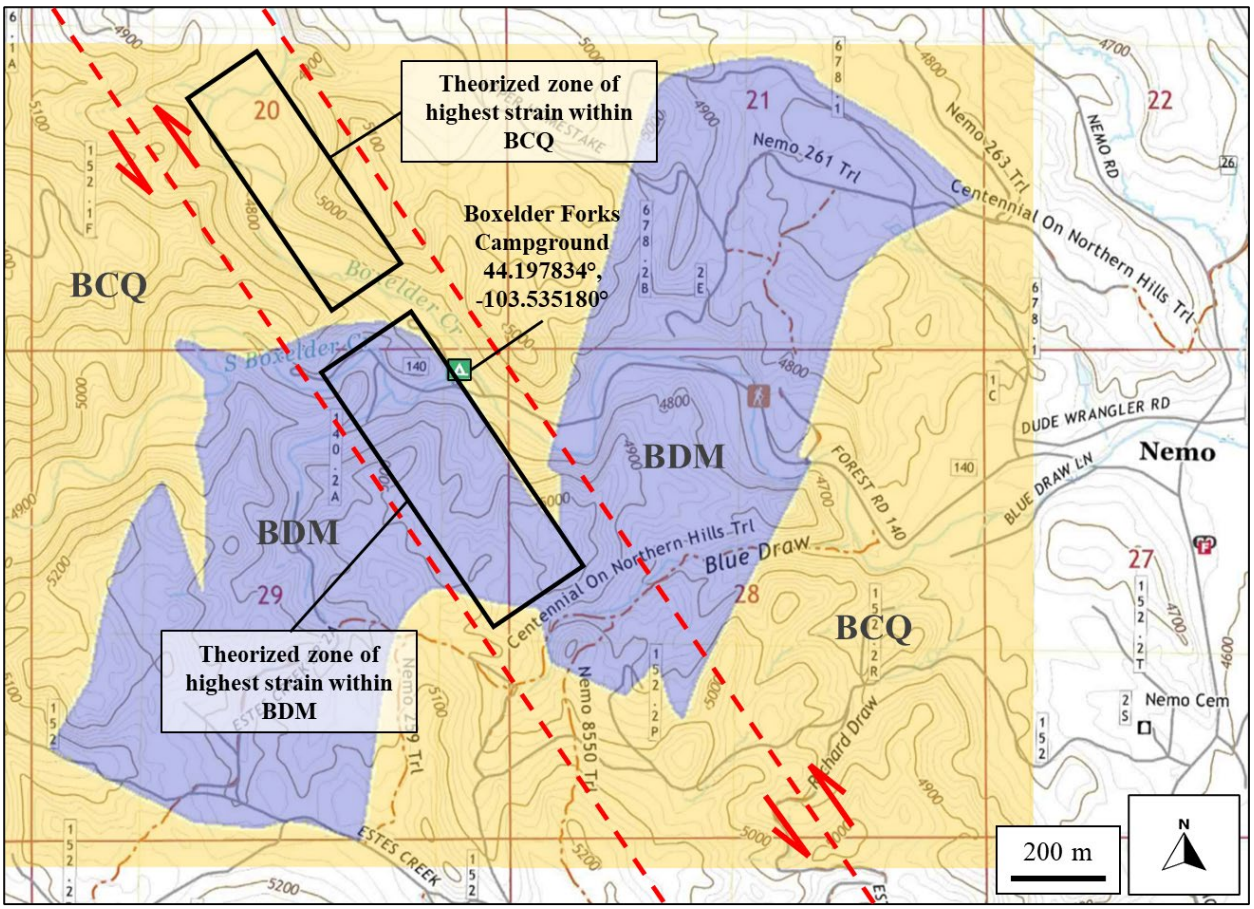

Figure 3-4: Hypothesized zones of highest strain based on relative topographic highs and lows (highest strained areas are hypothesized to be most highly eroded). Measurements were made at locations tens to hundreds of meters apart, based on the presence of measurable outcrop. Fabrics were measured traversing from NNW to SSE based on the presence of anastomosing shear bands (either in situ or as float). Red dashed lines indicate hypothesized zone of highest strain within the study area, based in part by field observations and Redden & Dewitt (2008) fault locations and orientations. Shear indicators based on Allard & Portis (2013) local and regional sinistral shear models.

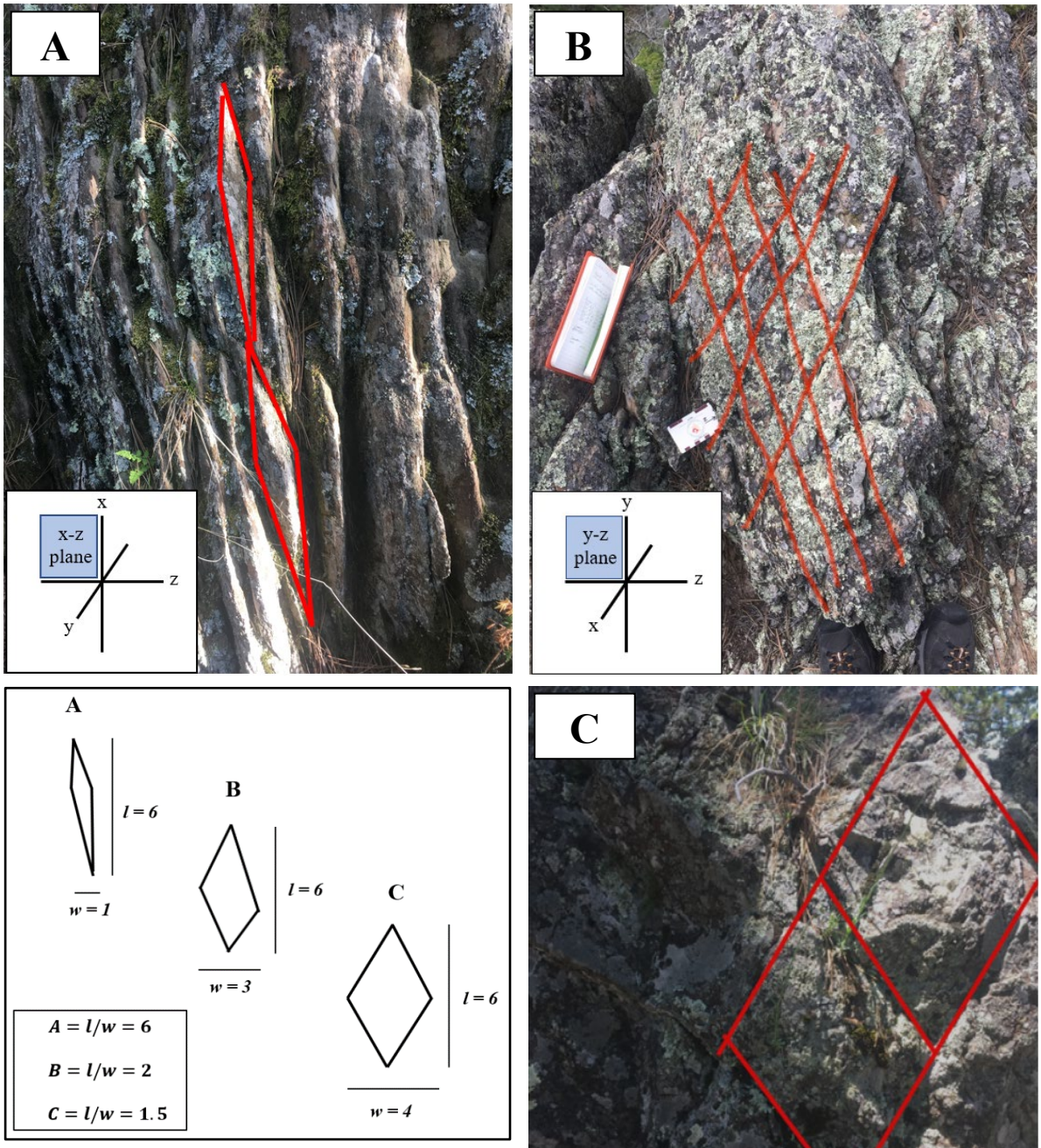

Figure 3-5: Examples of lozenge geometries from three planes of view. A: Vertical view down strike of foliation in the XZ-plane. B: View from above of the horizontal YZ-plane (plan view). C: Vertical view of the XY-plane (~foliation plane). Lower left pane shows how aspect ratios (unitless with arbitrary values) vary based on observation plane.

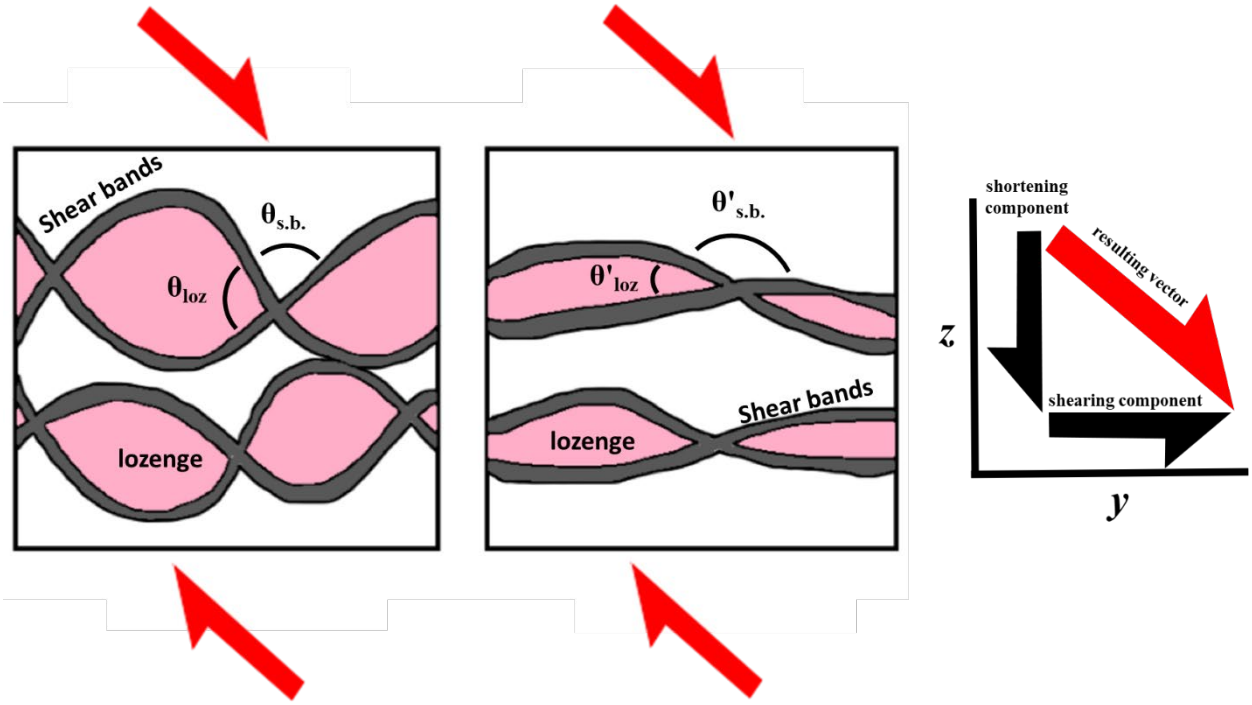

Figure 3-6: Schematic examples of changes in lozenge long-axis acute angles (in pink) and shear band (shown in grey) convergent angles. Left pane shows initial conditions with lozenge angles denoted as θ_{loz} and shear band angles as $\theta_{s.b.}$. Right pane shows progressive strain resulting in a decrease in lozenge acute angles (θ'_{loz}) and an increase in shear band convergent angles ($\theta'_{s.b.}$). The far-right graph shows the overall strain vector using a simple "tip-to-tail" vector analysis for components of shortening and lateral shear in the YZ-plane. This oblique strain causes rotation and/or flattening of the shear bands, thereby further affecting lozenge geometries.

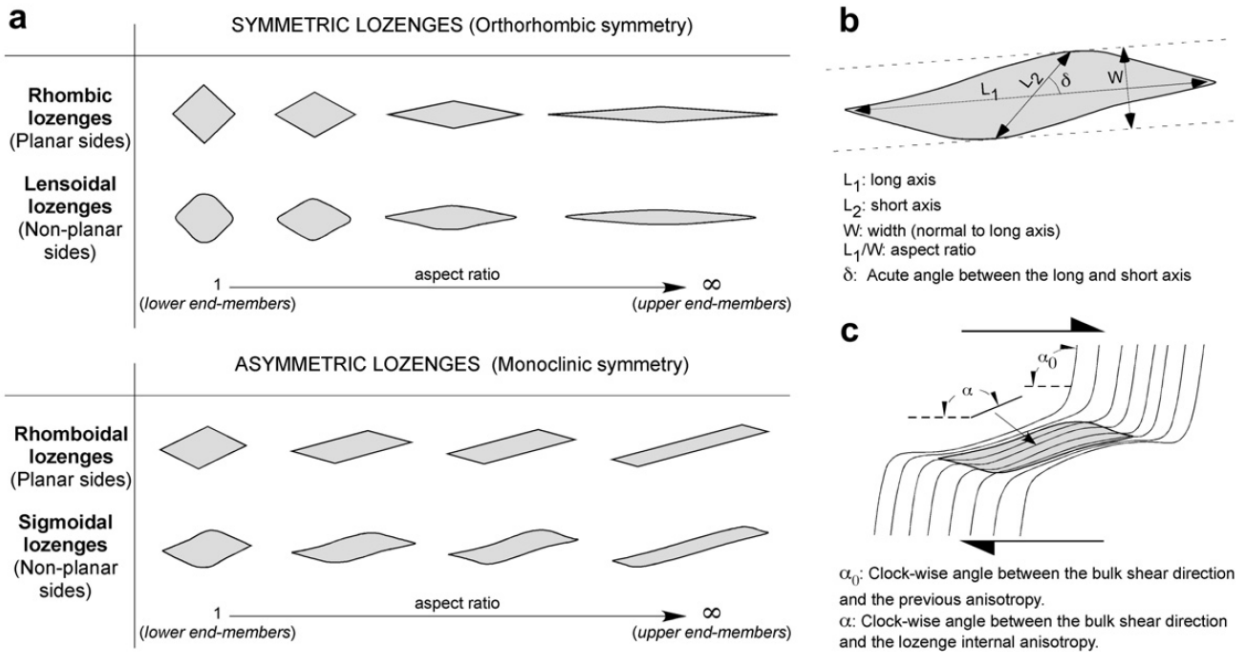

Figure 3-7: Schematic representation of various geometries and parameters for lozenges. (a) Different lozenge shapes according to their symmetry, to their linear or curvilinear outline, and to aspect ratio. These shapes can be applied to any 2D plane of observation. (b) Parameters used to geometrically define tectonic lozenges. (c) The angles α and α_0 that are applied to lozenges in anisotropic rocks. From Ponce et al., 2013.

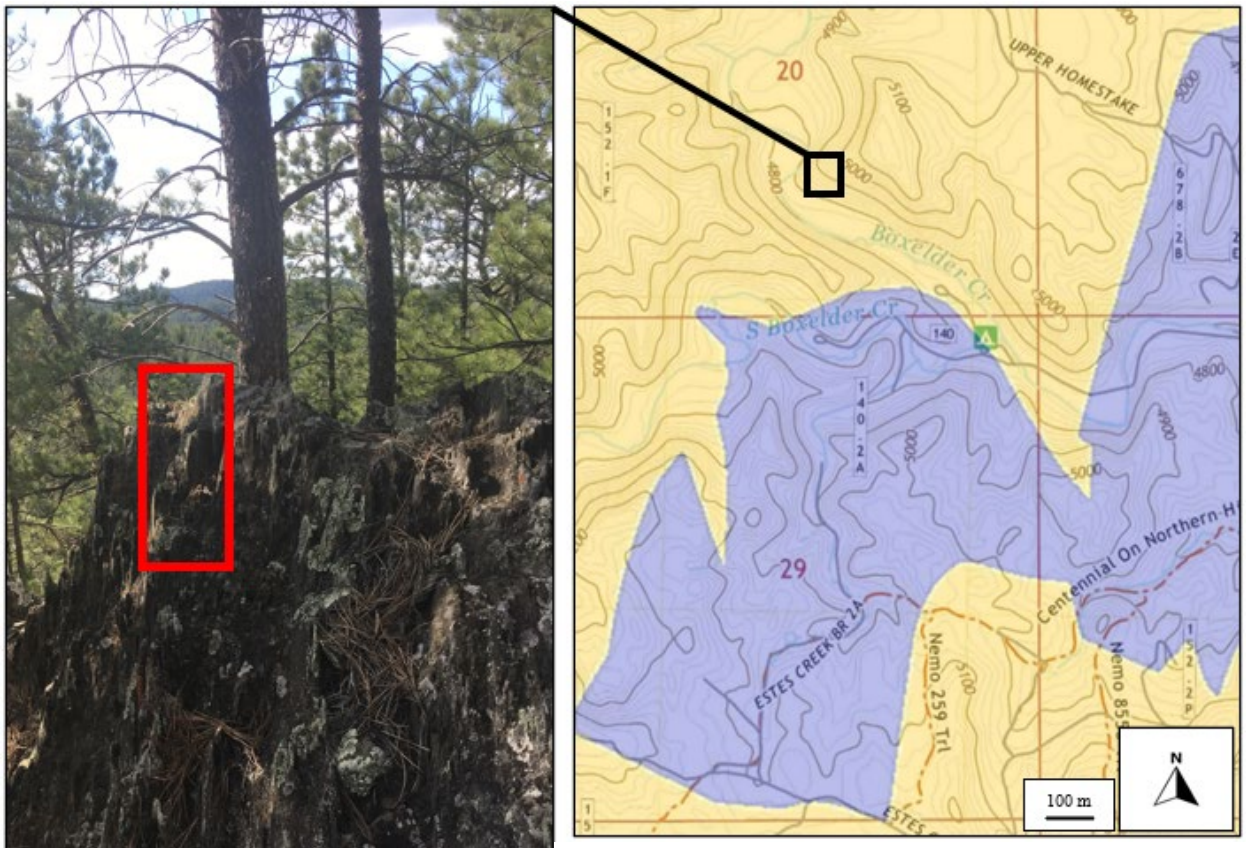

Figure 3-8: Sample site NG2132. Phyllite outcrop located within the BCQ proposed zone of high strain. Coordinates: 44.20309°, -103.54148°. Red box shows actual sample collected chosen based on observable lozenge morphology. Outcrop was determined to be in-situ in the field. Photograph view looks along strike of foliation, ~325° - 330° (azimuth).

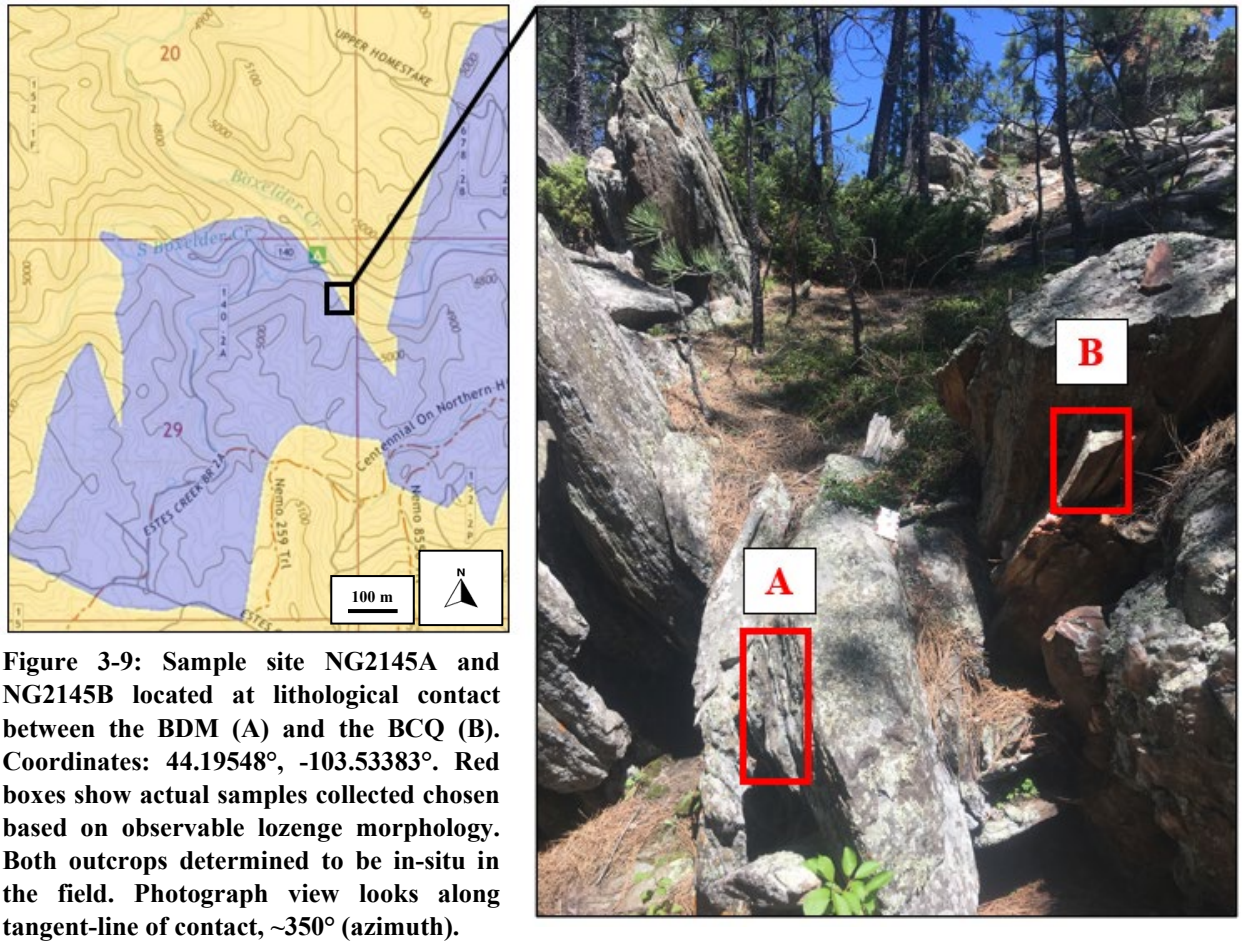

Figure 3-9: Sample site NG2145A and NG2145B located at lithological contact between the BDM (A) and the BCQ (B). Coordinates: 44.19548°, -103.53383°. Red boxes show actual samples collected chosen based on observable lozenge morphology. Both outcrops determined to be in-situ in the field. Photograph view looks along tangent-line of contact, ~350° (azimuth).

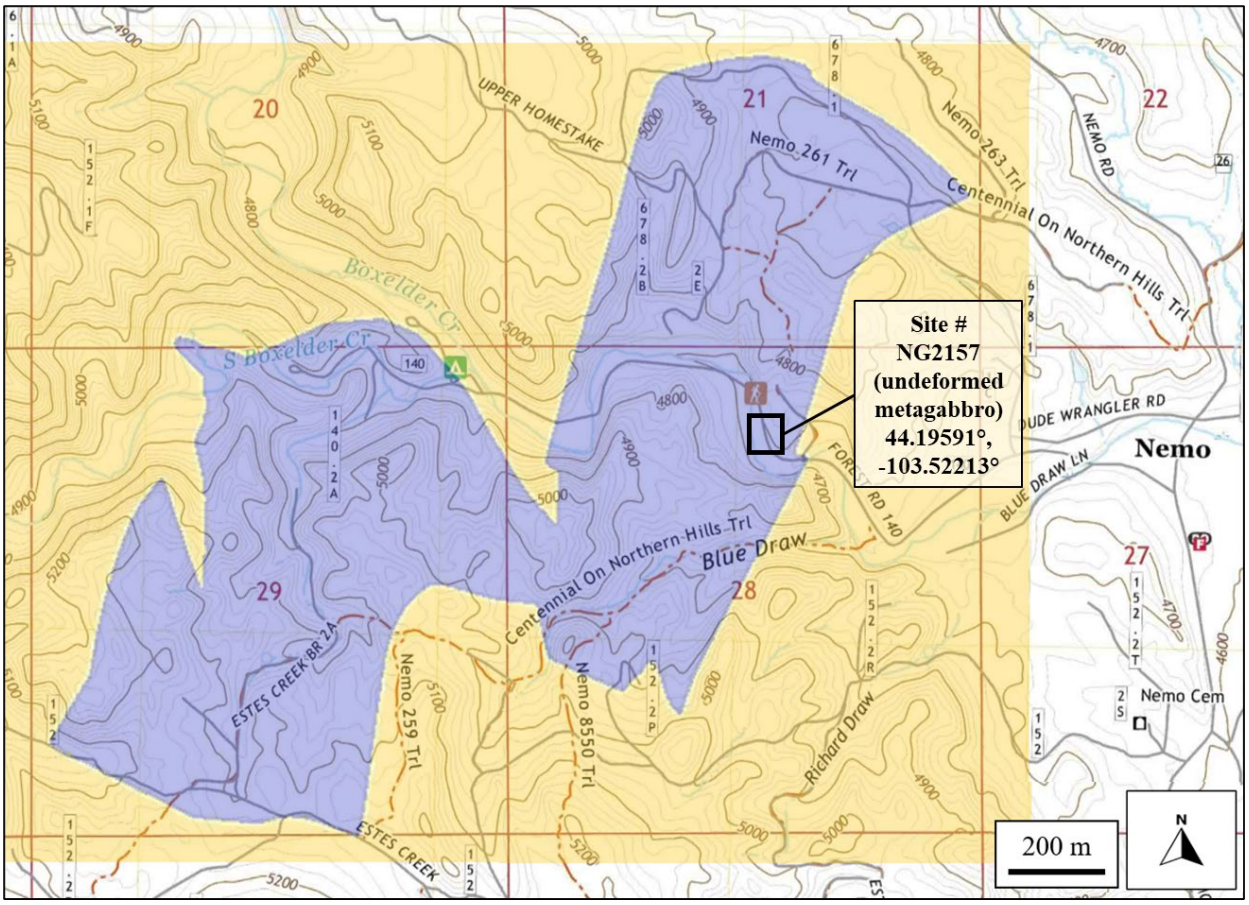

Figure 3-10: Sample site NG2157 (black box). Undeformed metagabbro, with no discernable foliation, lineation, or planar features of any type. Sample was collected from the east side of the road at an outcrop with massive morphology. Coordinates: 44.19591°, -103.52213°. Outcrop was determined to be in-situ in the field. No photograph available.

Chapter 4: Results

4.1. Foliations

The BCQ is well foliated at every observed outcrop; however, the BDM character ranges from non-foliated to strongly foliated, which suggests it is a more competent rock unit that concentrates deformation in a few locations. Field observations of the foliation in the BDM and BCQ indicate a change in character across the strain gradient, from planar to sub-planar with anastomosing (spaced) cleavage in the zones of low deformation and slatey to phyllitic (continuous) cleavage in zones of more ductile deformation. Mineral assemblages responsible for foliation in the BCQ are not apparent in hand-sample, though microstructure analysis indicate that there are discrete zones of quartz recrystallization and grain size reduction. In the BDM, some coarse-grained foliation planes show mineralization ranging from phyllitic to chloritic schistosity. This is particularly true near the BDM fold hinges where tightly-spaced shear fabrics bound less deformed blocks of metagabbro.

One such outcrop is located immediately west of the Boxelder Forks campground on the north side of Forest Rd. 140 (Fig. 3-2) and referred to as Knob Hill (KH). This outcrop records low and high strain in close proximity: both tightly-spaced shear bands (subparallel to the shear zone boundary, interpreted to be indicative of high strain) and nearly orthogonal shear bands (i.e., lozenges that have undergone low strain). Some of the highest strain within the Knob Hill outcrop is in the upper 5 meters, which is cut by an erosional valley trending ~165° bounded on either side by shear bands (Fig. 3-3). The trend of this minor valley was used to locate additional sites within the study area that were presumably inside the zone of highest shear within both the BDM and BCQ (Fig. 3-4).

The following stereonet plots were made from field measurements (**Appendix tables A1 & A2**). The stereonets and figure elements were generated by software designed by Allmendinger et al. (2013) and Cardozo & Allmendinger (2013), with additional Google Earth outputs designed by Blenkinsop (2012). Structural fabrics have been grouped by proximity within the study area into three main categories: central-area map foliations, Knob Hill foliations, and eastern-area map foliations. Sections of the data tables found in the appendix have been included in each figure for reference.

4.1.1. Central-area Map Foliations

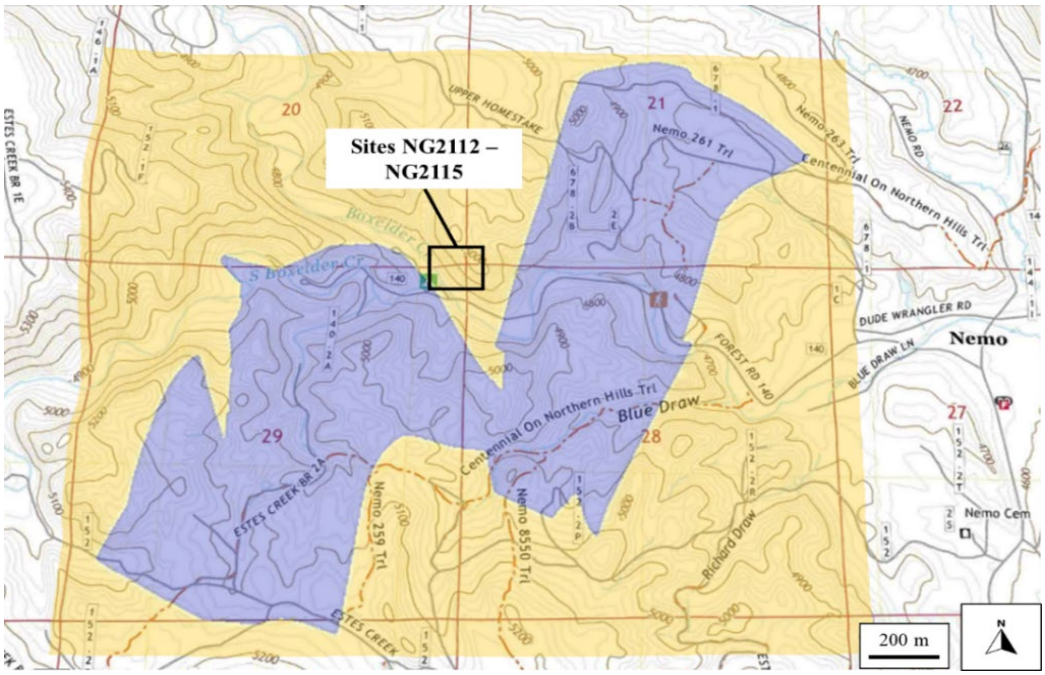

Site number	Latitude (deg.)	Longitude (deg.)	Lithology	Fol Strike RHR (az. deg.)	Fol Dip (deg.)	Dip Dir.
NG2112	44.19747	-103.53436	BCQ	354	76	E
NG2112	44.19747	-103.53436	BCQ	32	82	E
NG2113	44.19725	-103.53377	BCQ	356	64	E
NG2114	44.19758	-103.53393	BCQ	345	78	E
NG2115	44.19759	-103.53309	BCQ	170	82	W
NG2115	44.19759	-103.53309	BCQ	175	85	W

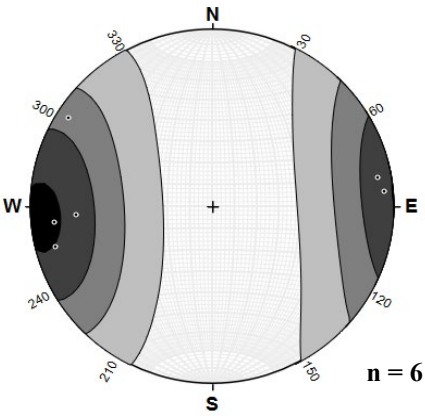

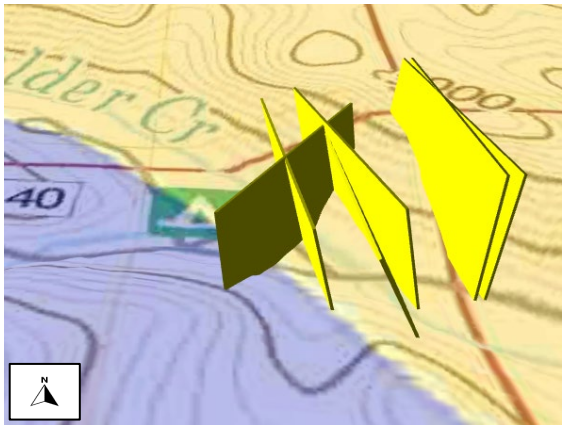

Figure 4-1: Sites NG2112 – NG2115, BCQ. Top map shows site location in the study area. The middle table contains the foliation data taken from the site. Poles to foliation planes are plotted on the stereonet in the lower left. Google Earth representation of plane orientations are shown in yellow in the lower right (Blenkinsop, 2012; Allmendinger et al., 2013; Cardozo & Allmendinger, 2013).

4.1.1. Central-area map foliations cont.

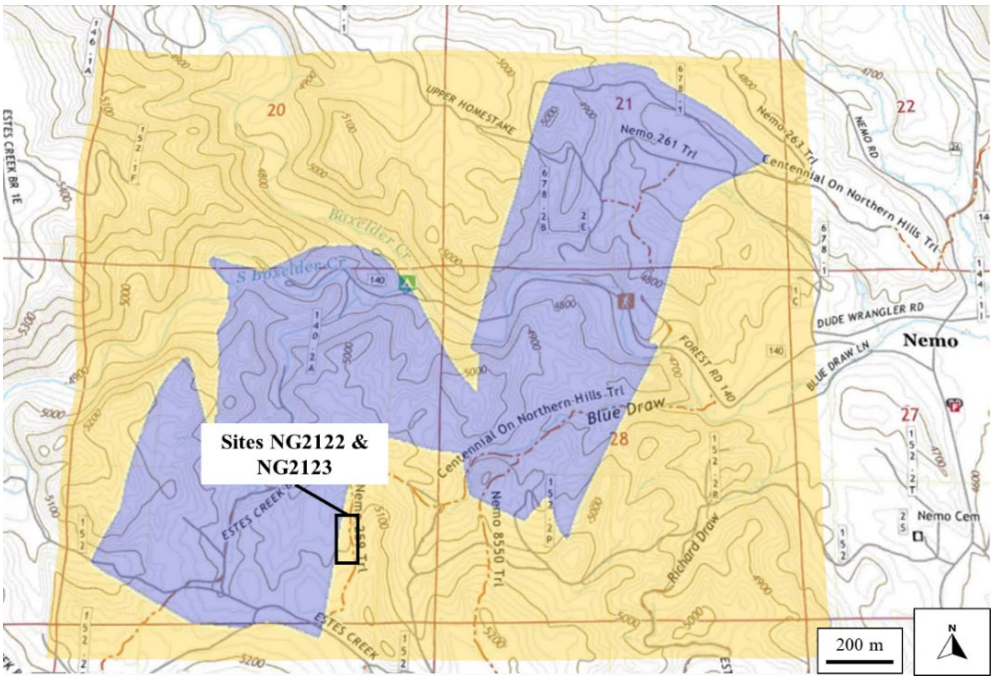

Site number	Latitude (deg.)	Longitude (deg.)	Lithology	Fol Strike RHR (az. deg.)	Fol Dip (deg.)	Dip Dir.
NG2122	44.18742	-103.53799	BCQ	175	87	W
NG2122	44.18742	-103.53799	BCQ	150	85	W
NG2122	44.18742	-103.53799	BCQ	350	82	E
NG2123	44.18917	-103.53809	BCQ	160	83	W

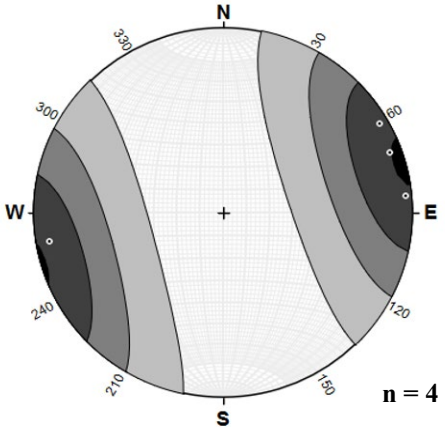

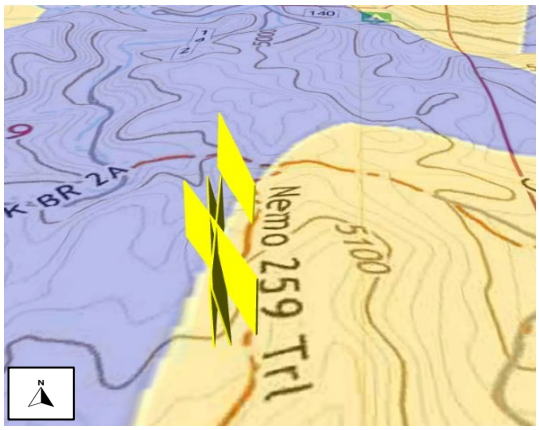

Figure 4-2: Sites NG2122 & NG2123, BCQ. Top map shows site location in the study area. The middle table contains the foliation data taken from the site. Poles to foliation planes are plotted on the stereonet in the lower left. Google Earth representation of plane orientations are shown in yellow in the lower right (Blenkinsop, 2012; Allmendinger et al., 2013; Cardozo & Allmendinger, 2013).

4.1.1. Central-area map foliations cont.

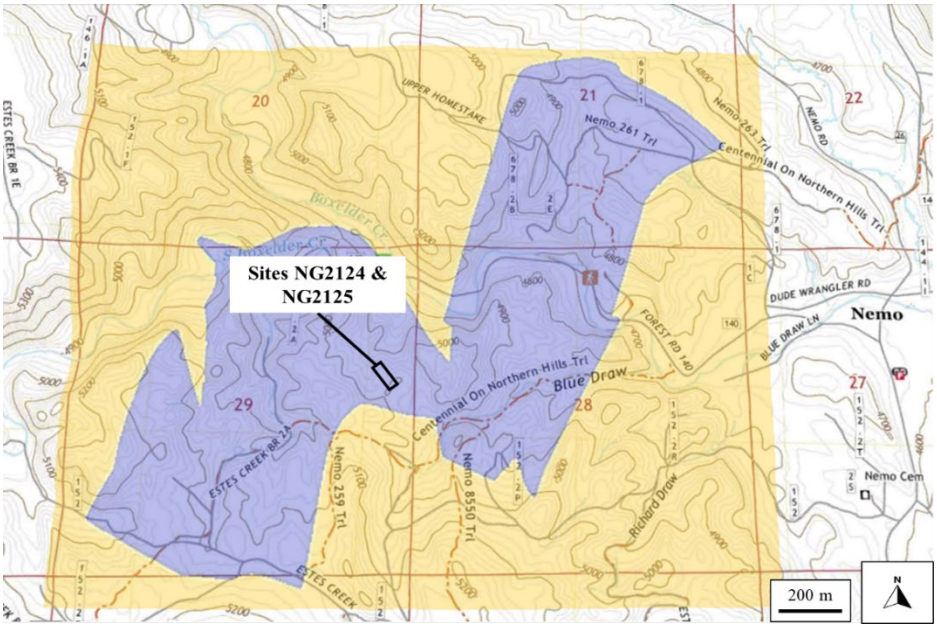

Site number	Latitude (deg.)	Longitude (deg.)	Lithology	Fol Strike RHR (az. deg.)	Fol Dip (deg.)	Dip Dir.
NG2124	44.19266	-103.5353	BDM	335	75	E
NG2124	44.19266	-103.5353	BDM	330	60	E
NG2124	44.19266	-103.5353	BDM	328	70	E
NG2124	44.19266	-103.5353	BDM	003	70	E
NG2124	44.19266	-103.5353	BDM	001	75	E
NG2124	44.19266	-103.5353	BDM	320	80	E
NG2125	44.19187	-103.53449	BDM	340	89	E

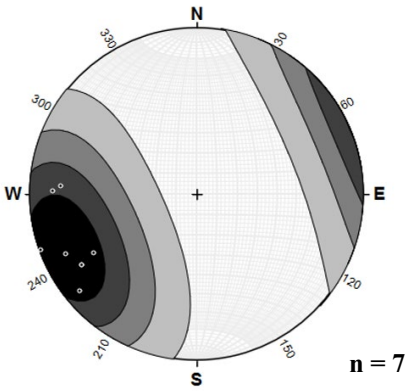

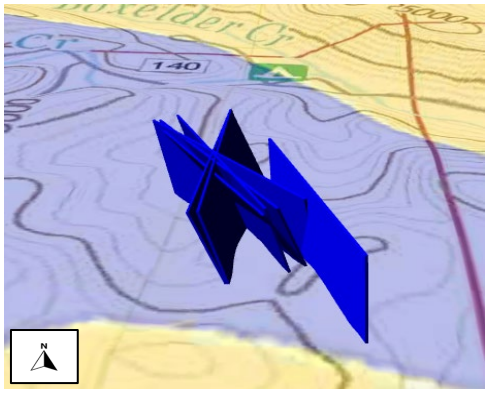

Figure 4-3: Sites NG2124 & NG2125, BDM. Top map shows site location in the study area. The middle table contains the foliation data taken from the site. Poles to foliation planes are plotted on the stereonet in the lower left. Google Earth representation of plane orientations are shown in blue in the lower right (Blenkinsop, 2012; Allmendinger et al., 2013; Cardozo & Allmendinger, 2013).

4.1.1. Central-area map foliations cont.

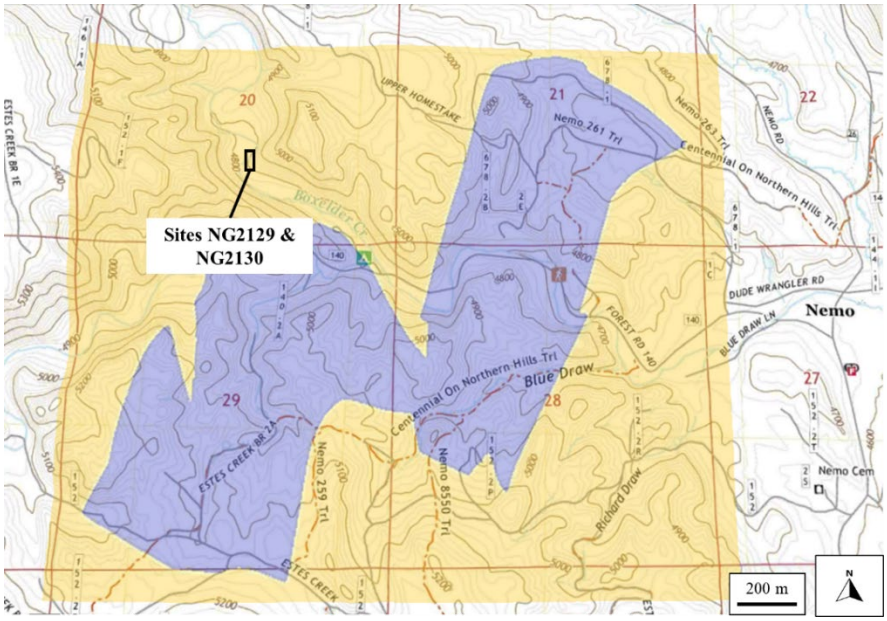

Site number	Latitude (deg.)	Longitude (deg.)	Lithology	Fol Strike RHR (az. deg.)	Fol Dip (deg.)	Dip Dir.
NG2129	44.20257	-103.54258	BCQ	338	86	E
NG2129	44.20257	-103.54258	BCQ	330	85	E
NG2129	44.20257	-103.54258	BCQ	151	88	W
NG2129	44.20257	-103.54258	BCQ	155	80	W
NG2129	44.20257	-103.54258	BCQ	331	86	E
NG2129	44.20257	-103.54258	BCQ	130	70	W
NG2129	44.20257	-103.54258	BCQ	153	85	W
NG2129	44.20257	-103.54258	BCQ	160	78	W
NG2129	44.20257	-103.54258	BCQ	150	70	W
NG2129	44.20257	-103.54258	BCQ	334	82	E
NG2130	44.20286	-103.54227	BCQ	160	73	W
NG2130	44.20286	-103.54227	BCQ	330	73	E

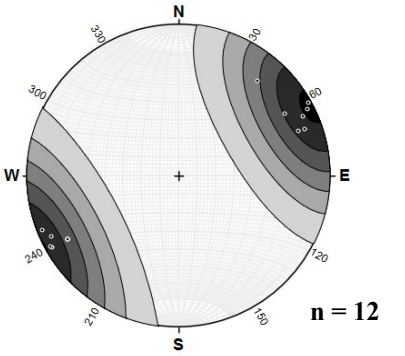

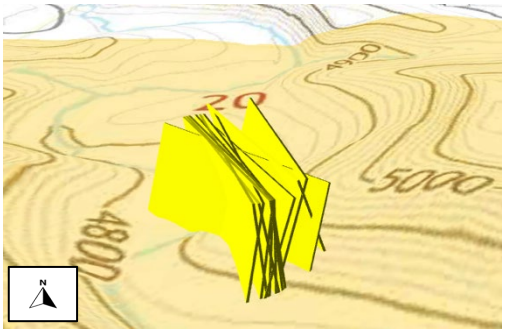

Figure 4-4: Sites NG2129 & NG2130, BCQ. Top map shows site location in the study area. The middle table contains the foliation data taken from the site. Poles to foliation planes are plotted on the stereonet in the lower left. Google Earth representation of plane orientations are shown in yellow in the lower right (Blenkinsop, 2012; Allmendinger et al., 2013; Cardozo & Allmendinger, 2013).

4.1.1. Central-area map foliations cont.

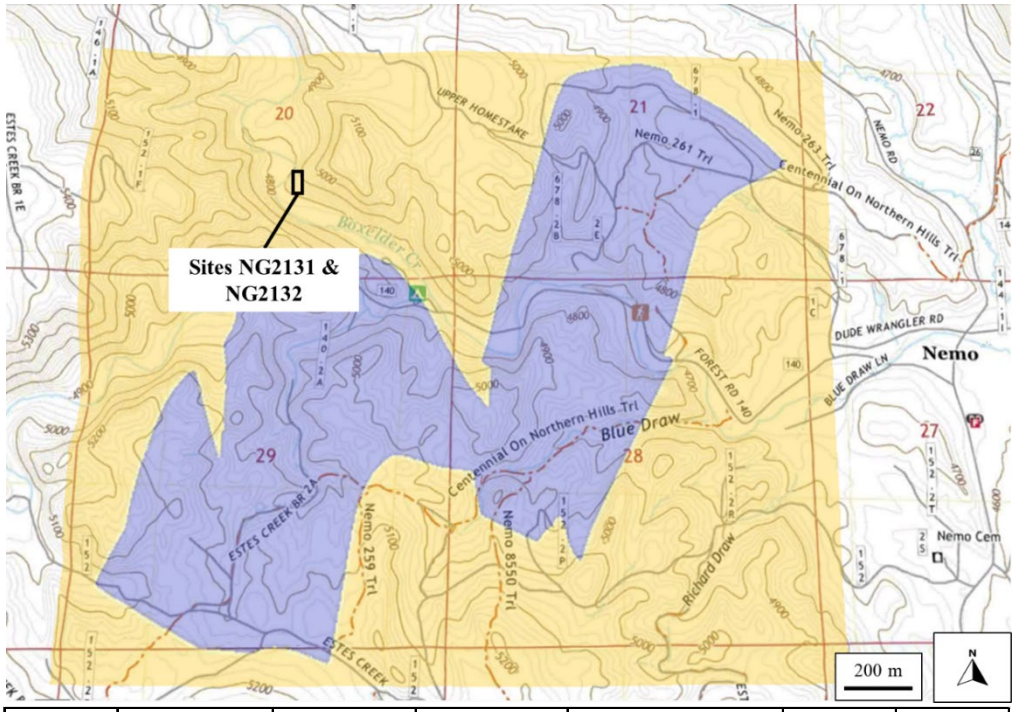

Site number	Latitude (deg.)	Longitude (deg.)	Lithology	Fol Strike RHR (az. deg.)	Fol Dip (deg.)	Dip Dir.
NG2131	44.203	-103.54167	BCQ	109	83	W
NG2131	44.203	-103.54167	BCQ	330	79	E
NG2132	44.20309	-103.54148	phyllite	140	87	W
NG2132	44.20309	-103.54148	phyllite	153	80	W
NG2132	44.20309	-103.54148	phyllite	149	80	W

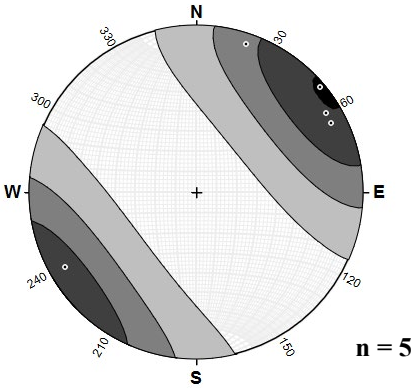

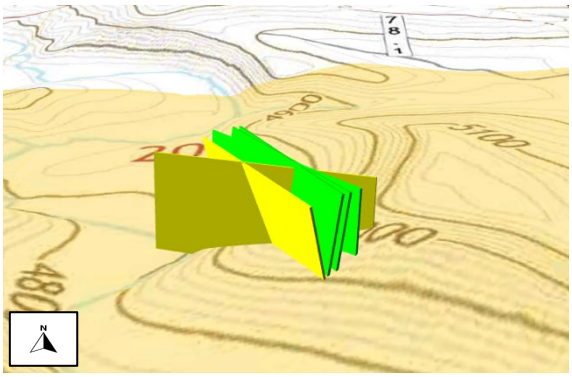

Figure 4-5: Sites NG2131 & NG2132, BCQ. Top map shows site location in the study area. The middle table contains the foliation data taken from the site. Poles to foliation planes are plotted on the stereonet in the lower left. Google Earth representation of plane orientations for quartzite are shown in yellow and phyllite in green in the lower right (Blenkinsop, 2012; Allmendinger et al., 2013; Cardozo & Allmendinger, 2013).

4.1.1. Central-area map foliations cont.

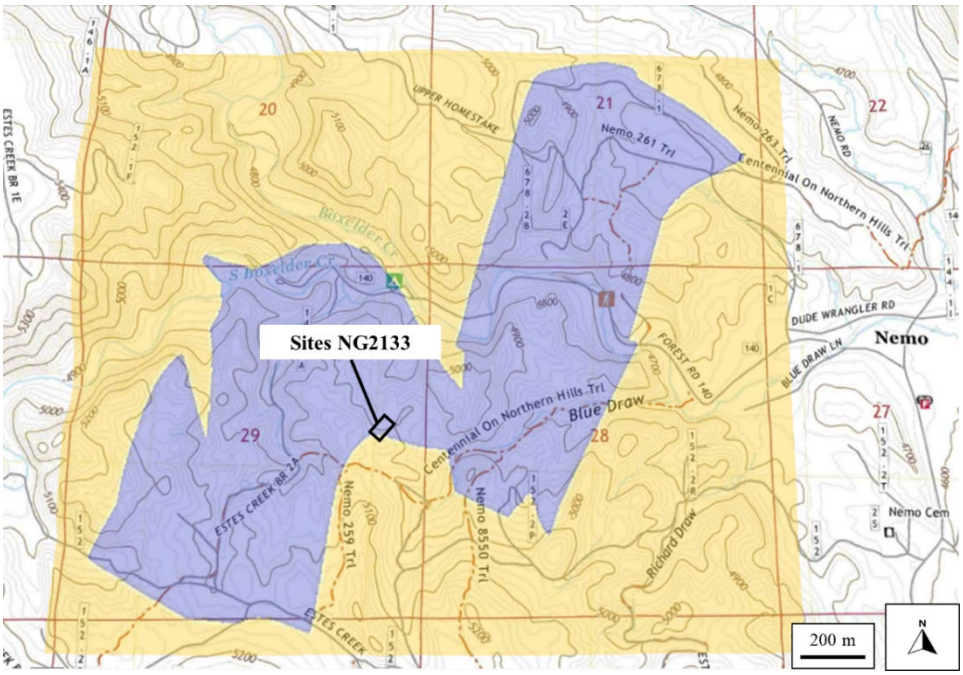

Site number	Latitude (deg.)	Longitude (deg.)	Lithology	Fol Strike RHR (az. deg.)	Fol Dip (deg.)	Dip Dir.
NG2133	44.19113	-103.53535	BDM	320	85	E
NG2133	44.19113	-103.53535	BDM	120	85	W
NG2133	44.19113	-103.53535	BDM	145	85	W
NG2133	44.19113	-103.53535	BDM	302	85	E
NG2133	44.19113	-103.53535	BDM	155	60	W
NG2133	44.19113	-103.53535	BDM	350	75	E

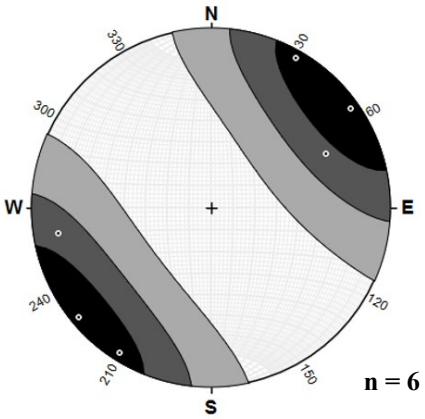

Figure 4-6: Site NG2133, BDM. Top map shows site location in the study area. The middle table contains the foliation data taken from the site. Poles to foliation planes are plotted on the stereonet in the lower left. Google Earth representation of plane orientations are shown in blue in the lower right (Blenkinsop, 2012; Allmendinger et al., 2013; Cardozo & Allmendinger, 2013).

4.1.1. Central-area map foliations cont.

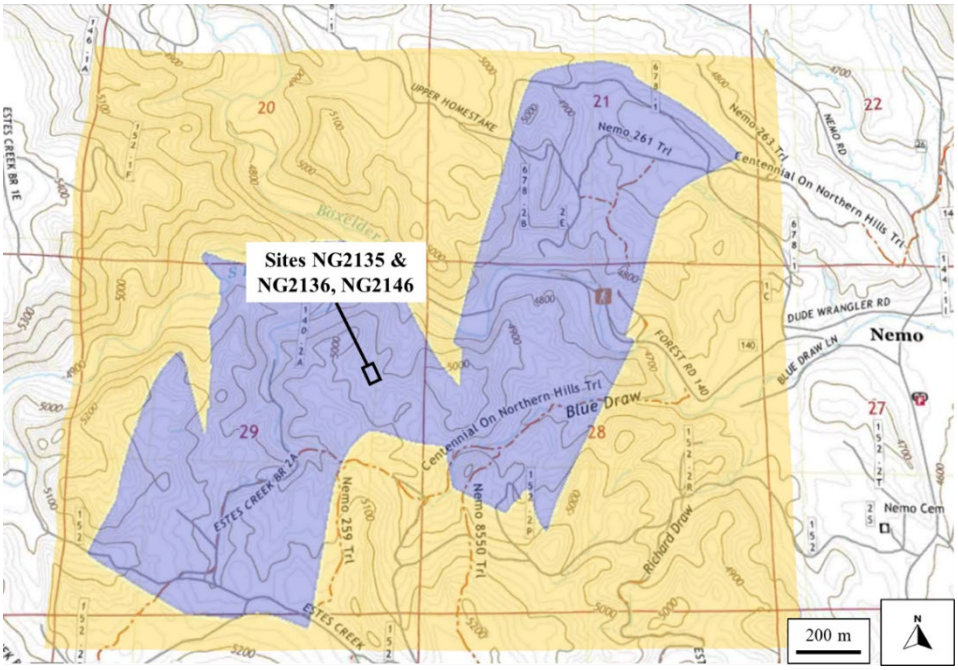

Site number	Latitude (deg.)	Longitude (deg.)	Lithology	Fol Strike RHR (az. deg.)	Fol Dip (deg.)	Dip Dir.
NG2135	44.19354	-103.53629	BDM	334	89	E
NG2135	44.19354	-103.53629	BDM	328	88	E
NG2136	44.19373	-103.53643	BDM	320	85	E
NG2136	44.19373	-103.53643	BDM	335	86	E
NG2146	44.19377	-103.53615	BDM	330	83	E

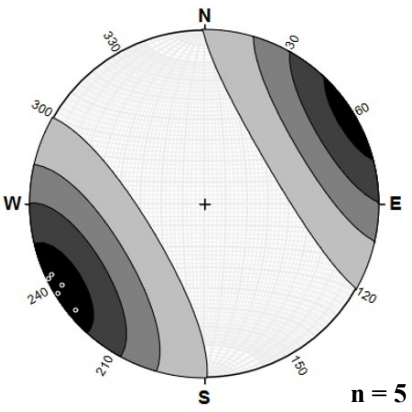

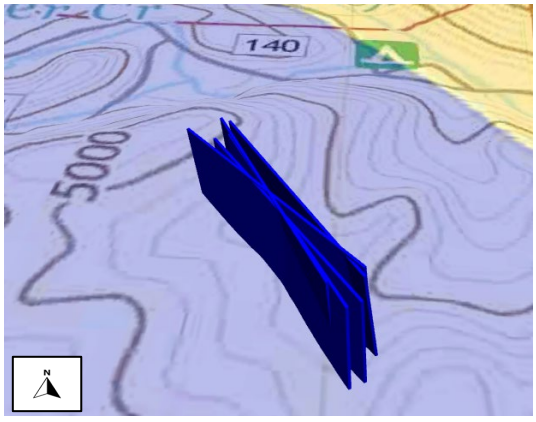

Figure 4-7: Sites NG2135, NG2136, & NG2146, BDM. Top map shows site location in the study area. The middle table contains the foliation data taken from the site. Poles to foliation planes are plotted on the stereonet in the lower left. Google Earth representation of plane orientations are shown in blue in the lower right (Blenkinsop, 2012; Allmendinger et al., 2013; Cardozo & Allmendinger, 2013).

4.1.1. Central-area map foliations cont.

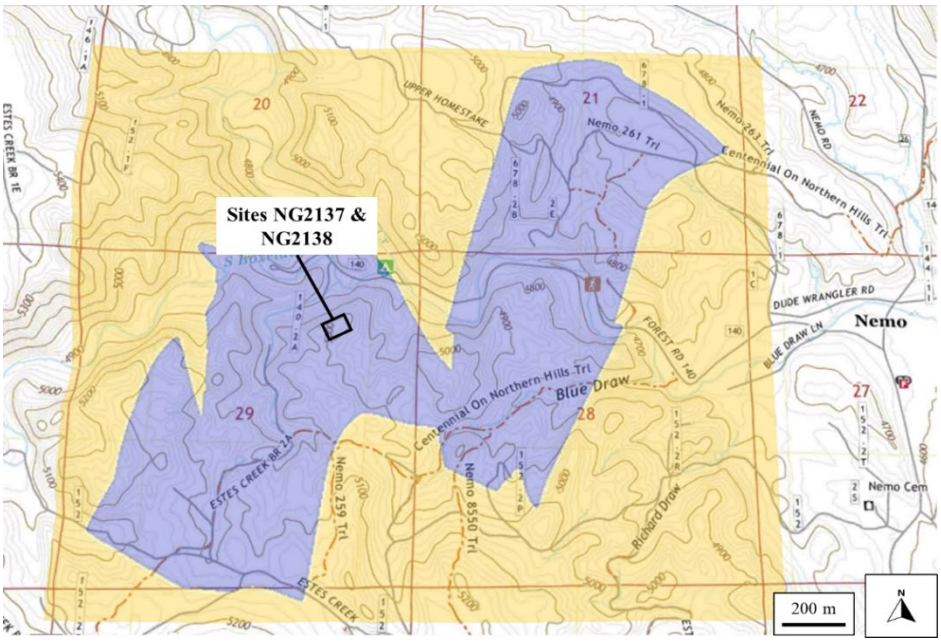

Site number	Latitude (deg.)	Longitude (deg.)	Lithology	Fol Strike RHR (az. deg.)	Fol Dip (deg.)	Dip Dir.
NG2137	44.19472	-103.53818	BDM	325	65	E
NG2137	44.19472	-103.53818	BDM	270	55	E
NG2138	44.19506	-103.53751	BDM	185	87	W
NG2138	44.19506	-103.53751	BDM	302	66	E
NG2138	44.19506	-103.53751	BDM	224	85	W
NG2138	44.19506	-103.53751	BDM	310	65	E
NG2138	44.19506	-103.53751	BDM	152	56	W
NG2138	44.19506	-103.53751	BDM	004	32	E

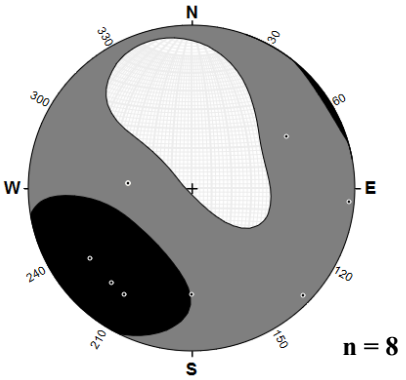

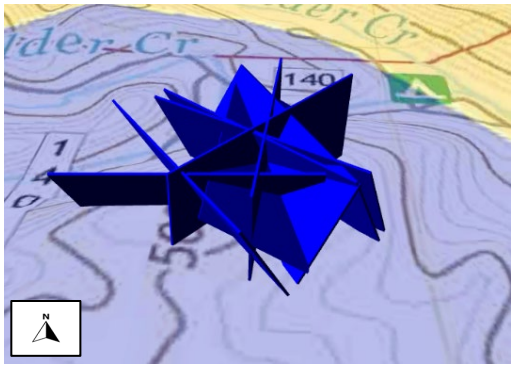

Figure 4-8: Sites NG2137 & NG2138, BDM. Top map shows site location in the study area. The middle table contains the foliation data taken from the site. Poles to foliation planes are plotted on the stereonet in the lower left. Google Earth representation of plane orientations are shown in blue in the lower right (Blenkinsop, 2012; Allmendinger et al., 2013; Cardozo & Allmendinger, 2013).

4.1.1. Central-area map foliations cont.

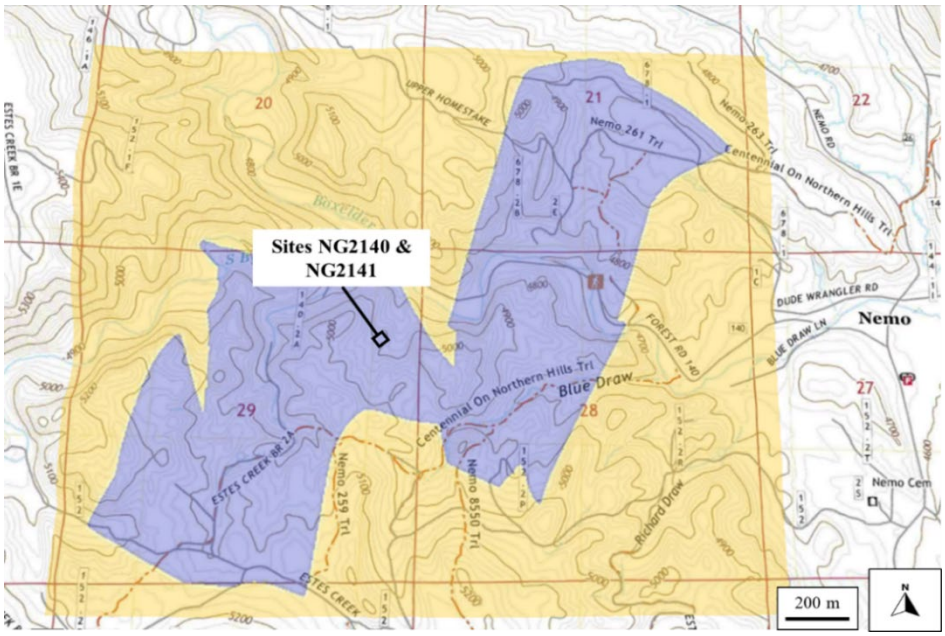

Site number	Latitude (deg.)	Longitude (deg.)	Lithology	Fol Strike RHR (az. deg.)	Fol Dip (deg.)	Dip Dir.
NG2140	44.19412	-103.53588	BDM	006	89	E
NG2140	44.19412	-103.53588	BDM	00	80	E
NG2140	44.19412	-103.53588	BDM	001	85	E
NG2140	44.19412	-103.53588	BDM	178	84	W
NG2140	44.19412	-103.53588	BDM	359	90	N/A
NG2141	44.19407	-103.53562	BDM	338	90	N/A
NG2141	44.19407	-103.53562	BDM	354	90	N/A
NG2141	44.19407	-103.53562	BDM	340	90	N/A

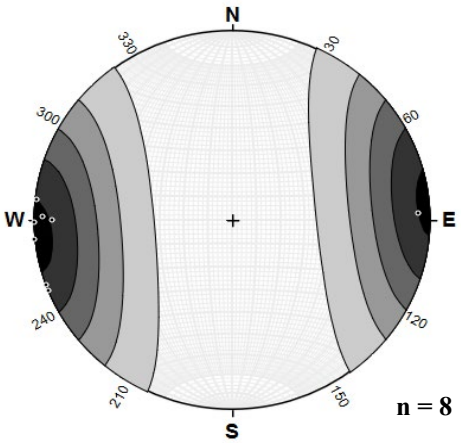

Figure 4-9: Sites NG2140 & NG2141, BDM. Top map shows site location in the study area. The middle table contains the foliation data taken from the site. Poles to foliation planes are plotted on the stereonet in the lower left. Google Earth representation of plane orientations are shown in blue in the lower right (Blenkinsop, 2012; Allmendinger et al., 2013; Cardozo & Allmendinger, 2013).

4.1.1. Central-area map foliations cont.

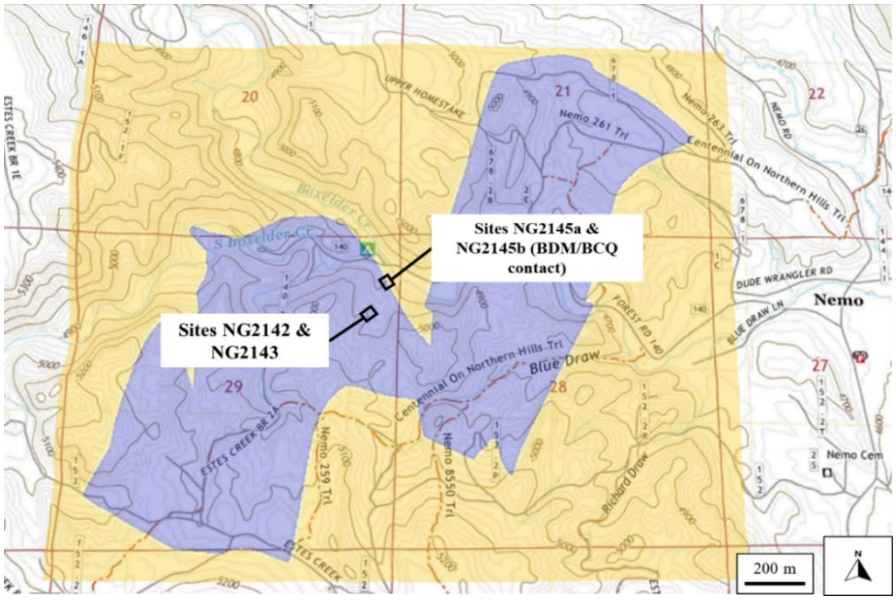

Site number	Latitude (deg.)	Longitude (deg.)	Lithology	Fol Strike RHR (az. deg.)	Fol Dip (deg.)	Dip Dir.
NG2142	44.19441	-103.53527	BDM	197	85	W
NG2142	44.19441	-103.53527	BDM	320	90	N/A
NG2143	44.19465	-103.53497	BDM	195	80	W
NG2143	44.19465	-103.53497	BDM	200	82	W
NG2143	44.19465	-103.53497	BDM	200	79	W
NG2145a	44.19548	-103.53383	BDM	349	65	E
NG2145b	44.19548	-103.53383	BCQ	354	75	E

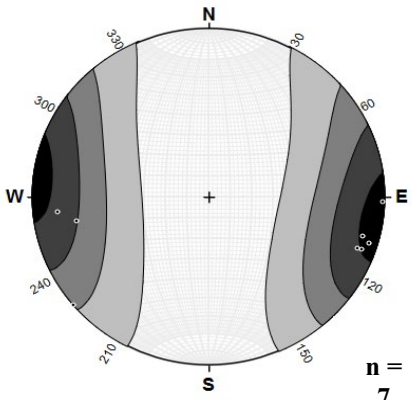

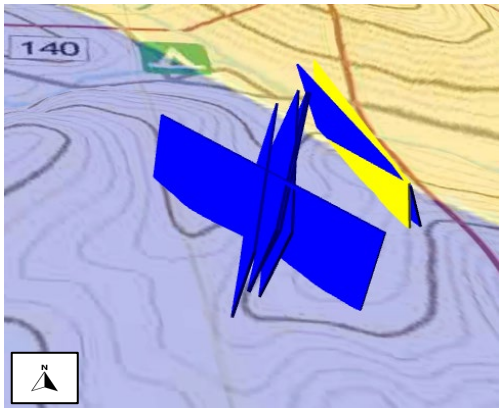

Figure 4-10: Sites NG2142, NG2143, NG2145a, & NG2145b, BDM/BCQ lithological contact. Top map shows site location in the study area. The middle table contains the foliation data taken from the site. Poles to foliation planes are plotted on the stereonet in the lower left. Google Earth representation of plane orientations are shown in blue (BDM) and yellow (BCQ) in the lower right (Blenkinsop, 2012; Allmendinger et al., 2013; Cardozo & Allmendinger, 2013).

4.1.2. Knob Hill Foliations

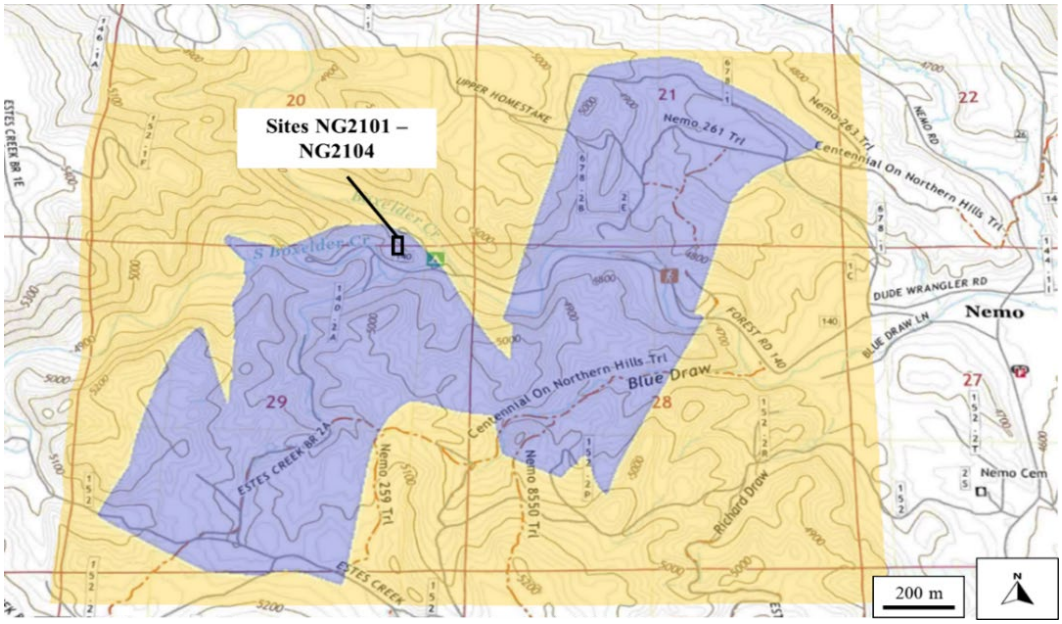

Site number	Latitude (deg.)	Longitude (deg.)	Lithology	Fol Strike RHR (az. deg.)	Fol Dip (deg.)	Dip Dir.
NG2101	44.1975	-103.53721	BDM	182	89	W
NG2101	44.1975	-103.53721	BDM	002	84	E
NG2102	44.19781	-103.53709	BDM	176	76	W
NG2103	44.19788	-103.53712	BDM	342	86	E
NG2104	44.1978	-103.53711	BDM	174	89	W
NG2104	44.1978	-103.53711	BDM	006	72	E
NG2104	44.1978	-103.53711	BDM	004	68	E
NG2104	44.1978	-103.53711	BDM	165	88	W
NG2104	44.1978	-103.53711	BDM	003	84	E
NG2104	44.1978	-103.53711	BDM	352	70	E

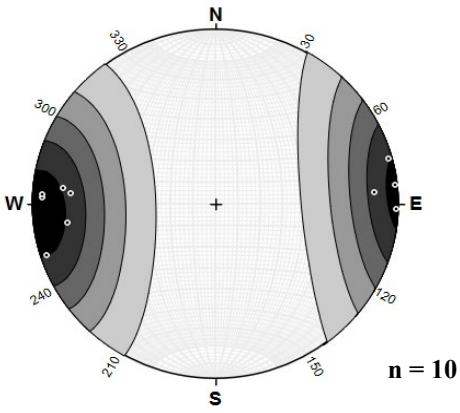

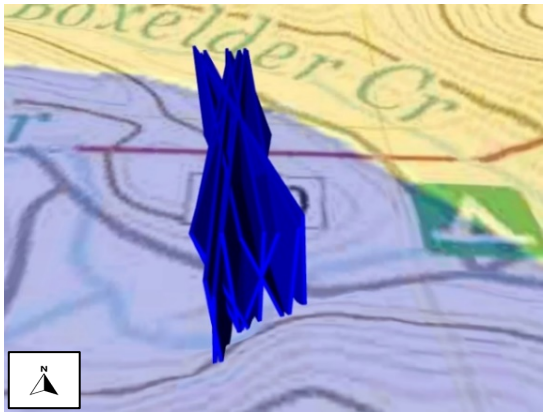

Figure 4-11: Sites NG2101 – NG2104, BDM. Top map shows site location in the study area. The middle table contains the foliation data taken from the site. Poles to foliation planes are plotted on the stereonet in the lower left. Google Earth representation of plane orientations are shown in blue in the lower right (Blenkinsop, 2012; Allmendinger et al., 2013; Cardozo & Allmendinger, 2013).

4.1.2. Knob Hill foliations cont.

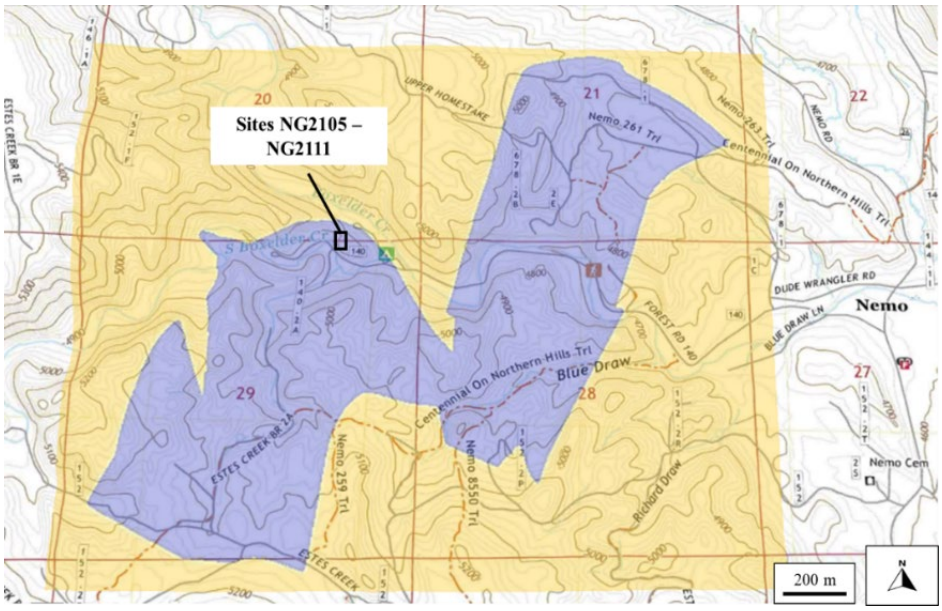

Site number	Latitude (deg.)	Longitude (deg.)	Lithology	Fol Strike RHR (az. deg.)	Fol Dip (deg.)	Dip Dir.
NG2105	44.19776	-103.53726	BDM	174	75	W
NG2106	44.19786	-103.53725	BDM	110	78	W
NG2106	44.19786	-103.53725	BDM	146	89	W
NG2107	44.19789	-103.53745	BDM	163	85	W
NG2108	44.198	-103.53749	BDM	345	58	E
NG2108	44.198	-103.53749	BDM	170	89	W
NG2109	44.19804	-103.53751	BDM	305	70	E
NG2109	44.19804	-103.53751	BDM	163	68	W
NG2111	44.19799	-103.53749	BDM	000	80	E
NG2111	44.19799	-103.53749	BDM	138	82	W

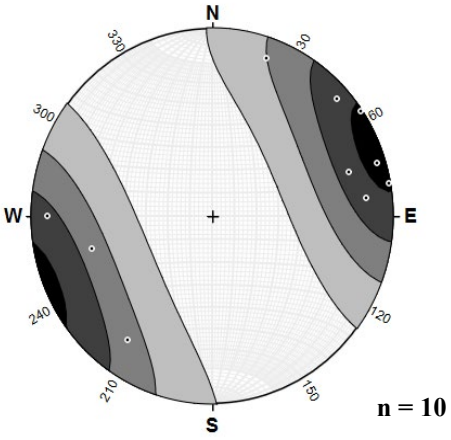

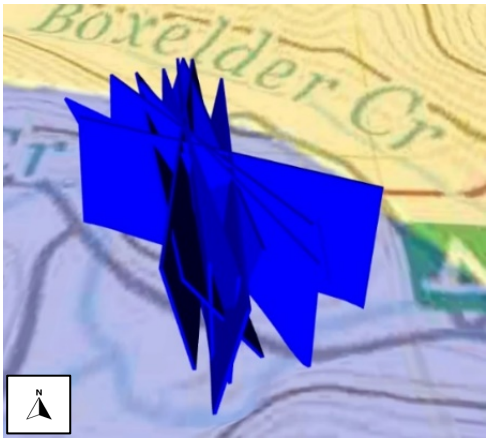

Figure 4-12: Sites NG2105 – NG2111, BDM. Top map shows site location in the study area. The middle table contains the foliation data taken from the site. Poles to foliation planes are plotted on the stereonet in the lower left. Google Earth representation of plane orientations are shown in blue in the lower right (Blenkinsop, 2012; Allmendinger et al., 2013; Cardozo & Allmendinger, 2013).

4.1.2. Knob Hill foliations cont.

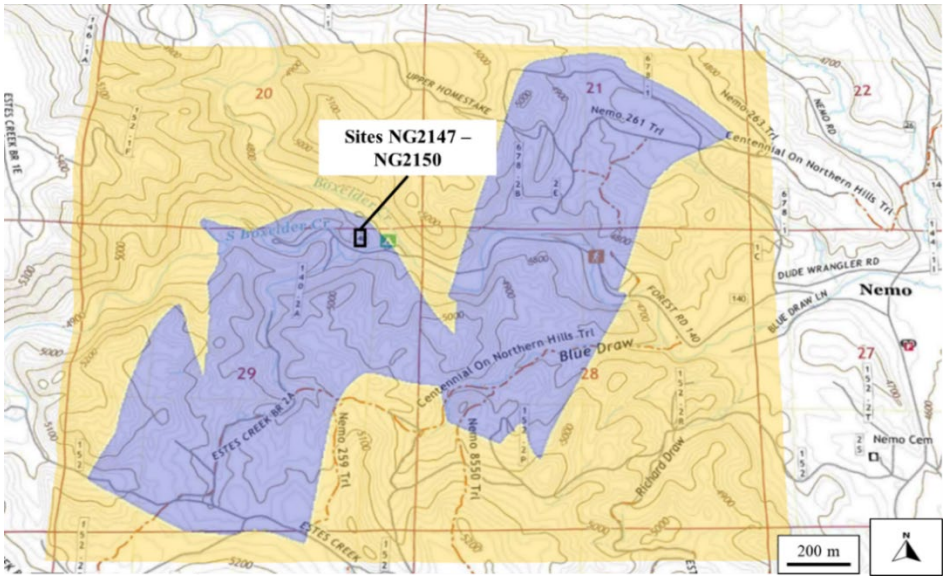

Site number	Latitude (deg.)	Longitude (deg.)	Lithology	Fol Strike RHR (az. deg.)	Fol Dip (deg.)	Dip Dir.
NG21-47	44.19785	-103.53697	BDM	146	83	W
NG21-47	44.19785	-103.53697	BDM	316	89	E
NG21-47	44.19785	-103.53697	BDM	280	87	E
NG21-48	44.1977	-103.53688	BDM	315	89	E
NG21-48	44.1977	-103.53688	BDM	277	78	E
NG21-48	44.1977	-103.53688	BDM	109	80	W
NG21-48	44.1977	-103.53688	BDM	155	55	W
NG21-49	44.19781	-103.53672	BDM	144	82	W
NG21-49	44.19781	-103.53672	BDM	310	84	E
NG21-50	44.19779	-103.53686	BDM	125	80	W
NG21-50	44.19779	-103.53686	BDM	162	42	W

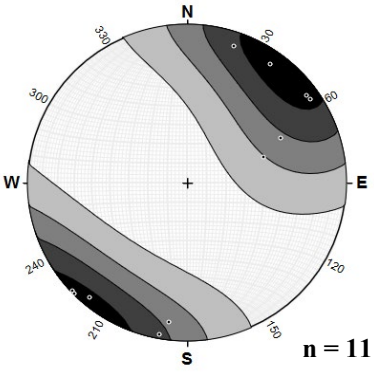

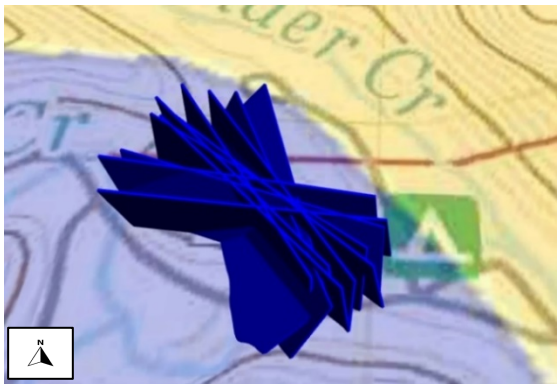

Figure 4-13: Sites NG2147 – NG2150, BDM. Top map shows site location in the study area. The middle table contains the foliation data taken from the site. Poles to foliation planes are plotted on the stereonet in the lower left. Google Earth representation of plane orientations are shown in blue in the lower right (Blenkinsop, 2012; Allmendinger et al., 2013; Cardozo & Allmendinger, 2013).

4.1.2. Knob Hill foliations cont.

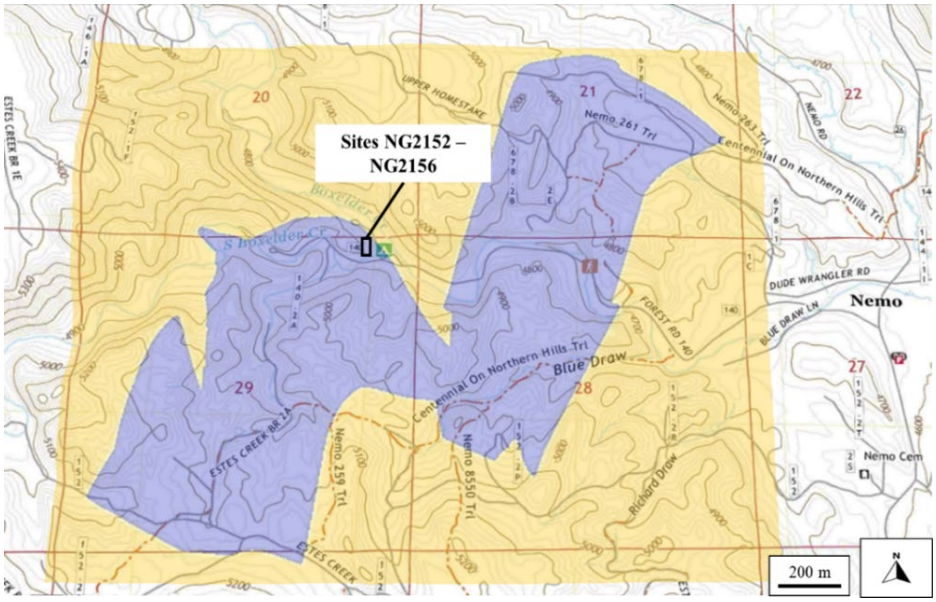

Site number	Latitude (deg.)	Longitude (deg.)	Lithology	Fol Strike RHR (az. deg.)	Fol Dip (deg.)	Dip Dir.
NG2152	44.19773	-103.53665	BDM	122	75	W
NG2152	44.19773	-103.53665	BDM	159	78	W
NG2153	44.19765	-103.53651	BDM	118	78	W
NG2153	44.19765	-103.53651	BDM	125	76	W
NG2155	44.19759	-103.53656	BDM	300	89	E
NG2155	44.19759	-103.53656	BDM	149	85	W
NG2155	44.19759	-103.53656	BDM	145	83	W
NG2155	44.19759	-103.53656	BDM	165	89	W
NG2156	44.19747	-103.53649	BDM	178	46	W
NG2156	44.19747	-103.53649	BDM	305	88	E
NG2156	44.19747	-103.53649	BDM	305	90	E

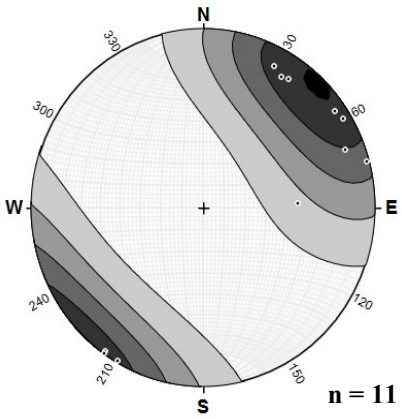

Figure 4-14: Sites NG2152 – NG2156, BDM. Top map shows site location in the study area. The middle table contains the foliation data taken from the site. Poles to foliation planes are plotted on the stereonet in the lower left. Google Earth representation of plane orientations are shown in blue in the lower right (Blenkinsop, 2012; Allmendinger et al., 2013; Cardozo & Allmendinger, 2013).

4.1.3. *Eastern-area Map Foliations*

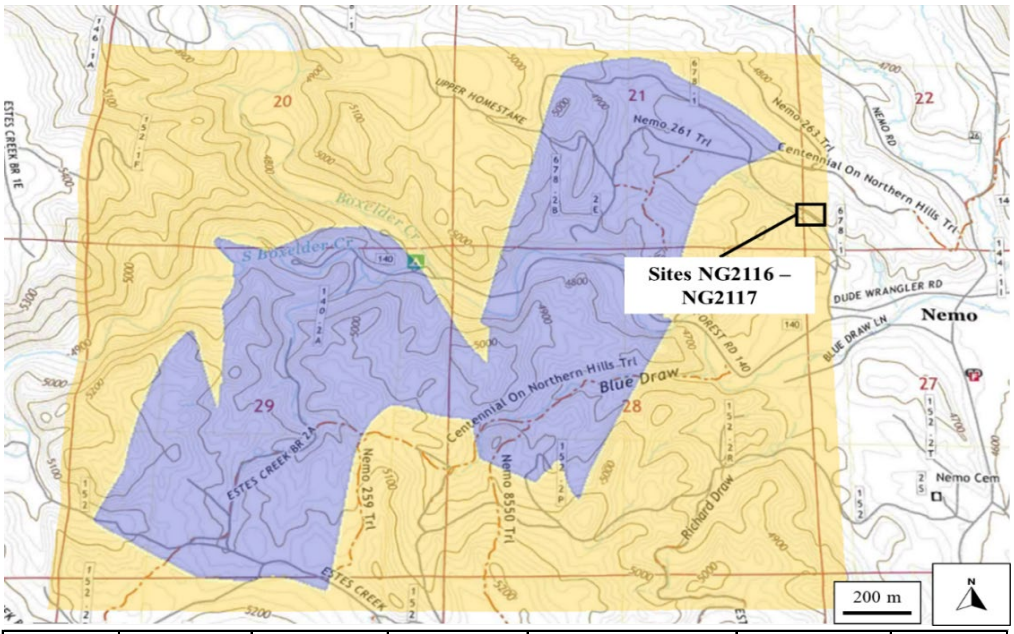

Site number	Latitude (deg.)	Longitude (deg.)	Lithology	Fol Strike RHR (az. deg.)	Fol Dip (deg.)	Dip Dir.
NG2116	44.19964	-103.51182	BCQ	165	82	W
NG2116	44.19964	-103.51182	BCQ	160	82	W
NG2116	44.19964	-103.51182	BCQ	178	71	W
NG2116	44.19964	-103.51182	BCQ	153	65	W
NG2117	44.19987	-103.51201	BCQ	140	86	W
NG2117	44.19987	-103.51201	BCQ	149	85	W
NG2117	44.19987	-103.51201	BCQ	151	85	W
NG2117	44.19987	-103.51201	BCQ	160	84	W

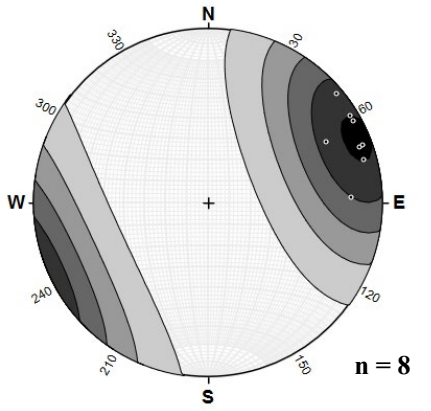

Figure 4-15: Sites NG2116 & NG2117, BCQ. Top map shows site location in the study area. The middle table contains the foliation data taken from the site. Poles to foliation planes are plotted on the stereonet in the lower left. Google Earth representation of plane orientations are shown in yellow in the lower right (Blenkinsop, 2012; Allmendinger et al., 2013; Cardozo & Allmendinger, 2013).

4.1.3. Eastern-area map foliations cont.

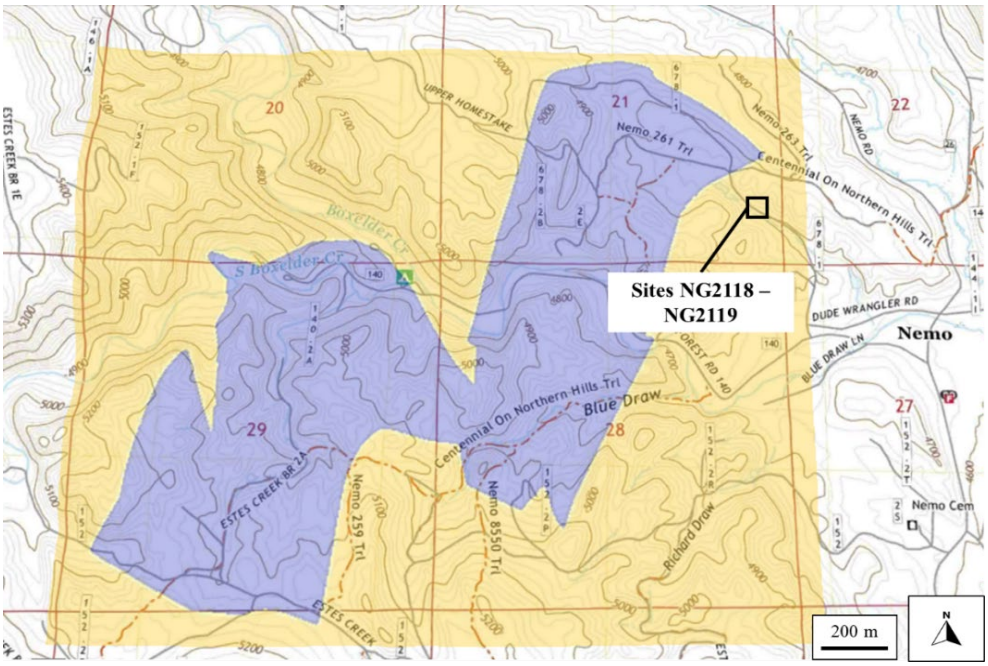

Site number	Latitude (deg.)	Longitude (deg.)	Lithology	Fol Strike RHR (az. deg.)	Fol Dip (deg.)	Dip Dir.
NG2118	44.20143	-103.51516	BCQ	135	65	W
NG2118	44.20143	-103.51516	BCQ	140	80	W
NG2119	44.20138	-103.51487	BCQ	173	85	W
NG2119	44.20138	-103.51487	BCQ	140	63	W
NG2119	44.20138	-103.51487	BCQ	150	80	W
NG2119	44.20138	-103.51487	BCQ	185	86	W

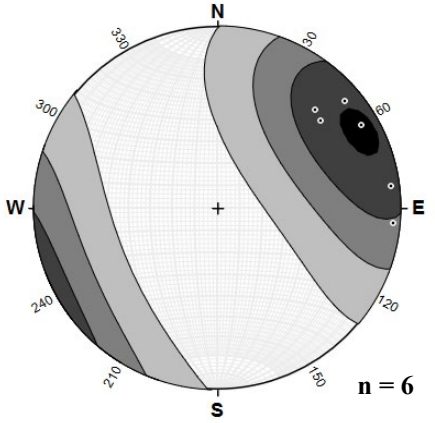

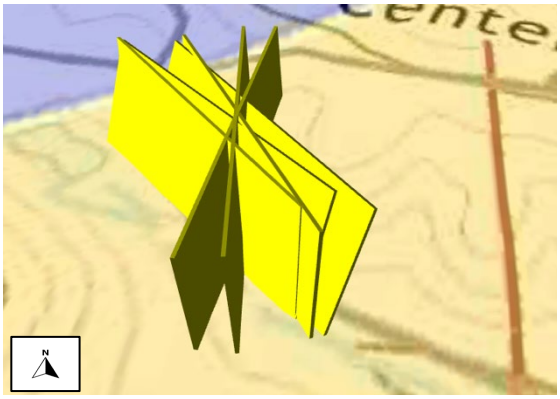

Figure 4-16: Sites NG2118 & NG2119, BCQ. Top map shows site location in the study area. The middle table contains the foliation data taken from the site. Poles to foliation planes are plotted on the stereonet in the lower left. Google Earth representation of plane orientations are shown in yellow in the lower right (Blenkinsop, 2012; Allmendinger et al., 2013; Cardozo & Allmendinger, 2013).

4.1.3. Eastern-area map foliations cont.

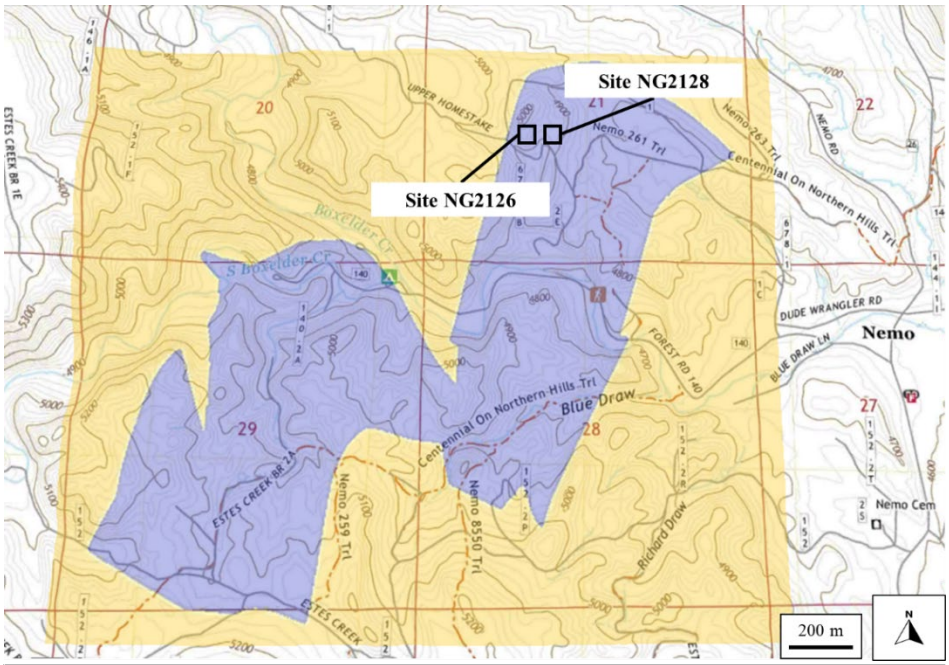

Site number	Latitude (deg.)	Longitude (deg.)	Lithology	Fol Strike RHR (az. deg.)	Fol Dip (deg.)	Dip Dir.
NG2126	44.20439	-103.52659	BDM	105	79	S
NG2126	44.20439	-103.52659	BDM	102	82	S
NG2126	44.20439	-103.52659	BDM	98	81	S
NG2126	44.20439	-103.52659	BDM	330	80	E
NG2128	44.20406	-103.52512	BDM	150	50	W
NG2128	44.20406	-103.52512	BDM	297	56	E

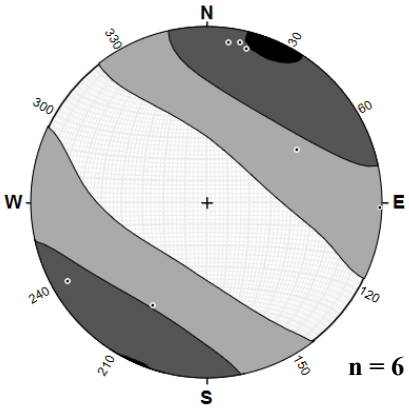

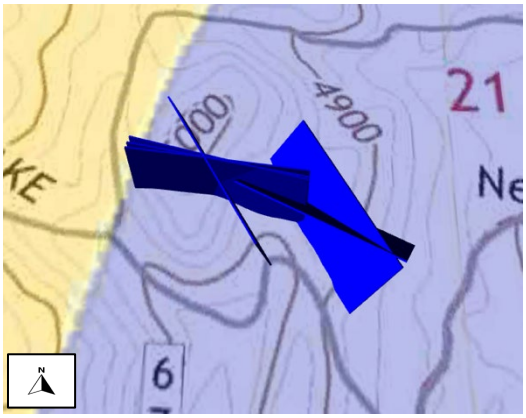

Figure 4-17: Sites NG2126 & NG2128, BDM. Top map shows site location in the study area. The middle table contains the foliation data taken from the site. Poles to foliation planes are plotted on the stereonet in the lower left. Google Earth representation of plane orientations are shown in blue in the lower right (Blenkinsop, 2012; Allmendinger et al., 2013; Cardozo & Allmendinger, 2013).

4.1.3. Eastern-area map foliations cont.

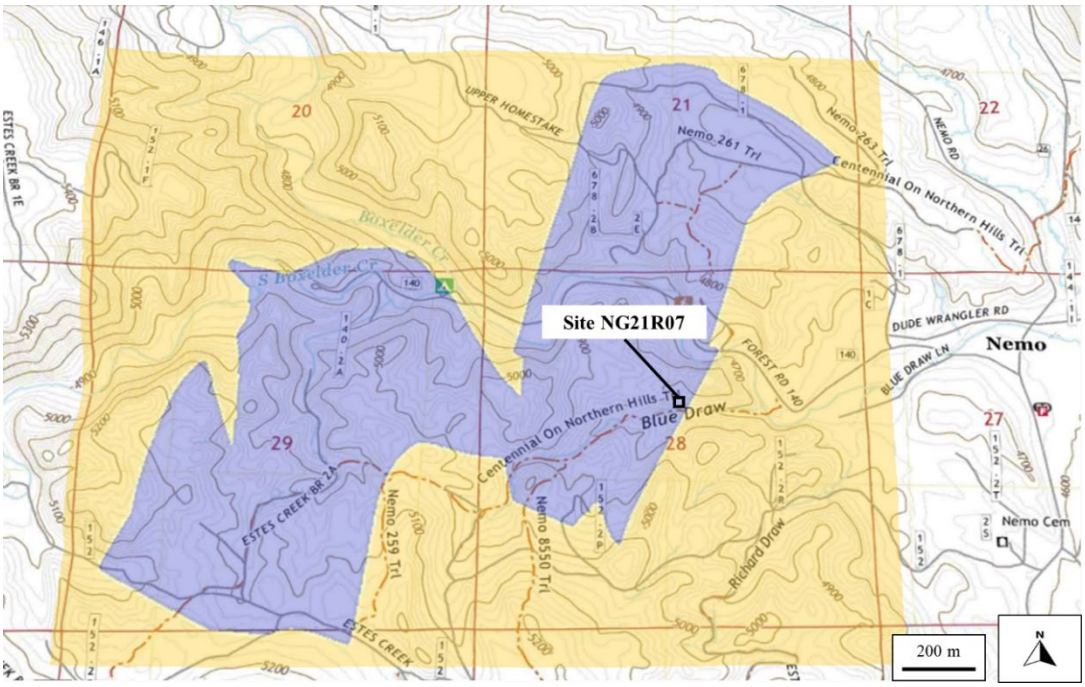

Site number	Latitude (deg.)	Longitude (deg.)	Lithology	Fol Strike RHR (az. deg.)	Fol Dip (deg.)	Dip Dir.
NG21R07	44.19285	-103.52275	BDM	152	73	W
NG21R07	44.19285	-103.52275	BDM	135	75	W
NG21R07	44.19285	-103.52275	BDM	166	84	W
NG21R07	44.19285	-103.52275	BDM	187	73	W

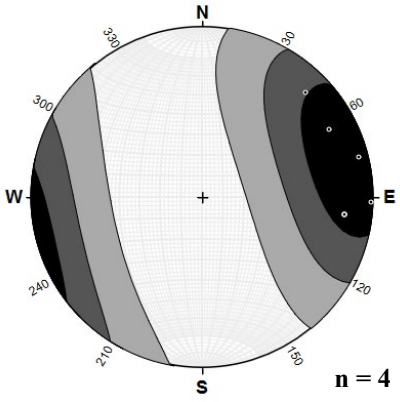

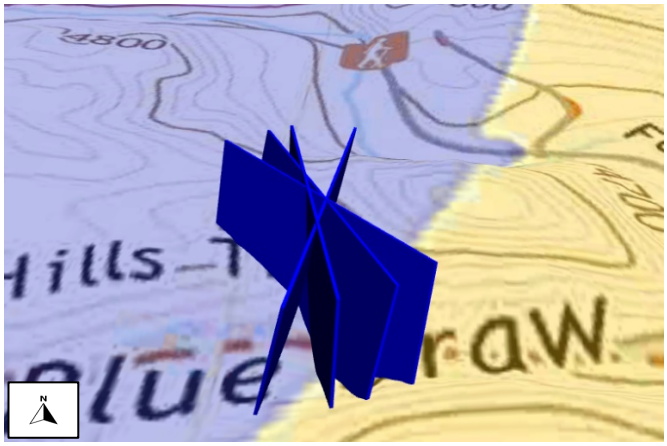

Figure 4-18: Site NG21R07, BDM. Top map shows site location in the study area. The middle table contains the foliation data taken from the site. Poles to foliation planes are plotted on the stereonet in the lower left. Google Earth representation of plane orientations are shown in blue in the lower right (Blenkinsop, 2012; Allmendinger et al., 2013; Cardozo & Allmendinger, 2013).

4.2. Lineations

Lineations were measured in the field, and the data can be found in **Tables A3 & A4** in the Appendix. Generally, lineations were difficult to observe in the field due to heavy organic cover and, in the case of the BDM, many structural fabrics may have been erased due to post-deformational hydrothermal alteration. However, where present, the lineation orientations were similar between both the BDM and the BCQ, with a common trend of ~330° to ~350° and plunges ranging from 40° to vertical, with plunges in both the NW and SE directions in the BDM and to the NW in the BCQ. In the BCQ, lineations were often composed of elongated quartz as opposed to those found in the BDM, which were composed of preferred alignment of micas and feldspar. Stereonet plots of the lineation geometries can be found below.

4.2.1. Lineations (BDM)

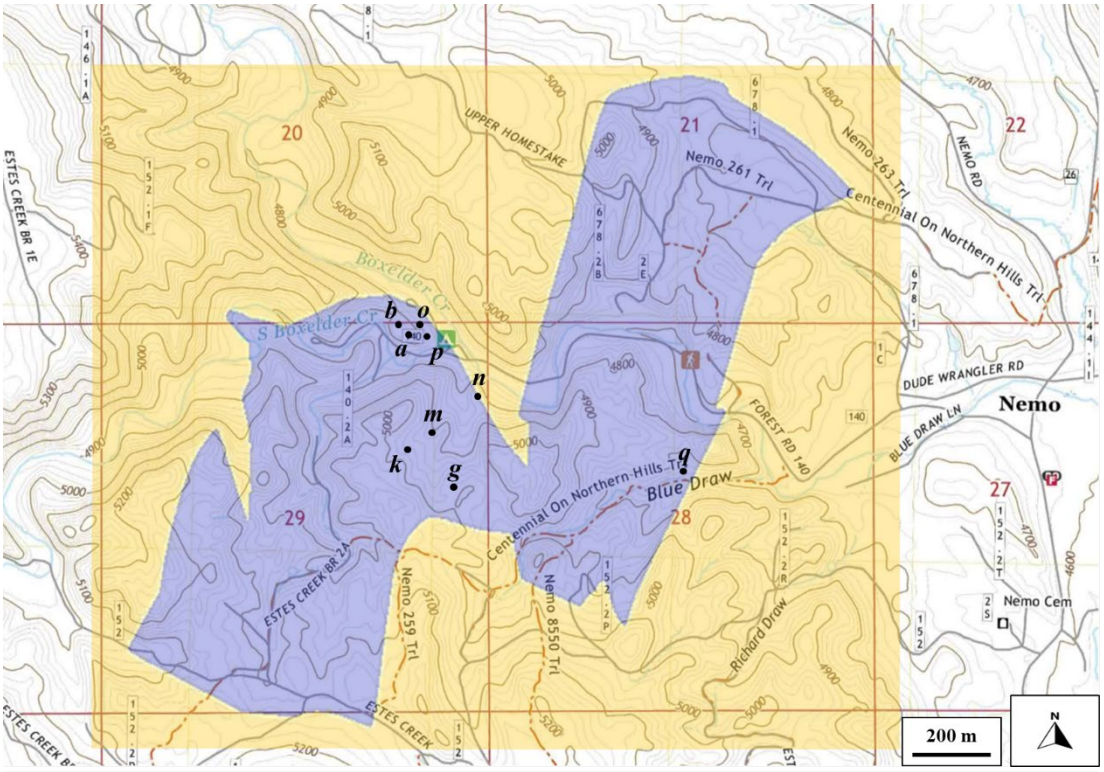

Map Letter	Site number	Latitude (deg.)	Longitude (deg.)	Lithology	Lineation Plunge (deg.)	Lineation Trend (azimuth deg.)
a	NG2101	44.1975	-103.53721	BDM	64	002
a	NG2103	44.19788	-103.53712	BDM	85	342
a	NG2104	44.1978	-103.53711	BDM	63	174
a	NG2104	44.1978	-103.53711	BDM	65	174
b	NG2105	44.19776	-103.53726	BDM	68	354
g	NG2124	44.19266	-103.5353	BDM	85	150
m	NG2140	44.19412	-103.53588	BDM	70	180
m	NG2140	44.19412	-103.53588	BDM	65	180
n	NG2145a	44.19548	-103.53383	BDM	85	350
k	NG2146	44.19377	-103.53615	BDM	50	330
o	NG2147	44.19785	-103.53697	BDM	85	320
p	NG2151	44.19777	-103.53672	BDM	57	135
q	NG21R07	44.19285	-103.52275	BDM	61	267

Figure 4-19: Sites where BDM lineation data was measured and plotted on both stereonets and with 3D orientations in Google Earth.

4.2.1. Lineation Orientations (BDM) cont.

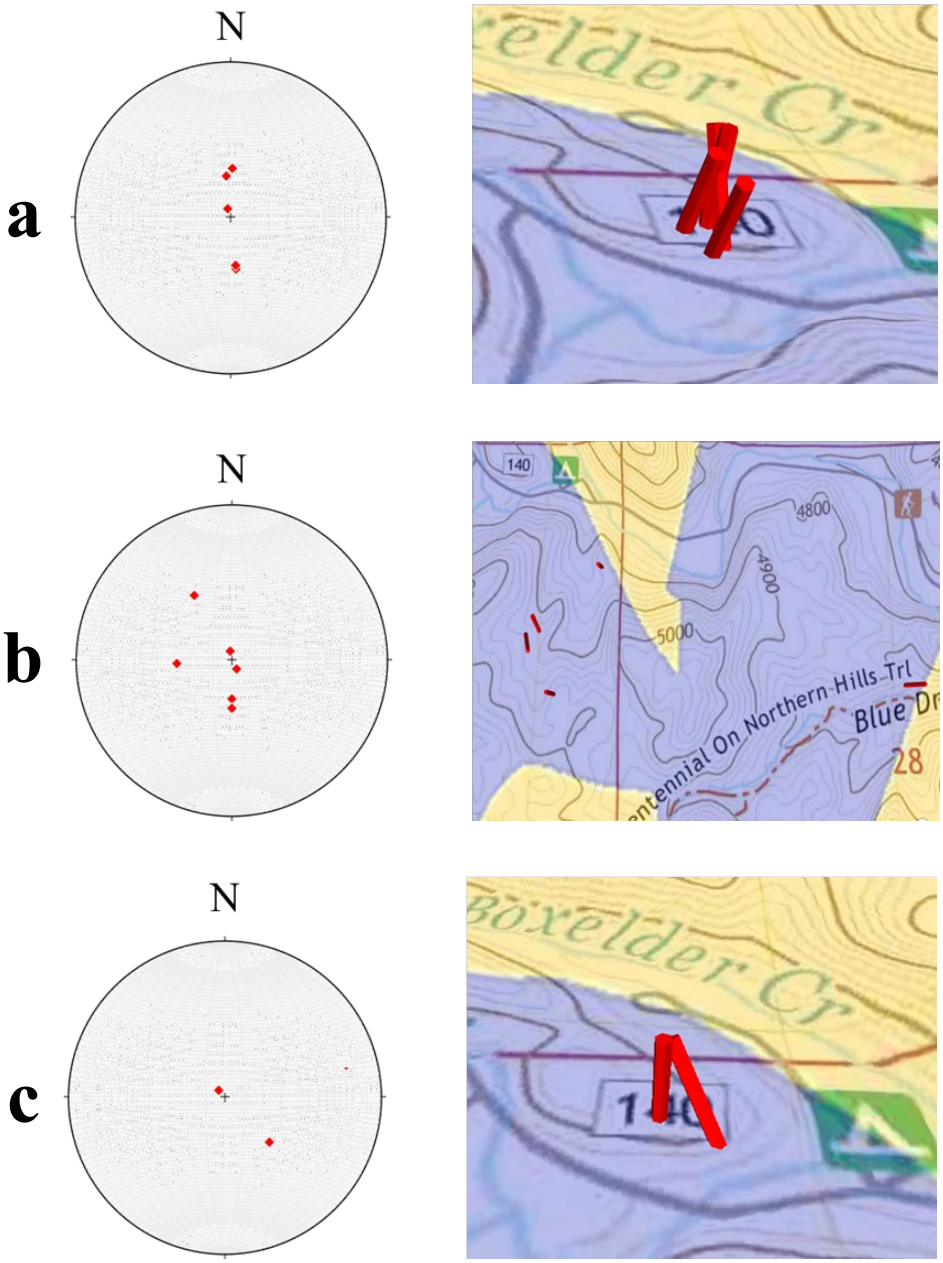

Figure 4-20: BDM sites with lineation measurements, plotted on stereonets and Google Earth (red arrows show down-plunge orientations in the column to the right; Blenkinsop, 2012; Allmendinger et al., 2013; Cardozo & Allmendinger, 2013). a: Sites NG2101 - NG2105; b: Sites NG2124, NG2140, NG2145a, NG2146, & NG21R07; c: NG2147 & NG2151

4.2.2. Lineation (BCQ)

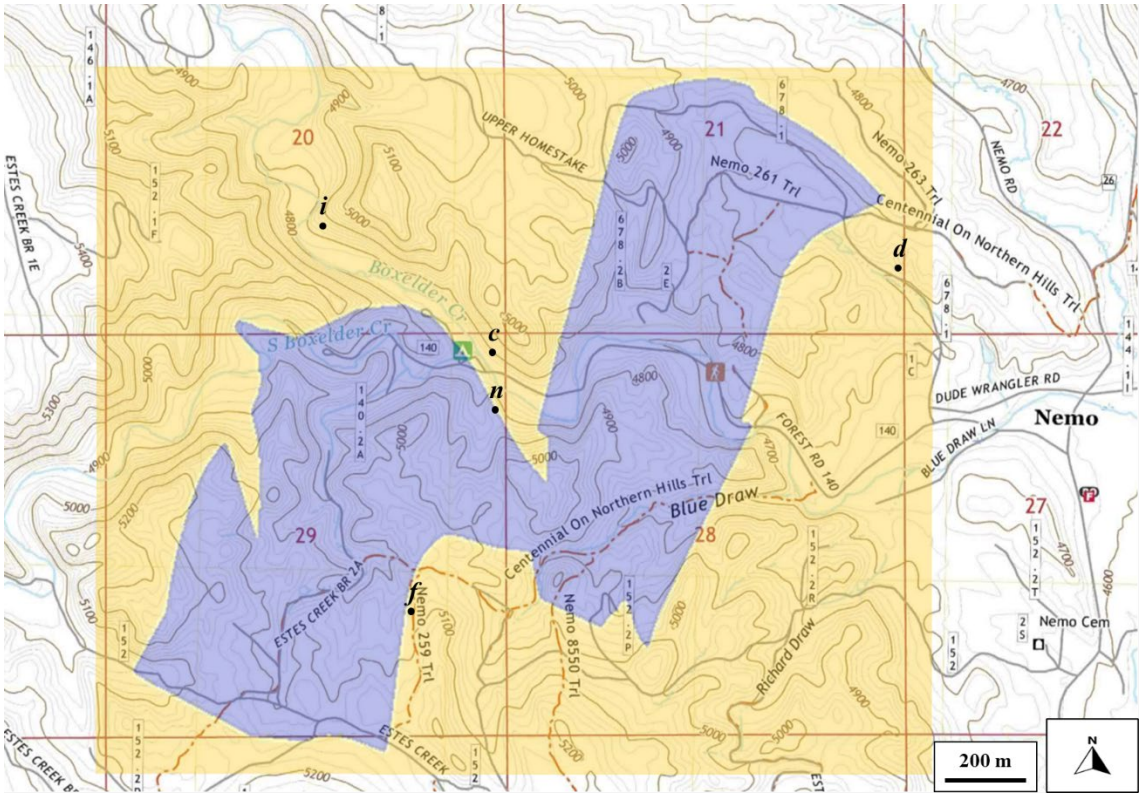

Map Letter	Site number	Latitude (deg.)	Longitude (deg.)	Lithology	Lineation Plunge (deg.)	Lineation Trend (azimuth deg.)
c	NG2113	44.19725	-103.53377	BCQ	30	356
c	NG2114	44.19758	-103.53393	BCQ	45	345
d	NG21R03	44.19989	-103.51201	BCQ	55	268
d	NG2116	44.19964	-103.51182	BCQ	55	350
d	NG2117	44.19987	-103.51201	BCQ	60	320
d	NG2117	44.19987	-103.51201	BCQ	60	320
f	NG2123	44.18917	-103.53809	BCQ	85	340
i	NG2129	44.20257	-103.54258	BCQ	68	345
i	NG2131	44.203	-103.54167	BCQ	65	330
n	NG2145b	44.19548	-103.53383	BCQ	65	354

Figure 4-21: Sites where BCQ lineation data was measured and plotted on both stereonets and with 3D orientations in Google Earth.

4.2.2. Lineation (BCQ) cont.

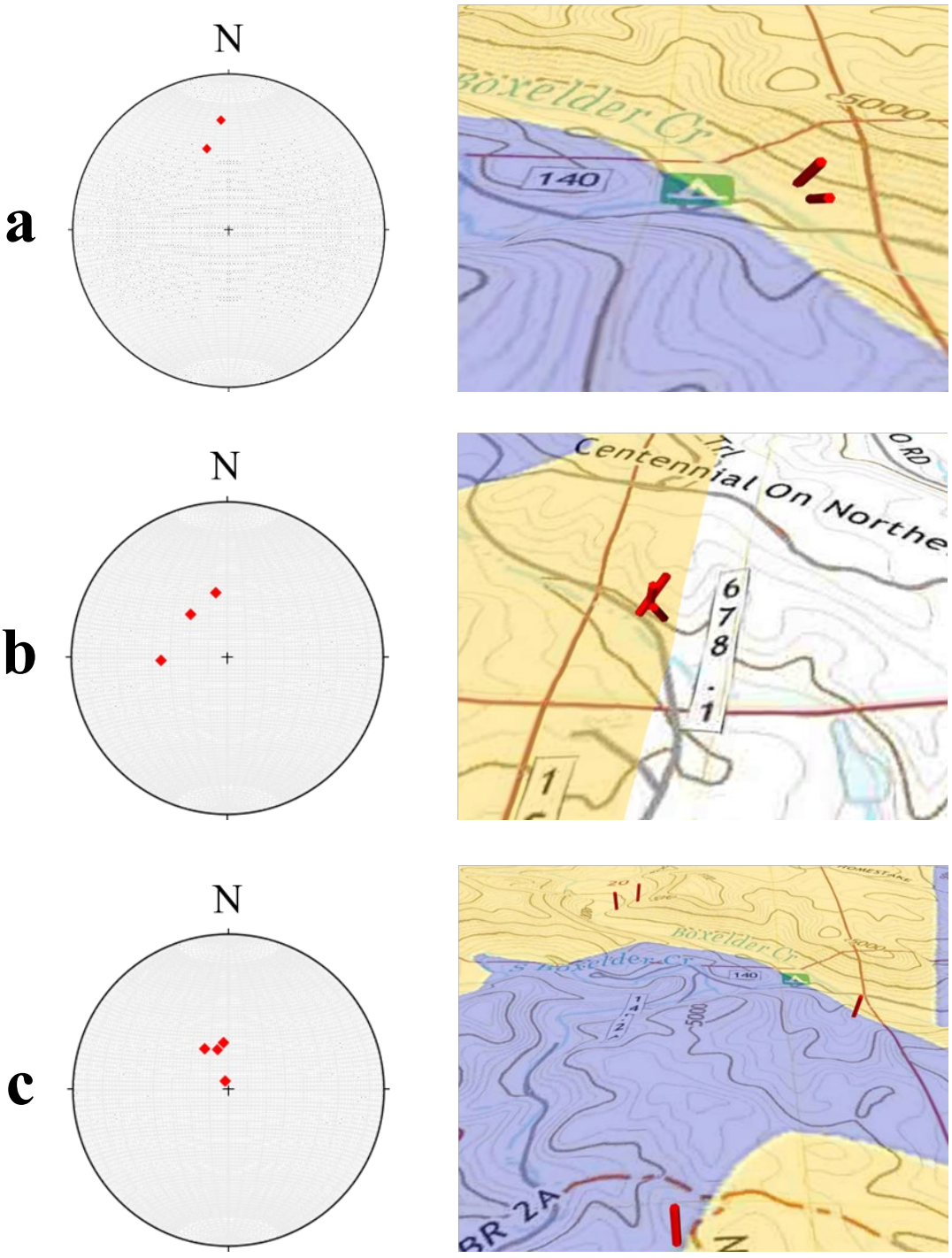

Figure 4-22: BCQ sites with lineation measurements, plotted on stereonets and Google Earth (red cylinders show down-plunge orientations in the column to the right; Blenkinsop, 2012; Allmendinger et al., 2013; Cardozo & Allmendinger, 2013). a: Sites NG2113 - NG2114; b: Sites NG21R03, NG2116, & NG2117; c: NG2123, NG2129, NG2131, & NG2145b.

4.2.3. Lineation Orientations Composite Map

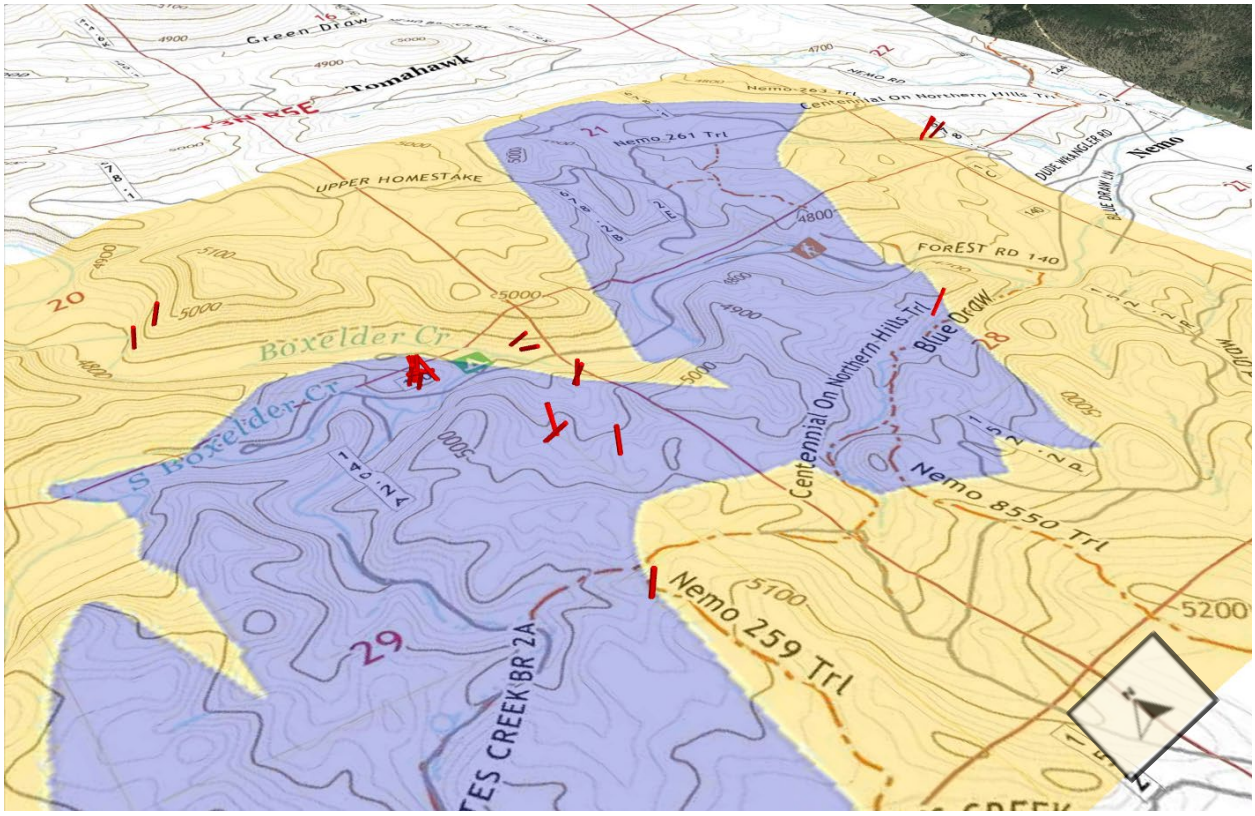

Figure 4-23: Composite map of all sites where lineation data was plotted on stereonets and transferred to Google Earth (red cylinders represent down-plunge orientations; Blenkinsop, 2012; Allmendinger et al., 2013; Cardozo & Allmendinger, 2013).

4.3 Kinematic indicators

Macroscopic kinematic indicators are only found in select locations and take the form of shear bands with refracted cleavage or asymmetric lozenge shapes in both lithologies and rare S-C fabric within the BCQ. Within both the BDM and BCQ, both sinistral and east-side up kinematic indicators can be found, sometimes within the same outcrop. However, the different types of shear sense indicators do not all show both orientations of shear. The refracted cleavage and asymmetric lozenge shapes indicate both sinistral and east side up sense of shear, but the S-

C fabric in the BCQ only displayed sinistral shear sense. For example, sites NG2107 (BDM; **Fig. 4-28**) and NG2117 (BCQ; **Fig. 4-32**) host shear sense markers that indicate sinistral shear and east-end up kinematics. Site NG2107 possesses asymmetric deflections in both the XZ and YZ planes consistent with left-lateral and east-end up shear sense. Site NG2117 possesses S-C fabrics in the YZ-plane that also indicate sinistral shear, accompanied by quartz rods plunging towards the NW at 320° azimuth.

4.4. Lozenge Geometries & Orientations

The presence of structures that form rhomboidal to lensoidal lozenge geometries were found at nearly all of the sites within the study area (save for NG2121 & NG2157, both located on the outer limbs of the BDM, possessing no discernible fabrics). The lozenges were bounded by anastomosing shear bands in the BDM and fractures in both the BDM and BCQ. These fractures generally follow the average strike of 340° and are steeply dipping. The observation planes that host the more discernable lozenge geometries are the XZ and YZ planes, which show a wide range of lozenge aspect raiots. The foliation planes which make up the sides of the lozenge octahedrons (XY plane) are harder to locate. While the lozenges were ubiquitous in both lithologies where deformation was observed, their aspect ratios (calculated by dividing the 2D long-axis by the short-axis in the XZ, YZ, and XY planes) varied throughout the study area. Similarly, the lozenges' long-axes trend and plunge varied in orientation throughout the study area. Where lineations were present, the lozenge long axes appeared subparallel. The long-axis orientations in the BDM, grouped by observation plane, can be found in **Appendix table A10**.

The groupings of these variances in lozenge geometry and orientation were noted in the field and guided the selection of sampling sites. The aspect ratio variance from low to high in the BDM metagabbro, grouped by the XZ, YZ, & XY planes, can be found in **Appendix table A8**. Generally, for the BDM metagabbros, areas of topographic highs (less eroded outcrops on hills and ridges) had lozenges with lower aspect ratios (1:1 – 4:1, for example), while areas in topographic lows (valleys) tended to have lozenges with intermediate (> 4:1 – 7:1) and high aspect ratios (> 7:1 – 20:1). In some cases (for example the area of Knob Hill; sites NG2101 – NG2104 & NG2147 – NG2155), lozenge geometries and orientations ranged across these demarcations (~3:1 – 14:1) as the outcrop was traversed from east to west.

In the BCQ quartzites, the variance in lozenge aspect ratios ranged from low (~1:1) to intermediate (6:1; **Appendix table A9**). The long-axis orientations in the BCQ, also grouped by observation plane, can be found in **Appendix table A11**. The bounding features around the BCQ are fractures, with minor tightly spaced shear banding closer to the BDM/BCQ contact. The relationship between the amount of deformation and topography (for example, the amount of erosion that exploited areas of higher shear) was not as apparent as the relationship observed in the BDM. Similar to features observed in the BDM, the lozenge geometries were more apparent in the XZ and YZ planes, with foliation strikes of 340° and steeply dipping, with some shallower dips (40°-50°) further away from the shear zone boundary.

4.5. Mesoscale Features

Several sites have been chosen to represent the features observed more generally across the study area. Lozenge aspect ratios, as denoted in the tables above, range from ~1.0 (with near orthogonal bounding shear bands) to ~10.0 and up (with nearly subparallel bounding shear bands). Foliation planes generally strike NW, though in certain areas in the middle of the study area foliations strike almost due north. The same directionality applies to the trend of lozenge long-axes when observed in map view. Largely the rocks in both the BDM and BCQ are fine grained, even in undeformed samples, though some rocks contain large enough grains to form measurable lineation. In both lithologies, lineations generally plunge greater than 45° from vertical in both the north and south directions. I also documented S-C fabrics and deflection in both the metagabbro and the quartzite. Selected sites are described below, with annotated photos of representative shear features common to the study area. The observation planes reported in the figure captions are the position of the photograph. For example, a reported observation plane of 250° would be the

left/right orientation of the photograph, looking into the page perpendicular to that plane at 340°, and a plane of 076° would look into the page to the south at 166°.

4.5.1. Sites NG2103 - NG2105 (Blue Draw Metagabbro)

Foliation and lineation present on a highly altered, "punky-green" metagabbro, making up the western face of Knob Hill and the eastern side of the minor erosional valley. Shear bands are tightly spaced and show a general trend to the N-NW. Looking in the XZ-plane (NG2103, **Fig. 4-25**), one can see that the lozenges curve to the west at high aspect ratios. In the YZ-plane (NG2104, **Fig. 4-26**) the metagabbro remains highly altered and foliated, with lineations changing from near vertical to south plunging. Directly to the west on the eastern facing side of the erosional valley, site NG2105 shows similar shear bands bounding more competent erosion-exposed lozenges (**Fig. 4-27**).

4.5.2 Sites NG2107 (Blue Draw Metagabbro)

This site has small shear bands (~7 cm wide) present in both the XY and XZ-planes with sinistral deflections (s-shaped). **Fig. 4-28** shows mylonitic banding in the XZ-plane, trending 343°.

4.5.3. Sites NG2109 & NG2115 (Blue Draw Metagabbro & Boxelder Creek Quartzite)

In both the BDM (NG2109; no picture available) & the BCQ (NG2115; **Fig. 4-29**), presumably sheared fold hinges (synformal) are present, and within these structures, lozenges with XY long-axes trending ~340° can be seen.

4.5.4. Sites NG2116 & NG2117 (Boxelder Creek Quartzite)

Site NG2116 contains quartzite with phyllite zones, grading to cleaner quartzite to the east. Lozenges were observed in both YZ and XY-planes (**Fig. 4-30**). The general trend and plunge of the lozenge long-axis (in this case in the Y-direction) within XY-plane is ~15° → 166° (**Fig. 4-31**). Site NG2117, approximately 2 meters to the west of NG2116 along the road cut, contains prevalent S-C fabrics in the YZ-plane and lineated rods in the XY-plane (**Fig. 4-32**). C-fabrics and porphyroclasts in the YZ-plane strike ~320°, with two measured S foliations measured at 331°/85° W & 340°/84° W. The general angle between S-C is approximately 15° - 20°. Lineated rods (**Fig. 4-33**) in the XY-plane have a trend and plunge of 60° → 325°.

4.5.5. Site NG2123 (Boxelder Creek Quartzite)

Lensoidal lozenge (**Fig. 4-34**) in the BCQ (non-planar sides, with rounded angles where foliation planes meet; see Ponce et al., 2013, Fig. 1a) with the long axis in the YZ-plane trending north/south (~358°/178°).

4.5.6. Site NG2124 (Blue Draw Metagabbro)

Foliated metagabbro exposure on the eastern slope of a north trending valley. Contains lozenges (**Fig. 4-35**) eroded out to expose 3-D geometries and aspect ratios in the XY-plane of ~6.0. Internal angle of the long-axis (acute angle) in the horizontal plane is approximately 30°.

4.5.7. Sites NG2127 & NG2128 (Blue Draw Metagabbro)

Low aspect ratio/near-orthogonal lozenges (internal angle of the acute axis is ~80°) exposed on a topographical high near the BDM/BCQ contact (not exposed) on the western edge of the BDM eastern limb. NG2127 (**Fig. 4-36**) shows an exposure in the YZ-plane with a characteristic fractal pattern, meaning the geometries and orientations of smaller lozenges make up a similar shape when grouped together. The long-axes of the lozenges generally trend ~330°. Site NG2128 (**Fig. 4-37**) shows similar lozenges with ~85° acute angles in the XZ-plane, trending 315° - 320°.

4.5.8. Sites NG2131 & NG2132 (Boxelder Creek Quartzite and phyllite)

Site NG2131 contains lozenges with long-axes in the XY-plane containing internal angles measuring approximately 40° (**Fig. 4-38**) and aspect ratios at ~3.5 to 6.0. An interbedded phyllite layer (**Fig. 4-39**), located approximately 2 meters uphill to the north, contains a few minor lozenge geometries but is primarily composed of schistose material with closely spaced shear bands with sub-parallel foliations striking ~325°.

4.5.9. Sites NG2137 (Blue Draw Metagabbro)

Low aspect ratio/near-orthogonal lozenges in the XY-plane (**Fig. 4-40**), corresponding to an XZ-plane trending ~340°, with the trend of the lozenge YZ short axis at ~070°. This outcrop is located in a topographical high (hill across from Boxelder Creek to the north). Typical to most lozenges in the XY-plane, aspect ratios measured here fall between ~1.0 – 2.0.

4.5.10. Site NG2143 (Blue Draw Metagabbro)

Metagabbro (**Fig. 4-41**) containing tightly-spaced foliations (~1.0 - 2.0 mm spacing) in a topographic low (valley) located between two bluffs (NG2141 to the west and NG2145 to the east). The average strike of these bands is ~015° - 020° and bounds sporadic lozenges located a half a meter to the east (not pictured).

4.5.11. Sites NG2148, NG2154, & NG2156 (Blue Draw Metagabbro)

Site NG2148, located on the north side of Knob Hill at the base of the exposure, contains lozenges with aspect ratios ranging from approximately ~7.0 to 14.0 (**Fig. 4-42**), with the increase occurring as one traverses east along the north face. At the peak of Knob Hill, site NG2156 contains lozenges with lower aspect ratios of approximately ~3.0 and is coarser grained (**Fig. 4-43**). Both sites are 2 – 3 meters to the east of the highly-sheared schistose material observed at NG2103 & NG2104, with the lower aspect ratios observed at the peak (presumably the center of Knob Hill). **Fig. 4-44** shows shear bands encircling Knob Hill, with a particularly well-exposed contact (NG2154) between the schistose material and the more competent lozenges beneath, on the east side of Knob Hill.

Figure 4-24: Site NG2103, BDM. Lozenges (outlined in red dashes) here are in the XZ observation plane of 250°/subvertical dip, with the trend of the lozenge Y-axis (looking into the page) at ~340°. Lozenge long axis plunges steeply to the east.

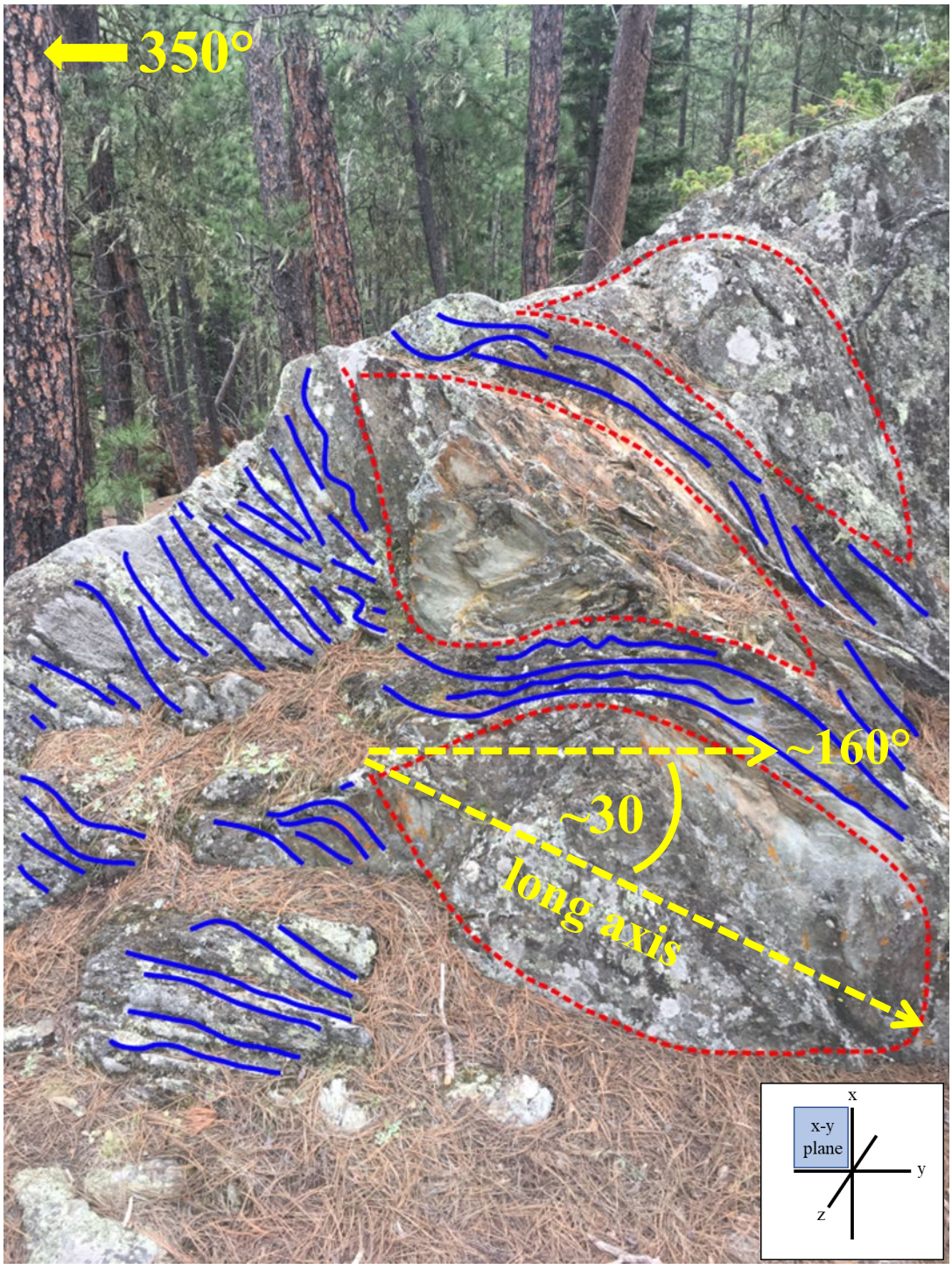

Figure 4-25: Site NG2104, BDM. Lozenges (outlined in red dashes) are in the XY observation plane striking 350°/subvertical dip, with the lozenge long axis trending ~160° and plunging ~30° to the south (shown in yellow). Anastomosing shear bands (blue lines) are bounding the lozenges, which are themselves highly altered (hydrothermally?). Some places on this outcrop contain highly-altered schistose chlorite with no visible fabrics.

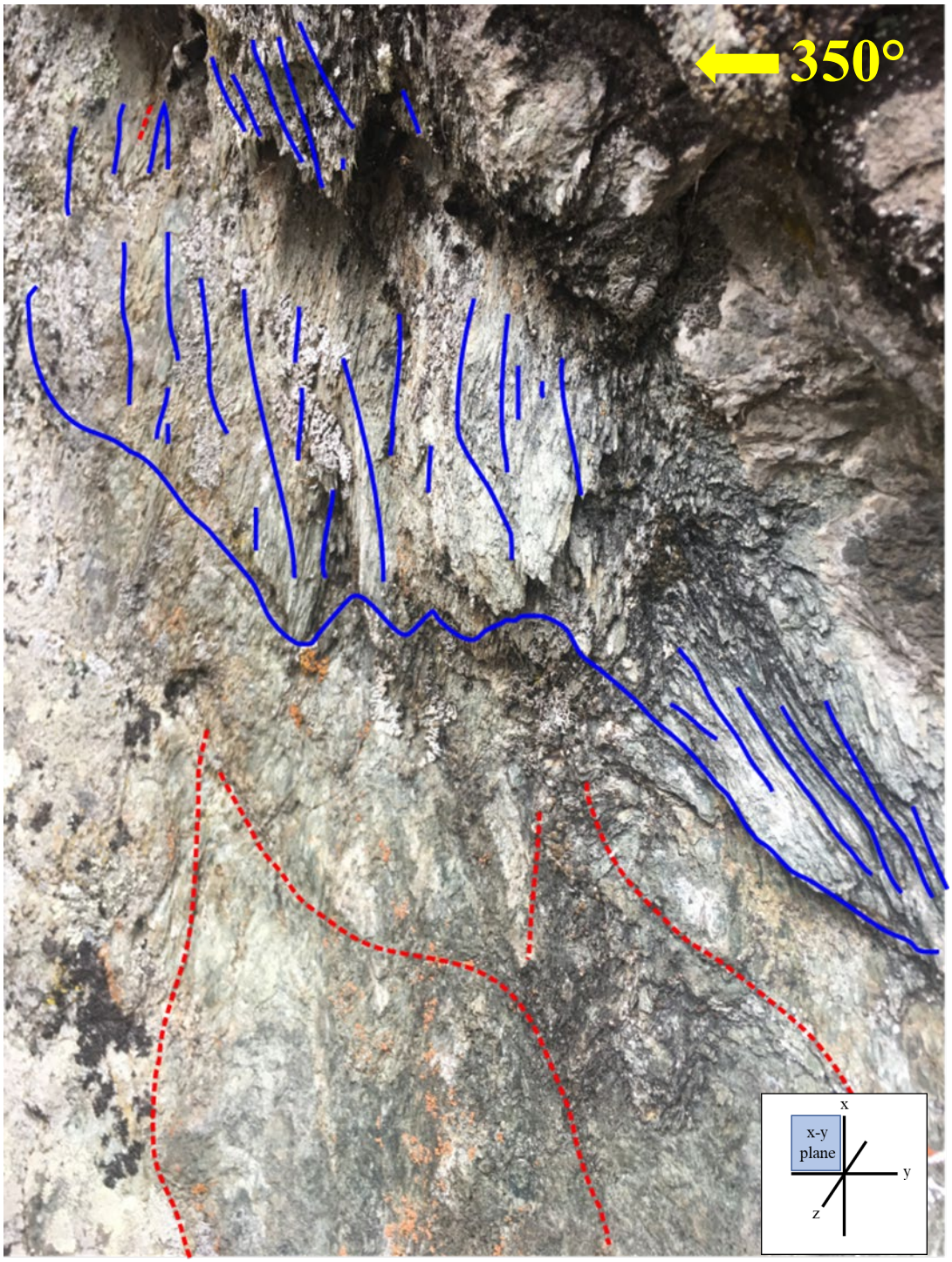

Figure 4-26: Site NG2105, BDM. Lozenges (outlined in red dashes) are in the XY observation plane of 350°/subvertical, with foliation plane 174°/75 W. The trend of the lozenge long axis plunging steeply to the south trending in the foliation plane ~174°. Blue lines are anastomosing shear bands bounding the lozenges.

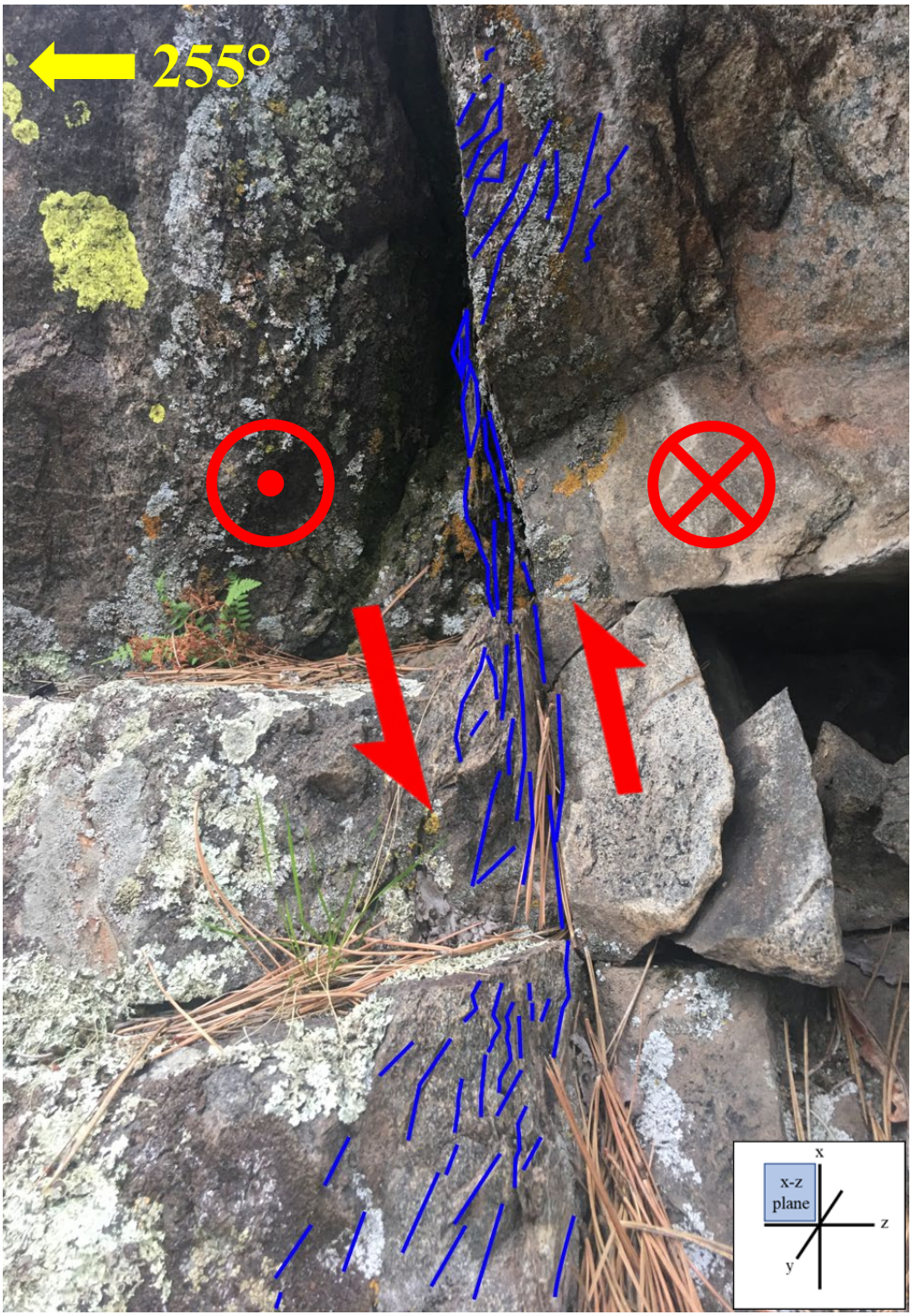

Figure 4-27: Site NG2107, BDM. Deflections (outlined by blue lines) in the XZ observation plane of 255°/subvertical, with the trend of the shear band in the Y-axis (into the page) at ~343°. The red arrows illustrate east-side-up vertical shear. This same deflection exists in the horizontal YZ-plane (not pictured) indicating left-lateral shear with a 340° strike and subvertical dip. This sinistral movement is indicated by the red crossed circle to the right (imagine the tail of a missile flying into the page) and the dotted circle to the left (imagine the tip of a missile moving out of the page) At the center, where the mylonite is the tightest, is ~7 cm wide.

Figure 4-28: Site NG2115, BCQ. Lozenges (outlined in red dashes) within a fold hinge (in green; dashed green lines are approximations) in the XZ observation plane of 250°/subvertical, with a trend and plunge of the hinge axis in the Y-axis (looking into the page) at 20° → 342°. Lozenge long axes are steeply plunging to the east and west.

Figure 4-29: Site NG2116, BCQ. Lozenges (outlined in red dashes) here are in the YZ observation plane of 250°/25°S, with the trend of the horizontal long-axis lozenge at ~345°. XY long-axes generally have a shallow plunge to the SE (see Figure 4-31).

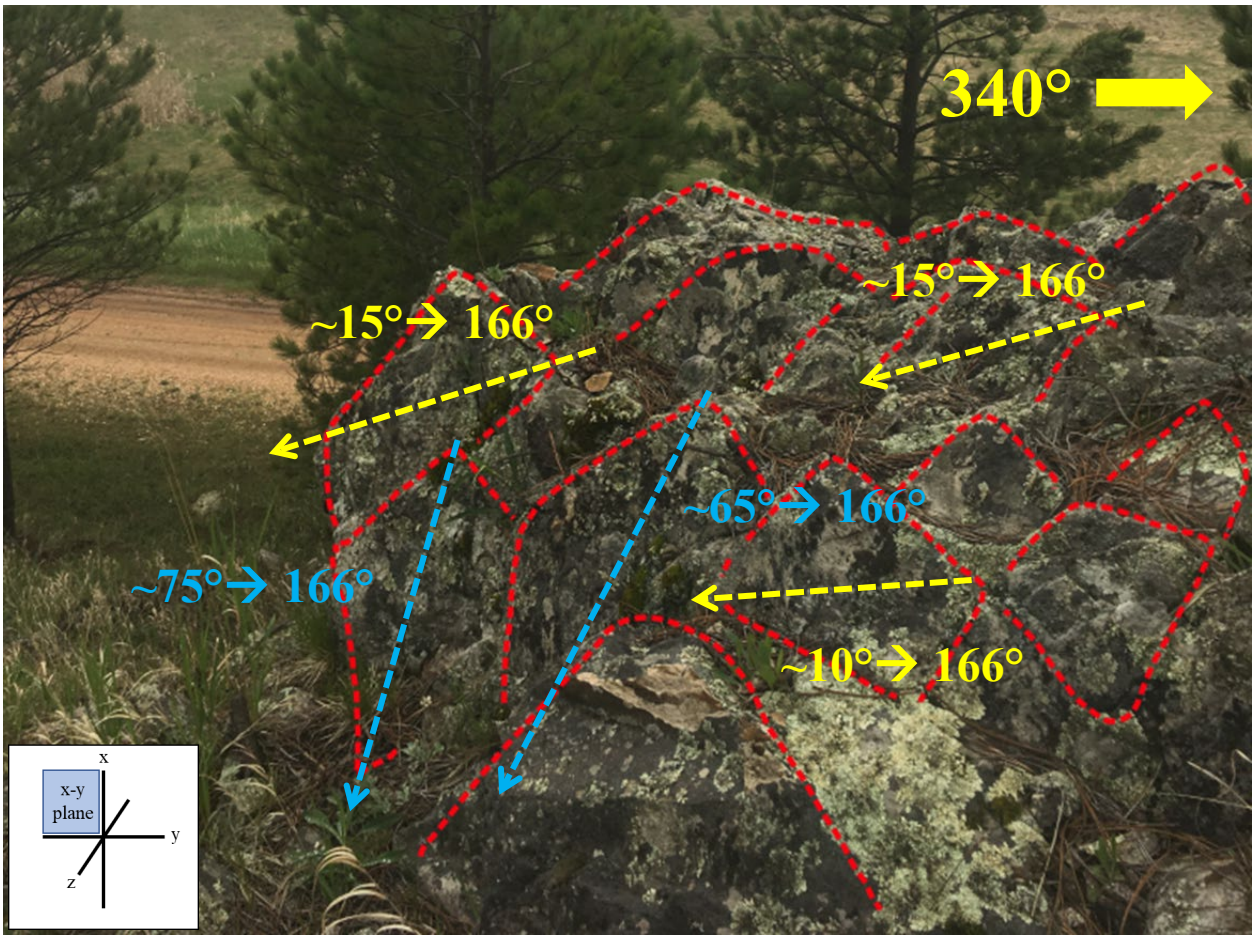

Figure 4-30: Site NG2116, BCQ. 2D lozenges (outlined in red dashes) shown here are in the XY observation plane of 340°/subvertical, with SE trend and plunge of the short axis to the SE (~10°-15° → 166°), shown by yellow dashed arrows. The lozenges' long axis plunges steeply to the SE (blue arrows). Not pictured: In the XZ-plane, the lozenge long axis plunges steeply to the NE.

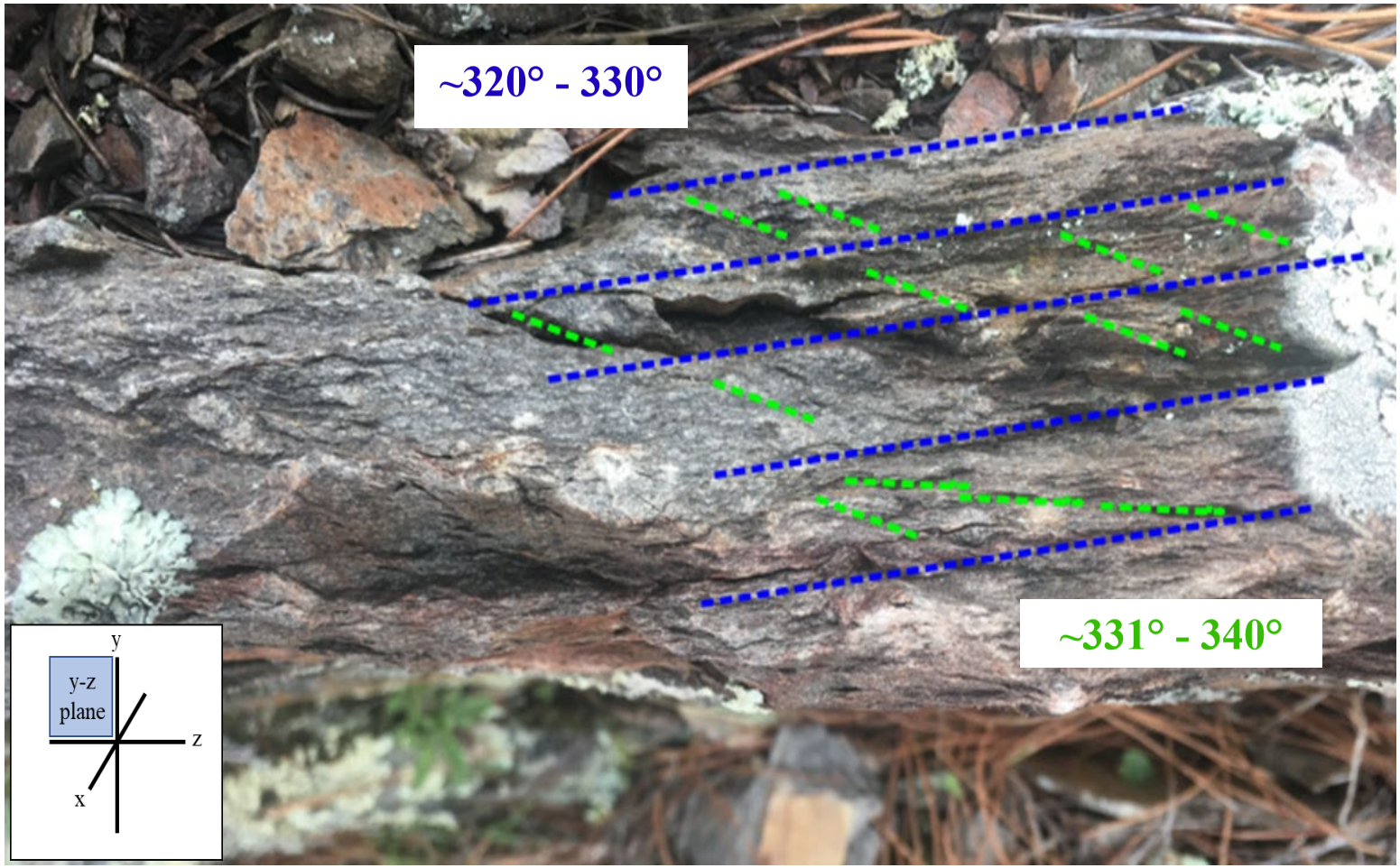

Figure 4-31: Site NG2117, BCQ. S-C fabrics and porphyroclasts at an outcrop striking ~331°. S-fabrics (outlined in green dashes) and C-fabrics (blue dashes) are shown here in the YZ observation plane of 250°. General angle between S-C = 15° - 20°.

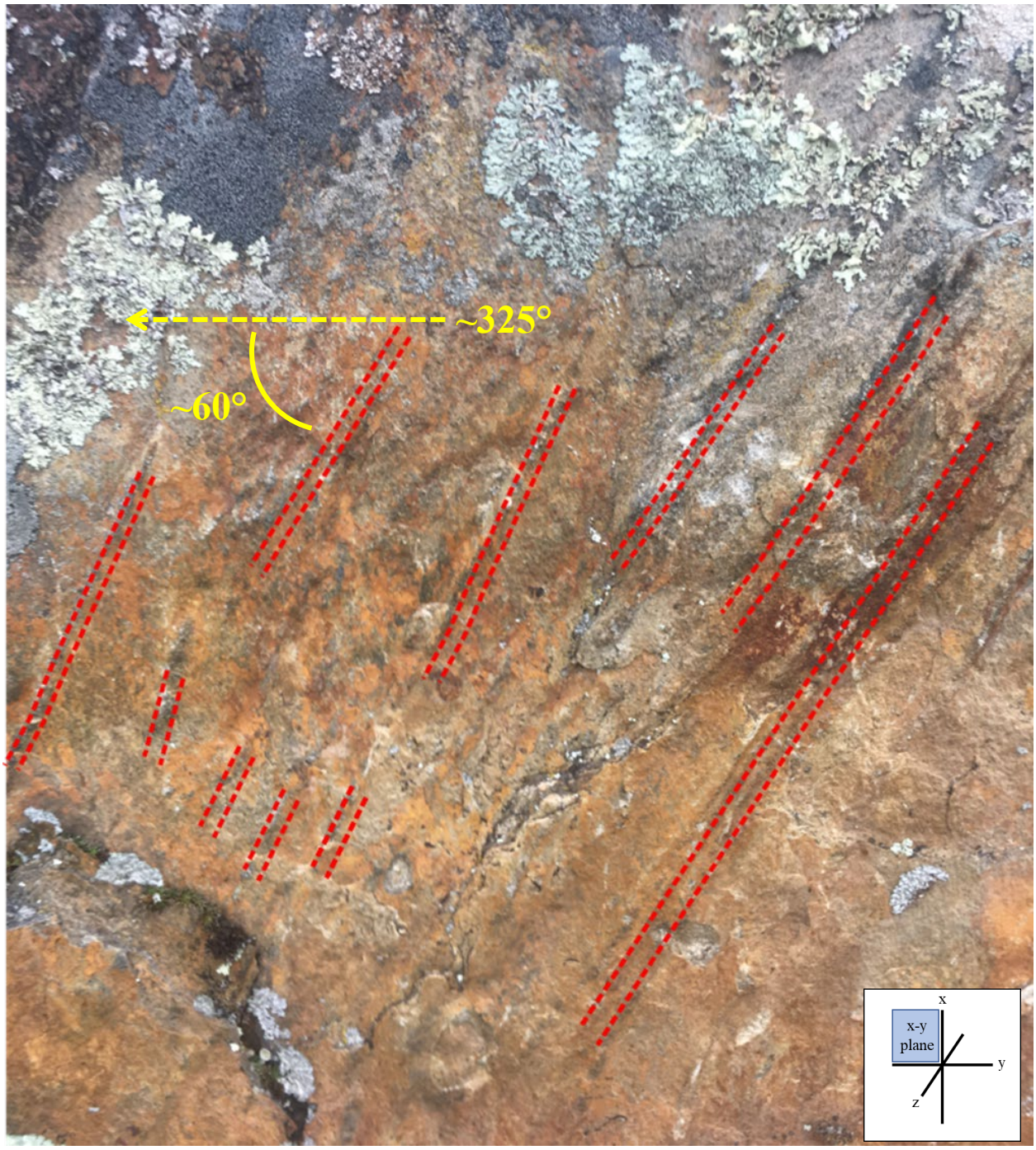

Figure 4-32: Site NG2117, BCQ. Lineated quartz rods (outlined in red dashes) in the XY observation plane of 335°, with the trend and plunge 60° → 325° shown in yellow.

Figure 4-33: Site NG2123, BCQ. Pristine example of a lensoidal (non-planar sided) lower end-member lozenge (outlined in red dashes) as discussed in Ponce et al., 2013, Fig. 1a. Lozenge is shown in the YZ observation plane of 245°/subhorizontal, with the lozenge's horizontal long-axis trending approximately due-north (~358°).

Figure 4-34: Site NG2124, BDM. Lozenges (outlined in red dashes) are in the observation plane of 275°/35°S, with the trend of the lozenges' horizontal long axis (pointing to the top the page) at ~340°.

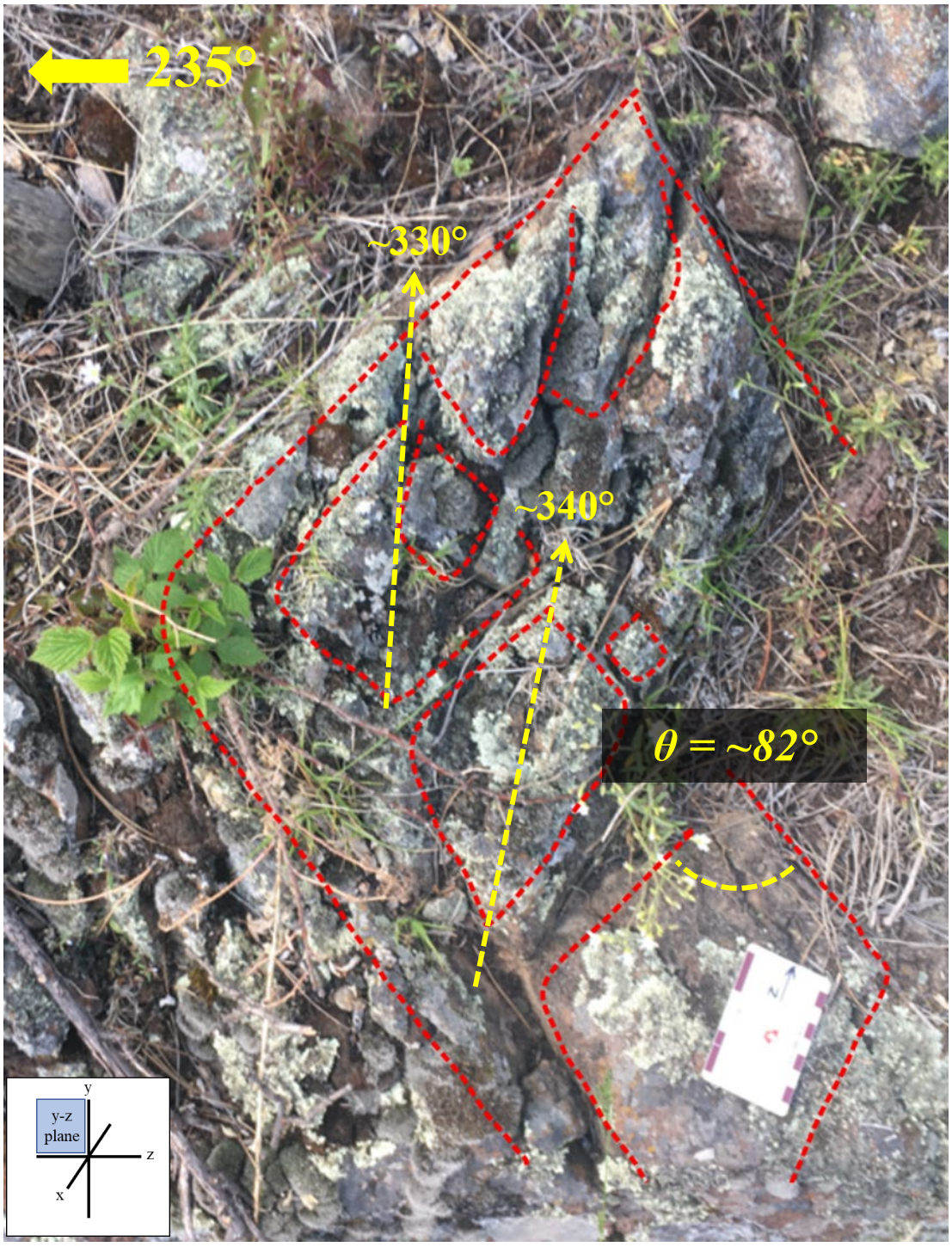

Figure 4-35: Site NG2127, BDM. Low aspect ratio/near-orthogonal lozenges (outlined in red dashes) here are in the YZ observation plane of 235°/subhorizontal, with the trend of the lozenge YZ axis (towards the top of the page) at ~330° - 345°, shown in yellow. Internal angle of the long axis is ~80°, shown in black.

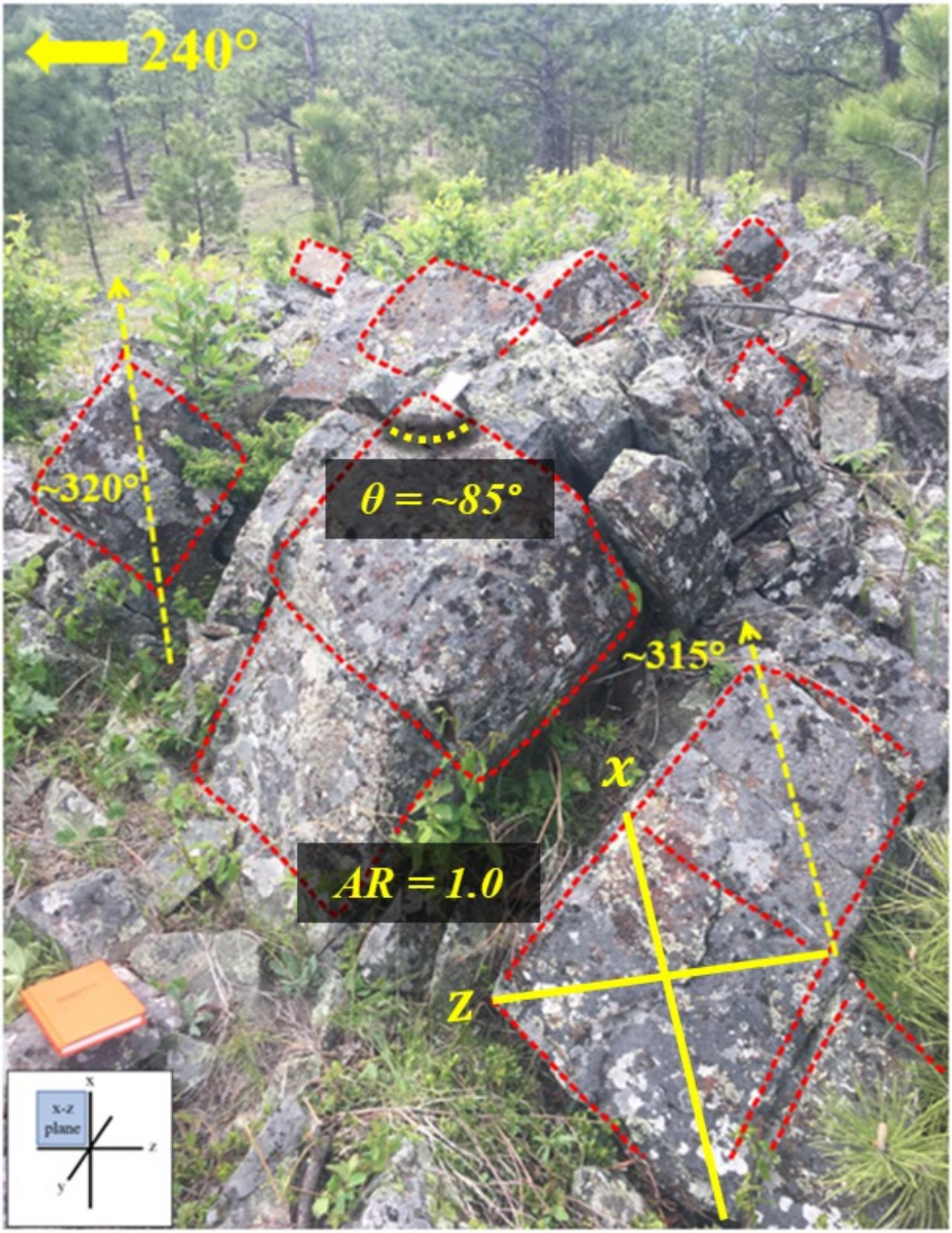

Figure 4-36: Site NG2128, BDM. Low aspect ratio/near-orthogonal lozenges (outlined in red dashes) here are in the XZ observation plane of 240°/35°S, with the trend of the lozenge YZ-axis (into the page) at ~315° - 320°.

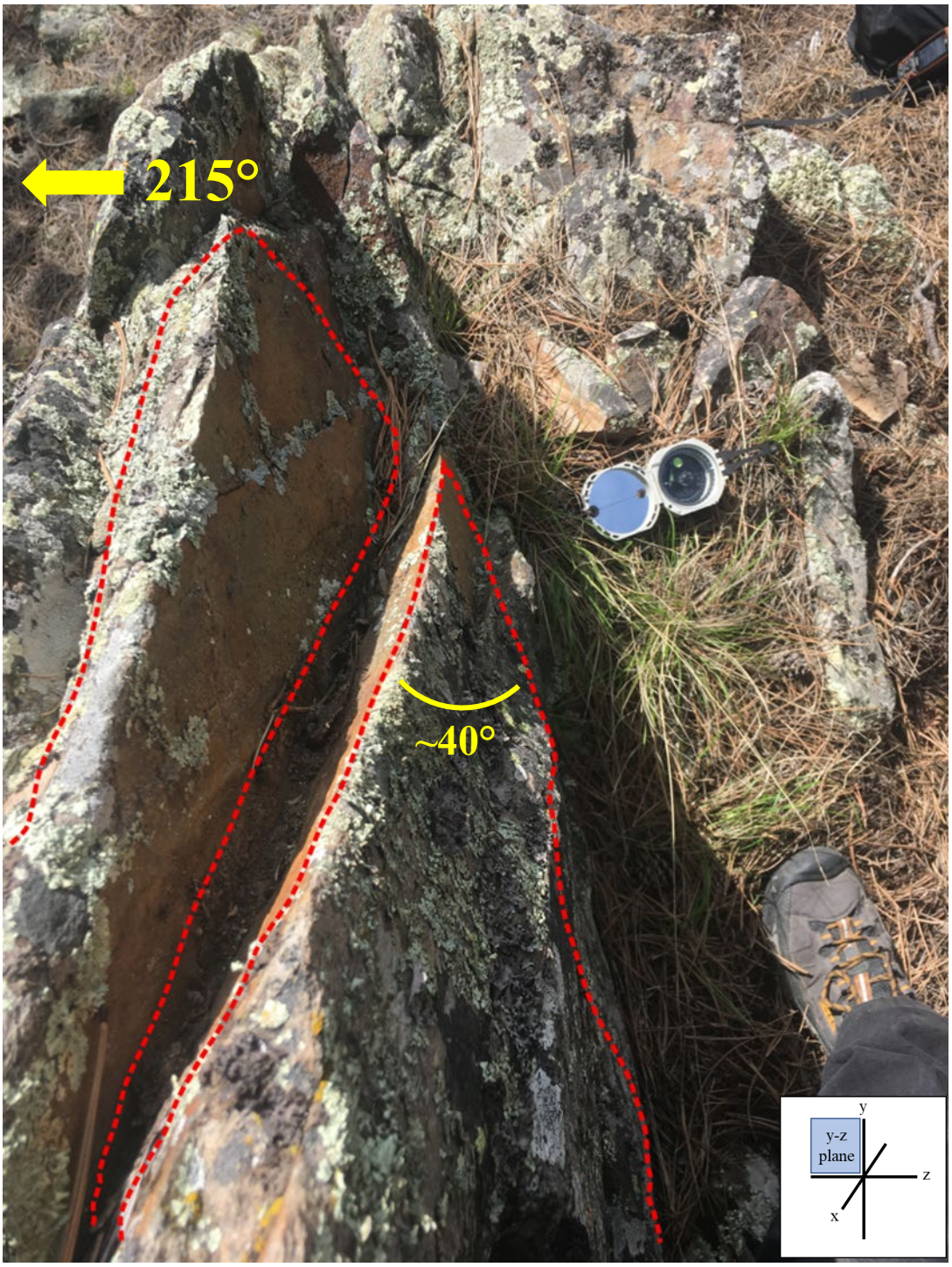

Figure 4-37: Site NG2131, BCQ. Lozenges (outlined in red dashes) in the YZ observation plane of 215°/subhorizontal, with the horizontal trend of the lozenge long-axis (toward the top of the page) at ~310° - 315°. Acute angle of the long-axis is ~40°, shown in yellow

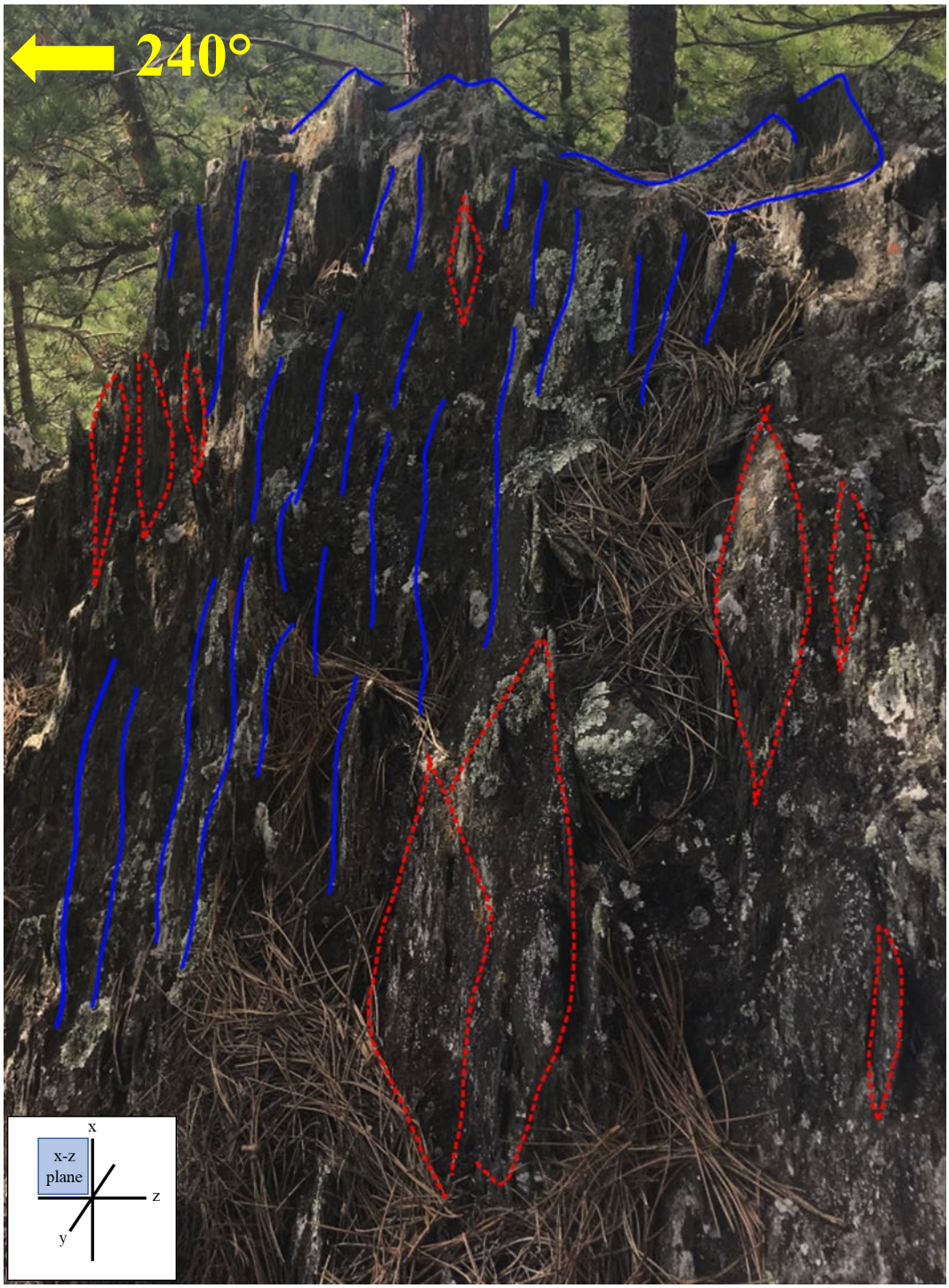

Figure 4-38: Site NG2132, phyllite within the BCQ. High aspect ratio lozenges (outlined in red dashes) are in the XZ observation plane of 240°/subvertical, with the lozenge long axis plunging steeply to the west. Blue lines mark shear banding/schistose material bounding the lozenges, striking 325° with a dip of ~85°W. This material has no observable secondary/oblique foliation and is sub-parallel.

Figure 4-39: Site NG2137, BDM. Low aspect ratio/near-orthogonal 2D lozenges (outlined in red dashes) are in the XY observation plane of 340°/subvertical, with the lozenge long axis plunging steeply to the north.

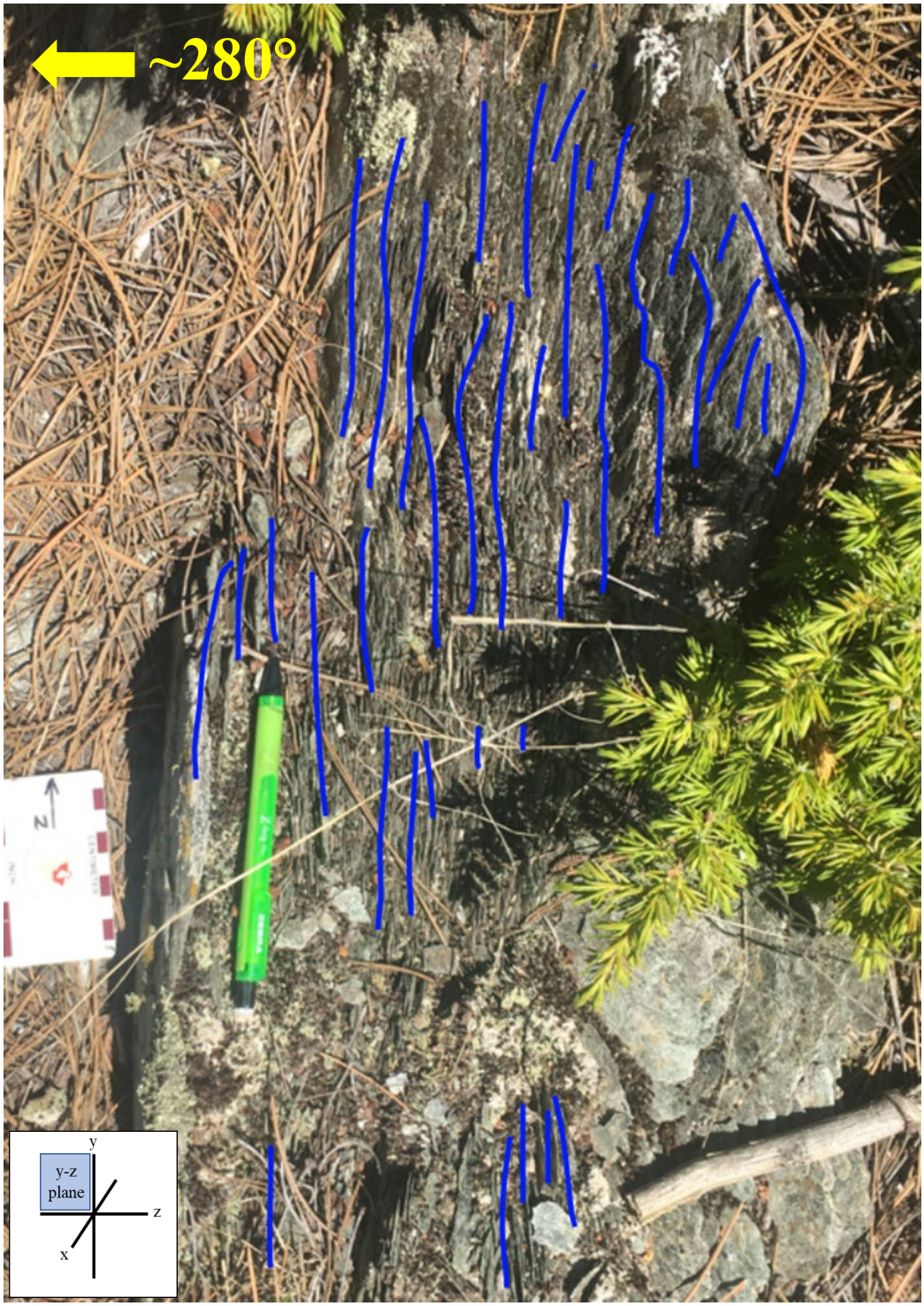

Figure 4-40: Site NG2143, BDM. Tightly spaced foliations at ~1-2 mm width (traced in blue) in the YZ observation plane of 280°/subhorizontal, striking (toward the top of the page) at ~015° - 020°. Observed in a topographic low (valley) between two higher-relief bluffs with lower aspect ratios/lower strained lozenges (NG2142 to the west & NG2145 to the east).

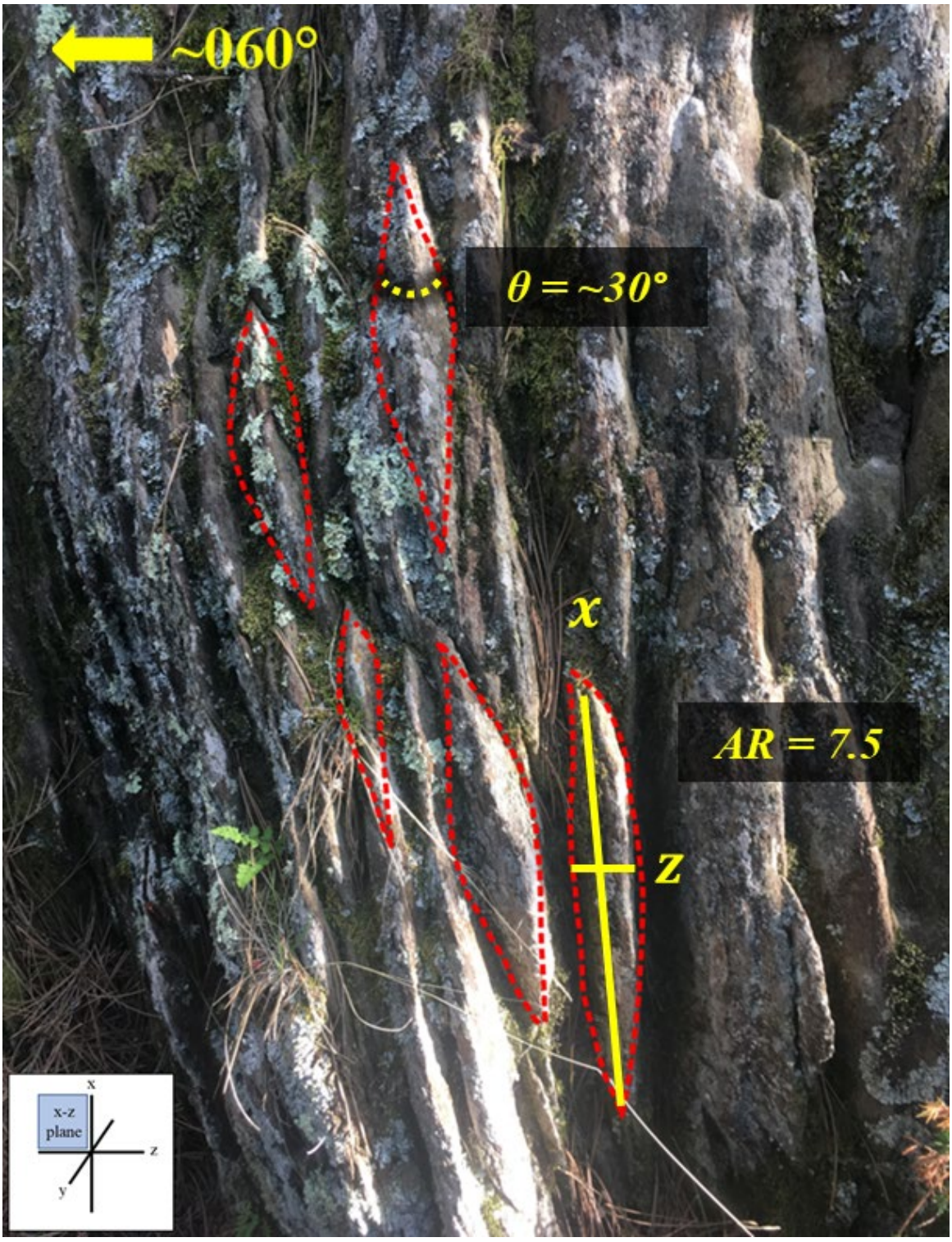

Figure 4-41: Site NG2148, BDM. High aspect ratio lozenges (outlined in red dashes) in the XZ observation plane of 060°/subvertical, with the lozenge long axis plunging ~80° to the west but is often near-vertical. Located on a north-facing outcrop on Knob Hill, 3 meters east of NG2104 (Fig. 4-26; shear-banded, with high aspect ratios for 2D lozenges in the XZ- and YZ-planes, and in some places highly-altered schistose chlorite with no visible fabrics).

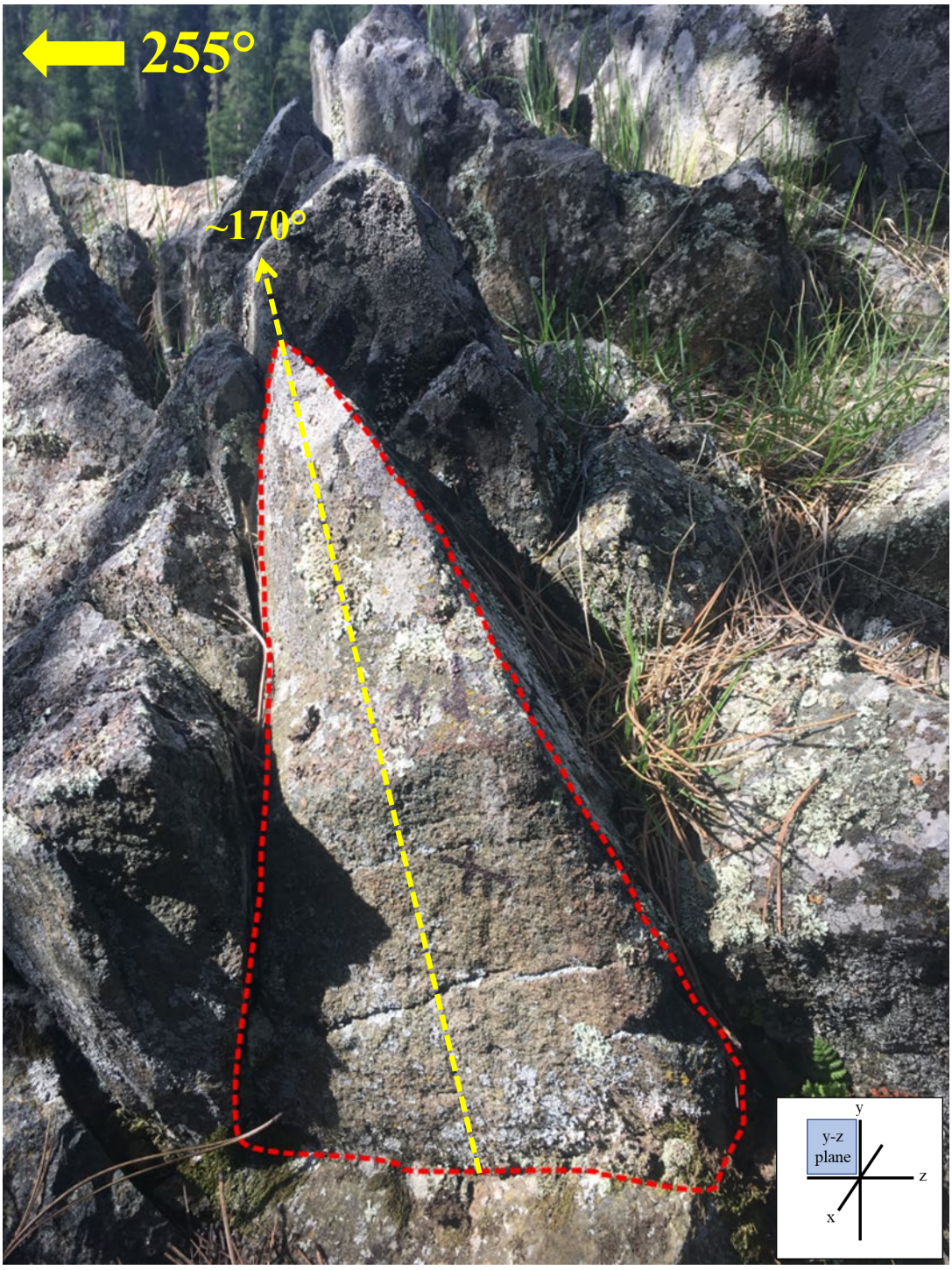

Figure 4-42: Site NG2156, BDM. Lozenges (outlined in red dashes) in the YZ observation plane of 090°/35°N, with the lozenge long axis trending to the south at 170° and plunging steeply to the west. Located at the peak of Knob Hill, 4 meters east of highly sheared erosional valley (NG2103, NG2104 & NG2105).

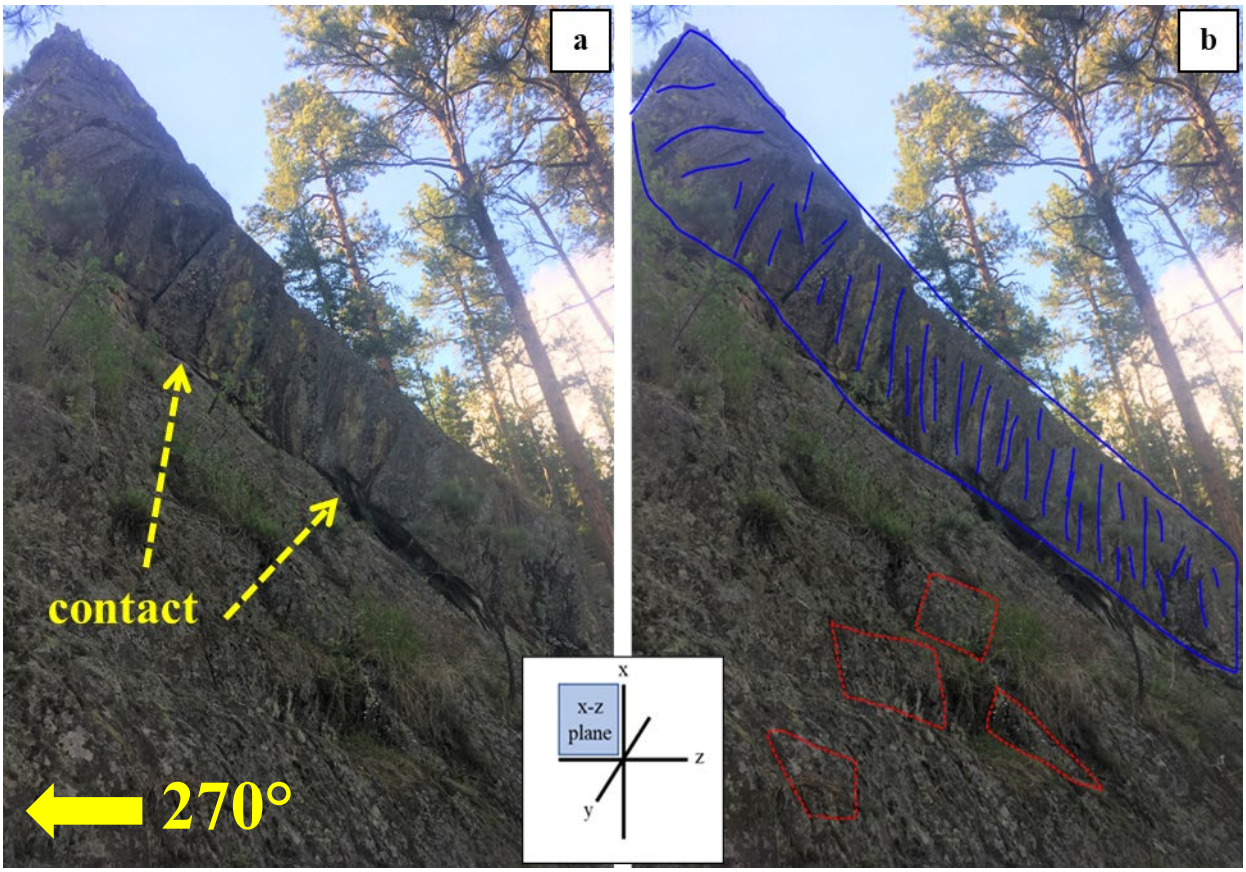

Figure 4-43: Site NG2154, BDM. a: Contact between low aspect ratio/more competent metagabbro layer and upper highly foliated layer (shown in yellow). b: Low aspect ratio/near-orthogonal lozenges (outlined in red dashes) in the YZ-plane (oblique to the observation plane of 270°/30°N), capped by shear-bands trending 360° and plunging steeply to the west (shown in blue). Portions of the upper sheared unit are schistose chlorite.

Chapter 5. Microstructure Analysis

Four samples are used to identify mineralogy, microstructures, and evidence for possible fluid influx. All samples are cut in the XZ-plane (or parallel to the regional XZ plane in the undeformed example), parallel to lineation and perpendicular to foliation with a view in the direction trending ~340° azimuth.

5.1. Undeformed Blue Draw Metagabbro (fabrics and mineralogy)

Sample NG2157-UND (**Fig. 5-1**) is an undeformed metagabbro and was analyzed in thin section with cross-polarized light (XPL) and plane-polarized light (PPL). The grains present are primarily twinned clinopyroxene, orthopyroxene, and plagioclase. Secondary quartz is present throughout the sample, and in every sample collected within the study area, likely due to later-stage contact metamorphism and mass transport related to the Harney Peak intrusion and the Central Planes Orogeny (Redden et al., 1990; Sims et al., 1991). While no structural fabrics are present, the sample is presumably hydrothermally-altered due to the presence of secondary quartz wherein no undulose extinction is observed.

5.2. Deformed Blue Draw Metagabbro (fabrics and mineralogy)

Sample NG2145a-mg-con (**Fig. 5-2**) is a metagabbro from the BDM/BCQ contact site. The matrix is predominantly chlorite, fine grained pyroxene, plagioclase, and secondary quartz, and it contains large porphyroclasts of twinned clinopyroxene. Asymmetrical strain shadows around clinopyroxene porphyroclasts indicate east side up sense of shear, best observed in PPL

(**Fig. 5-3**). The sample is strongly foliated with foliations formed primarily from alignment of chlorite and clinopyroxene grains. Parallel with the layering, compositional and grain-size segregated banding can be seen. Coarser grained layers contain larger clinopyroxene porphyroclasts, and finer grained layers contain more quartz.

5.3. Interstitial phyllite within the BCQ

Sample NG2132a was collected from an interstitial phyllite layer contained within the BCQ, from site NG2132, and analyzed in thin section in XPL (**Fig. 5-4**). The rock has uniformly fine grain size and strong foliation throughout. The grains that make up the bulk of the sample are clay minerals and secondary quartz. There are also some large porphyroclasts of opaque minerals. SEM dot-mapping raster analysis indicates these are iron sulfides, possibly pyrite oxidizing to a hematite pseudomorph while maintaining the original cubic morphology (**Fig. 5-5**). Symmetric and asymmetric strain shadows around these opaque minerals have inconsistent shear sense (**Fig. 5-6**).

5.4. Boxelder Creek Quartzite (fabrics and mineralogy)

Sample NG2145b-qtzt-con was collected from the BDM/BCQ contact site, NG2145b, and is shown in thin section with plane-polarized light in **Fig. 5-7**. Dissolution-seams have formed with infilled mica (as identified in XPL; bottom left panel in **Fig. 5-7**). Spaced foliation formed from dissolution seams and preferred alignment of mica grains within those seams. Quartz microstructures visible in XPL include recrystallized fine-grained quartz, bulged grain boundaries, sub-grain formation, and undulose extinction.

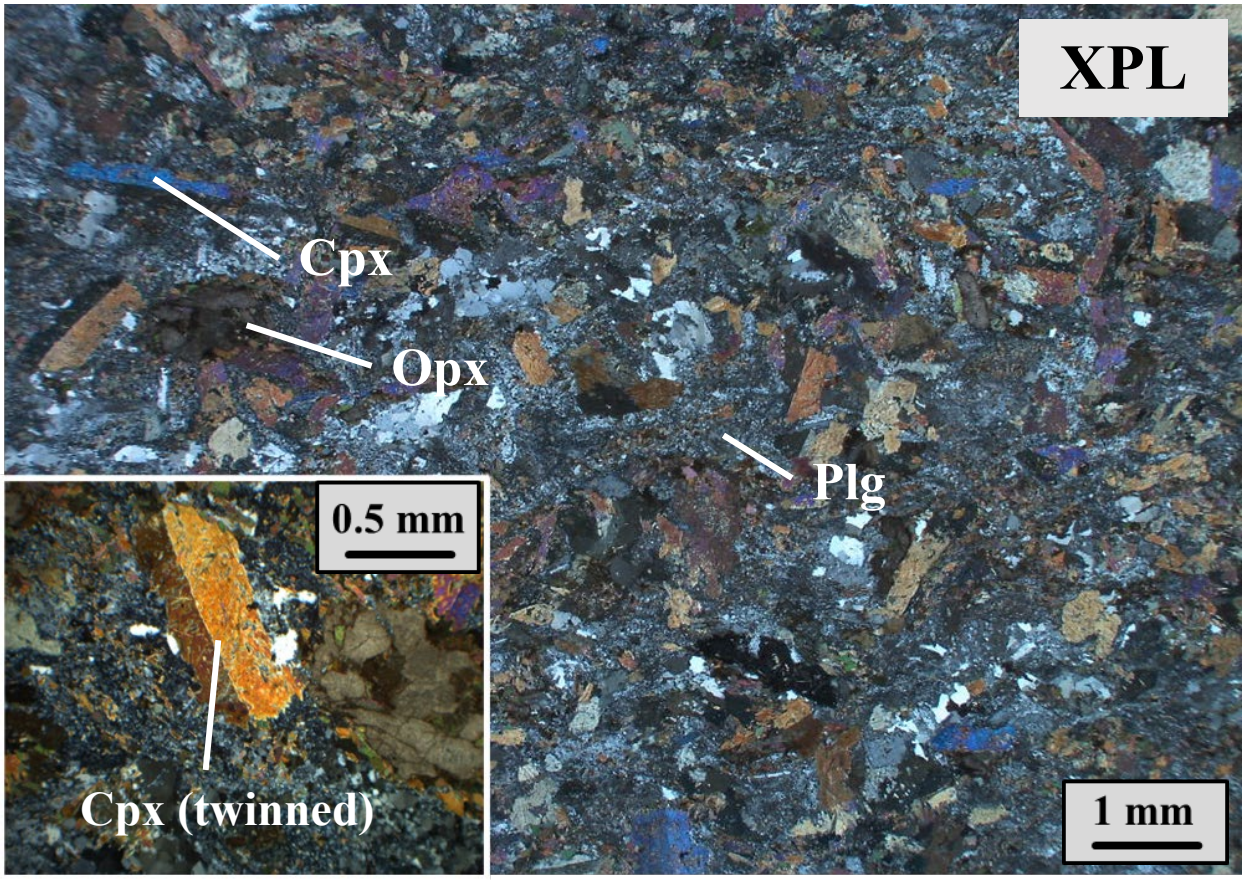

Figure 5-1: Sample NG2157-UND. Undeformed metagabbro in thin section in XPL. Grains present: clinopyroxene (Cpx), orthopyroxene (Opx), and plagioclase (Plg). Secondary quartz is present throughout the sample. The plane of observation is in the XZ-plane in the direction trending ~340° azimuth.

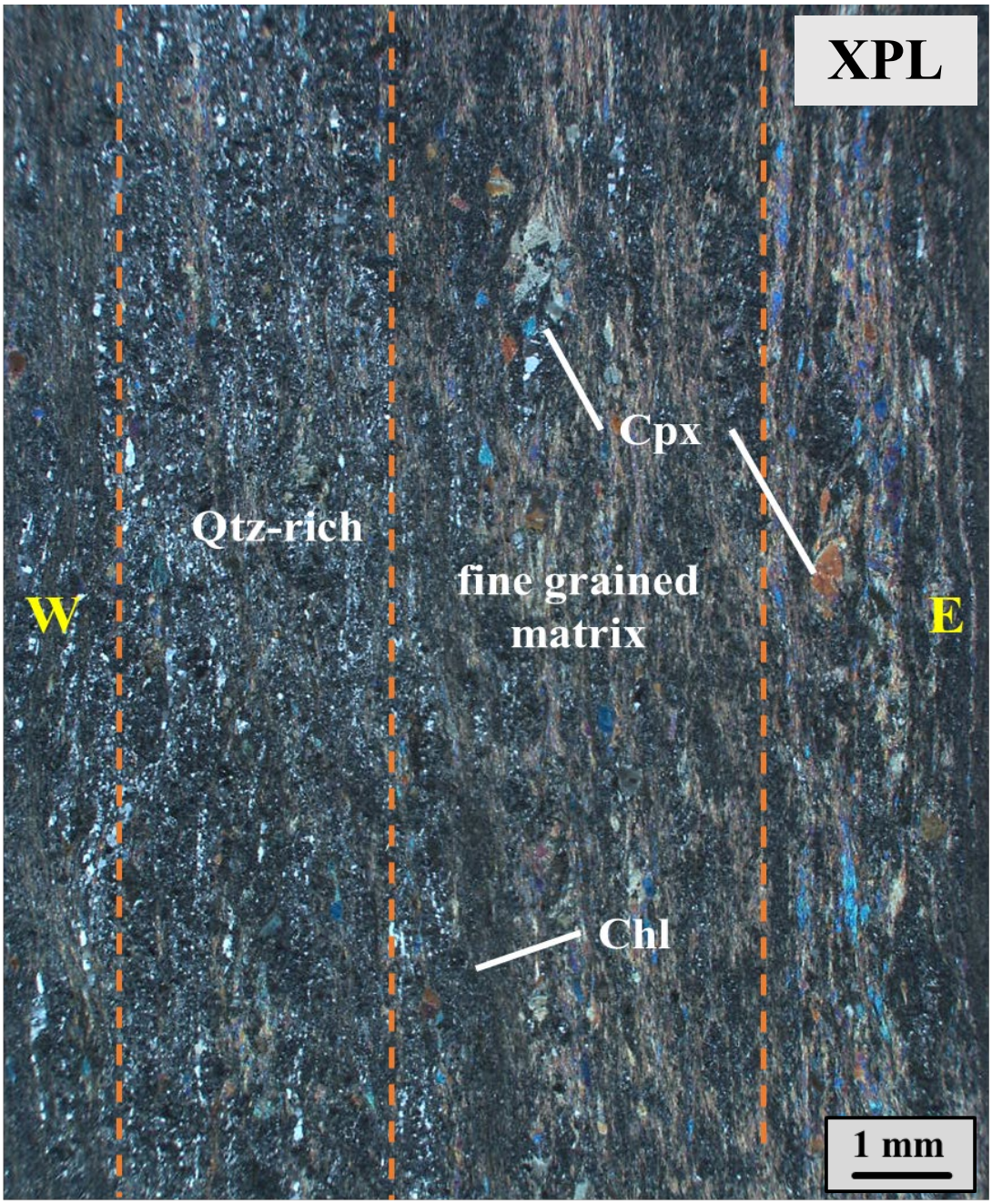

Figure 5-2: Sample NG2145a-mg-con. Metagabbro from the BDM/BCQ contact site NG2145a in XPL. Grains present: twinned clinopyroxene in a matrix of chlorite (Chl) and secondary quartz (Qtz). The plane of observation is looking into the XZ-plane in the direction trending ~340.

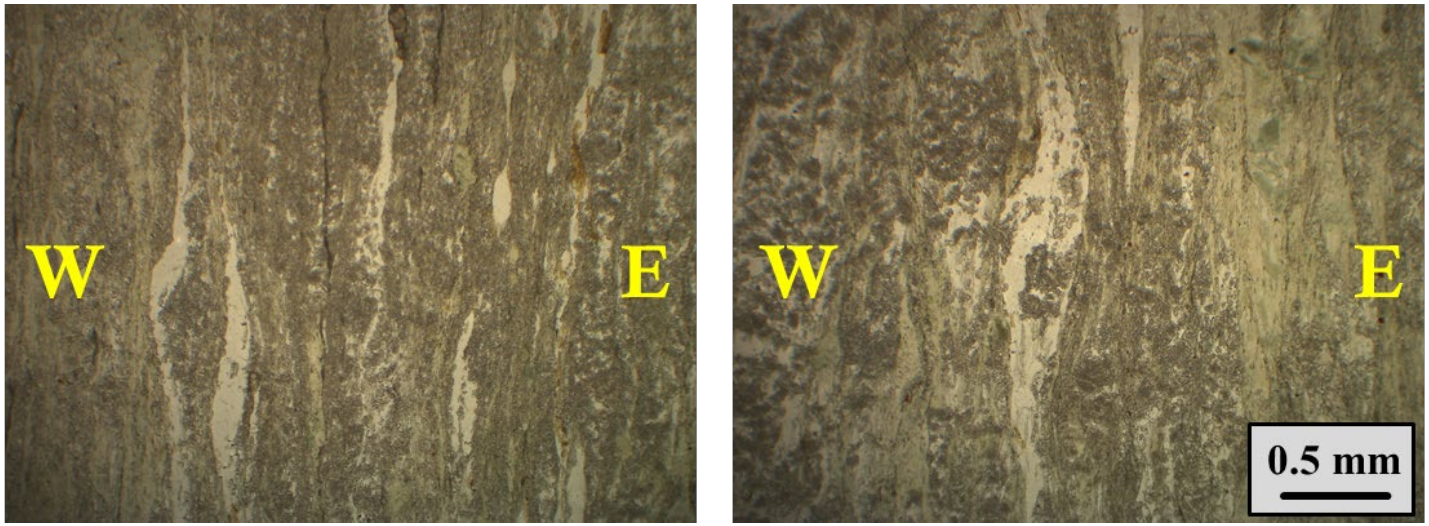

Figure 5-3: Sample NG2145a-mg-con. Metagabbro from the BDM/BCQ contact site NG2145a in PPL. Grains present: elongated clinopyroxene (lighter beige). In dark brown: a mixture of chlorite and fine-grained pyroxenes and plagioclase. The plane of observation is looking into the XZ-plane in the direction trending ~340°.

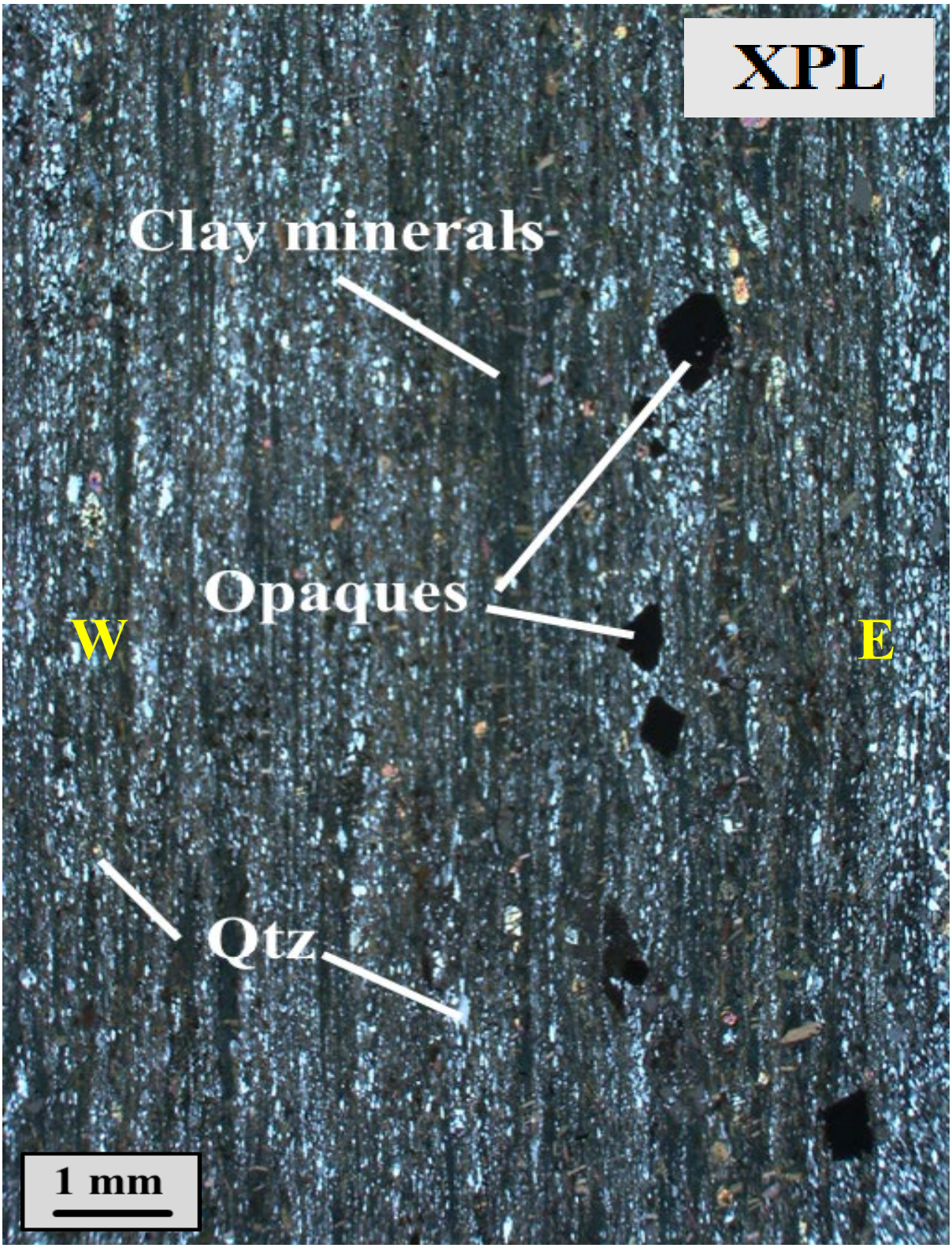

Figure 5-4: Sample NG2132a. Collected from an interstitial phyllite layer contained within the BCQ, from site NG2132 in XPL. Of note is the presence of abundant quartz that not only permeates the sample but concentrates along seams and bounds opaques as strain shadows trending N-S.

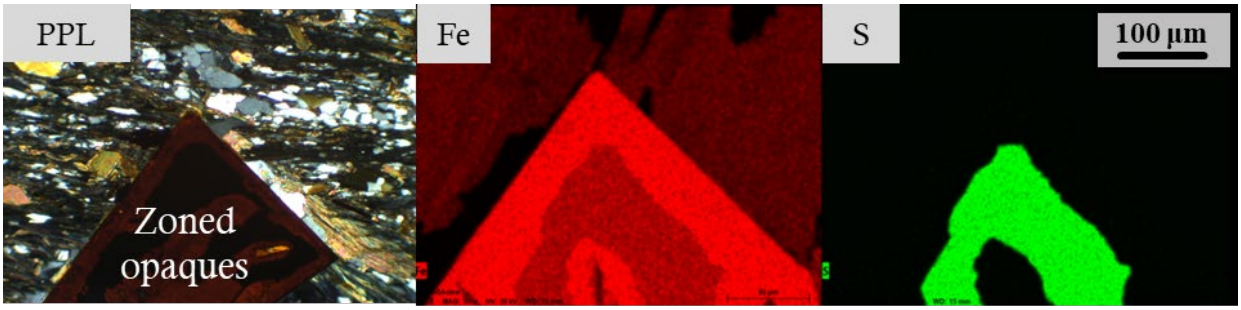

Figure 5-5: SEM raster analysis dot-maps of the opaques found in sample NG2132a. The left image shows the zoning in an opaque grain, with the middle image (iron content) and right image (sulfur content) show the bulk composition within the zones. The plane of observation is looking into the XZ-plane in the direction trending ~340°.

Figure 5-6: Sample NG2132a. From an interstitial phyllite layer contained within the BCQ, Site NG2132, in PPL. Of note are the strain shadows that have formed at the top and bottom of the iron-sulfide grains that have infilled with recrystallized quartz. The plane of observation is looking into the XZ-plane in the direction trending ~340°.

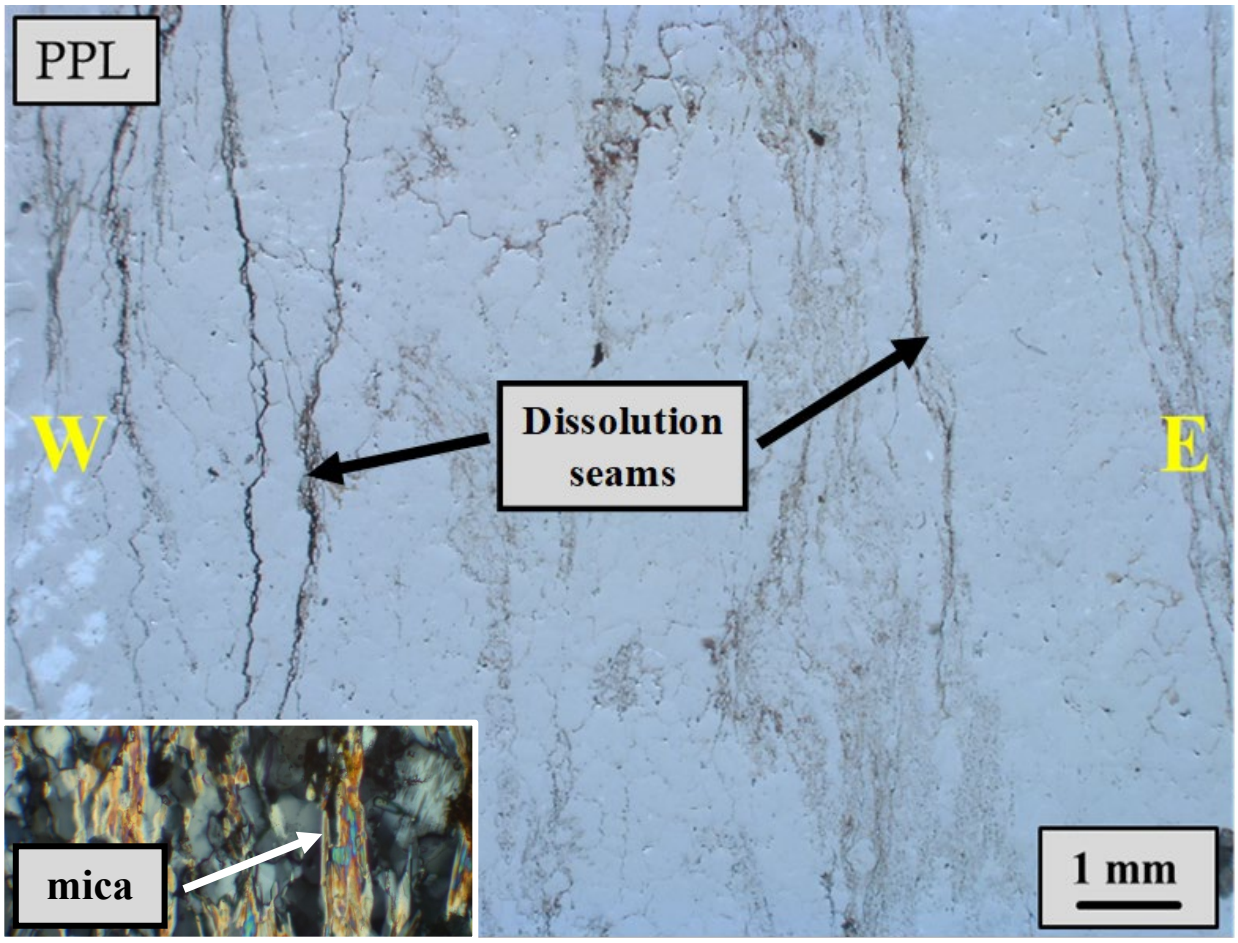

Figure 5-7: Sample NG2145b-qtzt-con. BCQ sample collected from the BDM/BCQ contact site NG2145b in PPL. Of note are the vertical dissolution seams. The plane of observation is looking into the XZ-plane in the direction trending ~340°. Inset image is aligned mica filling the dissolution seams.

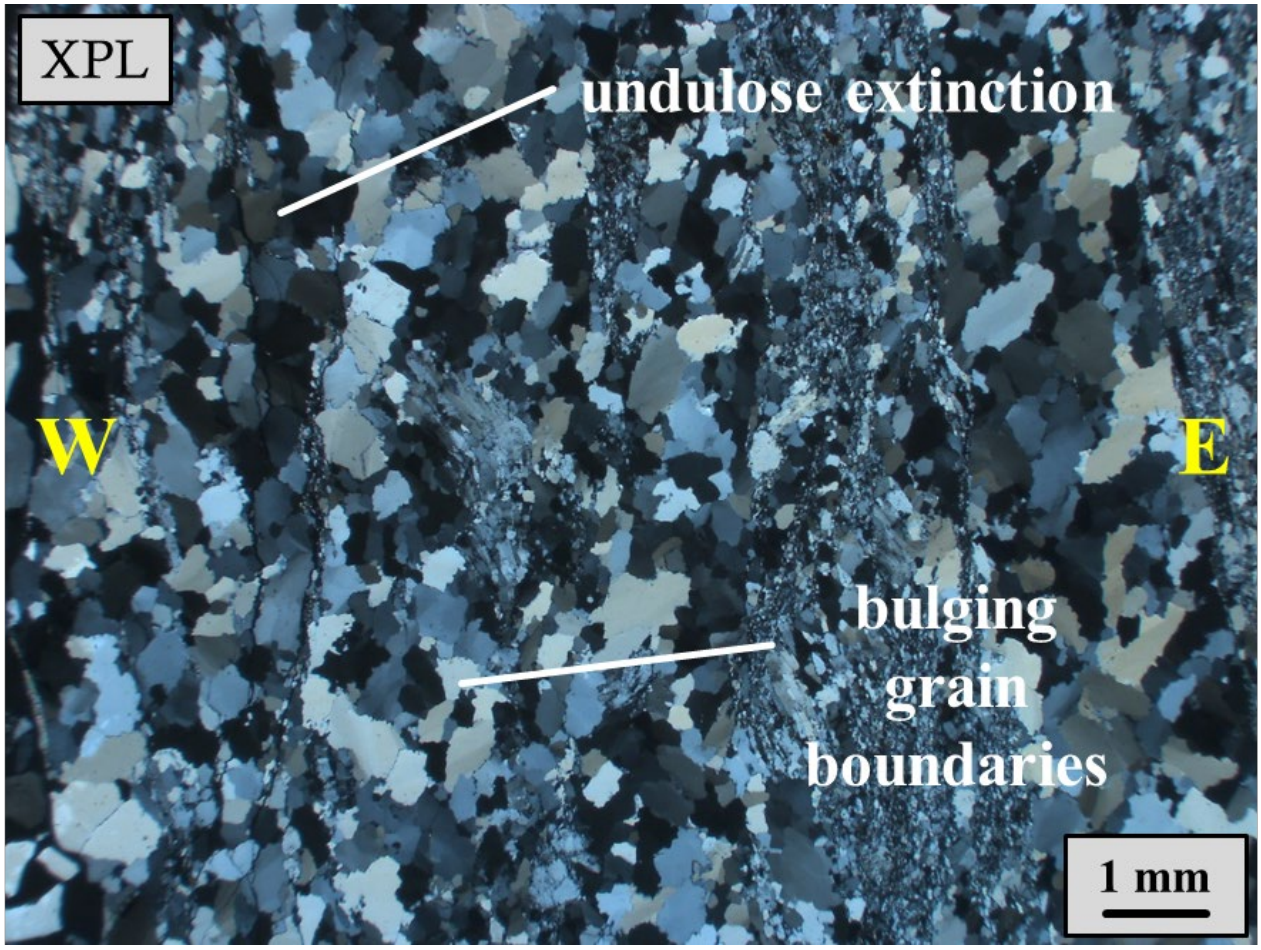

Figure 5-8: Sample NG2145b-qtzt-con. BCQ sample collected from the BDM/BCQ contact site NG2145b in XPL. Of note are the recrystallized fine-grained quartz, bulged grain boundaries, sub-grain formation, and undulose extinction. The plane of observation is looking into the XZ-plane in the direction trending ~340°.

Chapter 6. Interpretations

Towards the goal of evaluating transpression as a model for deformation in the Nemo area, I will consider structural features such as tectonic fabrics and lozenges. Fabric orientations are plotted on stereonet plots that were generated by software designed by Allmendinger et al. (2013) and Cardozo & Allmendinger (2013), with additional Google Earth outputs designed by Blenkinsop (2012). Structural fabrics have been grouped by proximity within the study area into three main categories: central-area map foliations, Knob Hill foliations, and eastern-area map foliations. Sections of the data tables found in **Appendix table A1** have been included in each figure for reference. Following a discussion of the foliation orientations, lineation orientations, and other properties at each study site, I will offer a broader kinematic interpretation of the whole study area. Shear zone kinematic models were generated using macros built into Microsoft Excel software by Fernández & Diaz-Azpiroz (2009), and field fabrics were compared to model predictions. Next, I will consider evidence for syntectonic fluid interaction and reflect on how that could impact the kinematic interpretations. Lastly, I will consider the variations in deformation style between the two lithologies and how this study informs our understanding of the tectonic history and deformation in the Black Hills.

6.1. Foliation Interpretations

The average strike of foliation within the entire field area is approximately ~335° - 350° with steep dip (**Fig. 6-1)**. While this indicates a broad consistency of foliation orientation within the study area, it should be noted that according to Allard & Portis (2013), these foliation orientations are likely representative of S_2 and S_3 fabrics and formed across multiple deformation

domains (Domains 1-4). Therefore, foliations can perhaps be only loosely correlated to Domain 3 shear fabrics. As such, two primary assumptions can be made. First, any foliations present within the field area cannot be used to refine kinematic models for Domain 3 conclusively. Secondly, the presence of foliation that was formed in D_1 likely influenced strain partitioning in D_2 events, and foliation that was formed in D_2 likely influenced strain partitioning in D_3 events, and so on. Indeed, Allard & Portis (2013) found that foliation didn't significantly vary in each of the domains. Moreover, foliation orientation does not significantly limit possible kinematic models (e.g. Fernández et al., 2013).

As a result of the above assumptions and observations, and the inherent limitations of incorporating the foliation data into a study of Domain 3 shear fabrics, only a qualitative interpretation of kinematic model as indicated by foliation orientations is appropriate. However, when qualitative foliation interpretations are coupled with additional data analysis, such as Flinn plots, which illustrate the deformation geometries of discrete/localized lozenge shapes and stretching lineation orientations that we measured in the field, a more complete picture emerges.

6.1.1. Foliation orientations, strain distribution, and Relationship to F_2 & F_3

The field area is divided into two regions where varying amounts of strain can be grouped. These regions are located in the central map area, within and to the north/south of the western-most metagabbro fold hinge (see "hypothesized zone of high strain" from **Ch. 3: Fig. 3-4**), and the eastern-most map-view metagabbro limb. The lozenge shapes and tectonic fabric orientations are likely a result of the entire deformation history, so analysis can help determine the finite strain history.

Two of the areas within the BDM that showed the least strain and lowest aspect ratios in lozenge geometry (which will be addressed in **section 6.3**) were found within the zone of highest strain, located in the central region of the mapping area proximal to the fold hinge, which agrees with the conclusions drawn by Allard & Portis (2013) that the metagabbro hinges are the least deformed. However, crosscutting and bounding these zones are anastomosing mylonitic fabrics, mineral alteration, and other indications of high strain (**Fig. 6-2**).

An estimated reconstruction can be found below, beginning with **Fig. 6-3** with the average stereonet plots of each outcrop or groupings of outcrops arranged on the field map. This reconstruction is based on the changes in foliation orientation, particularly around the Knob Hill sites, with "Bear Scat Valley" to the south and crossing the quartzite-metagabbro boundary into the north. The results resemble a z-structure consistent with left-lateral shear (**Fig. 6-4**).

6.2. Lineation Interpretations

Where lineations were observed, their orientations were generally plunging ~50° to subvertical and trended towards the NW quadrant in both the BDM and BCQ. However, within the BDM, at outcrops only 3-5 m apart, lineation plunges trended towards the SE within similar ranges (~50° to subvertical plunges) as shown in **Appendix table A3**. These measurements may indicate that both left lateral shear and thrusting occurred within the NGSZ and as the zone of highest strain is approached from both the east and west, both intermediately plunging and steeply plunging lineations are present, indicating concurrent thrusting and lateral shear (sinistral slip-strike). Alternatively, the extrusion orientations related to the pure shear component of deformation may have varied to create both southeast and northwest plunging lineations. The

close proximity of these lineation deviations could indicate that the left lateral shear zone contact may lie in the approximately meter wide zone that was weathered away. It is possible that this contact, which shows indications of greenschist facies metamorphism and alteration to chloritic recrystallization, was prone to weathering at not only this, but other "topographic lows" across the zone of high strain. However, this interpretation is complicated by the influence of hydrothermally active fluids resulting from the possible influence of the D_4 Harney Peak intrusion to the south, which also may have caused alteration at this later time.

However, field measurements indicate that there is a conformable pattern that permeates the central region of the field area, with mylonitic foliations striking ~340° azimuth based on the orientation of anastomosing fabrics that bound the homogeneous oblique to orthogonal foliation orientations of the larger undeformed blocks.

6.2.1. Comparisons to kinematic models

To constrain the conditions that produce the lineation orientations measured in this region, I generated models by varying the input values for kinematic vorticity, simple shear obliquity, and extrusion obliquity, with constant initial constraints on the hypothesized region-scale shear zone geometries (subvertical shear dip, ~340° shear strike, and sinistral lateral displacement).

Of the 627 models considered, 132 runs returned principal strain axis orientations consistent with the lineations and poles to foliation measured in the field (**Table 6-1**). However, no single run was favorable to both of these fabrics. Of the 132 runs that potentially accommodate the field orientations, 17 combinations produced x-axis or output ranges that

completely contain the measured ranges for the lineations. Additionally, nearly every one of the 132 runs encompassed the foliation criteria. Therefore, the 17 runs that showed a positive correlation between long axis rotations and lineation orientations were rerun with varying shear zone dips as an additional variable with an attempt to match the short axis rotations to poles to foliation trend and plunge. The shear zone dip inputs range from 70° - 90° in 5° increments. Of these final models, high kinematic vorticities of 0.8 and 0.9 are favored; near vertical extrusion obliquities of 0° to 20° & 160° to 180° are favored, and shear zone dips of 73° to 85° are favored, with only one true vertical dip present in the models (**Table 6-2**). When a small subset of these models are projected on Flinn Plots, chosen from various combinations of ϕ, v, W_k, and shear zone dip, flattening is the dominant strain which matches the field data from the lozenges described below (**Figs. 6-5, 6-6, & 6-7**).

These analyses indicate that globally the fabrics in the NGSZ are consistent with a left-lateral transpressional shear zone. The shear zone boundaries are likely steeply inclined, however it is not possible given the data to constrain this exactly.

The high kinematic vorticity numbers indicate that simple shear dominated over pure shear. The orientation of that shear component may vary. Most macro-scale shear sense indicators in the field indicated left-lateral shearing, so that as is often the case in transpression zones, the shear direction is nearly orthogonal to the lineations (which are steeply plunging). Some microstructural shear sense indicators indicate east side up (such as the tails on the clinopyroxene porphyroclasts shown in Fig. 5-3), however other strain shadows have ambiguous shear sense on the XZ plane (such as the hematite/pyrite porphyroblasts in Fig. 5-4). Because the clinopyroxene porphyroclasts are largely being replaced by chlorite, it is likely that their shear sense is related to an earlier phase of deformation in comparison to the hematite/pyrite

porphyroblasts which are clearly later features, likely associated with the NGSZ deformation. Although it was not tested in this thesis, those porphyroblasts would likely have consistent asymmetric strain shadows on a subhorizontal plane.

Extrusion directions favored by the modeling are largely steep to subvertical. The combination of subvertical extrusion directions and subhorizontal simple shear directions suggests that the transpression may be approximated by a steeply inclined zone with monoclinic symmetry, but small shifts in the extrusion direction result in local triclinic symmetry.

The exact kinematic parameters may vary throughout the NGSZ. For example, two models that were discarded from consideration in the global NGSZ analysis have much lower kinematic vorticity numbers (0.2, 0.5) can describe possible shear models for sites NG2116 and NG2117 (**Fig. 6-8**). These sampling sites are located in the BCQ and are the furthest geographically from the central region of the mapping area, where the zone of highest strain is likely located. This illustrates that certain models describe possible conditions at discrete locations within the larger NGSZ.

6.3. Lozenge Aspect Ratios & Distribution

To better constrain kinematic models with three-dimensional data, lozenge geometries can be used as analogues for the strain ellipsoid in discrete sampling areas and compared to kinematic models. Field measurements of exposed lozenge aspect ratios were primarily in the XZ and YZ planes. In the BDM, 24 sites provided adequate data for both planes, but in cases where one plane was not available for measurement for a single lozenge, the missing plane measurement was taken from a nearby lozenge in the same outcrop where that plane was

recorded, and this was used as an approximation for the calculation. However, the YZ (**Fig. 6-9**) and XZ planes (**Figs. 6-10 & 6-11**) have been mapped for reference. The geometries in both planes give a sense of the degree of strain in the NGSZ, both within the zone of high strain and along the limbs of the metagabbro z-structure, in addition to the general strain within the BCQ. The resulting geometries indicate that the quartzite shows more homogeneous strain regardless of outcrop proximity to the zone of highest strain, whereas the metagabbros have heterogeneous strain, particularly when the BDM outcrops are located near a fold hinge.

The exception to this is again Knob Hill, which is likely located directly in the strike of the shear zone contact and straddles the SW and NE sections that underwent lateral displacement. This can be seen in the high aspect ratios (denoted in red) which crosscut lozenges with intermediate to low aspect ratios (denoted in beige, yellow and green) in **Fig 6-10.** In some cases, the lozenges are in fact no longer detectable and only highly altered mylonitic fabrics remain with tightly spaced foliations that occasionally intersect at acute angles of 5° to 10°, indicating that lozenge geometries were once likely present prior to shearing. To quantify these observations, XY planes were calculated using the basic equation:

$$\frac{x}{y} = \frac{\frac{x}{z}}{\frac{y}{z}}$$

as only three XY planes were directly measured in the field. These calculated values were then used, along with the measured YZ planes, to populate the axes on a Flinn diagram, again assuming that the strain in the lozenges is a suitable analogue to the strain ellipse at each outcrop.

6.3.1. Flinn plot and interpretation

Comparisons of lozenge aspect ratios measured in all three observation planes support conclusions drawn from both the foliation orientations and the kinematic models. Measured YZ planes and calculated XY planes were determined and plotted on the y- and x-axes respectively (**Fig. 6-12**). Deformation in both the quartzite and metagabbro ranges from nearly plane-strain to significant flattening, with much stronger flattening shapes preserved in the metagabbro. This heterogeneity of deformation may be related to the influence of D_1, D_2, and D_3 fabrics that predated or formed syn-deformational in the NGSZ or may be due to heterogeneity in kinematics or degree of strain within the NGSZ.

Areas dominated by flattening (in the BDM) are located in the zone of high strain, with mylonitic fabrics as well as discrete zones of low strain. In the BCQ, approximate plane-strain and minor to moderate flattening is dominant, regardless of proximity to the zone of high strain, suggesting that the less competent quartzite conforms to more homogeneous deformation compared to the metagabbro. Oblate lozenge shapes indicate strain was dominantly in the flattening field, especially in the central part of the shear zone, which is consistent with transpression. Along limbs of the metagabbro z-structure and within the bounding BCQ, plane strain is observed, which suggests partitioning of simple shear to the zones of lower strain. It can therefore be concluded that metagabbro strain intensity is heterogeneous with most variability near fold hinges and quartzite strain intensity is relatively homogeneous.

6.4. Microstructures and Hydrothermal Fluid Alteration

Microstructural analysis highlights the presence of important fabrics that likely formed in the presence of fluids such as strain shadows and dissolution seams, which suggests there was fluid present during deformation. Due to the ubiquity of quartz in the metagabbro, regardless of deformation gradient, and the likewise presence of iron in the surrounding quartzite, notably north of the lithological contact, fluid mass transfer of constituent elements likely occurred. However, the timing of this hydrothermal alteration is unknown. What is unclear is why the P/T conditions required for alteration and mass transfer did not also erase many of mineral grains that remain in even the most undeformed metagabbros in the study area (twinned clinopyroxenes, for example). As a result, the influence of fluids, whether from existing water in the system during deformation, from the later D_4 Harney Peak intrusion, or both, remains a factor that will continue to complicate the story of the NGSZ.

Syntectonic or post tectonic fluid flow may affect the finite strain shapes, and thus impact the kinematic modeling, which assumed no volume loss. A key difficulty here is that the extant fabrics do not indicate whether volume loss took place, nor does it exclude the possibility of extensive volume loss. As such, the models require more field data to constrain the possible fabrics that may or may not result from the influence of fluid alteration. However, there was no indication in the field that the bulk constituents of the two lithologies, for example silica in the quartzite and plagioclase in the metagabbro, were dissolved and transferred across the lithological boundary in sufficient quantities to skew the models enough for volume loss to be a factor. Future work could focus on geochemical work that would help determine whether significant volume loss occurred requiring modification to the modeling results.

6.5. Rheology Contrasts

The bulk structural data indicates consistency with a transpression model, but the deformation was manifested differently in each lithology. Within the quartzite, the strain was more homogeneous indicated by consistent tightly spaced foliations. Strain geometries indicate plane strain to moderate flattening. Indications of previous deformation fabrics and folds were not generally observed. Within the metagabbro, strain was extremely heterogeneous on the meter scale, and the deformation was at least partially controlled by the influence of prior folds. Fold hinges nucleated blocks of low strain while high strain zones wrapped around these blocks. Strain shapes ranged from mild constriction to plane strain to flattening to extreme flattening, with most locations having either plane strain or flattening.

6.6. Tectonic Setting of the Black Hills Uplift suggested by NGSZ fabrics and modeling

The kinematic models and strain recorded by the lozenges, primarily suggests simultaneous left-lateral shearing and shortening at the NGSZ. In the central part of the NGSZ, high amounts of flattening developed with deformation closer to plane strain (simple shear) further out towards the shear zone boundaries. This would suggest oblique sinistral convergence between the Superior and Wyoming provinces, and the high kinematic vorticity numbers suggest that this part of the Black Hills accommodated mostly lateral motion. The common strike of foliation fabrics and lozenge long axes (~330° to ~350°) suggests that the existence of pre-D_2 foliations and other deformation fabrics had little effect on lozenge geometries. If in fact foliations from D_1 were present prior to the development of the shear zone, it would be expected

that remnant orientations of D_1 penetrative fabrics from northerly convergence to the south would be present and differ in orientation to D_2 & D_3.

6.1. Foliation

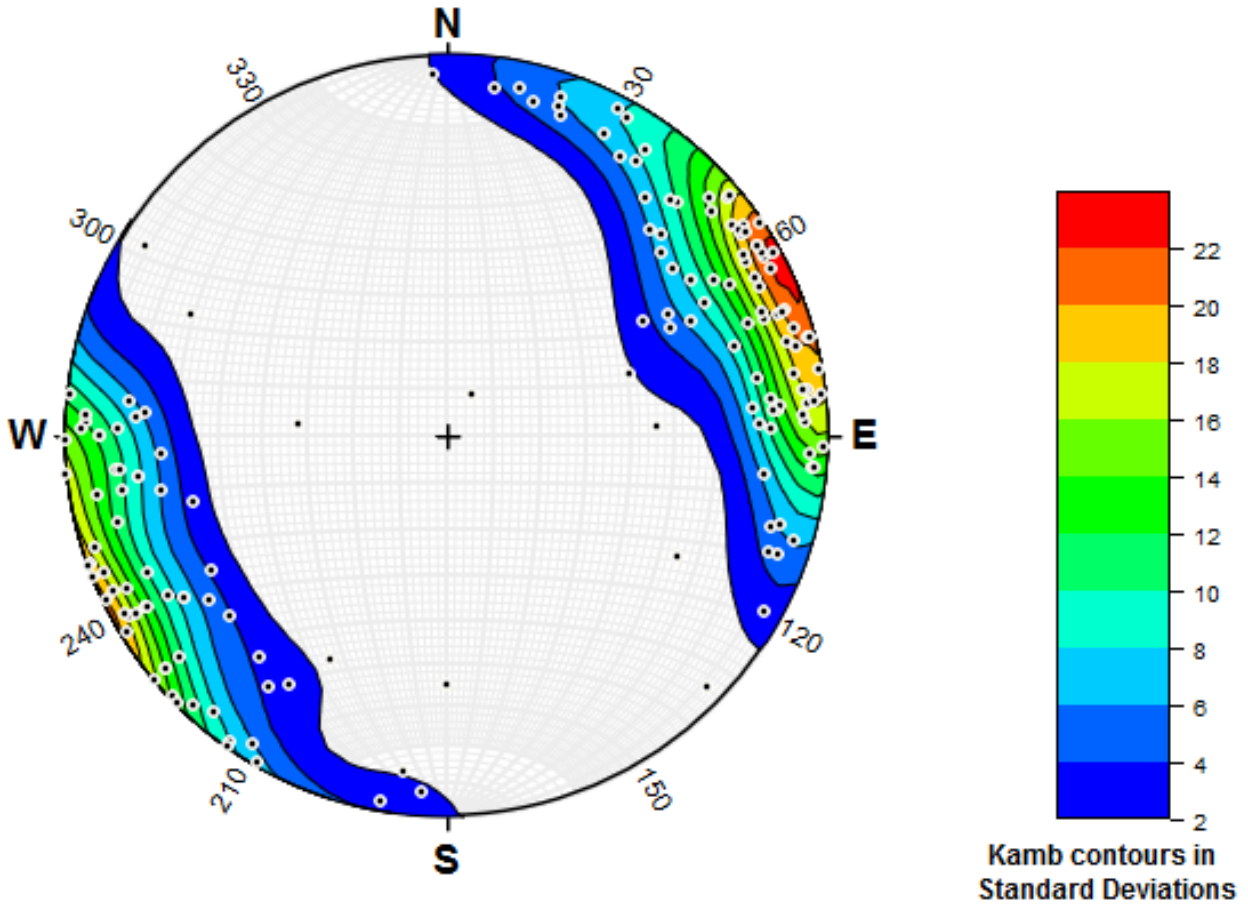

Figure 6-1: Stereonet plot of all poles to foliation in NGSZ study area. These poles concentrate at ~065° and ~245°, indicating an approximate average foliation plane striking ~335° and dipping steeply to the SW, though variation is observed within the study area. In areas of least strain, foliation planes within a single outcrop can have near orthogonal strikes.

6.1. Foliation

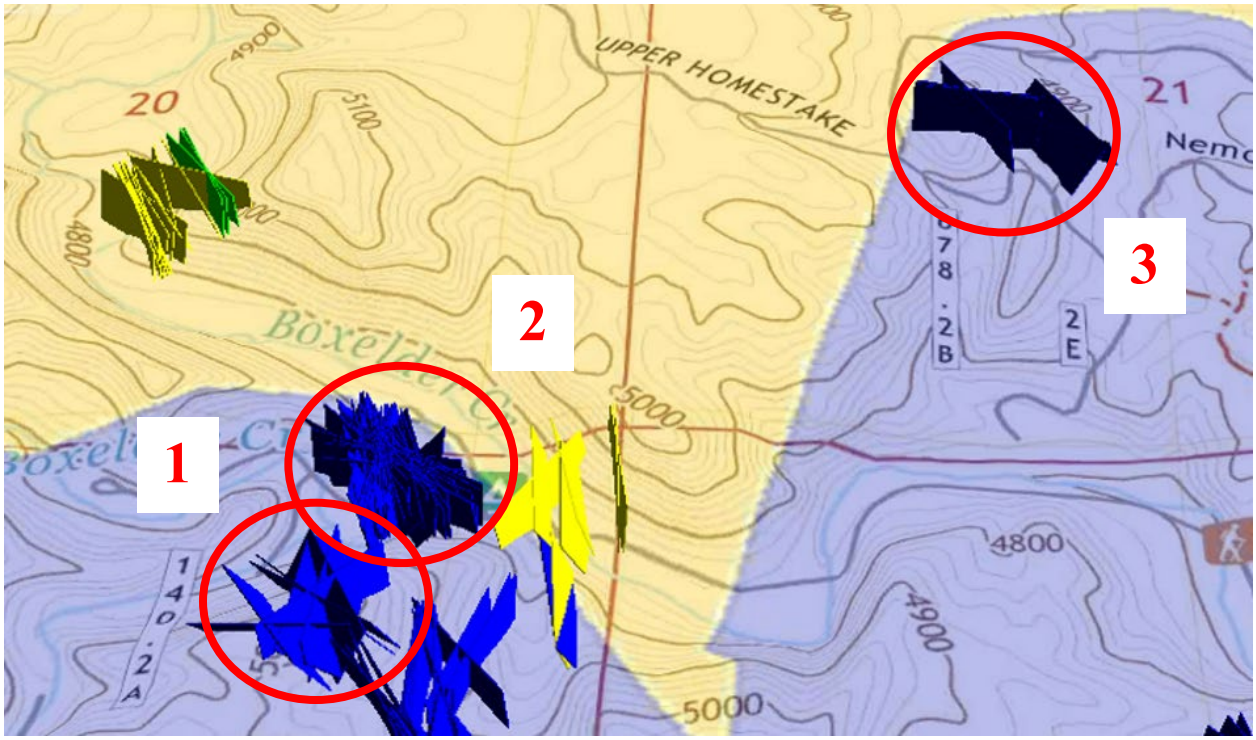

Figure 6-2: Composite map of the central zone sites (within and straddling the zone of high strain), plotted using Google Earth and stereonet output files created by Blenkinsop (2012). The blue planes represent metagabbro foliation planes, the yellow represent quartzite foliation planes, and the green represent interstitial phyllite layers within the quartzite. Of note are the orientations in the BDM at topographic highs near Boxelder Forks Campground (Areas 1 & 2), located at the hinges of the BDM z-fold structure (circled in red). These are areas where the XZ lozenge aspect ratios fall between 1-2 and are interpreted as the least deformed rocks in the study area. Unexpectedly, these two blocks are conspicuously located within the zone of high strain and remain mostly intact. In the case of Area 1, this lower strained block is pristine, with anastomosing shear bands in the valley boundaries. Area 2, however, is bounded *and* crosscut by mylonitic shear banding (bisecting the highly competent Knob Hill, regardless of the variance in preexisting strain), with extensive mineral alteration and intense fabric formation, indicating that this block lies directly within the shear zone contact. Area 3 (also circled in red) is presumably at a hinge, but the SE dipping limb is not exposed at the surface if it exists. These outcrops also exhibit nearly orthogonal terminal angles between foliation planes, with low aspect ratios across the three observation planes.

6.1.1. Reconstruction & Relationship to F_2 & F_3

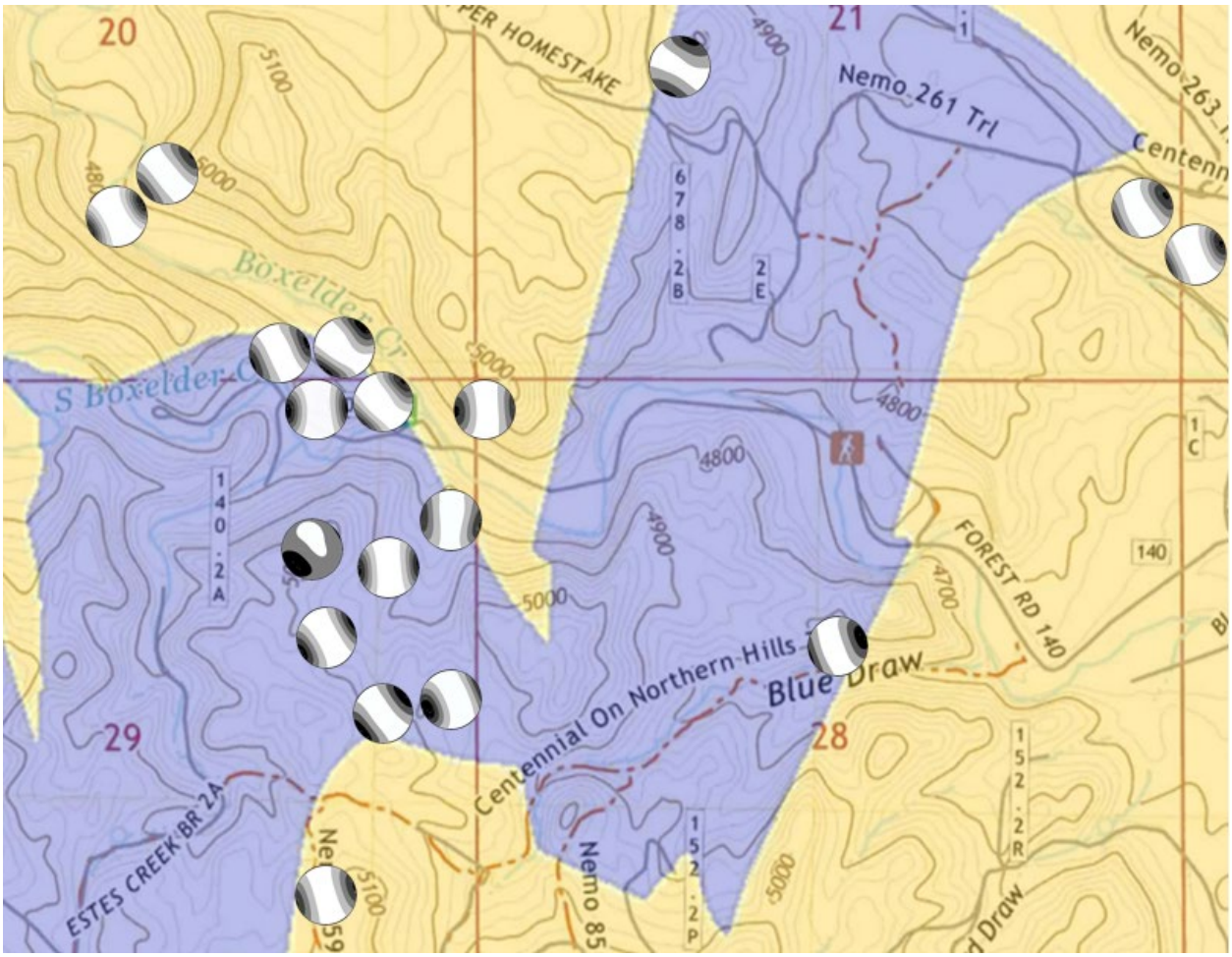

Figure 6-3: Foliations plotted using stereonets at all sites. Foliations have a N-S strike in both the BCQ and the BDM at the center of the map compared to a general NW strike that dominates the study area.

6.1.1. Reconstruction & relationship to F_2 & F_3

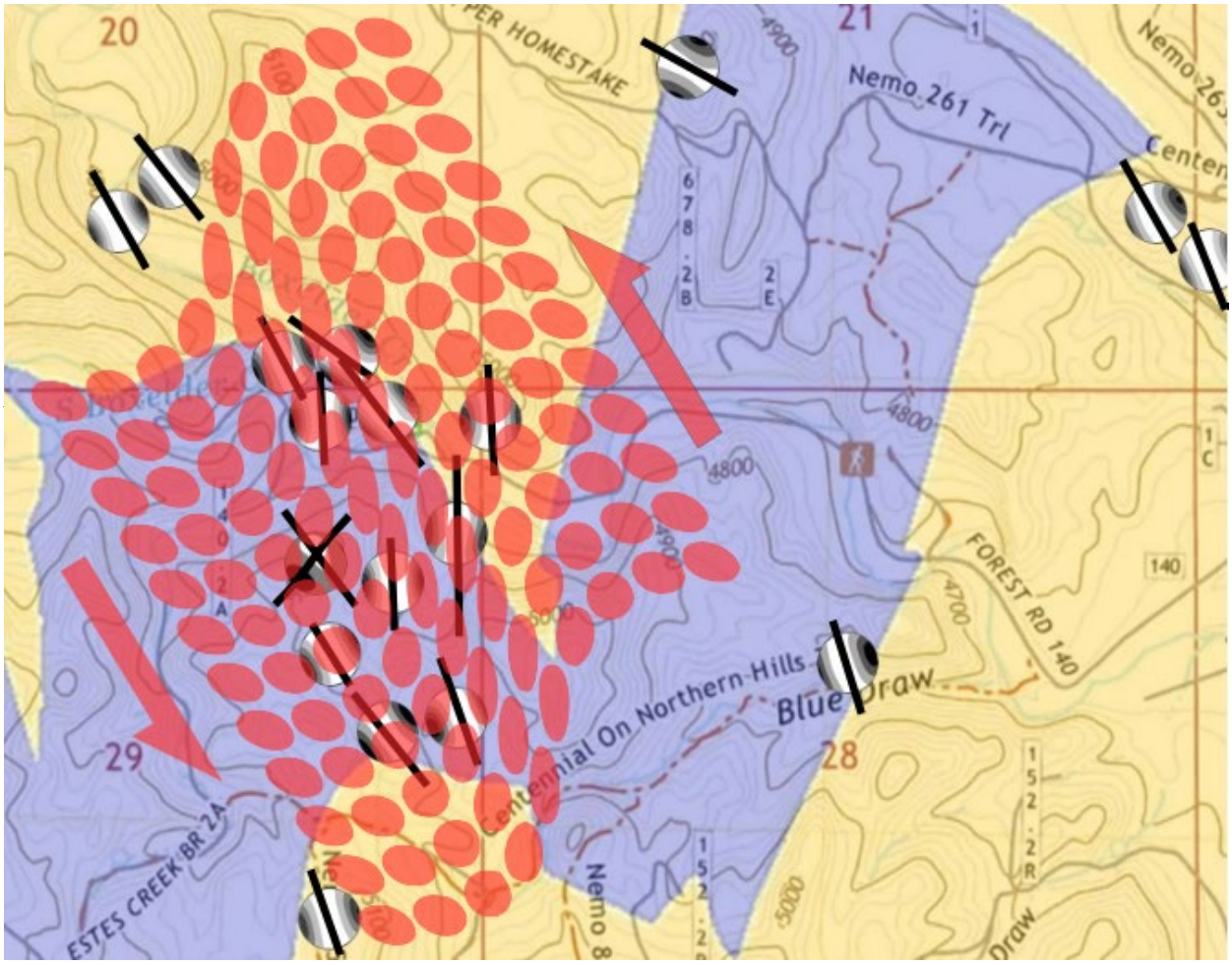

Figure 6-4: Grid markers approximating heterogeneous simple shear, based on the measured orientations of both anastomosing shear bands, changes in shear band strike bounding the large undeformed blocks at the central hinge (Knob Hill), and the S-C fabrics in parasitic fabrics in both the BDM and BCQ throughout the study area (see Results, Mesoscale Features, Figs. 4-32 & 4-33).

6.2.1 Best-fit relationships between lineation & shear zone models

Model Parameters				Model Output				Plunge of average pole to foliation (~12°) within range of model pole plunges (Z)? (Y: Yes; N: No)
Shear obliquity (ϕ)	Extrusion obliquity (υ)	Kinematic vorticity (Wk)	Dip of the shear zone boundary in degrees	Range of lineation plunges (X) in degrees		Range of foliation pole plunges (Z) in degrees		
				min.	max.	min.	max.	
-20	0	0.9	90	32	80	0	9	N
			85	28	79	5	13	Y
			80	25	76	10	17	Y
			75	21	72	15	21	N
			70	18	68	20	25	N
-20	10	0.8	90	49	74	0	6	N
			85	46	73	5	10	N
			80	42	71	9	14	Y
			75	38	68	14	18	N
			70	34	64	19	22	N
-20	10	0.9	90	33	71	0	7	N
			85	30	70	5	11	N
			80	26	68	10	15	Y
			75	23	65	15	19	N
			70	19	62	20	23	N
-20	20	0.8	90	44	65	0	4	N
			85	41	64	9	4	N
			80	38	63	9	13	Y
			75	34	61	14	17	N
			70	31	58	18	21	N
-20	160	0.9	90	16	70	0	12	N
			85	13	69	5	16	Y
			80	9	68	10	20	Y
			75	6	65	15	24	N
			70	3	62	20	28	N
-20	170	0.9	90	27	87	1	10	N
			85	23	84	5	14	Y
			80	20	79	10	18	Y
			75	16	75	15	22	N
			70	13	70	20	26	N

Table 6-1: Kinematic model outputs. The first 6 of 17 runs that predicted orientations that matched field data for at least one of the strain axes were rerun with varying shear zone dips as an additional variable. Cells in green indicate models that predicted long-axis, *x*, and short-axis, *z*, orientations that match the range of lineations and poles to foliation, respectively, that were measured in the field area. Cells in yellow indicate models that predict axes orientations that match some, but not all, measurements. Cells in red indicate models that predict axes orientations that do not match field measurements.

6.2.1 Lineation relationships to shear models (cont.)

Model Parameters				Model Output				Plunge of average pole to foliation (~12°) within range of model pole plunges (Z)? (Y: Yes; N: No)
Shear obliquity (ϕ)	Extrusion obliquity (υ)	Kinematic vorticity (Wk)	Dip of the shear zone boundary in degrees	Range of lineation plunges (X) in degrees		Range of foliation pole plunges (Z) in degrees		
				min.	max.	min.	max.	
-20	180	0.9	90	32	80	0	9	N
			85	28	79	5	13	Y
			80	25	76	10	17	Y
			75	21	72	15	21	N
			70	18	65	20	25	N
0	10	0.8	90	48	77	0	2	N
			85	45	76	2	5	N
			80	42	73	6	10	N
			75	39	70	10	15	Y
			70	35	66	15	20	N
0	10	0.9	90	11	73	0	2	N
			85	8	72	2	5	N
			80	5	70	6	10	N
			75	2	67	10	15	Y
			70	0	64	14	20	N
0	20	0.8	90	39	65	1	4	N
			85	36	64	0	4	N
			80	33	63	5	9	N
			75	30	60	9	14	N
			70	27	58	13	19	N
0	170	0.9	90	11	73	0	2	N
			85	14	72	5	6	N
			80	16	70	10	11	N
			78*	17	69	11	13	Y
			77*	17	69	12	14	Y
			75	18	67	14	16	N
			70	20	64	17	21	N
						*best fit is achieved at finer increments		
20	0	0.9	90	32	80	0	9	N
			85	35	79	1	5	N
			80	38	76	0	10	N
			75	41	72	3	15	Y
			70	43	68	7	20	Y

Table 6-1 (cont.): The second 6 of 17 runs that showed a positive correlation for at least one of the strain axes were rerun with varying shear zone dips as an additional variable. Cells in green indicate models that predicted long-axis, *x*, and short-axis, *z*, orientations that match the range of lineations and poles to foliation, respectively, that were measured in the field area. Cells in yellow indicate models that predict axes orientations that match some, but not all, measurements. Cells in red indicate models that predict axes orientations that do not match field measurements.

6.2.1 Lineation relationships to shear models (cont.)

Model Parameters				Model Output				Plunge of average pole to foliation (~12°) within range of model pole plunges (Z)? (Y: Yes; N: No)
				Range of lineation		Range of foliation pole		
Shear obliquity (ϕ)	Extrusion obliquity (υ)	Kinematic vorticity (Wk)	Dip of the shear zone boundary in degrees	min.	max.	min.	max.	
20	10	0.9	90	27	87	0	10	N
			85	30	85	1	6	N
			80	33	80	0	10	N
			75	36	75	2	15	Y
			70	38	70	6	20	Y
20	20	0.9	90	16	70	0	12	Y
			85	19	69	0	8	N
			80	21	68	1	10	N
			75	21	65	0	15	Y
			70	21	62	4	20	N
20	170	0.8	90	49	74	0	6	N
			85	52	74	0	5	N
			80	56	72	3	10	N
			75	57	69	7	15	N
			70	57	65	11	20	N
20	170	0.9	90	33	71	0	7	N
			85	36	70	1	5	N
			80	39	68	1	10	N
			77*	41	67	3	13	Y
			75	42	66	5	15	Y
			73*	42	65	6	17	Y
			70	43	63	9	20	N
							*best fit is achieved at finer increments	
20	180	0.9	90	32	80	0	9	N
			85	35	79	1	5	N
			80	38	76	0	10	N
			75	41	72	3	15	Y
			70	43	68	7	20	Y

Table 6-1 (cont.): The final 5 of 17 runs that showed a positive correlation for at least one of the strain axes were rerun with varying shear zone dips as an additional variable. Cells in green indicate models that predicted long-axis, *x*, and short-axis, *z*, orientations that match the range of lineations and poles to foliation, respectively, that were measured in the field area. Cells in yellow indicate models that predict axes orientations that match some, but not all, measurements. Cells in red indicate models that predict axes orientations that do not match field measurements.

6.2.1. Best fit models

Model Parameters				Model Output				Plunge of average pole to foliation (~12°) within range of model pole plunges (Z)? (Y: Yes; N: No)
Shear obliquity (*ϕ*)	Extrusion obliquity (υ)	Kinematic vorticity (Wk)	Dip of the shear zone boundary in degrees (*best fit is achieved at finer increments)	Range of lineation plunges (X) in degrees		Range of foliation pole plunges (Z) in degrees		
				min.	max.	min.	max.	
-20	0	0.9	85	28	79	5	13	Y
-20	0	0.9	80	25	76	10	17	Y
-20	10	0.8	80	42	71	9	14	Y
-20	10	0.9	80	26	68	10	15	Y
-20	160	0.9	85	13	69	5	16	Y
-20	160	0.9	80	9	68	10	20	Y
-20	170	0.9	85	23	84	5	14	Y
-20	170	0.9	80	20	79	10	18	Y
-20	180	0.9	**85†**	28	79	5	13	Y
-20	180	0.9	80	25	76	10	17	Y
0	10	0.8	**75§**	39	70	10	15	Y
0	10	0.9	75	2	67	10	15	Y
0	170	0.9	78*	17	69	11	13	Y
0	170	0.9	77*	17	69	12	14	Y
20	0	0.9	75	41	72	3	15	Y
20	0	0.9	70	43	68	7	20	Y
20	10	0.9	75	36	75	2	15	Y
20	20	0.9	**90¶**	16	70	0	12	Y
20	170	0.9	77*	41	67	3	13	Y
20	170	0.9	75	42	66	5	15	Y
20	170	0.9	73*	42	65	6	17	Y
20	180	0.9	75	41	72	3	15	Y
20	180	0.9	70	43	68	7	20	Y

Table 6-2: The models that combine varying *ϕ, v, Wk*, and shear zone dip values and produces models that globally encompass the lineation and poles to foliation orientations measured across the entire study area (shown in green). Highlighted in yellow, a subset of these combinations that have been graphed on Flinn plots below to illustrate the nature of strain (Figs. 6-5, 6-6, & 6-7). "*" Indicates models where finer increments were necessary to achieve the best-fit models.

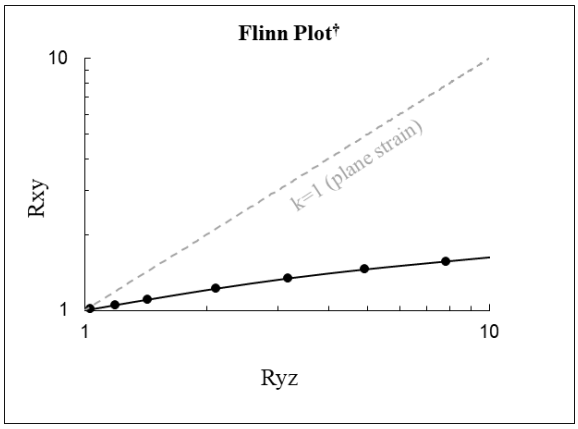

Figure 6-5: Flinn plot from Excel modeling software designed by Fernández & Diaz-Azpiroz (2009) with the following values: (*ϕ)*= -20°; *(v)*= 180°; *(Wk)*= 0.8; shear zone dip= 75°

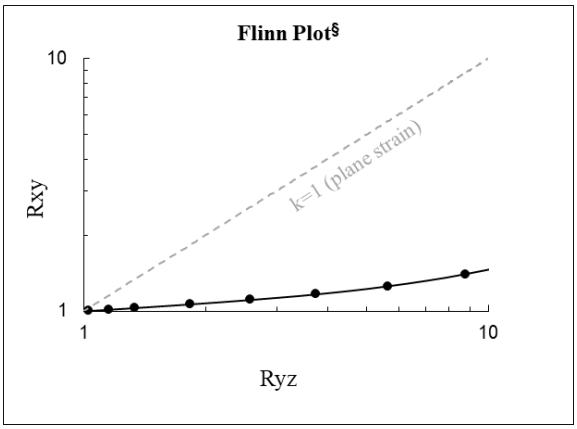

Figure 6-6: Flinn plot from Excel modeling software designed by Fernández & Diaz-Azpiroz (2009) with the following values: (*ϕ)*= 20°; *(v)*= 180°; *(Wk)*= 0.9; shear zone dip= 85°

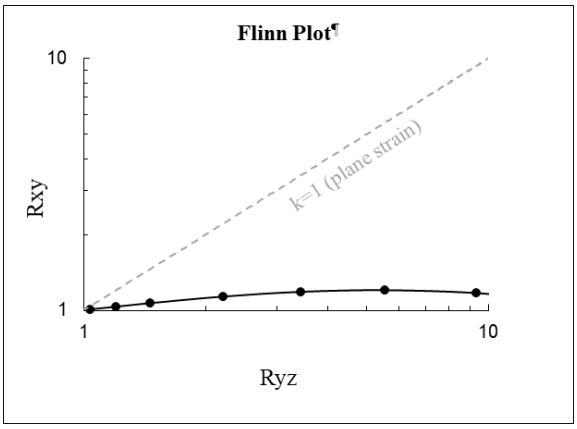

Figure 6-7: Flinn plot from Excel modeling software designed by Fernández & Diaz-Azpiroz (2009) with the following values: (*ϕ)*= 20°; *(v)*= 20°; *(Wk)*= 0.9; shear zone dip= 90°

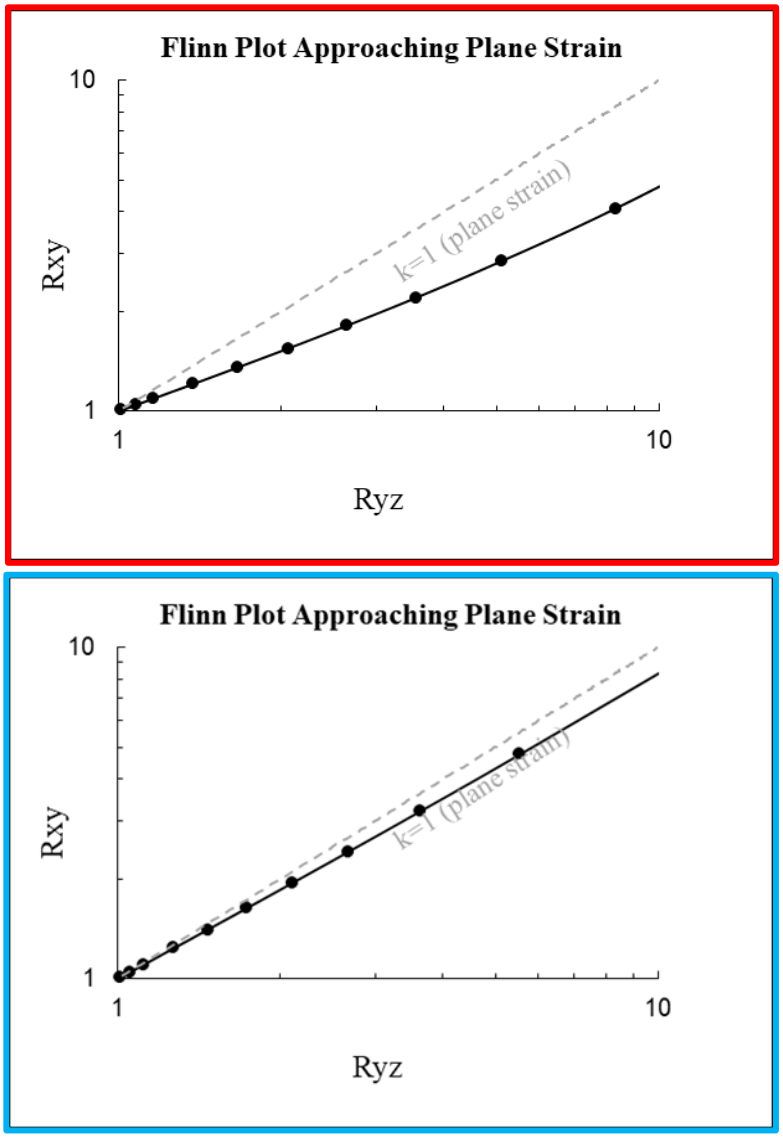

Figure 6-8: Flinn plot from Excel macros by Fernández & Diaz-Azpiroz (2009) with input values (bottom table that produce models that accommodate lineation model orientations in the BCQ at two sites, NG2116 (outlined in red) and NG2117 (outlined in blue), which are furthest from the zone of high shear. These models produce Flinn plots that show discrete plane-strain to sub-plane strain deformation, as opposed to the global models of the NGSZ which favor flattening & minor left lateral shear.

Site number	Latitude (deg.)	Longitude (deg.)	Lithology	Lineation Plunge (deg.)	Lineation Trend (azimuth deg.)
NG2116	44.19964	-103.51182	BCQ	55	350
NG2117	44.19987	-103.51201	BCQ	60	320
NG2117	44.19987	-103.51201	BCQ	60	320

Model Parameters			Model Output				Field data/model agreement? (M+: Best Fit; M: Maybe - at certain amounts of strain; N: No)
Shear obliquity (ϕ)	Extrusion obliquity (υ)	Kinematic vorticity (Wk)	Range of lineation plunges (X) in degrees.		Range of foliation pole plunges (Z) in degrees		
			min.	max.	min.	max.	
0	30	0.5	55	59	1	5	**M**
-20	150	0.2	60	60	1	5	**M**

6.3. Lozenge Aspect Ratios

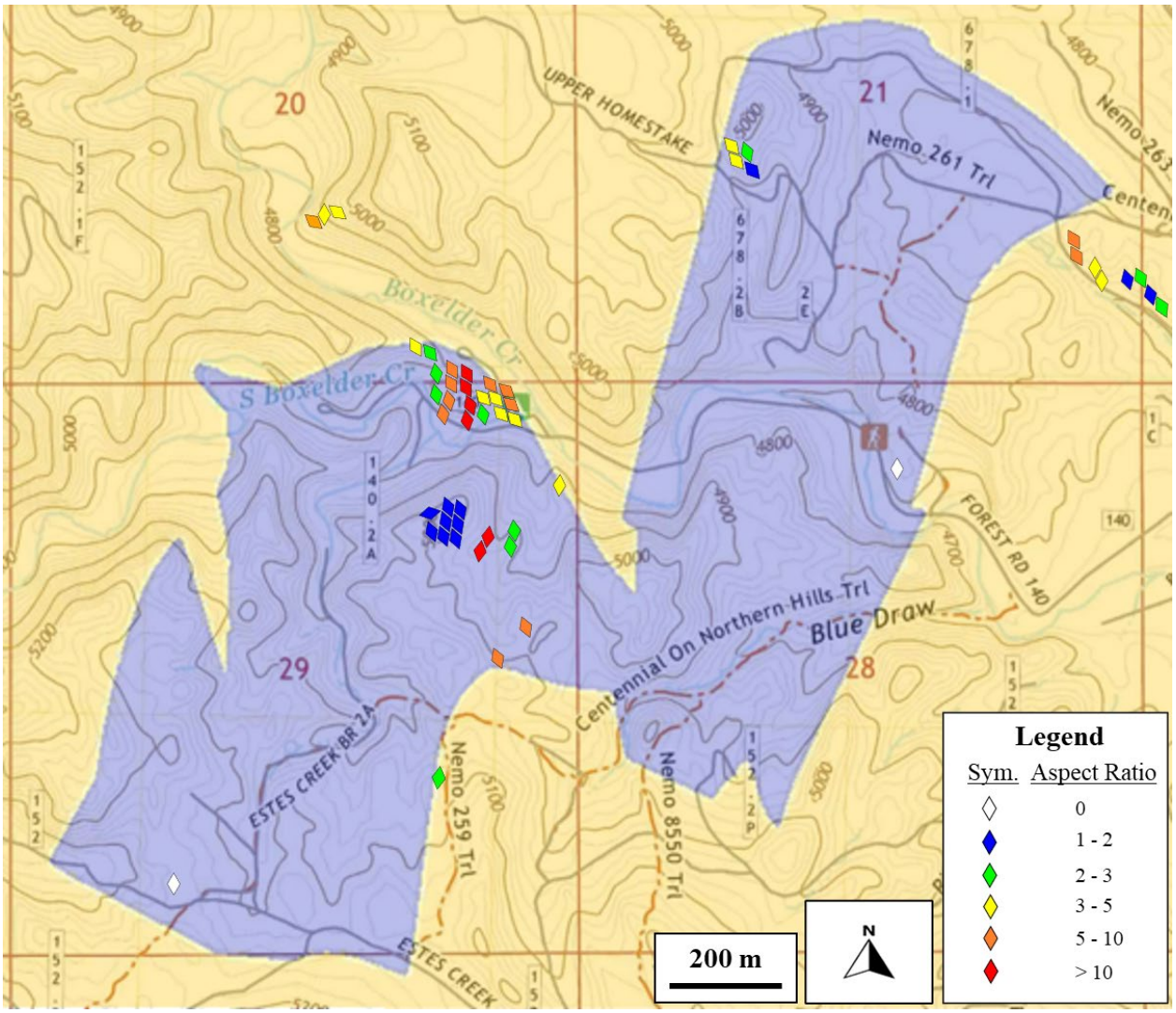

Figure 6-9: Map view (in the YZ-plane) of lozenge orientations and aspect ratios. Of note are the measurements located on Knob Hill, where vertical extrusion is overcome by flattening that crosses over into extrusion in both the XZ- and YZ-planes. The intermediate aspect ratios measured in the northeastern corner of the map, in the BCQ, may be a localized deformation related to the BDM/BCQ contact, where the more competent BDM caused higher strain in the quartzite at the presumed hinge of the metagabbro.

6.3. Lozenge Aspect Ratios (cont.)

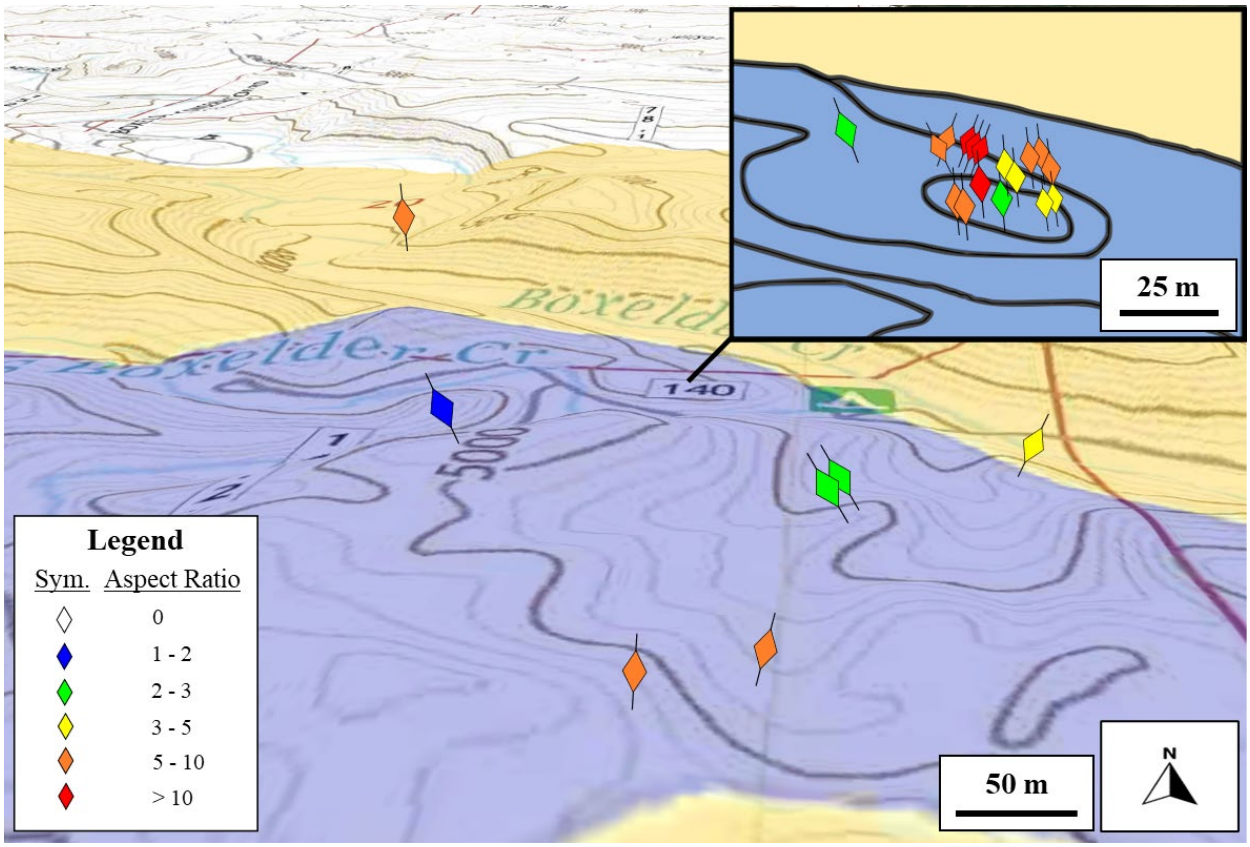

Figure 6-10: XZ-plane view of lozenge orientations and aspect ratios in the central region of the study area, nearest the proposed zone of high-shear.

6.3. Lozenge Aspect Ratios (cont.)

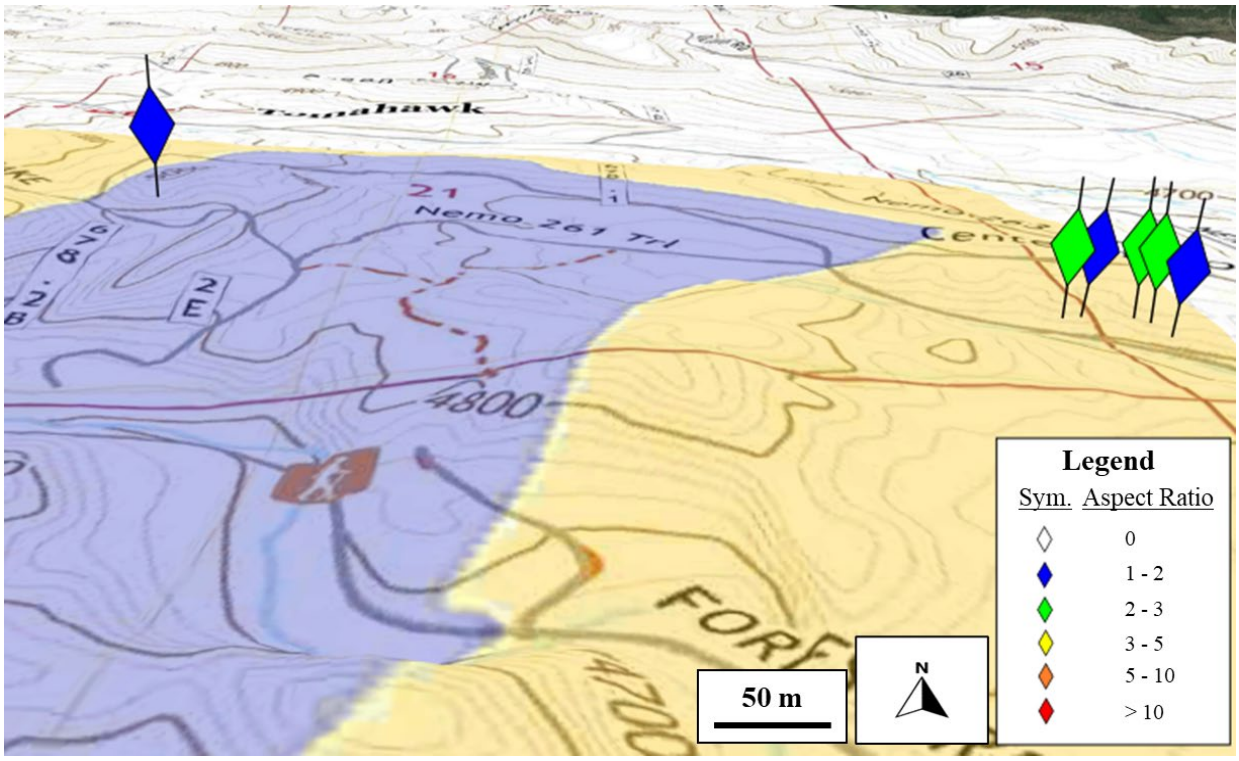

Figure 6-11: XZ-plane view of lozenge orientations and aspect ratios in the eastern region of the study area, furthest from the proposed zone of high-shear.

6.3.3 Flinn Plot

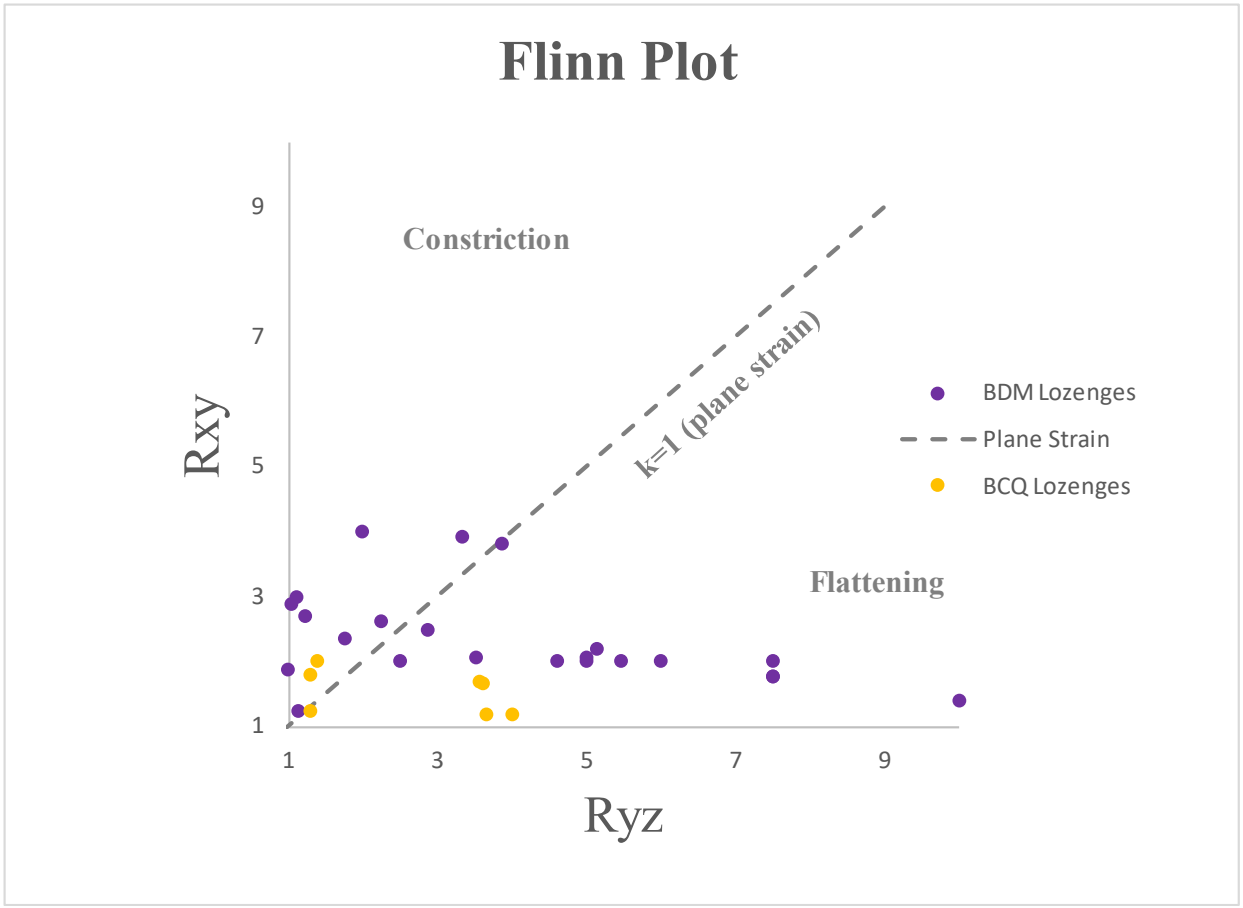

Figure 6-12: Flinn plot of lozenge shapes illustrating the variety of 3D strain shapes across both the BDM and the BCQ. Deformation in both quartzite and metagabbro ranges from nearly plane-strain to significant flattening, with much stronger flattening shapes preserved in the metagabbro. The outcrops that plot higher on the x-axis, showing more flattening, were measured on the eastern side of the proposed shear zone contact that bisects Knob Hill, within five to ten meters of where the highly weathered "punky green" chloritic alteration was observed (sites NG2148 – NG2153).

Ch 7: Conclusion

The data collected in this study combined with kinematic modeling supports the hypothesis that the NGSZ is a left-lateral transpression zone within the Black Hills that affects rocks of the Boxelder Creek quartzite (BCQ) and the Blue Draw metagabbro (BDM) near Nemo, SD. The zone strikes ~340 with steeply inclined boundaries, and affected rocks that were previously deformed in a series of folding events. The NGSZ accommodated both left-lateral simple shear and shortening accommodated by pure shear with steep to subvertical extrusion. The steep to subvertical foliations and generally steeply plunging lineations are consistent with most transpression models. Modeling results determined the fabrics most closely matched models with high kinematic vorticity numbers (0.8-0.9), suggesting that deformation was simple shear dominated. Lineation orientations vary significantly throughout the NGSZ, which is likely due to variations in strain magnitude and small changes in the pure shear related extrusion direction. Modeling results determined that extrusion likely deviated up to 20° from vertical in either NW or SE directions.

Shear zone bounded lozenges were present in both BCQ and BDM lithologies. Lozenge geometries were used as a proxy for strain ellipsoid shapes, both within the zone of high strain and along the limbs of the metagabbro z-structure, in addition to the general strain within the BCQ. Strain in the quartzite was relatively homogeneous regardless of outcrop proximity to the zone of highest strain, whereas the metagabbros have heterogeneous strain that varies on the meter scale, particularly where the BDM outcrops are located near a fold hinge from an earlier deformation event.

Strain ellipsoid shapes estimated from lozenge geometries indicating that strain was largely plane strain to flattening, in some cases rather extreme flattening in the metagabbros. (up to 10:1 X:Z ratios). Areas dominated by flattening (in the BDM) are located in the zone of high strain, with close proximity to both measured mylonitic fabrics as well as discrete zones of low strain. In the BCQ, approximate plane strain and minor to moderate flattening (up to 4:1 X:Z ratios) is dominant, regardless of proximity to the zone of high strain, suggesting that the less competent quartzite conforms to more homogeneous deformation compared to the metagabbro. This heterogeneity of deformation across lithologies may be related to the influence of D_1, D_2, and D_3 fabrics that predated or formed syn-deformationally in the NGSZ or may be due to heterogeneity in kinematics or degree of strain within the NGSZ.

Microstructural evidence indicates that fluid was present in the rocks during NGSZ deformation, but also may have infiltrated post-deformation during Harney Peak intrusion. Further research is required to know whether this fluid may have caused significant volume change which, if present, would require amendments to the strain estimations and kinematic modeling.

The transpressional nature of the NGSZ is consistent with oblique collision related to the formation of the Black Hills. The overprint of the NGSZ fabrics on prior folds suggests that deformation style related to the collision evolved over time.

References:

Allard, S.T., & Portis, D.H., 2013. Paleoproterozoic transpressional shear zone, eastern Black Hills, South Dakota: Implications for the late tectonic history of the southern Trans-Hudson Orogen. Rocky Mountain Geology, 48(2), p. 73-99.

Allmendinger, R.W., Cardozo, N.C., and Fisher, D., 2013. Structural Geology Algorithms: Vectors & Tensors: Cambridge, England, Cambridge University Press, 289 pp.

Bedrosian, P.A. and Finn, C.A., 2021. When Wyoming Became Superior: Oblique Convergence Along the Southern Trans-Hudson Orogen. Geophysical Research Letters, 48(13), p. e2021GL092970.

Bickford, M.E., Collerson, K.D., Lewry, J.F., Van Schmus, W.R. and Chiarenzelli, J.R., 1990. Proterozoic collisional tectonism in the Trans-Hudson orogen, Saskatchewan. Geology, 18(1), p. 14-18.

Blenkinsop, T.G., 2012. Visualizing structural geology: From Excel to Google Earth. Computers & Geosciences 45, p. 52–56.

Bush, J.G., 1982. Geology of the northeast part of the Nemo Quadrangle, Black Hills, South Dakota (Doctoral dissertation, South Dakota School of Mines and Technology, Rapid City).

Cardozo, N., and Allmendinger, R.W., 2013. Spherical projections with OSXStereonet: Computers & Geosciences, v. 51, no. 0, p. 193 - 205, doi: 10.1016/j.cageo.2012.07.021

Carreras, J., Druguet, E. and Griera, A., 2005. Shear zone-related folds. Journal of Structural Geology, 27(7), p. 1229-1251.

Carreras, J., Czeck, D.M., Druguet, E. and Hudleston, P.J., 2010. Structure and development of an anastomosing network of ductile shear zones. Journal of Structural Geology, 32(5), p. 656-666.

Chamberlain, K.R., Bauer, R.L., Frost, B.R. and Frost, C.D., 2002. Dakotan Orogen: Continuation of Trans-Hudson Orogen or younger, separate suturing of Wyoming and Superior cratons. In Geological Association of Canada–Mineralogical Association of Canada, Abstracts, 27, p. 18.

Chamberlain, K.R., Frost, C.D. and Frost, B.R., 2003. Early Archean to Mesoproterozoic evolution of the Wyoming Province: Archean origins to modern lithospheric architecture. Canadian Journal of Earth Sciences, 40(10), p. 1357-1374.

Ciborowski, T.J.R., Kerr, A.C., McDonald, I., Ernst, R.E. and Minifie, M.J., 2013. The geochemistry and petrogenesis of the Blue Draw Metagabbro. Lithos, 174, p. 271-290.

Ciborowski, T.J.R., Kerr, A.C., Ernst, R.E., McDonald, I., Minifie, M.J., Harlan, S.S. and Millar, I.L., 2015. The early proterozoic Matachewan large Igneous Province: Geochemistry, petrogenesis, and implications for earth evolution. Journal of Petrology, 56(8), p. 1459-1494.

Corrigan, D., Pehrsson, S., Wodicka, N. and De Kemp, E., 2009. The Paleoproterozoic Trans-Hudson Orogen: a prototype of modern accretionary processes. Geological Society, London, Special Publications, 327(1), p. 457-479.

Czeck, D.M. and Hudleston, P.J., 2003. Testing models for obliquely plunging lineations in transpression: a natural example and theoretical discussion. Journal of Structural Geology, 25(6), p. 959-982.

Dahl, P.S., Hamilton, M.A., Wooden, J.L., Foland, K.A., Frei, R., McCombs, J.A. and Holm, D.K., 2006. 2480 Ma mafic magmatism in the northern Black Hills, South Dakota: a new link connecting the Wyoming and Superior cratons. Canadian Journal of Earth Sciences, 43(10), pp.1579-1600.

Dahl, P.S., Holm, D.K., Gardner, E.T., Hubacher, F.A. and Foland, K.A., 1999. New constraints on the timing of Early Proterozoic tectonism in the Black Hills (South Dakota), with implications for docking of the Wyoming province with Laurentia. Geological Society of America Bulletin, 111(9), p. 1335-1349.

Díaz-Azpiroz, M., Barcos, L., Balanyá, J.C., Fernández, C., Expósito, I. and Czeck, D.M., 2014. Applying a general triclinic transpression model to highly partitioned brittle-ductile shear zones: A case study from the Torcal de Antequera massif, external Betics, southern Spain. Journal of Structural Geology, 68, p. 316-336.

Díaz-Azpiroz, M., Fernández, C. and Czeck, D.M., 2019. Are we studying deformed rocks in the right sections? Best practices in the kinematic analysis of 3D deformation zones. Journal of Structural Geology, 125, p. 218-225.

Druguet, E., Passchier, C.W., Carreras, J., Victor, P. and Den Brok, S., 1997. Analysis of a complex high-strain zone at Cap de Creus, Spain. Tectonophysics, 280(1-2), p. 31-45.

Dyar, M.D., Gunter, M.E. and Tasa, D., 2008. Mineralogy and optical mineralogy. Mineralogical Society of America. P. 708.

Ernst, R. and Bleeker, W., 2010. Large igneous provinces (LIPs), giant dyke swarms, and mantle plumes: significance for breakup events within Canada and adjacent regions from 2.5 Ga to the Present. Canadian Journal of Earth Sciences, 47(5), p. 695-739.

Fernández, C., Díaz Azpiroz, M., 2009. Triclinic transpression zones with oblique extrusion. Journal of Structural Geology, 31, 1255-1269

Fernández, C., Díaz Azpiroz, M., 2009. Supplemental Microsoft Excel software *based on* Triclinic transpression zones with oblique extrusion. Journal of Structural Geology, 31, 1255-1269

Fernández, C., Czeck, D.M. and Diaz-Azpiroz, M., 2013. Testing the model of oblique transpression with oblique extrusion in two natural cases: steps and consequences. Journal of Structural Geology, 54, p. 85-102.

Gapais, D., Bale, P., Choukroune, P., Cobbold, P., Mahjoub, Y. and Marquer, D., 1987. Bulk kinematics from shear zone patterns: some field examples. Journal of Structural Geology, 9(5-6), p. 635-646.

Goodwin, L.B. and Tikoff, B., 2002. Competency contrast, kinematics, and the development of foliations and lineations in the crust. Journal of structural Geology, 24(6-7), p. 1065-1085.

Gosselin, D.C., Papike, J.J., Zartman, R.E., Peterman, Z.E. and Laul, J.C., 1988. Archean rocks of the Black Hills, South Dakota: Reworked basement from the southern extension of the Trans-Hudson orogen. Geological Society of America Bulletin, 100(8), p. 1244-1259.

Hark, J.S., 2009. Zircon, monazite, and xenotime as provenance indicators in selected Precambrian crystalline rocks, Black Hills uplift, South Dakota (Doctoral dissertation, Kent State University).

Hark, J.S., Dahl, P.S., Frei, R., Ghosh, A.K., Whitehouse, M.J., Wooden, J. And Redden, J.A., 2010. U-Pb ages of zircon, monazite, and xenotime in the Harney Peak Granite, Black Hills, SD: Implications for the timing and duration of syn-to post-orogenic magmatism. In Geological Society of America Abstracts with Programs 42(3), p. 47.

Horsman, E., Tikoff, B. and Czeck, D., 2008. Rheological implications of heterogeneous deformation at multiple scales in the Late Cretaceous Sierra Nevada, California. Geological Society of America Bulletin, 120(1-2), p. 238-255.

Huntington, K.W., & Klepeis, K.A., 2018. Challenges and opportunities for research in tectonics: Understanding deformation and the processes that link Earth systems, from geologic time to human time. A community vision document submitted to the US National Science Foundation.

Lee, K.H., 1996. Structure and geochemistry of the Nemo area Black Hills, South Dakota, United States of America. Doctoral Dissertation, The University of Nebraska-Lincoln.

Mitra, G., 1979. Ductile deformation zones in Blue Ridge basement rocks and estimation of finite strains. Geological Society of America Bulletin, 90(10), p. 935-951.

Nabavi, S.T., Alavi, S.A., Díaz-Azpiroz, M., Mohammadi, S., Ghassemi, M.R., Fernández, C., Barcos, L. and Frehner, M., 2020. Deformation mechanics in inclined, brittle-ductile transpression zones: Insights from 3D finite element modelling. Journal of Structural Geology, 137, p. 104082.

Ponce, C., Druguet, E. and Carreras, J., 2013. Development of shear zone-related lozenges in foliated rocks. Journal of Structural Geology, 50, p.176-186.

Redden, J.A., Peterman, Z.E., Zartman, R.E., DeWitt, E., Lewry, J.F. and Stauffer, M.R., 1990. U-Th-Pb geochronology and preliminary interpretation of Precambrian tectonic events in the Black Hills, South Dakota. The Early Proterozoic Trans-Hudson Orogen of North America: Geological Association of Canada Special Paper, 37, p. 229-251.

Redden, J.A. and DeWitt, E., 2008. Maps showing geology, structure, and geophysics of the central Black Hills, South Dakota: US Geological Survey Scientific Investigations Map 2777, p. 44

Robin, P.Y.F. and Cruden, A.R., 1994. Strain and vorticity patterns in ideally ductile transpression zones. Journal of Structural Geology, 16(4), p. 447-466.

Runner, J.J., 1934. Pre-Cambrian geology of the Nemo District. Black Hills, South Dakota. American Journal of Science, 5(167), p. 353-372.

Sims, P. K., & Peterman, Z. E., 1986. Early Proterozoic Central Plains orogen: A major buried structure in the north-central United States. Geology, 14(6), p. 488-491.

Sims, P.K., Peterman, Z.E., Hildenbrand, T.G. and Mahan, S.A., 1991. Precambrian basement map of the Trans-Hudson orogen and adjacent terranes, northern Great Plains, USA. U.S. Department of the Interior, U.S. Geological Survey Report no. 2214.

St-Onge, M.R., Searle, M.P. and Wodicka, N., 2006. Trans-Hudson Orogen of North America and Himalaya-Karakoram-Tibetan Orogen of Asia: Structural and thermal characteristics of the lower and upper plates. Tectonics, 25(4).

Sullivan, W.A. and Law, R.D., 2007. Deformation path partitioning within the transpressional White Mountain shear zone, California and Nevada. Journal of Structural Geology, 29(4), pp.583-599.

Tikoff, B. and Fossen, H., 1993. Simultaneous pure and simple shear: the unifying deformation matrix. Tectonophysics, 217(3-4), p. 267-283.

Tikoff, B. and Greene, D., 1997. Stretching lineations in transpressional shear zones: an example from the Sierra Nevada Batholith, California. Journal of structural geology, 19(1), p. 29-39.

Van Boening, A.M., 2007. Petrogenesis And tectonic implications of mafic rocks in the Precambrian core of the Black Hills, South Dakota (Masters Thesis, University of Missouri – Columbia).

Van Boening, A.M., & Nabelek, P.I., 2008. Petrogenesis and tectonic implications of Paleoproterozoic mafic rocks in the Black Hills, South Dakota. Precambrian Research, 167(3-4), p. 363-376.

Weller, O., St-Onge, M. 2017. Record of modern-style plate tectonics in the Palaeoproterozoic Trans-Hudson orogen. Nature Geosci, 10, pp. 305–311

Whitmeyer, S.J. and Karlstrom, K.E., 2007. Tectonic model for the Proterozoic growth of North America. Geosphere, 3(4), p. 220-259.

APPENDICES

A.1. Orientations

A.1.1. Blue Draw Metagabbro Foliation

Site number	Latitude (deg.)	Longitude (deg.)	Lithology	Foliation Strike RHR (azimuth deg.)	Foliation Dip (deg.)	Dip Direction
NG21-01	44.1975	-103.53721	metagabbro	182	89	W
NG21-01	44.1975	-103.53721	metagabbro	2	84	E
NG21-02	44.19781	-103.53709	metagabbro	176	76	W
NG21-03	44.19788	-103.53712	metagabbro	342	86	E
NG21-04	44.1978	-103.53711	metagabbro	174	89	W
NG21-04	44.1978	-103.53711	metagabbro	6	72	E
NG21-04	44.1978	-103.53711	metagabbro	4	68	E
NG21-04	44.1978	-103.53711	metagabbro	165	88	W
NG21-04	44.1978	-103.53711	metagabbro	3	84	E
NG21-04	44.1978	-103.53711	metagabbro	352	70	E
NG21-05	44.19776	-103.53726	metagabbro	174	75	W
NG21-06	44.19786	-103.53725	metagabbro	110	78	W
NG21-06	44.19786	-103.53725	metagabbro	146	89	W
NG21-07	44.19789	-103.53745	metagabbro	163	85	W
NG21-08	44.198	-103.53749	metagabbro	345	58	E
NG21-08	44.198	-103.53749	metagabbro	170	89	W
NG21-09	44.19804	-103.53751	metagabbro	305	70	E
NG21-09	44.19804	-103.53751	metagabbro	163	68	W
NG21-11	44.19799	-103.53749	metagabbro	0	80	E
NG21-11	44.19799	-103.53749	metagabbro	138	82	W
NG21-24	44.19266	-103.5353	metagabbro	335	75	E
NG21-24	44.19266	-103.5353	metagabbro	330	60	E

Table A1: BDM foliation data

Site number	Latitude (deg.)	Longitude (deg.)	Lithology	Foliation Strike RHR (azimuth deg.)	Foliation Dip (deg.)	Dip Direction
NG21-24	44.19266	-103.5353	metagabbro	328	70	E
NG21-24	44.19266	-103.5353	metagabbro	328	70	E
NG21-24	44.19266	-103.5353	metagabbro	3	70	E
NG21-24	44.19266	-103.5353	metagabbro	1	75	E
NG21-24	44.19266	-103.5353	metagabbro	320	80	E
NG21-25	44.19187	-103.53449	metagabbro	340	89	E
NG21-26	44.20439	-103.52659	metagabbro	105	79	S
NG21-26	44.20439	-103.52659	metagabbro	102	82	S
NG21-26	44.20439	-103.52659	metagabbro	98	81	S
NG21-26	44.20439	-103.52659	metagabbro	330	80	E
NG21-28	44.20406	-103.52512	metagabbro	150	50	W
NG21-28	44.20406	-103.52512	metagabbro	297	56	E
NG21-33	44.19113	-103.53535	metagabbro	320	85	E
NG21-33	44.19113	-103.53535	metagabbro	120	85	W
NG21-33	44.19113	-103.53535	metagabbro	145	85	W
NG21-33	44.19113	-103.53535	metagabbro	302	85	E
NG21-33	44.19113	-103.53535	metagabbro	155	60	W
NG21-33	44.19113	-103.53535	metagabbro	350	75	E
NG21-35	44.19354	-103.53629	metagabbro	334	89	E
NG21-35	44.19354	-103.53629	metagabbro	328	88	E
NG21-36	44.19373	-103.53643	metagabbro	320	85	E
NG21-36	44.19373	-103.53643	metagabbro	335	86	E
NG21-37	44.19472	-103.53818	metagabbro	325	65	E
NG21-37	44.19472	-103.53818	metagabbro	270	55	E
NG21-38	44.19506	-103.53751	metagabbro	185	87	W
NG21-38	44.19506	-103.53751	metagabbro	302	66	E
NG21-38	44.19506	-103.53751	metagabbro	224	85	W
NG21-38	44.19506	-103.53751	metagabbro	310	65	E
NG21-38	44.19506	-103.53751	metagabbro	152	56	W
NG21-38	44.19506	-103.53751	metagabbro	4	32	E
NG21-40	44.19412	-103.53588	metagabbro	6	89	E
NG21-40	44.19412	-103.53588	metagabbro	0	80	E
NG21-40	44.19412	-103.53588	metagabbro	1	85	E
NG21-40	44.19412	-103.53588	metagabbro	178	84	W
NG21-40	44.19412	-103.53588	metagabbro	359	90	
NG21-41	44.19407	-103.53562	metagabbro	338	90	

Table A1 (cont.): BDM foliation data

Site number	Latitude (deg.)	Longitude (deg.)	Lithology	Foliation Strike RHR (azimuth deg.)	Foliation Dip (deg.)	Dip Direction
NG21-41	44.19407	-103.53562	metagabbro	354	90	
NG21-41	44.19407	-103.53562	metagabbro	340	90	
NG21-42	44.19441	-103.535268	metagabbro	197	85	W
NG21-42	44.19441	-103.535268	metagabbro	320	90	
NG21-43	44.19465	-103.53497	metagabbro	195	80	W
NG21-43	44.19465	-103.53497	metagabbro	200	82	W
NG21-43	44.19465	-103.53497	metagabbro	200	79	W
NG21-45	44.19548	-103.53383	metagabbro	349	65	E
NG21-46	44.19377	-103.53615	metagabbro	330	83	E
NG21-47	44.19785	-103.53697	metagabbro	146	83	W
NG21-47	44.19785	-103.53697	metagabbro	316	89	E
NG21-47	44.19785	-103.53697	metagabbro	280	87	E
NG21-48	44.1977	-103.53688	metagabbro	315	89	E
NG21-48	44.1977	-103.53688	metagabbro	277	78	E
NG21-48	44.1977	-103.53688	metagabbro	109	80	W
NG21-48	44.1977	-103.53688	metagabbro	155	55	W
NG21-49	44.19781	-103.53672	metagabbro	144	82	W
NG21-49	44.19781	-103.53672	metagabbro	310	84	E
NG21-50	44.19779	-103.53686	metagabbro	125	80	W
NG21-50	44.19779	-103.53686	metagabbro	162	42	W
NG21-52	44.19773	-103.53665	metagabbro	122	75	W
NG21-52	44.19773	-103.53665	metagabbro	159	78	W
NG21-53	44.19765	-103.53651	metagabbro	118	78	W
NG21-53	44.19765	-103.53651	metagabbro	125	76	W
NG21-55	44.19759	-103.53656	metagabbro	300	89	E
NG21-55	44.19759	-103.53656	metagabbro	149	85	W
NG21-55	44.19759	-103.53656	metagabbro	145	83	W
NG21-55	44.19759	-103.53656	metagabbro	165	89	W
NG21-56	44.19747	-103.53649	metagabbro	178	46	W
NG21-56	44.19747	-103.53649	metagabbro	305	88	E
NG21-56	44.19747	-103.53649	metagabbro	305	90	E
NG21R07	44.19285	-103.52275	metagabbro	152	73	W
NG21R07	44.19285	-103.52275	metagabbro	135	75	W
NG21R07	44.19285	-103.52275	metagabbro	166	84	W
NG21R07	44.19285	-103.52275	metagabbro	187	73	W
NG21R15	44.25187	-103.51264	metagabbro	352	70	E
NG21R15	44.25187	-103.51264	metagabbro	313	87	E

Table A1 (cont.): BDM foliation data

Site number	Latitude (deg.)	Longitude (deg.)	Lithology	Foliation Strike RHR (azimuth deg.)	Foliation Dip (deg.)	Dip Direction
NG22R16	44.24792	-103.5069	metagabbro	25	63	E
NG22R16	44.24792	-103.5069	metagabbro	177	83	W
NG21R16	44.15415	-103.5209	metagabbro	88	84	E
NG21R15	44.25187	-103.51264	metagabbro	352	70	E
NG21R15	44.25187	-103.51264	metagabbro	313	87	E
NG22R16	44.24792	-103.5069	metagabbro	177	83	W

Table A1 (cont.): BDM foliation data

A.1.2. Boxelder Creek Quartzite Foliations (w/ phyllite in grey)

Site number	Latitude (deg.)	Longitude (deg.)	Lithology	Foliation Strike RHR (azimuth deg.)	Foliation Dip (deg.)	Dip Direction
NG21-12	44.19747	-103.53436	quartzite	354	76	E
NG21-12	44.19747	-103.53436	quartzite	32	82	E
NG21-13	44.19725	-103.53377	quartzite	356	64	E
NG21-14	44.19758	-103.53393	quartzite	345	78	E
NG21-15	44.19759	-103.53309	quartzite	170	82	W
NG21-15	44.19759	-103.53309	quartzite	175	85	W
NG21-16	44.19964	-103.51182	quartzite	165	82	W
NG21-16	44.19964	-103.51182	quartzite	160	82	W
NG21-16	44.19964	-103.51182	quartzite	178	71	W
NG21-16	44.19964	-103.51182	quartzite	153	65	W
NG21-17	44.19987	-103.51201	quartzite	140	86	W
NG21-17	44.19987	-103.51201	quartzite	149	85	W
NG21-17	44.19987	-103.51201	quartzite	151	85	W
NG21-17	44.19987	-103.51201	quartzite	160	84	W
NG21-18	44.20143	-103.51516	quartzite	135	65	W
NG21-18	44.20143	-103.51516	quartzite	140	80	W
NG21-19	44.20138	-103.51487	quartzite	173	85	W
NG21-19	44.20138	-103.51487	quartzite	140	63	W
NG21-19	44.20138	-103.51487	quartzite	150	80	W
NG21-19	44.20138	-103.51487	quartzite	185	86	W
NG21-20	44.18924	-103.51587	quartzite	196	78	W

Table A2: BCQ foliation data

Site number	Latitude (deg.)	Longitude (deg.)	Lithology	Foliation Strike RHR (azimuth deg.)	Foliation Dip (deg.)	Dip Direction
NG21-20	44.18924	-103.51587	quartzite	175	77	W
NG21-20	44.18924	-103.51587	quartzite	179	74	W
NG21-20	44.18924	-103.51587	quartzite	170	72	W
NG21-20	44.18924	-103.51587	quartzite	175	70	W
NG21-20	44.18924	-103.51587	quartzite	176	75	W
NG21-22	44.18742	-103.53799	quartzite	175	87	W
NG21-22	44.18742	-103.53799	quartzite	150	85	W
NG21-22	44.18742	-103.53799	quartzite	350	82	E
NG21-23	44.18917	-103.53809	quartzite	160	83	W
NG21-29	44.20257	-103.54258	quartzite	338	86	E
NG21-29	44.20257	-103.54258	quartzite	330	85	E
NG21-29	44.20257	-103.54258	quartzite	331	86	E
NG21-29	44.20257	-103.54258	quartzite	151	88	W
NG21-29	44.20257	-103.54258	quartzite	155	80	W
NG21-29	44.20257	-103.54258	quartzite	130	70	W
NG21-29	44.20257	-103.54258	quartzite	153	85	W
NG21-29	44.20257	-103.54258	quartzite	160	78	W
NG21-29	44.20257	-103.54258	quartzite	150	70	W
NG21-29	44.20257	-103.54258	quartzite	334	82	E
NG21-30	44.20286	-103.54227	quartzite	160	73	W
NG21-30	44.20286	-103.54227	quartzite	330	73	E
NG21-31	44.203	-103.54167	quartzite	109	83	W
NG21-31	44.203	-103.54167	quartzite	330	79	E
NG21-32	44.20309	-103.54148	phyllite	140	87	W
NG21-32	44.20309	-103.54148	phyllite	153	80	W
NG21-32	44.20309	-103.54148	phyllite	149	80	W
NG21-45	44.19548	-103.53383	quartzite	354	75	E
NG21R01	44.19466	-103.51847	quartzite	208	58	W
NG21R03	44.19989	-103.51201	quartzite	173	84	W
NG21R03	44.19989	-103.51201	quartzite	94	83	E
NG21R04	44.20976	-103.54288	quartzite	183	85	W
NG21R05	44.2111	-103.54401	quartzite	118	86	W
NG21R09	44.17338	-103.52129	quartzite	326	84	W
NG21R10	44.17186	-103.51523	quartzite	209	85	W
NG21R12	44.199219	-103.502819	quartzite	148	65	W
NG21R12	44.199219	-103.502819	quartzite	144	63	W

Table A2 (cont.): BCQ foliation data with interstitial phyllite layer (site # NG2132) in grey.

Site number	Latitude (deg.)	Longitude (deg.)	Lithology	Foliation Strike RHR (azimuth deg.)	Foliation Dip (deg.)	Dip Direction
NG21R13	44.24634	-103.51915	quartzite	137	66	W
NG21R14	44.24365	-103.52119	quartzite	134	74	W
NG21R18	44.13797	-103.56593	phyllite	320	63	E
NG21R18	44.13797	-103.56593	phyllite	124	10	W

Table A2 (cont.): BCQ foliation data. The phyllite layer measurements (in grey) is reported but falls outside of the study area.

A.1.3. Blue Draw Metagabbro Lineations

Site number	Latitude (deg.)	Longitude (deg.)	Lithology	Lineation Plunge (deg.)	Lineation Trend (azimuth deg.)
NG21-01	44.1975	-103.53721	metagabbro	64	2
NG21-03	44.19788	-103.53712	metagabbro	85	342
NG21-04	44.1978	-103.53711	metagabbro	63	174
NG21-04	44.1978	-103.53711	metagabbro	65	174
NG21-05	44.19776	-103.53726	metagabbro	68	354
NG21-24	44.19266	-103.5353	metagabbro	85	150
NG21-40	44.19412	-103.53588	metagabbro	70	180
NG21-40	44.19412	-103.53588	metagabbro	65	180
NG21-45	44.19548	-103.53383	metagabbro	85	350
NG21-46	44.19377	-103.53615	metagabbro	50	330
NG21-47	44.19785	-103.53697	metagabbro	85	320
NG21-50	44.19779	-103.53686	metagabbro	21	75
NG21-51	44.19777	-103.53672	metagabbro	57	135
NG21R07	44.19285	-103.52275	metagabbro	61	267
NG21R16	44.15415	-103.5209	metagabbro	80	249

Table A3: BDM lineation data

A.1.4 Boxelder Creek Lineations

Site number	Latitude (deg.)	Longitude (deg.)	Lithology	Lineation Plunge (deg.)	Lineation Trend (azimuth deg.)
NG21-13	44.19725	-103.53377	quartzite	30	356
NG21-14	44.19758	-103.53393	quartzite	45	345
NG21-16	44.19964	-103.51182	quartzite	55	350
NG21-17	44.19987	-103.51201	quartzite	60	320
NG21-17	44.19987	-103.51201	quartzite	60	320
NG21-20	44.18924	-103.51587	quartzite	60	350
NG21-23	44.18917	-103.53809	quartzite	85	340
NG21-29	44.20257	-103.54258	quartzite	68	345
NG21-31	44.203	-103.54167	quartzite	65	330
NG21-45	44.19548	-103.53383	quartzite	65	354
NG21R03	44.19989	-103.51201	quartzite	55	268
NG21R04	44.20976	-103.54288	quartzite	57	187
NG21R14	44.24365	-103.52119	quartzite	83	25

Table A4: BCQ lineation data

A.1.5 Shear zone modeling data

Model Parameters			Model Output				Field data/model agreement? (M+: Best Fit; M: Maybe - at certain amounts of strain; N: No)
Shear obliquity (ϕ)	Extrusion obliquity (υ)	Kinematic vorticity (Wk)	Range of lineation plunges (X) in degrees.		Range of foliation pole plunges (Z) in degrees		
			min.	max.	min.	max.	
-20	0	0.9	32	80	0	9	M+
-20	10	0.8	49	74	0	6	M+
-20	10	0.9	33	71	0	7	M+
-20	20	0.8	44	65	0	4	M+
-20	160	0.9	16	70	0	12	M+
-20	170	0.9	27	87	1	10	M+
-20	180	0.9	32	80	0	9	M+
0	10	0.8	48	77	0	2	M+
0	10	0.9	11	73	0	2	M+
0	170	0.9	11	73	0	2	M+
20	0	0.9	32	80	0	9	M+
20	10	0.9	27	87	0	10	M+
20	20	0.9	16	70	0	12	M+
20	170	0.8	49	74	0	6	M+
20	170	0.9	33	71	0	7	M+
20	180	0.9	32	80	0	9	M+
0	10	0.8	48	77	0	2	M+
0	160	0.8	39	65	1	4	M+
-20	20	0.999999	20	58	0	30	M+
20	150	0.999999	20	51	0	38	M+
20	160	0.999999	20	58	0	30	M+
20	170	0.999999	20	63	0	35	M+
-20	20	0.6	59	68	0	2	M
-20	20	0.7	53	66	0	3	M
-20	0	0.8	55	85	0	7	M
-20	0	0.999999	20	63	0	1	M
-20	10	0.7	61	76	0	5	M
-20	10	0.999999	20	63	0	13	M
-20	20	0.5	63	69	0	2	M
-20	20	0.9	32	62	0	6	M
-20	30	0	60	60	14	30	M
-20	30	0.1	60	60	0	1	M
-20	30	0.2	55	60	0	1	M
-20	30	0.3	58	60	0	1	M
-20	30	0.4	56	59	0	2	M
-20	30	0.5	54	59	0	2	M
-20	30	0.6	50	58	0	2	M

Table A5: Kinematic model outputs

Model Parameters			Model Output				Field data/model agreement? (M+: Best Fit; M: Maybe - at certain amounts of strain; N: No)
Shear obliquity (ϕ)	Extrusion obliquity (υ)	Kinematic vorticity (Wk)	Range of lineation plunges (X) in degrees.		Range of foliation pole plunges (Z) in degrees		
			min.	max.	min.	max.	
-20	30	0.7	45	57	0	2	M
-20	30	0.8	39	56	0	4	M
-20	30	0.9	30	54	0	6	M
-20	40	0	50	50	17	40	M
-20	40	0.1	50	50	0	1	M
-20	40	0.2	49	50	0	1	M
-20	40	0.3	48	50	0	1	M
-20	140	0	50	50	17	39	M
-20	140	0.1	50	50	1	3	M
-20	140	0.2	50	50	1	5	M
-20	140	0.3	49	50	1	7	M
-20	150	0	60	60	14	30	M
-20	150	0.1	60	60	0	2	M
-20	150	0.2	60	60	1	5	M
-20	150	0.3	59	60	1	7	M
-20	150	0.4	59	60	1	8	M
-20	150	0.5	58	59	1	10	M
-20	150	0.6	56	59	1	11	M
-20	150	0.7	51	58	1	12	M
-20	150	0.8	30	57	1	13	M
-20	150	0.9	2	53	1	14	M
-20	150	0.999999	2	20	0	1	M
-20	170	0.999999	20	54	0	1	M
-20	180	0.8	55	85	0	7	M
-20	180	0.999999	20	63	0	1	M
0	20	0.6	62	68	1	4	M
0	20	0.7	55	67	1	4	M
0	20	0.9	16	60	0	3	M
0	30	0	60	60	14	30	M
0	30	0.1	60	60	0	1	M
0	30	0.2	60	60	1	2	M
0	30	0.3	58	60	1	3	M
0	30	0.4	57	59	1	4	M
0	30	0.5	55	59	1	5	M
0	30	0.6	51	58	1	5	M
0	30	0.7	44	56	1	5	M
0	30	0.8	33	54	1	5	M

Table A5 (cont.): Kinematic model outputs

Model Parameters			Model Output				Field data/model agreement? (M+: Best Fit; M: Maybe - at certain amounts of strain; N: No)
Shear obliquity (ϕ)	Extrusion obliquity (υ)	Kinematic vorticity (Wk)	Range of lineation plunges (X) in degrees.		Range of foliation pole plunges (Z) in degrees		
			min.	max.	min.	max.	
0	30	0.9	17	51	1	5	M
0	40	0	50	50	17	40	M
0	40	0.1	50	50	0	1	M
0	40	0.2	49	50	1	3	M
0	40	0.3	48	50	1	4	M
0	140	0	50	50	17	40	M
0	140	0.1	50	50	0	1	M
0	140	0.2	49	50	1	3	M
0	140	0.3	48	50	1	4	M
0	150	0	60	60	14	30	M
0	150	0.1	60	60	0	1	M
0	150	0.2	59	60	1	2	M
0	150	0.3	58	60	1	3	M
0	150	0.4	57	59	1	4	M
0	150	0.5	55	59	1	5	M
0	150	0.6	51	58	1	5	M
0	150	0.7	44	56	1	5	M
0	150	0.8	33	54	1	5	M
0	150	0.9	17	51	1	5	M
0	160	0.6	62	68	1	4	M
0	160	0.7	55	67	1	4	M
0	160	0.9	16	60	0	3	M
20	0	0.8	55	85	0	7	M
20	0	0.999999	20	63	0	1	M
20	10	0.8	63	89	0	9	M
20	10	0.999999	20	54	0	1	M
20	30	0	60	60	14	30	M
20	30	0.1	60	60	0	2	M
20	30	0.2	60	60	1	5	M
20	30	0.3	59	60	1	7	M
20	30	0.4	59	60	1	8	M
20	30	0.5	58	59	1	10	M
20	30	0.6	56	59	1	11	M
20	30	0.7	51	58	1	12	M
20	30	0.8	30	57	1	13	M
20	30	0.9	2	53	1	14	M
20	40	0	50	50	17	40	M

Table A5 (cont.): Kinematic model outputs

Model Parameters			Model Output				Field data/model agreement? (M+: Best Fit; M: Maybe - at certain amounts of strain; N: No)
Shear obliquity (ϕ)	Extrusion obliquity (υ)	Kinematic vorticity (Wk)	Range of lineation plunges (X) in degrees.		Range of foliation pole plunges (Z) in degrees		
			min.	max.	min.	max.	
20	40	0.1	50	50	1	3	M
20	40	0.2	50	50	1	5	M
20	40	0.3	49	50	1	7	M
20	150	0	60	60	14	30	M
20	150	0.1	60	60	0	1	M
20	150	0.2	59	60	0	1	M
20	150	0.3	58	60	0	1	M
20	150	0.4	56	59	0	2	M
20	150	0.5	54	59	0	2	M
20	150	0.6	50	58	0	2	M
20	150	0.7	45	57	0	2	M
20	150	0.8	39	56	0	4	M
20	150	0.9	30	54	0	6	M
20	160	0.5	63	69	0	2	M
20	160	0.6	59	68	0	2	M
20	160	0.7	53	66	0	3	M
20	160	0.8	44	65	0	4	M
20	160	0.9	32	62	0	6	M
20	170	0.7	61	76	0	5	M
20	180	0.8	55	85	0	7	M
20	180	0.999999	20	63	0	1	M
-20	180	0	0*	90*	0	0	N
-20	20	0	70	70	9	20	N
-20	20	0.1	70	70	0	0	N
-20	20	0.2	69	70	0	1	N
-20	20	0.3	68	70	0	1	N
-20	20	0.4	66	69	0	1	N
-20	0	0	0	0	0	0	N
-20	0	0.1	89	89	0	1	N
-20	0	0.2	87	89	0	2	N
-20	0	0.3	87	90	0	3	N
-20	0	0.4	85	89	0	4	N
-20	0	0.5	83	89	0	5	N
-20	0	0.6	79	88	0	5	N
-20	0	0.7	71	87	0	6	N
-20	10	0	80	80	5	10	N
-20	10	0.1	80	80	0	1	N

Table A5 (cont.): Kinematic model outputs

Model Parameters			Model Output				Field data/model agreement? (M+: Best Fit; M: Maybe - at certain amounts of strain; N: No)
Shear obliquity (ϕ)	Extrusion obliquity (υ)	Kinematic vorticity (Wk)	Range of lineation plunges (X) in degrees.		Range of foliation pole plunges (Z) in degrees		
			min.	max.	min.	max.	
-20	10	0.2	79	80	0	1	N
-20	10	0.3	78	80	0	2	N
-20	10	0.4	76	79	0	2	N
-20	10	0.5	73	79	0	3	N
-20	10	0.6	69	78	0	4	N
-20	30	0.999999	20	51	0	38	N
-20	40	0.4	47	49	0	2	N
-20	40	0.5	45	49	0	2	N
-20	40	0.6	42	48	0	2	N
-20	40	0.7	38	47	0	2	N
-20	40	0.8	34	47	0	4	N
-20	40	0.9	27	45	1	6	N
-20	40	0.999999	20	44	0	46	N
-20	50	0	40	40	19	50	N
-20	50	0.1	40	40	0	0	N
-20	50	0.2	39	40	0	1	N
-20	50	0.3	39	40	0	1	N
-20	50	0.4	38	39	0	1	N
-20	50	0.5	36	39	0	2	N
-20	50	0.6	34	39	0	2	N
-20	50	0.7	32	38	0	3	N
-20	50	0.8	28	38	0	5	N
-20	50	0.9	24	37	0	7	N
-20	50	0.999999	20	36	0	55	N
-20	60	0	30	30	19	59	N
-20	60	0.1	30	30	0	1	N
-20	60	0.2	30	30	0	1	N
-20	60	0.3	29	30	0	2	N
-20	60	0.4	29	30	0	2	N
-20	60	0.5	28	30	0	3	N
-20	60	0.6	27	29	0	4	N
-20	60	0.7	25	29	0	5	N
-20	60	0.8	23	29	0	6	N
-20	60	0.9	21	29	0	8	N
-20	60	0.999999	20	28	0	65	N
-20	70	0	20	20	16	70	N
-20	70	0.1	20	20	0	1	N

Table A5 (cont.): Kinematic model outputs

Model Parameters			Model Output				Field data/model agreement? (M+: Best Fit; M: Maybe - at certain amounts of strain; N: No)
Shear obliquity (ϕ)	Extrusion obliquity (υ)	Kinematic vorticity (Wk)	Range of lineation plunges (X) in degrees.		Range of foliation pole plunges (Z) in degrees		
			min.	max.	min.	max.	
-20	70	0.2	20	20	0	2	N
-20	70	0.3	20	20	0	3	N
-20	70	0.4	20	20	0	4	N
-20	70	0.5	19	20	0	5	N
-20	70	0.6	19	20	0	6	N
-20	70	0.7	18	20	0	3	N
-20	70	0.8	18	20	0	9	N
-20	70	0.9	17	20	0	10	N
-20	70	0.999999	20	20	0	70	N
-20	80	0	10	10	10	77	N
-20	80	0.1	10	10	0	1	N
-20	80	0.2	10	10	0	3	N
-20	80	0.3	10	10	1	4	N
-20	80	0.4	10	11	1	6	N
-20	80	0.5	10	11	1	7	N
-20	80	0.6	11	12	1	9	N
-20	80	0.7	11	13	1	10	N
-20	80	0.8	11	14	1	11	N
-20	80	0.9	11	15	1	13	N
-20	80	0.999999	12	20	0	9	N
-20	90	0	0	0	0	0	N
-20	90	0.1	0	0	0	2	N
-20	90	0.2	0	0	1	4	N
-20	90	0.3	0	1	1	6	N
-20	90	0.4	1	2	1	8	N
-20	90	0.5	1	3	1	9	N
-20	90	0.6	1	4	2	11	N
-20	90	0.7	2	6	2	12	N
-20	90	0.8	2	8	1	14	N
-20	90	0.9	3	11	1	14	N
-20	90	0.999999	4	20	0	86	N
-20	100	0	10	10	10	77	N
-20	100	0.1	10	10	0	2	N
-20	100	0.2	9	10	1	5	N
-20	100	0.3	9	10	1	7	N
-20	100	0.4	8	9	2	9	N
-20	100	0.5	6	9	2	11	N

Table A5 (cont.): Kinematic model outputs

Model Parameters			Model Output				Field data/model agreement? (M+: Best Fit; M: Maybe - at certain amounts of strain; N: No)
Shear obliquity (ϕ)	Extrusion obliquity (υ)	Kinematic vorticity (Wk)	Range of lineation plunges (X) in degrees.		Range of foliation pole plunges (Z) in degrees		
			min.	max.	min.	max.	
-20	100	0.6	4	8	2	13	N
-20	100	0.7	1	7	2	14	N
-20	100	0.8	0	7	2	15	N
-20	100	0.9	1	8	1	16	N
-20	100	0.999999	1	19	0	4	N
-20	110	0	20	20	16	69	N
-20	110	0.1	20	20	1	3	N
-20	110	0.2	19	20	1	5	N
-20	110	0.3	18	20	2	8	N
-20	110	0.4	17	19	2	10	N
-20	110	0.5	15	19	2	12	N
-20	110	0.6	12	18	2	14	N
-20	110	0.7	8	17	2	15	N
-20	110	0.8	3	16	2	16	N
-20	110	0.9	1	14	1	17	N
-20	110	0.999999	1	20	0	78	N
-20	120	0	30	30	19	59	N
-20	120	0.1	30	30	1	3	N
-20	120	0.2	29	30	1	6	N
-20	120	0.3	28	30	2	8	N
-20	120	0.4	27	29	2	10	N
-20	120	0.5	25	29	2	12	N
-20	120	0.6	21	28	2	14	N
-20	120	0.7	16	26	2	15	N
-20	120	0.8	9	25	2	16	N
-20	120	0.9	0	22	1	17	N
-20	120	0.999999	1	20	0	57	N
-20	130	0	40	40	19	50	N
-20	130	0.1	40	40	1	3	N
-20	130	0.2	39	40	1	6	N
-20	130	0.3	39	40	2	8	N
-20	130	0.4	37	39	2	10	N
-20	130	0.5	35	39	2	12	N
-20	130	0.6	31	38	2	13	N
-20	130	0.7	25	36	2	15	N
-20	130	0.8	15	34	2	16	N
-20	130	0.9	0	31	1	16	N

Table A5 (cont.): Kinematic model outputs

Model Parameters			Model Output				Field data/model agreement? (M+: Best Fit; M: Maybe - at certain amounts of strain; N: No)
Shear obliquity (ϕ)	Extrusion obliquity (υ)	Kinematic vorticity (Wk)	Range of lineation plunges (X) in degrees.		Range of foliation pole plunges (Z) in degrees		
			min.	max.	min.	max.	
-20	130	0.999999	1	23	0	7	N
-20	140	0.4	48	49	2	9	N
-20	140	0.5	46	49	2	11	N
-20	140	0.6	43	48	2	12	N
-20	140	0.7	36	47	2	14	N
-20	140	0.8	21	45	1	14	N
-20	140	0.9	0	40	1	15	N
-20	140	0.999999	0	23	0	4	N
-20	160	0	70	70	10	20	N
-20	160	0.1	70	70	0	2	N
-20	160	0.2	70	70	1	4	N
-20	160	0.3	70	70	1	5	N
-20	160	0.4	70	70	1	7	N
-20	160	0.5	70	70	1	8	N
-20	160	0.6	70	70	1	9	N
-20	160	0.7	70	70	1	10	N
-20	160	0.8	70	70	1	11	N
-20	160	0.999999	20	20	0	4	N
-20	170	0	80	80	5	10	N
-20	170	0.1	80	80	0	1	N
-20	170	0.2	80	80	0	3	N
-20	170	0.3	80	81	0	4	N
-20	170	0.4	80	81	1	5	N
-20	170	0.5	81	82	1	6	N
-20	170	0.6	81	83	1	7	N
-20	170	0.7	81	86	0	8	N
-20	170	0.8	63	89	0	9	N
-20	180	0.1	89	90	0	1	N
-20	180	0.2	88	90	0	2	N
-20	180	0.3	87	90	0	3	N
-20	180	0.4	85	89	0	4	N
-20	180	0.5	83	89	0	5	N
-20	180	0.6	79	88	0	5	N
-20	180	0.7	71	87	0	6	N
0	0	0	0	0	0	0	N
0	0	0.1	0	0	0	0	N
0	0	0.2	0	0	0	0	N

Table A5 (cont.): Kinematic model outputs

Model Parameters			Model Output				Field data/model agreement? (M+: Best Fit; M: Maybe - at certain amounts of strain; N: No)
Shear obliquity (ϕ)	Extrusion obliquity (υ)	Kinematic vorticity (Wk)	Range of lineation plunges (X) in degrees.		Range of foliation pole plunges (Z) in degrees		
			min.	max.	min.	max.	
0	0	0.3	0	0	0	0	N
0	0	0.4	0	0	0	0	N
0	0	0.5	0	0	0	0	N
0	0	0.6	0	0	0	0	N
0	0	0.7	0	0	0	0	N
0	0	0.8	0	0	0	0	N
0	0	0.9	0	0	0	0	N
0	0	0.999999	0	0	0	0	N
0	10	0	80	80	0	0	N
0	10	0.1	80	80	0	0	N
0	10	0.2	80	80	0	1	N
0	10	0.3	79	80	0	1	N
0	10	0.4	79	80	0	2	N
0	10	0.5	78	79	0	2	N
0	10	0.6	75	79	0	2	N
0	10	0.7	70	78	0	2	N
0	10	0.999999	0	34	0	0	N
0	20	0	70	70	10	20	N
0	20	0.1	70	70	0	1	N
0	20	0.2	70	70	1	2	N
0	20	0.3	69	70	1	2	N
0	20	0.4	68	69	1	3	N
0	20	0.5	66	69	1	3	N
0	20	0.999999	0	43	0	0	N
0	30	0.999999	0	43	0	4	N
0	40	0.4	47	49	1	5	N
0	40	0.5	44	49	2	6	N
0	40	0.6	41	48	2	6	N
0	40	0.7	35	46	1	6	N
0	40	0.8	27	45	1	6	N
0	40	0.9	16	42	1	5	N
0	40	0.999999	0	38	0	47	N
0	50	0	40	40	19	49	N
0	50	0.1	40	40	0	1	N
0	50	0.2	39	40	1	3	N
0	50	0.3	38	40	1	4	N
0	50	0.4	37	39	2	5	N

Table A5 (cont.): Kinematic model outputs

Model Parameters			Model Output				Field data/model agreement? (M+: Best Fit; M: Maybe - at certain amounts of strain; N: No)
Shear obliquity (ϕ)	Extrusion obliquity (υ)	Kinematic vorticity (Wk)	Range of lineation plunges (X) in degrees.		Range of foliation pole plunges (Z) in degrees		
			min.	max.	min.	max.	
0	50	0.5	35	39	2	6	N
0	50	0.6	32	38	2	6	N
0	50	0.7	27	37	2	7	N
0	50	0.8	22	36	1	6	N
0	50	0.9	14	34	1	6	N
0	50	0.999999	0	31	0	58	N
0	60	0	30	30	19	60	N
0	60	0.1	30	30	0	1	N
0	60	0.2	29	30	1	2	N
0	60	0.3	29	30	1	4	N
0	60	0.4	27	29	1	4	N
0	60	0.5	26	29	2	5	N
0	60	0.6	23	28	2	6	N
0	60	0.7	20	27	2	6	N
0	60	0.8	16	27	2	6	N
0	60	0.9	11	25	1	5	N
0	60	0.999999	0	24	0	66	N
0	70	0	20	20	16	68	N
0	70	0.1	20	20	0	1	N
0	70	0.2	20	20	1	2	N
0	70	0.3	19	20	1	3	N
0	70	0.4	18	19	1	3	N
0	70	0.5	17	19	1	4	N
0	70	0.6	15	19	1	4	N
0	70	0.7	13	18	1	5	N
0	70	0.8	11	18	1	5	N
0	70	0.9	7	17	1	4	N
0	70	0.999999	0	16	0	74	N
0	80	0	10	10	10	77	N
0	80	0.1	10	10	0	0	N
0	80	0.2	10	10	0	1	N
0	80	0.3	9	10	0	1	N
0	80	0.4	9	10	1	2	N
0	80	0.5	8	10	1	2	N
0	80	0.6	8	9	1	2	N
0	80	0.7	7	9	1	3	N
0	80	0.8	5	9	1	3	N

Table A5 (cont.): Kinematic model outputs

Model Parameters			Model Output				Field data/model agreement? (M+: Best Fit; M: Maybe - at certain amounts of strain; N: No)
Shear obliquity (ϕ)	Extrusion obliquity (υ)	Kinematic vorticity (Wk)	Range of lineation plunges (X) in degrees.		Range of foliation pole plunges (Z) in degrees		
			min.	max.	min.	max.	
0	80	0.9	4	5	1	2	N
0	80	0.999999	0	8	0	82	N
0	90	0	0	0	0	0	N
0	90	0.1	0	0	0	0	N
0	90	0.2	0	0	0	0	N
0	90	0.3	0	0	0	0	N
0	90	0.4	0	0	0	0	N
0	90	0.5	0	0	0	0	N
0	90	0.6	0	0	0	0	N
0	90	0.7	0	0	0	0	N
0	90	0.8	0	0	0	0	N
0	90	0.9	0	0	0	0	N
0	90	0.999999	0	0	0	0	N
0	100	0	10	10	10	77	N
0	100	0.1	10	10	0	0	N
0	100	0.2	10	10	0	1	N
0	100	0.3	9	10	0	1	N
0	100	0.4	9	10	1	2	N
0	100	0.5	8	10	1	2	N
0	100	0.6	8	9	1	2	N
0	100	0.7	7	9	1	3	N
0	100	0.8	5	9	1	3	N
0	100	0.9	4	9	1	2	N
0	100	0.999999	0	8	0	82	N
0	110	0	20	20	16	68	N
0	110	0.1	20	20	0	1	N
0	110	0.2	20	20	1	2	N
0	110	0.3	19	20	1	3	N
0	110	0.4	18	19	1	3	N
0	110	0.5	17	19	1	4	N
0	110	0.6	15	19	1	4	N
0	110	0.7	13	18	1	5	N
0	110	0.8	11	18	1	5	N
0	110	0.9	7	17	1	4	N
0	110	0.999999	0	16	0	74	N
0	120	0	30	30	19	59	N
0	120	0.1	30	30	0	1	N

Table A5 (cont.): Kinematic model outputs

Model Parameters			Model Output				Field data/model agreement? (M+: Best Fit; M: Maybe - at certain amounts of strain; N: No)
Shear obliquity (ϕ)	Extrusion obliquity (υ)	Kinematic vorticity (Wk)	Range of lineation plunges (X) in degrees.		Range of foliation pole plunges (Z) in degrees		
			min.	max.	min.	max.	
0	120	0.2	29	30	1	2	N
0	120	0.3	29	30	1	4	N
0	120	0.4	27	29	1	4	N
0	120	0.5	26	29	2	5	N
0	120	0.6	23	28	2	6	N
0	120	0.7	20	27	2	6	N
0	120	0.8	16	27	2	6	N
0	120	0.9	11	25	1	5	N
0	120	0.999999	0	24	0	66	N
0	130	0	40	40	19	49	N
0	130	0.1	40	40	0	1	N
0	130	0.2	39	40	1	3	N
0	130	0.3	38	40	1	4	N
0	130	0.4	37	39	2	5	N
0	130	0.5	35	39	2	6	N
0	130	0.6	32	38	2	6	N
0	130	0.7	27	37	2	7	N
0	130	0.8	22	36	1	6	N
0	130	0.9	14	34	1	6	N
0	130	0.999999	0	31	0	58	N
0	140	0.4	47	49	1	5	N
0	140	0.5	44	49	2	6	N
0	140	0.6	41	48	2	6	N
0	140	0.7	35	46	1	6	N
0	140	0.8	27	45	1	6	N
0	140	0.9	16	42	1	5	N
0	140	0.999999	0	38	0	47	N
0	150	0.999999	0	43	0	4	N
0	160	0	70	70	10	20	N
0	160	0.1	70	70	0	1	N
0	160	0.2	70	70	1	2	N
0	160	0.3	69	70	1	2	N
0	160	0.4	68	69	1	3	N
0	160	0.5	66	69	1	3	N
0	160	0.999999	0	43	0	1	N
0	170	0	80	80	5	10	N
0	170	0.1	80	80	0	0	N

Table A5 (cont.): Kinematic model outputs

Model Parameters			Model Output				Field data/model agreement? (M+: Best Fit; M: Maybe - at certain amounts of strain; N: No)
Shear obliquity (ϕ)	Extrusion obliquity (υ)	Kinematic vorticity (Wk)	Range of lineation plunges (X) in degrees.		Range of foliation pole plunges (Z) in degrees		
			min.	max.	min.	max.	
0	170	0.2	80	80	0	1	N
0	170	0.3	79	80	0	1	N
0	170	0.4	79	80	0	2	N
0	170	0.5	78	79	0	2	N
0	170	0.6	75	79	0	2	N
0	170	0.7	70	78	0	2	N
0	170	0.8	48	77	0	2	N
0	170	0.999999	0	34	0	0	N
0	180	0	0*	90*	0	0	N
0	180	0.1	0*	90*	0	0	N
0	180	0.2	0*	90*	0	0	N
0	180	0.3	0*	90*	0	0	N
0	180	0.4	0*	90*	0	0	N
0	180	0.5	0*	90*	0	0	N
0	180	0.6	0*	90*	0	0	N
0	180	0.7	0*	90*	0	0	N
0	180	0.8	0*	90*	0	0	N
0	180	0.9	0*	90*	0	0	N
0	180	0.999999	0	0	0	0	N
20	0	0	0	0	0	0	N
20	0	0.1	89	90	0	1	N
20	0	0.2	88	90	0	2	N
20	0	0.3	87	90	0	3	N
20	0	0.4	85	89	0	4	N
20	0	0.5	83	83	0	5	N
20	0	0.6	79	88	0	5	N
20	0	0.7	71	87	0	6	N
20	10	0	80	80	5	10	N
20	10	0.1	80	80	0	1	N
20	10	0.2	80	80	0	3	N
20	10	0.3	80	81	0	4	N
20	10	0.4	80	81	1	5	N
20	10	0.5	81	82	1	6	N
20	10	0.6	81	83	1	7	N
20	10	0.7	81	86	0	8	N
20	20	0	70	70	10	20	N
20	20	0.1	70	70	0	2	N

Table A5 (cont.): Kinematic model outputs

Model Parameters			Model Output				Field data/model agreement? (M+: Best Fit; M: Maybe - at certain amounts of strain; N: No)
Shear obliquity (ϕ)	Extrusion obliquity (υ)	Kinematic vorticity (Wk)	Range of lineation plunges (X) in degrees.		Range of foliation pole plunges (Z) in degrees		
			min.	max.	min.	max.	
20	20	0.2	70	70	1	4	N
20	20	0.3	70	70	1	5	N
20	20	0.4	70	70	1	7	N
20	20	0.5	70	70	1	8	N
20	20	0.6	70	70	1	9	N
20	20	0.7	70	70	1	10	N
20	20	0.8	70	70	1	11	N
20	20	0.999999	20	20	0	4	N
20	30	0.999999	2	20	0	1	N
20	40	0.4	48	49	2	9	N
20	40	0.5	46	49	2	11	N
20	40	0.6	43	48	2	12	N
20	40	0.7	36	47	2	14	N
20	40	0.8	21	45	1	14	N
20	40	0.9	0	40	1	15	N
20	40	0.999999	2	23	0	1	N
20	50	0	40	40	19	49	N
20	50	0.1	40	40	1	3	N
20	50	0.2	39	40	1	6	N
20	50	0.3	39	40	2	8	N
20	50	0.4	37	39	2	10	N
20	50	0.5	35	39	2	12	N
20	50	0.6	31	38	2	13	N
20	50	0.7	25	36	2	15	N
20	50	0.8	15	34	2	16	N
20	50	0.9	0	31	1	16	N
20	50	0.999999	1	23	0	7	N
20	60	0	30	30	19	60	N
20	60	0.1	30	30	1	3	N
20	60	0.2	29	30	1	6	N
20	60	0.3	28	30	2	8	N
20	60	0.4	27	29	2	10	N
20	60	0.5	25	29	2	12	N
20	60	0.6	21	28	2	14	N
20	60	0.7	16	26	2	15	N
20	60	0.8	9	25	2	16	N
20	60	0.9	0	22	1	17	N

Table A5 (cont.): Kinematic model outputs

Model Parameters			Model Output				Field data/model agreement? (M+: Best Fit; M: Maybe - at certain amounts of strain; N: No)
Shear obliquity (ϕ)	Extrusion obliquity (υ)	Kinematic vorticity (Wk)	Range of lineation plunges (X) in degrees.		Range of foliation pole plunges (Z) in degrees		
			min.	max.	min.	max.	
20	60	0.999999	1	20	0	57	N
20	70	0	20	20	16	68	N
20	70	0.1	20	20	1	3	N
20	70	0.2	19	20	1	5	N
20	70	0.3	18	20	2	8	N
20	70	0.4	17	19	2	10	N
20	70	0.5	15	19	2	12	N
20	70	0.6	12	18	2	14	N
20	70	0.7	8	17	2	15	N
20	70	0.8	3	16	2	16	N
20	70	0.9	1	14	1	17	N
20	70	0.999999	1	20	0	78	N
20	80	0	10	10	10	77	N
20	80	0.1	10	10	0	2	N
20	80	0.2	9	10	1	5	N
20	80	0.3	9	10	1	7	N
20	80	0.4	8	9	2	9	N
20	80	0.5	6	9	2	11	N
20	80	0.6	4	8	2	13	N
20	80	0.7	1	7	2	14	N
20	80	0.8	0	7	2	15	N
20	80	0.9	1	8	1	16	N
20	80	0.999999	1	20	0	85	N
20	90	0	0	0	0	0	N
20	90	0.1	0	0	0	2	N
20	90	0.2	0	0	1	4	N
20	90	0.3	0	1	1	6	N
20	90	0.4	1	2	1	8	N
20	90	0.5	1	3	1	9	N
20	90	0.6	1	4	2	11	N
20	90	0.7	2	6	2	12	N
20	90	0.8	2	8	1	14	N
20	90	0.9	3	11	1	14	N
20	90	0.999999	4	20	0	86	N
20	100	0	10	10	10	77	N
20	100	0.1	10	10	0	1	N
20	100	0.2	10	10	0	3	N

Table A5 (cont.): Kinematic model outputs

Model Parameters			Model Output				Field data/model agreement? (M+: Best Fit; M: Maybe - at certain amounts of strain; N: No)
Shear obliquity (ϕ)	Extrusion obliquity (υ)	Kinematic vorticity (Wk)	Range of lineation plunges (X) in degrees.		Range of foliation pole plunges (Z) in degrees		
			min.	max.	min.	max.	
20	100	0.3	10	10	1	4	N
20	100	0.4	10	11	1	6	N
20	100	0.5	10	11	1	7	N
20	100	0.6	11	12	1	9	N
20	100	0.7	11	13	1	10	N
20	100	0.8	11	14	1	11	N
20	100	0.9	11	15	1	13	N
20	100	0.999999	12	20	0	78	N
20	110	0	20	20	16	68	N
20	110	0.1	20	20	0	1	N
20	110	0.2	20	20	0	2	N
20	110	0.3	20	20	0	3	N
20	110	0.4	20	20	0	4	N
20	110	0.5	19	20	0	5	N
20	110	0.6	19	20	0	6	N
20	110	0.7	18	20	0	7	N
20	110	0.8	18	20	0	9	N
20	110	0.9	17	20	0	10	N
20	110	0.999999	20	20	0	70	N
20	120	0	30	30	19	59	N
20	120	0.1	30	30	0	1	N
20	120	0.2	30	30	0	1	N
20	120	0.3	29	30	0	2	N
20	120	0.4	29	30	0	2	N
20	120	0.5	28	30	0	3	N
20	120	0.6	27	29	0	4	N
20	120	0.7	25	29	0	5	N
20	120	0.8	23	29	0	6	N
20	120	0.9	21	29	0	8	N
20	120	0.999999	20	28	0	62	N
20	130	0	40	40	19	49	N
20	130	0.1	40	40	0	0	N
20	130	0.2	39	40	0	1	N
20	130	0.3	39	40	0	1	N
20	130	0.4	38	39	0	1	N
20	130	0.5	36	39	0	2	N
20	130	0.6	34	39	0	2	N

Table A5 (cont.): Kinematic model outputs

Model Parameters			Model Output				Field data/model agreement? (M+: Best Fit; M: Maybe - at certain amounts of strain; N: No)
Shear obliquity (ϕ)	Extrusion obliquity (υ)	Kinematic vorticity (Wk)	Range of lineation plunges (X) in degrees.		Range of foliation pole plunges (Z) in degrees		
			min.	max.	min.	max.	
20	130	0.7	32	38	0	3	N
20	130	0.8	28	38	0	5	N
20	130	0.9	24	37	0	7	N
20	130	0.999999	20	36	0	55	N
20	140	0	50	50	17	40	N
20	140	0.1	50	50	0	1	N
20	140	0.2	49	50	0	1	N
20	140	0.3	48	50	0	1	N
20	140	0.4	47	49	0	2	N
20	140	0.5	45	49	0	2	N
20	140	0.6	42	48	0	2	N
20	140	0.7	38	47	0	2	N
20	140	0.8	34	47	0	4	N
20	140	0.9	27	45	1	6	N
20	140	0.999999	20	44	0	46	N
20	160	0	70	70	10	20	N
20	160	0.1	70	70	0	0	N
20	160	0.2	69	70	0	1	N
20	160	0.3	69	70	0	1	N
20	160	0.4	66	69	0	1	N
20	170	0	80	80	5	10	N
20	170	0.1	80	80	0	1	N
20	170	0.2	79	80	0	1	N
20	170	0.3	78	80	0	2	N
20	170	0.4	76	79	0	2	N
20	170	0.5	73	79	0	3	N
20	170	0.6	69	78	0	4	N
20	180	0	0*	90*	0	0	N
20	180	0.1	89	90	0	1	N
20	180	0.2	88	90	0	2	N
20	180	0.3	87	90	0	3	N
20	180	0.4	85	89	0	4	N
20	180	0.5	83	89	0	5	N
20	180	0.6	79	88	0	5	N
20	180	0.7	71	87	0	6	N

Table A5 (cont.): Kinematic model outputs

A.2. Lozenges

A.2.1. Blue Draw Metagabbro

Site number	Latitude (deg.)	Longitude (deg.)	Lithology	Lozenge observation plane 2D axes	Lozenge observation plane strike (azim deg.)	Lozenge observation plane dip (in deg. if numbered)	Lozenge long axis (cm)	Lozenge short axis (cm)	Lozenge aspect ratio	2D lozenge long axis trend (in deg.; X on the XZ-plane; Y on the YZ-plane)	2D long axis plunge (deg.)
NG2101	44.1975	-103.53721	BDM	XZ	260	Subvertical	62	6	10.3	080	85
NG2101	44.1975	-103.53721	BDM	XZ	260	Subvertical	62	8.5	7.3	080	86
NG2101	44.1975	-103.53721	BDM	XZ	260	Subvertical	120	15	8.0	080	88
NG2102	44.19781	-103.53709	BDM	XY	350	Subvertical	75	30	2.5	350	62
NG2103	44.19788	-103.53712	BDM	XZ	260	Subvertical	17*	1.5*	11.3	070	65
NG2104	44.1978	-103.53711	BDM	XY	354	Subvertical	11*	5*	2.2	174	30
NG2106	44.19786	-103.53725	BDM	XZ	225	Subvertical	10*	4.5*	2.2	315	80
NG2108	44.198	-103.53749	BDM	YZ	240	25 SE	6*	2*	3.0	060	70
NG2121	44.18553	-103.54756	BDM	N/A	000	N/A	N/A	N/A	massive	N/A	N/A
NG2124	44.19266	-103.5353	BDM	YZ	275	35 S	30	5	6.0	095	85
NG2126	44.20439	-103.52659	BDM	YZ	230	Subhorizontal	30	9	3.3	050	80
NG2126	44.20439	-103.52659	BDM	YZ	235	Subhorizontal	31	8	3.9	235	80
NG2127	44.20471	-103.52587	BDM	YZ	235	Subhorizontal	45	20	2.3	235	80
NG2128	44.20406	-103.52512	BDM	XZ	240	Subvertical	118	82	1.4	060	80
NG2133	44.19113	-103.53535	BDM	XZ	252	Subvertical	254	30	8.5	252	85
NG2137	44.19472	-103.53818	BDM	XY	350	Subvertical	7.5*	5.0*	1.5	350	80
NG2138	44.19506	-103.53751	BDM	XZ	260	Subvertical	84	60	1.4	080	65
NG2139	44.19526	-103.53735	BDM	YZ	250	Subhorizontal	31	25	1.2	250	90
NG2139	44.19526	-103.53735	BDM	YZ	250	Subhorizontal	29	27.5	1.1	250	90
NG2139	44.19526	-103.53735	BDM	YZ	250	Subhorizontal	45	45	1.0	250	90

Table A6: BDM lozenge aspect ratios and orientations. *Denotes measurements from field photos

A.2.1. Blue Draw Metagabbro cont.

Site number	Latitude (deg.)	Longitude (deg.)	Lithology	Lozenge observation plane 2D axes	Lozenge observation plane strike (azim deg.)	Lozenge observation plane dip (in deg. if numbered)	Lozenge long axis (cm)	Lozenge short axis (cm)	Lozenge aspect ratio	2D lozenge long axis trend (in deg.; X on the XZ-plane; Y on the YZ-plane)	2D long axis plunge (deg.)
NG2139	44.19526	-103.53735	BDM	YZ	250	Subhorizontal	68	60	1.1	250	90
NG2139	44.19526	-103.53735	BDM	YZ	250	Subhorizontal	28	25	1.1	250	90
NG2139	44.19526	-103.53735	BDM	YZ	250	Subhorizontal	100	94	1.1	250	90
NG2140	44.19412	-103.53588	BDM	YZ	190	Subhorizontal	7	0.5	14.0	190	15
NG2140	44.19412	-103.53588	BDM	YZ	190	Subhorizontal	6	0.3	20.0	190	10
NG2142	44.19441	-103.535268	BDM	XZ	265	Subvertical	39	19	2.1	265	60
NG2142	44.19441	-103.535268	BDM	XZ	265	Subvertical	26	10	2.6	265	60
NG2147	44.19785	-103.53697	BDM	XZ	240	Subvertical	6*	1*	6.0	240	65
NG2148	44.1977	-103.53688	BDM	XZ	060	Subvertical	36	5	7.2	060	70
NG2148	44.1977	-103.53688	BDM	XZ	060	Subvertical	53	4	13.3	060	70
NG2148	44.1977	-103.53688	BDM	XZ	060	Subvertical	42	3	14.0	060	70
NG2148	44.1977	-103.53688	BDM	XZ	060	Subvertical	53.5	4	13.4	060	70
NG2149	44.19781	-103.53672	BDM	YZ	233	Subhorizontal	29	5	5.8	233	75
NG2151	44.19777	-103.53672	BDM	XZ	228	Subvertical	19	6	3.2	228	80
NG2151	44.19777	-103.53672	BDM	XZ	220	Subvertical	39	12	3.3	220	85
NG2152	44.19773	-103.53665	BDM	XZ	222	Subvertical	58	6.5	8.9	222	80
NG2153	44.19765	-103.53651	BDM	XZ	220	Subvertical	36	4	9.0	220	85
NG2153	44.19765	-103.53651	BDM	XZ	225	Subvertical	42	5.5	7.6	225	85
NG2153	44.19765	-103.53651	BDM	XZ	220	Subvertical	71	17	4.2	220	85
NG2155	44.19759	-103.53656	BDM	XZ	230	Subvertical	340	100	3.4	230	89

Table A6 (cont.): BDM lozenge aspect ratios orientations. *Denotes measurements from field photos

A.2.2. Boxelder Creek Quartzite

Site number	Latitude (deg.)	Longitude (deg.)	Lithology	Lozenge observation plane 2D axes	Lozenge observation plane strike (azim deg.)	Lozenge observation plane dip (in deg. if numbered)	Lozenge long axis (cm)	Lozenge short axis (cm)	Lozenge aspect ratio	2D lozenge long axis trend (in deg.; X on the XZ-plane; Y on the YZ-plane)	2D long axis plunge (deg.)
NG2116	44.19964	-103.51182	BCQ	XZ	255	Subvertical	25	14	1.8	255	80
NG2116	44.19964	-103.51182	BCQ	XZ	245	Subvertical	44	18	2.4	245	80
NG2116	44.19964	-103.51182	BCQ	YZ	165	Subhorizontal	25*	20*	1.3*	165	85
NG2116	44.19964	-103.51182	BCQ	XZ	245	Subvertical	30	13	2.3	245	79
NG2116	44.19964	-103.51182	BCQ	XY	340	Subvertical	4*	3.4*	1.17*	166	75
NG2116	44.19964	-103.51182	BCQ	XY	340	Subvertical	6*	5*	1.2*	166	65
NG2117	44.19987	-103.51201	BCQ	XZ	255	Subvertical	25	14	1.8	255	75
NG2117	44.19987	-103.51201	BCQ	XZ	245	Subvertical	44	18	2.4	245	80
NG2118	44.20143	-103.51516	BCQ	YZ	225	Subhorizontal	30	6	5.0	225	85
NG2118	44.20143	-103.51516	BCQ	YZ	220	Subhorizontal	20	4	5.0	220	75
NG2119	44.20138	-103.51487	BCQ	YZ	265	Subhorizontal	22	6	3.7	265	90
NG2119	44.20138	-103.51487	BCQ	YZ	270	Subhorizontal	14	3	4.7	270	90
NG2123	44.18917	-103.53809	BCQ	YZ	245	Subhorizontal	13*	6.5*	2.0	245	75
NG2130	44.20286	-103.54227	BCQ	YZ	280	Subhorizontal	29	8	3.6	280	0
NG2131	44.203	-103.54167	BCQ	XZ	270	Subvertical	18*	3*	6.0	270	86
NG2131	44.203	-103.54167	BCQ	YZ	219	Subhorizontal	10.7*	3.0*	3.5	330	0
NG2145	44.19548	-103.53383	BCQ	XZ	270	Subvertical	7.5*	2.0*	3.8	270	65

Table A7: BCQ lozenge aspect ratios orientations. *Denotes measurements from field photos

A.2.3. Lozenge Aspect Ratio Groupings by Observation Plane (BDM)

Site number	Latitude (deg.)	Longitude (deg.)	Lithology	Lozenge observation plane 2D axes	Lozenge observation plane strike (azim deg.)	Lozenge observation plane dip (in deg. if numbered)	Lozenge long axis (cm)	Lozenge short axis (cm)	Lozenge aspect ratio
NG2121	44.18553	-103.54756	BDM	N/A	000	N/A	N/A	N/A	0
NG2137	44.19472	-103.53818	BDM	XY	350	Subvertical	7.5*	5.0*	1.5
NG2104	44.1978	-103.53711	BDM	XY	354	Subvertical	11*	5*	2.2
NG2102	44.19781	-103.53709	BDM	XY	350	Subvertical	75	30	2.5
NG2138	44.19506	-103.53751	BDM	XZ	260	Subvertical	84	60	1.4
NG2128	44.20406	-103.52512	BDM	XZ	240	Subvertical	118	82	1.4
NG2142	44.19441	-103.535268	BDM	XZ	265	Subvertical	39	19	2.1
NG2106	44.19786	-103.53725	BDM	XZ	225	Subvertical	10*	4.5*	2.2
NG2142	44.19441	-103.535268	BDM	XZ	265	Subvertical	26	10	2.6
NG2151	44.19777	-103.53672	BDM	XZ	228	Subvertical	19	6	3.2
NG2151	44.19777	-103.53672	BDM	XZ	220	Subvertical	39	12	3.3
NG2155	44.19759	-103.53656	BDM	XZ	230	Subvertical	340	100	3.4
NG2153	44.19765	-103.53651	BDM	XZ	220	Subvertical	71	17	4.2
NG2147	44.19785	-103.53697	BDM	XZ	240	Subvertical	6*	1*	6.0
NG2148	44.1977	-103.53688	BDM	XZ	060	Subvertical	36	5	7.2
NG2101	44.1975	-103.53721	BDM	XZ	260	Subvertical	62	8.5	7.3
NG2153	44.19765	-103.53651	BDM	XZ	225	Subvertical	42	5.5	7.6
NG2101	44.1975	-103.53721	BDM	XZ	260	Subvertical	120	15	8.0
NG2133	44.19113	-103.53535	BDM	XZ	252	Subvertical	254	30	8.5
NG2152	44.19773	-103.53665	BDM	XZ	222	Subvertical	58	6.5	8.9
NG2153	44.19765	-103.53651	BDM	XZ	220	Subvertical	36	4	9.0
NG2101	44.1975	-103.53721	BDM	XZ	260	Subvertical	62	6	10.3
NG2103	44.19788	-103.53712	BDM	XZ	260	Subvertical	17*	1.5*	11.3
NG2148	44.1977	-103.53688	BDM	XZ	060	Subvertical	53	4	13.3
NG2148	44.1977	-103.53688	BDM	XZ	060	Subvertical	53.5	4	13.4
NG2148	44.1977	-103.53688	BDM	XZ	060	Subvertical	42	3	14.0
NG2139	44.19526	-103.53735	BDM	YZ	250	Subhorizontal	45	45	1.0
NG2139	44.19526	-103.53735	BDM	YZ	250	Subhorizontal	29	27.5	1.1
NG2139	44.19526	-103.53735	BDM	YZ	250	Subhorizontal	100	94	1.1
NG2139	44.19526	-103.53735	BDM	YZ	250	Subhorizontal	28	25	1.1
NG2139	44.19526	-103.53735	BDM	YZ	250	Subhorizontal	68	60	1.1
NG2139	44.19526	-103.53735	BDM	YZ	250	Subhorizontal	31	25	1.2
NG2127	44.20471	-103.52587	BDM	YZ	235	Subhorizontal	45	20	2.3
NG2108	44.198	-103.53749	BDM	YZ	240	25 SE	6*	2*	3.0
NG2126	44.20439	-103.52659	BDM	YZ	230	Subhorizontal	30	9	3.3
NG2126	44.20439	-103.52659	BDM	YZ	235	Subhorizontal	31	8	3.9
NG2149	44.19781	-103.53672	BDM	YZ	233	Subhorizontal	29	5	5.8
NG2124	44.19266	-103.5353	BDM	YZ	275	35 S	30	5	6.0
NG2140	44.19412	-103.53588	BDM	YZ	190	Subhorizontal	7	0.5	14.0
NG2140	44.19412	-103.53588	BDM	YZ	190	Subhorizontal	6	0.3	20.0

Table A8: BDM. Lozenge aspect ratios ranging, from low to high, grouped by observation plane.

A.2.4. Lozenge Aspect Ratio Groupings by Observation Plane (BCQ)

Site number	Latitude (deg.)	Longitude (deg.)	Lithology	Lozenge observation plane 2D axes	Lozenge observation plane strike (azim deg.)	Lozenge observation plane dip (in deg. if numbered)	Lozenge long axis (cm)	Lozenge short axis (cm)	Lozenge aspect ratio
NG2116	44.19964	-103.51182	BCQ	XY	340	Subvertical	4*	3.4*	1.17*
NG2116	44.19964	-103.51182	BCQ	XY	340	Subvertical	6*	5*	1.2*
NG2116	44.19964	-103.51182	BCQ	XZ	255	Subvertical	25	14	1.8
NG2117	44.19987	-103.51201	BCQ	XZ	255	Subvertical	25	14	1.8
NG2116	44.19964	-103.51182	BCQ	XZ	245	Subvertical	30	13	2.3
NG2116	44.19964	-103.51182	BCQ	XZ	245	Subvertical	44	18	2.4
NG2117	44.19987	-103.51201	BCQ	XZ	245	Subvertical	44	18	2.4
NG2145	44.19548	-103.53383	BCQ	XZ	270	Subvertical	7.5*	2.0*	3.8
NG2131	44.203	-103.54167	BCQ	XZ	270	Subvertical	18*	3*	6.0
NG2116	44.19964	-103.51182	BCQ	YZ	165	Subhorizontal	25*	20*	1.3*
NG2123	44.18917	-103.53809	BCQ	YZ	245	Subhorizontal	13*	6.5*	2.0
NG2131	44.203	-103.54167	BCQ	YZ	219	Subhorizontal	10.7*	3.0*	3.5
NG2130	44.20286	-103.54227	BCQ	YZ	280	Subhorizontal	29	8	3.6
NG2119	44.20138	-103.51487	BCQ	YZ	265	Subhorizontal	22	6	3.7
NG2119	44.20138	-103.51487	BCQ	YZ	270	Subhorizontal	14	3	4.7
NG2118	44.20143	-103.51516	BCQ	YZ	225	Subhorizontal	30	6	5.0
NG2118	44.20143	-103.51516	BCQ	YZ	220	Subhorizontal	20	4	5.0

Table A9: BCQ. Lozenge aspect ratios ranging, from low to high, grouped by observation plane.

A.2.5. Lozenge Long-Axis Orientation Groupings by Observation Plane (BDM)

Site number	Latitude (deg.)	Longitude (deg.)	Lithology	Lozenge observation plane 2D axes	Lozenge observation plane strike (azim deg.)	Lozenge observation plane dip (in deg. if numbered)	2D lozenge long axis trend (in deg.; X on the XZ-plane; Y on the YZ-plane)	2D long axis plunge (deg.)
NG2104	44.1978	-103.53711	BDM	XY	354	Subvertical	174	30
NG2102	44.19781	-103.53709	BDM	XY	350	Subvertical	350	62
NG2137	44.19472	-103.53818	BDM	XY	350	Subvertical	350	80
NG2142	44.19441	-103.535268	BDM	XZ	265	Subvertical	265	60
NG2142	44.19441	-103.535268	BDM	XZ	265	Subvertical	265	60
NG2103	44.19788	-103.53712	BDM	XZ	260	Subvertical	070	65
NG2138	44.19506	-103.53751	BDM	XZ	260	Subvertical	080	65
NG2147	44.19785	-103.53697	BDM	XZ	240	Subvertical	240	65
NG2148	44.1977	-103.53688	BDM	XZ	060	Subvertical	060	70
NG2148	44.1977	-103.53688	BDM	XZ	060	Subvertical	060	70
NG2148	44.1977	-103.53688	BDM	XZ	060	Subvertical	060	70
NG2148	44.1977	-103.53688	BDM	XZ	060	Subvertical	060	70
NG2128	44.20406	-103.52512	BDM	XZ	240	Subvertical	060	80
NG2152	44.19773	-103.53665	BDM	XZ	222	Subvertical	222	80
NG2151	44.19777	-103.53672	BDM	XZ	228	Subvertical	228	80
NG2106	44.19786	-103.53725	BDM	XZ	225	Subvertical	315	80
NG2101	44.1975	-103.53721	BDM	XZ	260	Subvertical	080	85
NG2151	44.19777	-103.53672	BDM	XZ	220	Subvertical	220	85
NG2153	44.19765	-103.53651	BDM	XZ	220	Subvertical	220	85
NG2153	44.19765	-103.53651	BDM	XZ	220	Subvertical	220	85
NG2153	44.19765	-103.53651	BDM	XZ	225	Subvertical	225	85
NG2133	44.19113	-103.53535	BDM	XZ	252	Subvertical	252	85
NG2101	44.1975	-103.53721	BDM	XZ	260	Subvertical	080	86
NG2101	44.1975	-103.53721	BDM	XZ	260	Subvertical	080	88
NG2155	44.19759	-103.53656	BDM	XZ	230	Subvertical	230	89
NG2140	44.19412	-103.53588	BDM	YZ	190	Subhorizontal	190	10
NG2140	44.19412	-103.53588	BDM	YZ	190	Subhorizontal	190	15
NG2108	44.198	-103.53749	BDM	YZ	240	25 SE	060	70
NG2149	44.19781	-103.53672	BDM	YZ	233	Subhorizontal	233	75
NG2126	44.20439	-103.52659	BDM	YZ	230	Subhorizontal	050	80
NG2126	44.20439	-103.52659	BDM	YZ	235	Subhorizontal	235	80
NG2127	44.20471	-103.52587	BDM	YZ	235	Subhorizontal	235	80
NG2124	44.19266	-103.5353	BDM	YZ	275	35 S	095	85
NG2139	44.19526	-103.53735	BDM	YZ	250	Subhorizontal	250	90
NG2139	44.19526	-103.53735	BDM	YZ	250	Subhorizontal	250	90
NG2139	44.19526	-103.53735	BDM	YZ	250	Subhorizontal	250	90
NG2139	44.19526	-103.53735	BDM	YZ	250	Subhorizontal	250	90
NG2139	44.19526	-103.53735	BDM	YZ	250	Subhorizontal	250	90
NG2139	44.19526	-103.53735	BDM	YZ	250	Subhorizontal	250	90

Table A10: BDM. Lozenge long-axis orientations, from shallow to steeply plunging, grouped by observation plane.

A.2.6. Lozenge Long-Axis Orientation Groupings by Observation Plane (Boxelder Creek Quartzite)

Site number	Latitude (deg.)	Longitude (deg.)	Lithology	Lozenge observation plane 2D axes	Lozenge observation plane strike (azim deg.)	Lozenge observation plane dip (in deg. if numbered)	2D lozenge long axis trend (in deg.; X on the XZ-plane; Y on the YZ-plane)	2D long axis plunge (deg.)
NG2116	44.19964	-103.51182	BCQ	XY	340	Subvertical	166	65
NG2116	44.19964	-103.51182	BCQ	XY	340	Subvertical	166	75
NG2145	44.19548	-103.53383	BCQ	XZ	270	Subvertical	270	65
NG2117	44.19987	-103.51201	BCQ	XZ	255	Subvertical	255	75
NG2116	44.19964	-103.51182	BCQ	XZ	245	Subvertical	245	79
NG2116	44.19964	-103.51182	BCQ	XZ	255	Subvertical	255	80
NG2116	44.19964	-103.51182	BCQ	XZ	245	Subvertical	245	80
NG2117	44.19987	-103.51201	BCQ	XZ	245	Subvertical	245	80
NG2131	44.203	-103.54167	BCQ	XZ	270	Subvertical	270	86
NG2130	44.20286	-103.54227	BCQ	YZ	280	Subhorizontal	280	0
NG2131	44.203	-103.54167	BCQ	YZ	219	Subhorizontal	330	0
NG2118	44.20143	-103.51516	BCQ	YZ	220	Subhorizontal	220	75
NG2123	44.18917	-103.53809	BCQ	YZ	245	Subhorizontal	245	75
NG2116	44.19964	-103.51182	BCQ	YZ	165	Subhorizontal	165	85
NG2118	44.20143	-103.51516	BCQ	YZ	225	Subhorizontal	225	85
NG2119	44.20138	-103.51487	BCQ	YZ	265	Subhorizontal	265	90
NG2119	44.20138	-103.51487	BCQ	YZ	270	Subhorizontal	270	90

Table A11: BCQ. Lozenge long-axis orientations, from shallow to steeply plunging, grouped by observation plane.

A.2.7. Data Table for Lozenge Flinn Plot

	Lozenge axis length (cm)					
Site #	**x**	**y**	**z**	**Lithology**	**Ryz**	**Rxy**
NG2101	62	30	6	BDM	**5.0**	**2.1**
NG2101	62	30	8.5	BDM	**3.5**	**2.1**
NG2101	120	30	15	BDM	**2.0**	**4.0**
NG2103	17	7.7	1.5	BDM	**5.1**	**2.2**
NG2106	10	13.5	4.5	BDM	**3.0**	**0.7**
NG2126	118	30	9	BDM	**3.3**	**3.9**
NG2126	118	31	8	BDM	**3.9**	**3.8**
NG2127	118	45	20	BDM	**2.3**	**2.6**
NG2137	84	56	60	BDM	**0.9**	**1.5**
NG2139	84	31	25	BDM	**1.2**	**2.7**
NG2139	84	29	27.5	BDM	**1.1**	**2.9**
NG2139	84	45	45	BDM	**1.0**	**1.9**
NG2139	84	68	60	BDM	**1.1**	**1.2**
NG2139	84	28	25	BDM	**1.1**	**3.0**
NG2139	84	100	94	BDM	**1.1**	**0.8**
NG2148	36	14.4	5	BDM	**2.9**	**2.5**
NG2148	53	30	4	BDM	**7.5**	**1.8**
NG2148	42	30	3	BDM	**10.0**	**1.4**
NG2148	53.5	30	4	BDM	**7.5**	**1.8**
NG2149	29	30	5	BDM	**6.0**	**2.0**
NG2151	19	30	6	BDM	**5.0**	**2.0**
NG2151	39	30	12	BDM	**2.5**	**2.0**
NG2152	58	30	6.5	BDM	**4.6**	**2.0**
NG2153	36	30	4	BDM	**7.5**	**2.0**
NG2153	42	30	5.5	BDM	**5.5**	**2.0**
NG2153	71	30	17	BDM	**1.8**	**2.4**
	Lozenge axis length (cm)					
Site #	**x**	**y**	**z**	**Lithology**	**Ryz**	**Rxy**
NG2116	25	19.2	15	BCQ	**1.3**	**1.2**
NG2116	44	25	18	BCQ	**1.4**	**2.0**
NG2116	60	30	6	BCQ	**1.3**	**1.8**
NG2117	40	20	4	BCQ	**4.0**	**1.2**
NG2117	33	22	6	BCQ	**3.7**	**1.2**
NG2130	48	29	8	BCQ	**3.6**	**1.7**
NG2131	18	10.7	3	BCQ	**3.6**	**1.7**

Table A12: Lozenge aspect ratios calculated from the *x*, *y*, and *z* axes lengths, used to represent the strain ellipsoid Flinn plot (Fig. 6-12 in Chapter 6). The BDM is in purple and the BCQ is in orange. Ryz and Rxy are shown in grey, and were plotted on the *x*- and *y*-axes, respectively.